Copyright

by

Chae Bin Kim

2016

The Dissertation Committee for Chae Bin Kim Certifies that this is the approved version of the following dissertation:

Photodirecting Surface Energy Driven Marangoni Convection to Pattern Thin Polymer Films

Committee:

____
Christopher J. Ellison, Supervisor

____
Roger T. Bonnecaze

____
Carlton G. Willson

____
Isaac C. Sanchez

____
Wei Li

Photodirecting Surface Energy Driven Marangoni Convection to Pattern Thin Polymer Films

by

Chae Bin Kim, B.S.CH.E

Dissertation

Presented to the Faculty of the Graduate School of

The University of Texas at Austin

in Partial Fulfillment

of the Requirements

for the Degree of

Doctor of Philosophy

The University of Texas at Austin

August 2016

Dedication

Dedicated to my family.

Acknowledgements

First, I would like to thank Professor Chris Ellison for being the greatest advisor. He has been always there to offer his expertise and guidance through the process. Only under his advisement, I could have the best possible training in the area of polymers which has also given me the opportunity to lay a solid foundation for my personal and academic growth and for my future as an independent researcher. Also, I am really delighted to work with and learn from the prominent faculty members and amazing peers at the University of Texas at Austin. I am sure that the University of Texas at Austin has provided the best environment for me to continue and broaden my research objectives and enhance my research skills during past years.

Secondly, I couldn't have made it through my Ph.D. without the support I received from several colleagues. My labmates and close friends Reika Katsumata, Sunshinze Zhou, Dr. Dustin Janes, Yunping Fei, Dr. Amanda Jones, Heonjoo Ha, Dr. Kadhir Shanmuganathan, Dr. Sateesh Peddini, Dr. Joshua Katzenstein, Dr. Yichen Fang, Dr. Zhenpeng Li, and Han Xiao were always there to offer invaluable supports. I am also very grateful for my undergraduate researchers, Nathan Prisco, Dana McGuffin, Zach Dotson, Austin Dulaney, Drew Heilman, and Rohan Makhija, who performed much of the tedious work and contributed to make many projects to work. This research in its entirety would be incomplete at best if not for the collective contributions from the aforementioned individuals. I am very grateful to have had the opportunity to work with

all of these talented people and a significant amount of credit for the successful results presented in this document goes to them for their contributions.

Photodirecting Surface Energy Driven Marangoni Convection to Pattern Thin Polymer Films

Chae Bin Kim, Ph.D.

The University of Texas at Austin, 2016

Supervisor: Christopher J. Ellison

Significant research effort in the last several decades has been devoted to controlling surface topography at different length scales. Especially important are the micro- to nano-meter length scales because of their overarching importance in a variety of applications including cell biology, tissue engineering, coatings, optics, and microelectronics. While the requirements of many applications are well-served by conventional patterning methods such as photolithography and contact printing, there still remains a need for processes possessing eco-friendly and non-contact fabrication steps. These aspects are particularly crucial in laboratory and industrial settings where access to expensive clean room infrastructure, use of toxic developing solvents, and etching protocols required for conventional methods are often not readily available.

Bearing the aforementioned perspective in mind, my research topic has been focused on developing a new polymer film patterning method by photodirecting Marangoni flow in thin films. The Marangoni effect causes liquids to flow towards

localized regions of higher surface tension. In a thin film, such flow results in smooth thickness variations and may represent a practically useful route to manufacture topographically patterned surfaces. This document describes my research efforts first focused on fundamentally understanding the Marangoni effect. This fundamental understanding is then exploited for developing and optimizing a number of different materials and processing protocols that enable generalization of the approach as a polymer film patterning method. Finally, taking these findings in entirety, this thesis suggests this eco-friendly and non-contact fabrication approach could potentially be implemented in high-throughput manufacturing environments.

Table of Contents

List of Tables xv

List of Figures xvi

Chapter 1: Micron and Sub-micron Patterning of Polymer Thin Films 1

1.1 Background and Significance 1

1.2 The Marangoni Effect 2

1.3 Marangoni Driven Patterning of Polystyrene Thin Films 3

1.4 Summary 5

1.5 References..8

Chapter 2: Theoretical Framework to Predict Marangoni Patterning for PS.........11

2.1 Introduction...11

2.2 Theoretical Model...12

2.2.1 Model and Numerical Method 12

2.2.2 Scaling & Linearized Solution...14

2.3 Experimental..16

2.3.1 Materials 16

2.3.2 Sample Preparation 17

2.3.3 UV Exposure...17

2.3.4 Topography Creation and Characterization 18

2.4 Results and Discussion 19

2.4.1 Physical Property Values 19

2.4.2 Evolution of Topographical Features after Annealing above T_g 21

2.4.3 Quantitative Comparison of the Model to Experimental Data ...25

2.4.4 Model Predictions of Marangoni-Driven Flow at Various Conditions 27

2.5 Conclusion 30

2.6 References...31

Chapter 3: Bidirectional Control of Flow in Thin Polymer Films by Photochemically Manipulating Surface Tension 33
3.1 Introduction 33
3.2 Methods 34
3.2.1 Materials 34
3.2.2 Film Preparation and Characterization 34
3.2.3 Topography Formation and Characterization 34
3.2.4 Characterization of Properties and Composition 35
3.2.5 Predictive Estimates of Surface Energy Changes 37
3.2.6 Contact Angle Analysis of Dewetted Polymer 37
3.3 Results and Discussion 38
3.3.1 Photochemical Transformation Strategy 38
3.3.2 Pattern Formation and Directionality 41
3.3.3 Molecular Characterization Upon Chemical Transformations 44
3.3.3.1 Composition Changes Due to Decarboxylation 44
3.3.3.2 Composition Changes Due to Dehydrogenation 46
3.3.3.3 Surface Tension Changes 48
3.3.4 Bidirectional Flow in One Polymer Film 50
3.4 Conclusions 53
3.5 References 54
Chapter 4: Generating Large and Thermally Stable Marangoni-driven Topographical Patterns in Thin Polymer Films by Photochemically Stabilizing the Surface Energy Gradient 55
4.1 Introduction 55
4.2 Experimental Methods 56
4.2.1 Materials 56
4.2.2 Polymer Synthesis and Characterization 56
4.2.3 Thin Film Sample Preparation and Characterization 57
4.2.4 Topography Formation and Characterization 59
4.3 Results and Discussion 60
4.3.1 Polymer Design 60

4.3.2 Topography Formation 63
4.3.3 Photochemical Mechanism and Characterization.......................66
4.3.4 Physical Patterning Behavior..69
4.4 Conclusions...73
4.5 References...73

Chapter 5: Patterning Thin Polymer Films by Photodirecting the Marangoni Effect using a Photosensitizer...75
5.1 Introduction...75
5.2 Experimental...76
5.2.1 Materials 76
5.2.2 Film Preparation...76
5.2.3 Light Exposure Conditions 76
5.2.4 Feature Development...77
5.2.5 Characterization 77
5.3 Results and Discussion 79
5.3.1 Chemical Patterning Mechanism 82
5.3.2 Physical Patterning Mechanism..89
5.4 Conclusions...92
5.5 References...93

Chapter 6: A Photochemical Approach to Stabilizing Marangoni-driven Patterned Polymer Films using Photosensitizers 95
6.1 Introduction...95
6.2 Experimental...96
6.2.1 Materials 96
6.2.2 Film Preparation and Characterization 96
6.2.3 UV/Vis Spectroscopy...97
6.2.4 Topography Formation and Characterization 98
6.2.5 Fourier Transform Infrared Spectroscopy (FTIR) 99
6.2.6 Sol Fraction Measurements...99

6.3 Results and Discussion 100
6.3.1 Patterning of Topographic Features..100
6.3.2 Patterning Throughput and Aspect Ratio.................................103
6.3.3 Photochemical Conversion of Benzophenone Groups 104
6.3.4 Factors Contributing to Feature Formation..............................111
6.3.5 Directing the Morphology of a Structured Overlayer...............114
6.4 Conclusions...117
6.5 References...118

Chapter 7: Marangoni Instability Driven Surface Relief Grating in an Azobenzene Containing Polymer Film..120
7.1 Introduction...120
7.2 Experimental...122
7.2.1 Materials 122
7.2.2 Synthesis of 4-(acryloyloxyhexyloxy)-4′-pentylazobenzene (5Az6A) 122
7.2.3 Polymerization and Polymer Characterization 123
7.2.4 Film Preparation..126
7.2.5 Topography Formation and Characterization 126
7.2.6 Film Characterization..127
7.3 Results and Discussion 128
7.4 Conclusions...139
7.5 Referencees...139

Chapter 8: Future Work 142
8.1 BCP/LCP Directed Self-assembly...142
8.1.1 Shear Alignment 143
8.1.2 Direct Marangoni Flow on BCP 144
8.1.3 Surface Roughening...144
8.2 Improve Feature Aspect Ratio 145
8.2.1 Exploiting Secondary Peak Formation 147
8.2.2 Controlled PAG/PBG Diffusion Method to Reduce the Critical Dimension of the Surface Energy Gradient 148

8.2.3 Smaller Periodicity using Shrinking Substrates........................148
8.3 References..149

Appendices..151

Appendix A: Theoretical Framework to Predict Marangoni Patterning for PS...151
A.1 Initial Concentration Profile...151
A.2 Glass Transition Temperature of PS 152
A.3 Viscosity of PS blend at 120 °C...154
A.4 Extracting Surface Tension Gradients and Diffusivities......................155
A.5 Secondary Peaks at Short Times..157

Appendix B: Bidirectional Control of Flow in Thin Polymer Films by hotochemically Manipulating Surface Tension...158
B.1 UV/Vis Spectra after Chemical Transformations 158
B.2 Carbon NMR Analysis...159
B.3 Example Feature Development Curves at 150 °C...............................160
B.4 Photochemical Mechanism of PBG 161
B.5 Glass Transition Temperatures of Films 164
B.6 Chemical Characterization of Film γ^{-}...165
B.7 Chemical Characterization of Film γ^{+}...167
B.8 AFM of Dewetted Host Polymer Film on Crosslinked PCHE............169

Appendix C: Generating Large and Thermally Stable Marangoni-driven Topographical Patterns in Thin Polymer Films by Photochemically Stabilizing the Surface Energy Gradient...171
C.1 Polymer characterization..171
C.2 Polymer Thin Film Characterization...173
C.3 Control Experiements for Feature Development. 173
C.4 Polymer Miscibility Calculations...176
C.5 Directionality of Flow 178
C.6 Marangoni and Capillary Velocity Calculations.................................178

Appendix D: Patterning Thin Polymer Films by Photodirecting the Marangoni Effect using a Photosensitizer....181

Appendix E: A Photochemical Approach to Stabilizing Marangoni-driven Patterned Polymer Films using Photosensitizers....185

E.1 Synthesis of Bis-Benzophenone....185

E.2 T_g of PiBMA Blends....185

E.3 UV/Vis Spectra After Exposure....187

E.4 SEC of Exposed PiBMA Films....187

E.5 Supporting IR Absorbance Spectra....188

E.6 T_g of PiBMA/MK Film....189

E.7 Viscosity and Self-Diffusion Coefficient of PiBMA....190

E.8 Photochemical Modification of Polymer Surfaces Using Michler's Ketone....191

E.9 Graphical Representation of Hole/Island Morphologies....194

Appendix F: Marangoni Instability Driven Surface Relief Grating in an Azobenzene Containing Polymer Film....195

F.1 Orientation of P5Az6A in Supported Thin Films....195

F.2 Surface Tension Changes....197

F.3 365 nm UV Exposure to Isomerize Trans to Cis....198

F.4 Viscosity of P5Az6A upon UV Exposure....199

F.5 Cis to Trans Relaxation Time....200

References....203

List of Tables

Table 2.1: Physical property values used in model predictions. 20

Table 3.1: Changes of a single film (γ^0) after sequential decarboxylation then dehydrogenation transformation procedures....................................44

Table C.1: Effect of full deprotection on film thickness of all blends.............174

Table C.2: Parameters used in miscibility calculations 176

Table C.3: Calculations of Marangoni and capillary velocities........................180

Table D.1: Percent of polymer film that remained as characterized by spectroscopy ellipsometry after the described procedure was performed on the film (5 wt% DBA) followed by soaking the film in THF and drying. Photo-exposure with 400 (± 50) nm wavelength light was used...............181

Table E.1: Tg of various compositions showing the plasticization effect of small molecules on PiBMA.. 186

List of Figures

Figure 1.1: (a) Schematic of the dehydrogenation of PS upon exposure to light. (b) THF solution-state fluorescence emission spectra from neat PS (solid line) and PS that was UV-exposed for two minutes (broken line). For both samples $\lambda_{excitation}$ = 310 nm. (c) Percent conversion of the PS backbone to carbon-carbon double bonds as a function of exposure dose measured by FTIR spectroscopy. The calculation of conversion is based on the decrease in the area of the peak corresponding to alkane bonds in the backbone (2800-2964 cm^{-1}) compared to the area under the peak at 1720 cm^{-1}, corresponding to the carbonyl present in the polymerization initiator, a constant. The filled data point represents the typical dose and conversion used for patterning purposes. Reproduced from Ref. 31 with permission from American Chemical Society, Copyright 2012.........3

Figure 1.2: Schematic illustration of the steps involved in Marangoni-flow-induced feature formation in a PS thin film. (a) A bright-field micrograph of a glassy polymer film (~150 nm thick) after exposure to light through a photomask which induces a photochemical reaction in exposed regions and an associated patterned surface energy. For the PS films employed here, there is higher surface energy in the light-exposed regions. No topography can be detected by optical microscopy or atomic force microscopy after this stage. (b) A bright-field micrograph of the same polymer film shown after heating to 110 °C, where the polymer is a liquid. The patterned surface energy drives formation of topographic features via the Marangoni effect. Reproduced from Ref. 31 with permission from American Chemical Society, Copyright 2012.........5

Figure 2.1: Patterning schematic. (a) UV illumination through a line-and-space photo-mask possessing a half-periodicity, λ, while the polymer film is in the solid state with an initial film thickness, h_0. (b) The topographical profile after a short period of thermal annealing above the glass transition temperature of the polymer shows its melt-state flow is first initiated near the boundary between UV exposed and unexposed regions. (c) Further annealing develops the topographical profile into a complete sinusoidal shape with the same periodicity as the mask reaching the maximum peak-to-valley height, h_{max}, then, (d) the topography dissipates after extended thermal annealing. 22

Figure 2.2: Representative 100 μm wide optical micrographs of one 128 nm thick PS film supported on a Si wafer after short (a,b) and long periods (c,d) of thermal annealing at120 °C. Prior to the heating, the PS film was exposed to UV light through a 25 μm pitch photo-mask. Different colors observed in the optical micrograph are light interference patterns resulting from the film thickness variations. Experimentally characterized height profiles for one periodicity from the same polymer film are shown in (e) and (f) after short and long periods of heating, respectively. Two different film thickness profiles were also theoretically predicted for a 128 nm thick film and are shown in (g) and (h), respectively..24

Figure 2.3: Comparison of peak-to-valley height evolution between experimental results (opened circle) and model predictions (solid line) at (a) 120 °C, (b) 126 °C, (c) 136 °C, and (d) 140 °C for PS films on glass...........26

Figure 2.4: (a) Attainable maximum feature size and (b) associated thermal annealing time as a function of temperature....................................27

Figure 2.5: Normalized maximum peak-to-valley height, h_{max}/h_0, and heating time as a function of resolution (photo-mask half-periodicity) for different film thicknesses (a, b), surface tension differentials (c, d), and heating temperatures (e, f). Data points represent model predictions and lines are guides to the eye. All case studies are otherwise at identical conditions as a base condition with h0 = 145 nm, c_0 Δγ = 0.004, and/or T = 120 °C. 28

Figure 3.1: Chemical transformation scheme. The first chemical transformation, a decarboxylation, is shown from Film γ_0 to Film γ^-. The second chemical transformation, a dehydrogenation, is shown from Film γ^- to Film γ^+.40

Figure 3.2: Patterning schematic. (a) 365 nm UV light exposed through a mask activates PBG in the exposed regions. Upon thermal annealing to liquefy the polymer, activated PBG also locally decarboxylates the polymer. This lowers the melt-state surface tension from γ^0 to γ^-, and polymer flows out of the exposed regions. Alternatively, after uniformly decarboxylating a film, (b) broadband UV exposure applied through a mask selectively increases the melt-state surface tension from γ^- to γ^+. Upon thermal annealing, polymer flows into the exposed regions...41

Figure 3.3: Representative optical and AFM images after heating the films with lower surface tension in the exposed regions (top row) and analogous images after heating the films with higher surface tension in the exposed regions (bottom row). Both samples were thermally annealed for 5 minutes at 150 °C after the patterned light illumination step. The initial film thicknesses were 530 nm. Scale bars in optical micrographs indicate 90 μm. 43

Figure 3.4: (a) Representative FTIR spectra for decarboxylation upon thermal annealing at 150 °C for 0 and 5 minutes. Spectra were normalized by the area under the alkyl stretches from 2850–3100 cm^{-1}. (b) The extent of decarboxylation at different cumulative heating times. 45

Figure 3.5: Solution fluorimetry using 310 nm wavelength excitation light. All signals were normalized to the fluorescence intensity of γ^+ at 404 nm. The concentration for all samples was 0.5 mg/mL. 46

Figure 3.6: SEC chromatograms of re-dissolved films after being subjected to representative processing conditions. Solid black lines indicate normalized RI responses while dashed red lines represent normalized fluorescence responses. $\lambda_{excitation}$ = 310 nm and $\lambda_{emission}$ = 400 nm were used to detect the fluorescence signals in this study.........................48

Figure 3.7: Contact angles for dewetted styrene-acrylic acid copolymers after chemical transformations. Data points represent polymer droplets whose volumes ranged from only 0.004 to 0.01 μm^3. Error bars represent 95 % confidence intervals based on 5 – 8 different droplets on each sample. 49

Figure 3.8: Representative optical micrographs of a single film possessing spatially programmed regions of lower (γ^-, hexagons) and higher (γ^+, triangular) surface energy at different heating times at 150 °C. Note that the hexagons are only patterned over half of the image. Scale bar indicates 50 μm. Photographs of the sample before and after thermal annealing are shown as insets in the initial and final optical micrographs. The initial film thickness was 360 nm...51

Figure 3.9: Top down optical micrographs (a) after decarboxylation was applied through hexagonal mask and annealing at 150 °C for one minute, and (b) after dehydrogenation was performed through triangular mask and annealing at 150 °C for one minute. Corresponding optical profilometer results are shown below each optical micrograph (c and d) showing directionality and height. The initial total film thickness was 530 nm. Scale bar indicates 50 μm. 53

Figure 4.1: Photochemical transformation of P(tBOS-ran-S) to P(HOST-ran-S) with the aid of PAG. Thin films were exposed to UV light and subsequent heating led to the removal of the tert-butoxystyrene moiety in P(tBOS-ran-S)..61

Figure 4.2: DSC traces showing immiscibility between bulk P(tBOS-ran-S) and P(HOST-ran-S) as indicated by two Tgs, but a single Tg for PS blended with either 30 wt% P(tBOS-ran-S) or 30 wt% P(HOST-ran-S) indicating miscibility. For reference the DSC trace for the low molecular weight PS homopolymer is also given. 62

Figure 4.3: Polymer patterning methodology. (1) Schematic of the polymer blend which is comprised of a low molecular weight PS (solid purple) and a high molecular weight copolymer, P(tBOS-ran-S) (blue hashed circles). Spatial control of the surface energy gradient is achieved by exposing films through a photomask and the subsequent annealing of these films leads to a photochemical transformation of P(tBOS-ran-S) into P(HOST-ran-S) (red dotted circles) with the aid of a photoacid generator. (2) With extended annealing time, polymer flows from regions of low to high surface energy and (3) the long term behavior (dissipation or stability of topography) is determined by whether capillary or Marangoni forces dominate, respectively. 64

Figure 4.4: Representative profilometry traces and corresponding optical images of feature formation in a 30 and 10 wt% P(tBOS-ran-S) in PS blend (initial film thickness= 288 nm). All films were exposed to UV light for 1 min (34 J/cm^2) and annealed at 120°C. Stable features with twice the initial film thickness are observed for 30 wt% P(tBOS-ran-S), while features decayed for 10 wt% P(tBOS-ran-S)...66

Figure 4.5: Excerpts from representative FTIR traces of both protected polymer (P(tBOS-ran-S)) and deprotected polymer (P(HOST-ran-S)). Deprotection was confirmed by the presence of OH-stretching between 3200-3600 cm^{-1} and the reduction of the peak at 2980 cm^{-1} due to C-H stretching. All spectra were normalized by a light insensitive peak in the phenyl ring region at 2926 cm^{-1}. 68

Figure 4.6: Effect of wt% P(tBOS-ran-S) in PS on contact angle measurements both before and after deprotection (exposure to UV and subsequent annealing). The wt% PAG for these measurements was 5 wt% with respect to tBOS in P(tBOS-ran-S). The test liquid used in this study was glycerol and error bars represent the standard deviation between three test droplets on the same sample. Films used here were exposed to UV light for 1 min and annealed 150°C for 1 min. 69

Figure 4.7: (a) Evolution of feature development for 10, 20, and 30 wt% P(tBOS-ran-S) for the case of full deprotection. Inset showing the short term annealing behavior. (b) Comparison of calculations of the Marangoni and capillary velocities for all blends tested (including incomplete deprotection which is marked by open symbols). Error bars represent minimum and maximum calculated values for surface energy. A full description of the calculations is given in Supporting Information, Section C6 in the Appendix C. 70

Figure 5.1: Patterning schematic of (a) NUV-vis light exposure in ambient air atmosphere, and (b) subsequent thermal annealing. Exposed regions (higher surface energy) rise while the unexposed regions (lower surface energy) sink upon thermal annealing. 79

Figure 5.2: Optical micrographs of the patterned samples using (a) 12.5 μm, (b) 5 μm, and (c) 800 nm half-pitch "line and space" masks. All scale bars indicate 25 μm. AFM images of the corresponding patterned samples are shown below. Initial film thicknesses were 300 nm. All samples were light exposed for 15 minutes. 81

Figure 5.3: Optical micrographs of samples patterned using sunlight through various photo-masks. Scale bars indicate 100 μm. Samples were subsequently annealed for 30 minutes at 120 °C. 82

Figure 5.4: Proposed reaction scheme for DBA doped into a polymer matrix with extractable hydrogens... 83

Figure 5.5: Optical micrographs of polymer films (a) after patterned light exposure, and (b) after subsequent thermal annealing at 120 °C for 60 minutes. PiBMA containing 5 wt% DBA exposed in ambient atmosphere (top row), neat PiBMA exposed in ambient atmosphere (middle row), and PiBMA containing 5 wt% DBA exposed in an argon purged atmosphere (bottom row). The scale bars indicate 25 µm. The films were exposed to light through a 12.5 µm half-pitch line and space photomask. Initial film thicknesses were 250 nm. 84

Figure 5.6: UV-vis absorption spectra of a PiBMA film containing 5 wt% DBA with varying light exposure time from 0 to 5 minutes in (a) ambient air atmosphere, and in (b) argon atmosphere. Films were all approximately 250 nm thick on quartz. One sample was used for each plot............86

Figure 5.7: SEC fluorescence detector responses near the host polymer retention volume (a) before light exposure, (b) after light exposure and (c) after light exposure and subsequent thermal annealing. $\lambda_{excitation}$ = 380 nm and $\lambda_{emission}$ = 405 nm were used to detect the fluorescence signals in this study. Total polymer concentration for each plot was approximately constant. 88

Figure 5.8: Water contact angle goniometry results: diamonds are the water contact angle measurements after NUV-vis blanket exposures, and squares are the measurements after post exposure thermal annealing for 30 minutes at 120 °C. Error bars are standard deviation calculated from three water contact angle measurements on the same sample. Between measurements the sample was blown dry with filtered dry air. The triangles represent the relative amount of DBA endoperoxide based on UV-Vis absorption peak changes along with photo exposure in ambient air atmosphere. 10 wt% of DBA dopant was used. 90

Figure 5.9: Peak to valley height at 120 °C (squares) and 130 °C (triangles), respectively, as a function of cumulative heating time after 60 seconds of photo-exposure. The initial film thicknesses were 250 nm.. 91

Figure 6.1: Structures of Michler's ketone (MK) and bis-benzophenone (BB)..96

Figure 6.2: Schematic of process for forming and stabilizing topographic features in a polymer film. 365 nm UV light exposed through a mask photo-reduces a fraction of blended sensitizers to prescribe melt-state flow into the exposed regions. Features dissipate or distort after excessive heating. However, a second exposure to UVB/UVC light fully activates a crosslinker, bis-benzophenone, which stabilizes the topographic features. 100

Figure 6.3: Representative 200 µm wide optical micrographs and height profiles of topographically patterned films prepared by the procedure defined by **Figure 6.2**. The left column depicts the samples after thermal development of photopatterned features. The right column depicts the samples after extensive thermal annealing. A crosslinking exposure was applied between these heating steps. The film thickness values have been set so that their mean matches the initial film thickness, 167 nm. 101

Figure 6.4: Representative 200 µm wide optical micrographs of PiBMA films prepared by procedure described by **Figure 6.2**, but with the crosslinking exposure step omitted. The upper row contained 10 wt. % BB and 2 wt. % MK and the lower row contained only 2 wt. % MK.102

Figure 6.5: Representative 200 µm wide optical micrographs of a PiBMA film containing 2 wt. % MK and 10 wt. % BB after 30 seconds of photoexposure at an elevated intensity and b) after 30 seconds of subsequent heating at 150 °C. 103

Figure 6.6: Grafting benzophenones to polymers by light irradiation.[11, 18-20] ...105

Figure 6.7: UV/Vis absorption spectra of PiBMA (solid line), MK (dashed line), BB (dotted line). ε was calculated on the basis of repeat unit molecular weight (PiBMA) or molecular weight per benzophenone group (MK and BB). PiBMA data represents an average of 3 films on quartz (thicknesses 1211, 990, and 781 nm). MK and BB were measured from methanol and tetrahydrofuran solutions, respectively, held in quartz cuvettes. The MK concentration was 4.6×10^{-4} mg/mL in a) and 2.345×10^{-2} mg/mL in b). The BB concentration was 3.6×10^{-3} mg/mL in a) and 1.65 mg/mL in b). Shaded regions in a) depict transmission bands of optical filters used to photopattern (365 nm) and crosslink (UVB/UVC). 105

Figure 6.8: SEC chromatograms for PiBMA with 2 wt. % MK. a) is a directly injected solution and b) is composed of films that were exposed to 20 J/cm^2 of light with λ = 365 nm and re-dissolved. The fluorescence detector was operated with an excitation wavelength of 386 nm, and detected fluorescence emitted at λ = 457 nm. 106

Figure 6.9: Benzophenone converted fraction and sol fraction for a PiBMA film containing 10 wt.% BB at different cumulative exposure doses of UVB/UVC light. The solid line depicts Equation 6.2 with εk_{BB} = 0.28 cm^{2}J^{-1} and γ = 1.47 found by a regression. The dashed line depicts sol fraction predictions from an adaptation of Miller-Macosko theory[28,29] that includes a grafting efficiency, η_{eff} = 0.64, for photochemically activated benzophenone groups. 108

Figure 6.10: Conversion of BB and MK by exposure to λ = 365 nm light. a) Representative IR absorbance spectra for a PiBMA film containing 2 wt. % MK and 10 wt. % BB and b) converted fraction of BB and MK at different cumulative doses. The solid line depicts Equation 6.2 with k_{MK} = 3 × 10^{-9} mol/J and γ = 3.42 found by a regression......................111

Figure 6.11: Thickness variations of a PiBMA film containing 2 wt. % MK at different cumulative heating times. The samples were photopatterned by the same conditions used in **Figure 6.4** and then heated at 125 ^{o}C. The dashed line indicates τ = 130 min. 113

Figure 6.12: Thermochemically stable topographical features directed the morphology of an inherently structured overlayer. 120 µm wide optical micgrographs of the starting topography, the film after coating with a block copolymer (BCP) overlayer, and the film after annealing are shown in parts a), b), and d), respectively. The thickness profile of the film before and after coating with BCP is shown in part c). All data is representative and does not correspond to identical sample regions.117

Figure 7.1: Synthesis of 5Az6A monomer.. 123

Figure 7.2: Synthesis of poly(4-(acryloyloxyhexyloxy)-4’-pentylazobenzene)..124

Figure 7.3: ^{13}C-NMR of the dried P5Az6A...125

Figure 7.4: DSC thermogram of P5Az6A taken upon the second heating at a rate of 10 °C/min showing a Tg of 12 °C..126

Figure 7.5: Schematic describing photochemical conformation changes and corresponding changes in the films’ water contact angle (boxed values). A lower contact angle corresponds to a higher surface tension. α indicates the molecular angle of the cis-isomer.. 129

Figure 7.6: (a) UV–vis absorption spectra of a film (141 nm thick) after annealing for 1 hr at room temperature (solid), 365 nm UV exposure for 30 sec (dotted), and 450 nm light exposure for 30 sec (dashed). (b,c) FTIR spectra of a film (183 nm thick) demonstrating the dipole moment of azobenzene changes before (solid) and after (dashed) 365 nm UV exposure.. 131

Figure 7.7: Patterning schematic. (a) 365 nm UV light exposed through a photomask selectively yields cis-rich domains in the exposed regions (i.e. relatively higher surface tension) with trans-rich surroundings (i.e. lower surface tension). Due to the prescribed surface tension gradient between exposed and unexposed regions, polymer flowed into the exposed regions, as described by the Marangoni effect. Alternatively, after uniformly converting a film into cis-rich isomers, (b) 450 nm light exposure applied through a photomask selectively yielded trans-rich regions in the exposed regions. Therefore, the polymer flowed out of the exposed regions. 132

Figure 7.8: Representative optical and AFM images (a) before and (b) after room temperature annealing the films with higher surface tension in the exposed hexagonal regions (Method 1, top row) and analogous images of the films with lower surface tension in the exposed hexagonal regions (Method 2, bottom row). Both samples were annealed for 1 hr at room temperature after the patterned light illumination step. The initial film thicknesses were 183 nm. Scale bars in optical micrographs indicate 60 μm.. 133

Figure 7.9: Peak to valley height measured by AFM upon annealing at room temperature as a function of cumulative annealing time. Different symbols indicate identically prepared samples. The initial film thicknesses were ca. 135 nm. Samples were exposed for 30 sec through a 12.5 μm (λ) half-pitch line and space photo-mask. The data set shown here are averaged height values of four different periodicities. The vertical dotted line indicates the relaxation time of the corresponding cis-isomer, τ, at room temperature. Two fits are provided corresponding to different decaying behaviors of the features as a result of capillary levelling with different capillary velocities (solid line, Equation 7.7 and dashed line, Equation 7.4)..136

Figure A.1: Normalized fluorescence intensity profile obtained experimentally from fluorescence microscopy using NBD labeled PS after typical exposure protocol for patterning was performed. Solid line represents the initial concentration profile used in the model prediction........................152

Figure A.2: DSC thermogram of PS taken upon the last heating cycle at a rate of 15 °C/min to 300 °C..153

Figure A.3: Effect of 140 J/cm^2 blanket exposure to broadband light on the glass transition of a PS film supported by a Si substrate as determined by spectroscopic ellipsometry. For clarity, only every 100th data point is displayed. The solid lines represent regressions of Eq. A1 to the data.154

Figure A.4: Viscosity of the polystyrene blend (99 wt.% Mn = 2.9 kDa PS, 1 wt.% Mn = 50 kDa PS) was measured at 120 ^{o}C using a TA Instruments AR-2000ex rheometer under steady shear...154

Figure A.5: (a) Experimental results at short times (b) Non-dimensional surface tension difference values extracted from experimental data at four different temperatures. 155

Figure A.6: (a) Experimental results at 120°C for long times (b) Diffusivity values extracted from experimental data at 120°C and extrapolated to higher temperatures as in Ref. 5...156

Figure A.7: Simulated film height profiles at short times clearly depict secondary peaks at four different annealing temperatures. Thicknesses of the film at each annealing temperature are identical to those used in **Figure 2.3**.157

Figure B.1: UV/Vis spectra of films γ_0, γ^-, and γ^+. 158

Figure B.2: ^{13}C-NMR of neat Joncryl as received. 160

Figure B.3: Variation in film thickness as a function of cumulative heating time at 150 °C. An identical photomask used for **Figure 3.3** in the main manuscript was used for this study. Each data point was characterized using a Veeco Dektak 6M stylus profiler with a stylus diameter of 25 microns and stylus force of 3 mg.. 161

Figure B.4: (a) illustrates a reaction scheme of PBG upon 365 nm UV exposures. (b) shows representative IR peak changes upon light exposures. All peaks were normalized by the area under the alkyl stretches from 2850 – 3100 cm^{-1}. (c) is conversion data characterized by the area under IR peaks, *v*(N-H), as exposure dose increases. (d) UV/Vis and (e) fluorescence emission spectra using a solution sample containing only PBG in diglyme (0.15 mg/ml). For the fluorescence spectra, $\lambda_{excitation}$ = 310 nm was used. 163

Figure B.5: The glass transitions of a Joncryl films as determined by spectroscopic ellipsometry after being subjected to representative processing conditions: (a) neat Joncryl without PBG, (b) Joncryl with 30 wt% PBG, (c) after decarboxylation, and (d) after dehydrogenation. For clarity only every 100th data point is displayed. The solid lines represent regressions of Eq. 1 in the main manuscript to the full data set. 165

Figure B.6: FTIR for decarboxylation upon thermal annealing at 150 °C from 0 to 5 minutes. Prior to the thermal annealing, PBG was fully activated by exposing 365 nm UV light with dose of 0.4 J/cm^2. All spectra were normalized by area under the alkyl stretches (insensitive through this chemical transformation) from 2850–3100 cm^{-1}. Inset shows magnified region showing carbonyl peak reductions before and after thermal annealing for 5 minutes..166

Figure B.7: Normalized film thickness upon thermal annealing. Prior to this heating the 365 nm UV exposure was given with a dose of 0.4 $J/cm^{2.}$ 167

Figure B.8: FTIR for dehydrogenation upon broadband UV exposure from 0 to 420 J/cm^2. All spectra were normalized by area under the carbonyl from 1670 – 1870 cm^{-1} since the carbonyl is insensitive through this chemical transformation. A left hand side inset is a magnified region showing alkyl C-H stretch reductions while the right hand side inset shows alkenyl C=C signal intensifies upon broadband UV exposures.168

Figure B.9: AFM height profile of dewetted host polymer (a) after decarboxylation, (b) neat, (c) after dehydrogenation and (d) after even further dehydrogenation. Scale bars indicate 1 μm. Arrows on each image indicate the droplet used for measuring contact angle. (e) Representative height profile of one droplet on each sample. The droplet for this comparison has identical volume of 0.004 μm^3..............................169

Figure C.1: Gel permeation chromatography of synthesized PS (Mn=2.6 kDa, Đ=1.1) and P(tBOS-ran-S) (Mn=42 kDa, Đ =1.01) in tetrahydrofuran (THF). 171

Figure C.2: Molecular weight distribution of the low molecular weight PS (Mn=2.6 kDa, Đ =1.1) by MALDI. 172

Figure C.3: ^{1}H NMR of P(tBOS-ran-S) used to calculate the molar ratio of tert-butoxystyrene: styrene.. 172

Figure C.4: UV/Vis spectrum of a 30 wt% P(tBOS-ran-S) in PS film showing high transmittance in the mid-UV range...173

Figure C.5: FTIR (a) and feature development (b) for a 30 wt% P(tBOS-ran-S) film without PAG. Exposure (1 min UV, 34 J/cm^2) and annealing at 120°C for 10 minutes shows no deprotection. Feature height, for a film exposed and annealed through a line-and-space photomask, increased to a maximum of 60 nm and slowly decayed over 24 h.. 174

Figure C.6: FTIR spectra of P(HOST-ran-S) synthesized in a solution of hydrochloric acid and dioxane as described in the experimental methods section. 175

Figure C.7: (a) Full FTIR spectra of protected (neat P(tBOS-ran-S)) and deprotected polymer (P(HOST-ran-S)). (b) Selected spectra for neat P(tBOS-ran-S), after only UV, and after UV and annealing at 120°C for 10 min demonstrating that both UV and heat were required for deprotection to occur. All spectra were normalized to the light insensitive phenyl peak at 2926 cm^{-1}... 175

Figure C.8: Predictions of the mol% tBOS required to ensure miscibility of P(tBOS-ran-S) and P(HOST-ran-S) with PS (χ-$\chi_{critical}$<0), while maximizing immiscibility between P(tBOS-ran-S) and P(HOST-ran-S) (χ-$\chi_{critical}$>0). Predictions shown are calculated based on the molecular weights of polymers used in this study and the ratio of PS to P(tBOS-ran-S) or P(HOST-ran-S) of 30wt%...177

Figure C.9: DSC traces of homopolymers P(tBOS-ran-S) and P(HOST-ran-S).178

Figure C.10: Directionality of flow as confirmed using a photomask patterned with isolated hexagons. Here, regions of exposure were hexagonal in shape and subsequent annealing produced hexagonal regions of P(HOST-ran-S). Thus, polymer flowed towards the hexagonal regions with increasing time. Lines represent the direction of the corresponding profilometry traces. 178

Figure C.11: Effect of PAG concentration on evolution of features for (a) 10 wt% P(tBOS-ran-S) and (b) 20 wt% P(tBOS-ran-S). All PAG concentrations were calculated based on the percentage of tBOS incorporated in P(tBOS-ran-S)..179

Figure C.12: Calculation of % deprotection from FTIR. (a) Representative FTIR spectra showing a decrease in the peak at 2900 cm^{-1} due to deprotection. (b) FTIR trace for a neat 20 wt% P(tBOS-ran-S) blend after peak deconvolution showing the area for peak A1, area for peak A2, and cumulative fit which includes all peaks that were fitted. (c) Ratios of A2/A1 before (neat) and after deprotection (deprotected) for increasing PAG concentration. Dashed lines show average neat values used to represent 0% deprotection...179

Figure D.1: Normalized SEC RI response plot: (a) before UV exposure, (b) after 400 (± 50) nm light exposure (for 15 minutes), and (c) after thermal annealing at 120 °C for 30 minutes. 181

Figure D.2: UV-vis absorption spectra of neat PiBMA and 5 wt% DBA dopant in the PiBMA matrix. Initial film thickness was 150 nm on quartz. The wavelength range from 350 to 450 nm was used only during the photo-exposure. 182

Figure D.3: Comparison of feature formations resulting from photo-exposure in air (solid line) and argon (dotted line) atmospheres. The representative topographical film thickness variations for two periodicities of each sample are shown which were collected with profilometry. Both samples were exposed to light for five minutes and annealed at 120 °C for 60 minutes. 182

Figure D.4: FTIR spectra of the same DBA (10 wt%) doped PiBMA film: before photo-exposure, after 15 minutes of irradiation, and after 30 minutes of subsequent thermal annealing at 120 °C. Inset is a magnified window showing the hydroxyl signal. All spectra are normalized to the tallest ester peak at 1730 cm-1 corresponding to the ester on PiBMA which is a constant during the experiment. Films were all approximately 250 nm thick on double side polished silicon substrates. 183

Figure D.5: Optical micrographs of patterned films with DBA in different host polymers: (a) polystyrene (PS) (Mn = 2.9 kDa, PDI = 1.36, Tg = 61 oC), and (b) poly(methyl methacrylate) (PMMA) (Mn = 9.6 kDa, PDI = 1.43). Scale bars indicate 50 μm. Both films contain 5 wt% DBA. 60 J/cm2 of NUV-vis light exposure (15 minutes) was applied through a 25 μm pitch photomask for both samples. The PS film was heated at 126 ^{o}C for 30 min, and the PMMA film was heated at 176 ^{o}C for 30 min. The sinusoidal thickness profiles possessed peak-to-valley heights of 450 nm and 40 nm, respectively. 184

Figure E.1: UV/Vis spectra of a 110 nm thick PiBMA film containing 10 wt. % BB and 2 wt. % MK (solid line) after blanket exposures typical for patterning (long-dashed line) and crosslinking (short-dashed line)..187

Figure E.2: SEC chromatograms for unexposed PiBMA and redissolved PiBMA films that were exposed to 32 J/cm^2 of UVB/UVC light...............188

Figure E.3: Representative IR absorbance spectra for a PiBMA film containing MK and/or BB, before and after exposure to UV light. 189

Figure E.4: Effect of blanket exposure to 10 J/cm^2 of light with $\lambda = 365$ nm on the glass transition of a PiBMA film containing 2 wt. % MK, as determined by spectroscopic ellipsometry. For clarity only every 100th data point is displayed. The solid lines represent regressions of Eq. E1 to the data.190

Figure E.5: Viscosity of Mn = 10 kDa PiBMA at varying temperature. 191

Figure E.6: Representative optical micrographs of film morphologies and water contact angles after different processing steps. Water contact angles of polymer films after various exposure times are plotted below. 193

Figure E.7: Graphical representation of hole/island morphologies. 194

Figure F.1: UV–vis absorption spectra of a film (141 nm thick) after various annealing intervals at room temperature. The arrow indicates the effect of increasing time on the UV-vis spectra......................................196

Figure F.2: FTIR spectra of the film (183 nm thick) after various annealing intervals at room temperature. Arrows show the effect of increasing annealing time on the spectra. All spectra in this study were normalized by the ester peak areas (1720 – 1770 cm^{-1}) (measured on the associated OMNIC software) which represent the peaks present in the polymer repeat units. 197

Figure F.3: Water contact angle goniometry results. Diamonds represent the water contact angle measurements on a film after 450 nm light exposure, and squares are the measurements after 365 nm UV exposure. The exposure time was kept constant at 30 sec. In-between measurements, the sample was blown dry with filtered dry air. 198

Figure F.4: UV–vis absorption spectra of the film (141 nm thick) after various exposure times with 365 nm UV light. 198

Figure F.5: Zero shear viscosity measurements before and during UV exposure. Open diamonds are measurements made in an absence of UV irradiation while the filled circles are data taken during UV irradiation. The dotted line in this figure indicates when the UV irradiation was initiated..199

Figure F.6: UV–vis absorption spectra of the UV exposed (365 nm) film (141 nm thick) after various annealing intervals at room temperature. 200

Figure F.7: Extraction of τ from the UV-vis absorption spectra shown in **Figure F6**. Using Equation F.1, τ can be extracted from the reduction in the characteristic absorbance peak for cis at wavelength = 444 nm over various intervals of annealing at room temperature.......................201

Chapter 1: Micron and Sub-micron Patterning of Polymer Thin Films

1.1 BACKGROUND AND SIGNIFICANCE

The ability to precisely and efficiently produce patterned surfaces is important in numerous fields[1,2] including cell biology,[3,4] tissue engineering,[5] coatings,[6-10] optics,[11-14] and microelectronics.[15] In particular, micron and submicron length scale patterned polymer films have been adapted for many specific purposes including reducing biofouling,[6,7,10] controlling wettability,[9] improving adhesion between two surfaces,[8] directing cellular alignment,[16] and increasing the energy efficiency of light emitting diodes[12,13] or photovoltaics.[11,17] This diverse range of areas has motivated the continuous development of new patterning approaches directed towards expanding the range of accessible pattern complexities and aspect ratios, or improving process speed and resolution. While many applications are well-served by conventional patterning methods such as photolithography,[18,19] contact printing,[20,21] and/or the directed self-assembly of block copolymer thin films,[22–24] a need still exists to develop new, versatile and high-throughput patterning methodologies that are amenable to a broader range of purposes. However, introduction of any new patterning method in both industrial and laboratory settings must additionally consider that access to very expensive clean room infrastructure, toxic developing solvents, or etching protocols may not be readily available.

One alternative patterning paradigm that has recently attracted attention leverages instabilities generated at fluid interfaces to direct convection in thin polymer films.[25] These techniques include patterning using the coffee ring effect,[26] thermocapillary flow,[27] lithographically induced self-assembly,[28] and electrohydrodynamic patterning.[29, 30] In addition to the aforementioned techniques, our group has recently explored generating

topographic patterns by photochemically-directing Marangoni instabilities with subtle gradients in surface tension which is a common theme in this thesis.[31]

1.2 THE MARANGONI EFFECT

The Marangoni effect describes how a fluid flows through convective motion in response to gradients in surface tension.[32,33] At a fluid interface, gradients in surface tension are often generated by variations in local temperature and/or composition. This effect is familiar to most people as the "tears" that form in a glass of wine. It was first observed in 1855 by James Thomson (brother of Lord Kelvin)[34] and named after the Italian physicist Carlo Marangoni who studied the effect at the University of Pravia in 1865,[35] which the effect was then further quantitatively validated by Scriven and coworkers in 1960.[33] The effect manifests in many other phenomena as well, from thickening of a tear film lipid layer in the human eye[36] to "fingering instabilities" in spreading thin films.[37] Moreover, living organisms have evolved to exploit the Marangoni effect. For example, water striders of the genus *Microvelia* possess an emergency ability to propel themselves forward by directing surface tension gradients on the water surface. By excreting organic, surfactant-like molecules from their stern, they create localized regions where the surface tension is lower than the surroundings. As a result, the water striders are pulled in the direction of higher surface tension via the Marangoni effect at twice their normal water walking speed.[38] In general, the magnitude of surface tension variations needed to promote Marangoni flow are exceedingly small; not surprisingly this effect seemingly appears spontaneously in a broad range of contexts to produce defense mechanisms in nature, the "tears of wine" phenomenon and development of striation defects in films,[39] among many others.

1.3 MARANGONI DRIVEN PATTERNING OF POLYSTYRENE THIN FILMS

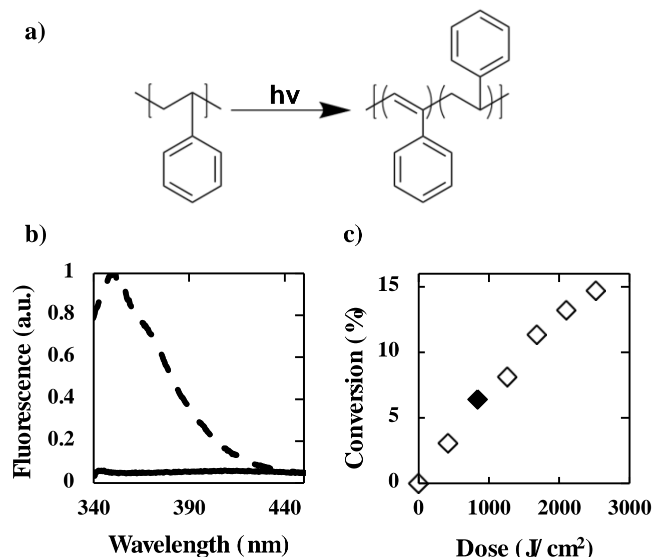

Figure 1.1: (a) Schematic of the dehydrogenation of PS upon exposure to light. (b) THF solution-state fluorescence emission spectra from neat PS (solid line) and PS that was UV-exposed for two minutes (broken line). For both samples λexcitation = 310 nm. (c) Percent conversion of the PS backbone to carbon-carbon double bonds as a function of exposure dose measured by FTIR spectroscopy. The calculation of conversion is based on the decrease in the area of the peak corresponding to alkane bonds in the backbone (2800-2964 cm-1) compared to the area under the peak at 1720 cm-1, corresponding to the carbonyl present in the polymerization initiator, a constant. The filled data point represents the typical dose and conversion used for patterning purposes. Reproduced from Ref. 31 with permission from American Chemical Society, Copyright 2012.

Our group recently developed a method for photochemically programming prescribed surface energy patterns in glassy polystyrene (PS) thin films.[31,40] As the reaction scheme in Figure 1.1a demonstrates, UV irradiation dehydrogenates the PS backbone forming carbon-carbon double bonds.[41-45] These double bonds form 'stilbene-like' chemical structures in a portion of the repeat units which have significantly red-shifted fluorescence spectra relative to neat PS. Accordingly, solution fluorimetry was used to qualitatively confirm the creation of 'stilbene-like' structures as evidenced by

significant fluorescence signal at wavelengths where PS precursors do not fluoresce (Figure 1.1b).[43] A typical UV exposure dose in this study dehydrogenated 6.4 % of the backbone repeat units, as characterized by Fourier transform infrared spectroscopy (FTIR) (Figure 1.1c). This partially backbone dehydrogenated PS possesses a higher surface energy than neat PS. The surface energy change was predicted using a group contribution method ($\Delta\gamma \sim 0.44$ dyne/cm) and also confirmed experimentally by a decrease in static water contact angle on a PS film after blanket UV irradiation.[31]

In a thin film, UV irradiation through a photo-mask selectively dehydrogenates the PS backbone locally. A schematic describing the patterning process can be seen in Figure 1.2. It is important to note that the polymer film is a glassy solid during the UV irradiation step, thus no macroscopic flow of the film materials can occur at this stage. This is evidenced by a uniform reflected interference color in the optical micrograph of the film shown in Figure 1.2a, indicating uniform film thickness immediately after light exposure. The film uniformity was also confirmed by tapping-mode atomic force microscopy. However, only after heating the film to the liquid state does polymer flow into the exposed regions from the unexposed areas due to the photochemically patterned surface energy gradient, creating a three-dimensional topography reflective of the light exposure pattern. Longer time and higher temperature annealing conditions can be used to cause these structures to dissipate completely, resulting in recovery of a featureless flat film. This flat film can be re-exposed to light in the glassy state and the corresponding topographies developed once again upon subsequent heating.[40]

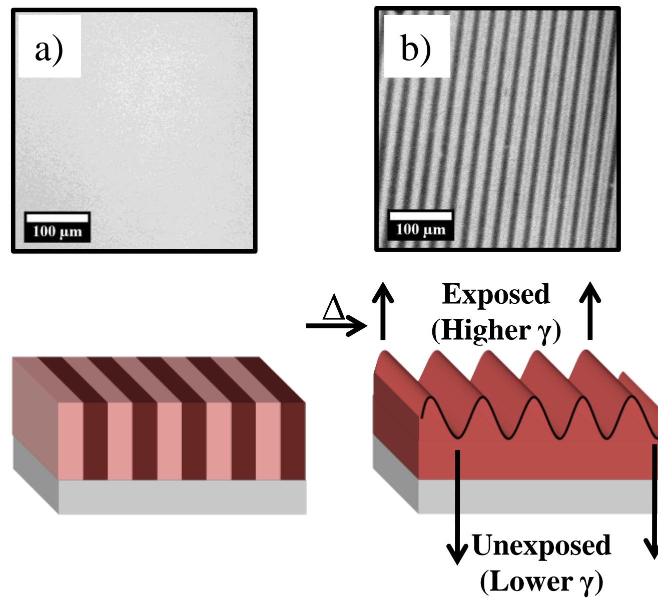

Figure 1.2: Schematic illustration of the steps involved in Marangoni-flow-induced feature formation in a PS thin film. (a) A bright-field micrograph of a glassy polymer film (~150 nm thick) after exposure to light through a photomask which induces a photochemical reaction in exposed regions and an associated patterned surface energy. For the PS films employed here, there is higher surface energy in the light-exposed regions. No topography can be detected by optical microscopy or atomic force microscopy after this stage. (b) A bright-field micrograph of the same polymer film shown after heating to 110 °C, where the polymer is a liquid. The patterned surface energy drives formation of topographic features via the Marangoni effect. Reproduced from Ref. 31 with permission from American Chemical Society, Copyright 2012.

1.4 SUMMARY

This Marangoni-driven patterning method is expected to be fully compatible with existing lithography tools but may have additional advantages in that the formation of topographical features occurs in the absence of a mask, solvents, or etching protocols. Complex patterns can be easily fabricated since the patterns are directly controlled by the mask design. Given that as little as several seconds of light exposure time is sufficient to induce feature formation, this approach could be compatible with high speed roll-to-roll processes for patterning large areas. If this patterning method is further fundamentally

investigated, optimized, and/or generalized for many classes of polymers, it could potentially be advantageous for a variety of applications if implemented into high-throughput manufacturing environments.

First, in order to quantify and fundamentally understand this phenomenon, a theoretical model that gives a more thorough understanding of the physics of this process was developed through collaboration with Dr. Roger Bonnecaze's group, and this collaborative effort is described in Chapter 2. The resulting model prediction agreed very well with our experimental observations without any adjustable parameters. Also, the model further revealed ways to apply the Marangoni driven patterning method more efficiently for various target metrics, such as the maximum achievable feature height and annealing times necessary to achieve it.

Next, other material candidates (i.e., besides neat PS) for the Marangoni-driven patterning methodology were designed and evaluated. Real world applications typically require coatings/films with complex patterns of sufficiently high aspect ratio that are stable at elevated temperatures and/or solvent-rich conditions. An especially versatile material for easily forming complicated patterns should be able to be spatially programmed to possess regions of higher or lower relative surface tension so that the direction of flow into or out of those areas could be directed with precision. To this end, Chapter 3 describes a photopolymer where the melt-state surface tension could be selectively raised or lowered in the light exposed regions depending on the wavelength and dose of applied light. The ability to control film convection into or out of exposed regions on-demand enables a greater diversity of accessible topographical structures than if flow is restricted to one direction.

Based on the modeling results in Chapter 2, a strategy to rapidly produce large and thermally stable features is described in Chapter 4. Additionally, Chapters 5 and 6

outline a set of photosensitizing compounds, doped into an otherwise optically transparent polymer, that provide pathways to form thermo-chemically stable features so patterned films can act as an underlayer in a multilayered system. This photosensitizers approach further enables significant increases in feature aspect ratio compared to earlier work and expands the applicability of the Marangoni patterning method to more readily available light sources (i.e., visible light and sunlight) and other classes of polymers.

Lastly, a potentially related phenomenon that various research groups have reported independently is that azo-benzene containing polymers (azo-polymers), either linked to a polymeric chain or as part of azobenzene dye doped in a polymer matrix, can generate topography during light irradiation in the form of a crossed laser interference pattern.[46,47] The hypothesis tested in Chapter 7 is that the underlying physio-chemical mechanism of this topography generation (also known as surface relief gratings in the literature; SRG) is due to migration of azo-benzene containing polymers by the Marangoni effect. Chapter 7 describes an initial demonstration showing that the surface tension gradient imposed by photo-isomerization of azobenzene causes the flow of polymer and subsequent topographical feature formation.

While Marangoni-driven patterning itself could be used as a powerful patterning method for some applications, an even greater variety of applications could be realized if the Marangoni strategy can be used to align nano-structured materials such as liquid crystals (LCs), liquid crystalline polymers (LCPs), and block copolymers (BCPs). These applications of the Marangoni effect will be described as future work in Chapter 8. Achieving orientation control and directed self-assembly of BCPs and LCPs in thin films is especially necessary for applications including lithography for microelectronics and data storage devices,[48-50] oxygen barrier films for packaging[51,52] and displays,[53] etc. To make these objectives feasible, developing strategies to maximize and optimize the local

shear stress and curvature created by the Marangoni-driven patterning method will be the first priority. For this reason, several non-conventional approaches to improve the Marangoni feature aspect ratios without adapting sophisticated and complex tools are also proposed in detail in Chapter 8 as a future work.

1.5 REFERENCES

1. Nie, Z.; Kumacheva, E. *Nat. Mater*. **2008**, 7, 277–290.
2. Campo A. D.; Arzt E. Generating Micro- and Nanopatterns on Polymeric Materials; Wiley-VCH: Weinheim, **2011**.
3. Thery, M. ; Racine, V.; Pepin, A.; Piel, M.; Chen, Y.; Sibarita, J. B.; Bornens, M. *Nature Cell Biol.* **2005**, 7, 947–953.
4. Thery, M.; Racine, V.; Piel, M.; Pepin, A.; Dimitrov, A.; Chen, Y.; Sibarita, J. B. *Proc. Natl Acad. Sci. USA* **2006**, 103, 19771–19776.
5. Hollister, S. J. *Nature Mater.* **2005**, 4, 518–524.
6. Efimenko, K.; Finlay, J.; Callow, M. E.; Callow, J. A.; Genzer, J. *ACS Appl. Mater. Interfaces* **2009**, 1, 1031−1040.
7. Bixler, G. D.; Bhushan B. *Adv. Funct. Mater.* **2013**, 23, 4507-4528.
8. Davis, C. S.; Martina, D.; Creton, C.; Lindner, A.; Crosby, A. J. *Langmuir*, **2012**, 28, 14899−14908.
9. Feng, L.; Li, S.; Li, Y.; Li, H.; Zhang, L.; Zhai, J.; Song, Y.; Liu, B.; Jiang, L.; Zhu, D. *Adv. Mater.* **2002**, 14, 1857−1860.
10. Schumacher, J. F.; Carman, M. L.; Estes, T. G.; Feinberg, A. W.; Wilson, L. H.; Callow, M. E.; Callow, J. A.; Finlay, J. A.; Brennan, A. B. *Biofouling* **2007**, 23, 55−62.
11. Kim, J. B.; Kim, P.; Pegard, N. C.; Oh, S. J.; Kagan, C. R.; Fleischer, J. W.; Stone, H. A.; Loo, Y.-L. *Nat. Photon*. **2012**, 6, 327-332.
12. Bay, A.; André, N.; Sarrazin, M.; Belarouci, A.; Aimez, V.; Francis, L. A.; Vigneron, J. P. *Opt. Express* **2013**, 21, A179-A189.
13. Koo, W. H.; Jeong, S. M.; Araoka, F.; Ishikawa, K.; Nishimura, S.; Toyooka, T.; Takezoe, H. *Nat. Photon.* **2010**, 4, 222-226.
14. Park, B.; Jeon, H. G. *Opt. Express* **2011**, 19, A1117-A1125.
15. Thompson, S. E.; Parthasarathy, S.; *Mater. Today* **2006**, 9, 20–25, 7747-7759.
16. Aubin, H.; Nichol, J. W.; Hutson, C. B.; Bae, H.; Sieminski, A. L.; Cropek, D. M.; Akhyari, P.; Khademhosseini, A. *Biomaterials* **2010**, 31, 6941-6951.
17. Moungthai, S.; Mahadevapuram, N.; Ruchhoeft, P.; Stein, G. E. *ACS Appl. Mater. Interfaces* **2012**, 4, 4015-4023.
18. Bruning, J. H.; *Proc. SPIE* **2007**, 6520, 652004
19. Thompson, S. E.; Parthasarathy, S. *Mater. Today* **2006**, 9, 20–25.
20. Chou, S. Y.; Krauss, P. R.; Preston, J. R. *Science* **1996**, 272,85–87.
21. Resnick, D. J. Sreenivasan, S. V.; Willson, C. G; Mater. Today 2005, 8, 34–42.
22. Herr, D. J. C. *J. Mater. Res.* **2011**, 26, 122–139.

23. Liu, C.-C.; Thode, C. J.; Delgadillo, P. A. R.; Craig, G. S. W.; Nealey, P. F.; Gronheid, R. *J. Vac. Sci. Technol. B* **2011**, 29, 06F203.
24. Stoykovich, M. P.; Kang, H.; Daoulas, K. C.; Liu, G.; Liu, C.-C.; de Pablo, J.J.; Muller, M.; Nealey, P. F. *ACS Nano* **2007**, 1,168–175.
25. Steiner, U. In Nanoscale Assembly Chemical Techniques; W. T. S. Huck, Ed.; Springer Science Business Media, Inc.: New York, **2005**, p 1–24.
26. Han, W.; Lin, Z. Q. *Angewandte Chemie-International Edition* **2012**, 51, 1534-1546.
27. Singer, J. P.; Lin, P. T.; Kooi, S. E.; Kimerling, L. C.; Michel, J.; Thomas, E. L. *Adv. Mater.* **2013**, 25, 6100-6105.
28. Chou, S. Y.; Zhuang, L. *J. Vac. Sci. Technol. B* **1999**, 17, 3197-3202.
29. Schaffer, E.; Thurn-Albrecht, T.; Russell, T. P.; Steiner, U. *Nature* **2000**, 403, 874-877.
30. Verma, R.; Sharma, A.; Kargupta, K.; Bhaumik, J. *Langmuir* **2005**, 21, 3710-3721.
31. Katzenstein, J. M.; Janes, D. W.; Cushen, J. D.; Hira, N. B.; McGuffin, D. L.; Prisco, N. A.; Ellison, C. J. *ACS Macro Lett.* **2012**, 1, 1150-1154.
32. Larson, R. G. *Angewandte Chemie International Edition* **2012**, 51, 2546-2548.
33. Scriven, L. E.; Sternling, C. V. *Nature* **1960**, 187, 186-188.
34. Thomson, J. On certain curious motions observable at the surfaces of wine and other alcoholic liquors, **1855**.
35. Marangoni, C. Sull'espansione delle gocce liquide, **1865**.
36. Bron, A. J.; Tiffany, J. M.; Gouveia, S. M.; Yokoi, N.; Voon, L. W. *Exp. Eye Res.* **2004**, 78, 347-360.
37. Cazabat, A. M.; Heslot, F.; Troian, S. M.; Carles, P. *Nature* **1990**, 346, 824-826.
38. Bush, J. W. M.; Hu, D. L. *Annu. Rev. Fluid Mech.* **2006**, 38, 339–369.
39. Haas, D. E.; Birnie, D. P., III. *J. Mater. Sci.* **2002**, 37, 2109-2116.
40. Janes, D. W.; Katzenstein, J. M.; Shanmuganathan, K.; Ellison, C. J. *J. Polym. Sci., Part B: Polym. Phys.* **2013**, 51, 535–545.
41. Millan, M. D.; Locklin, J.; Fulghum, T.; Baba, A.; Advincula, R. C. *Polymer* **2005**, 46, 5556-5568.
42. Nagai, N.; Matsunobe, T.; Imai, T. *Polym. Degrad. Stabil.* **2005**, 88, 224-233.
43. Nurmukhametov, R.; Volkova, L.; Kabanov, S. *Journal of Applied Spectroscopy* **2006**, 73, 55-60.
44. Simons, J. K.; Chen, J. M.; Taylor, J. W.; Rosenberg, R. A. *Macromolecules* **1993**, 26, 3262-3266.
45. Zhang, D.; Dougal, S. M.; Yeganeh, M. S. *Langmuir* **2000**, 16, 4528-4532.
46. Rochon, P.; Batalla, E.; Natansohn, A. *Appl. Phys. Lett.* **1995**, 66, 136.
47. Kim, D.Y.; Tripathy, S.K.; Li, L.; Kumar, J. *Appl. Phys. Lett.* **1995**, 66, 1166.
48. Park, S. M.; Stoykovich, M. P.; Ruiz, R.; Zhang, Y.; Black, C. T.; Nealey, P. E. *Adv. Mater.* **2007**, 19, 607-611.
49. Bita, I.; Yang, J. K. W.; Jung, Y. S.; Ross, C. A.; Thomas, E. L.; Berggren, K. K. *Science* **2008**, 321, 939-943.
50. Segalman, R. A.; Yokoyama, H.; Kramer, E. J. *Adv. Mater.* **2001**, 13, 1152-1155.

51. Weinkauf, D. H.; Kim, H. D.; Paul, D. R. *Macromolecules* **1992**, 25,788-796.
52. Park, J. Y.; Paul, D. R.; Haider, I.; Jaffe, M. *J. Polym. Sci., Part B: Polym. Phys.***1998**, 34,1741-1745.
53. Grell, M.; Bradley, D. D. C.; Inbasekaran, M.; Woo, E. P. *Adv Mater.* **1997**, 9, 798-802.

Chapter 2: Theoretical Framework to Predict Marangoni Patterning for PS

2.1 INTRODUCTION

While progress has been made toward qualitatively understanding the parameters that impact the Marangoni patterning technique on a phenomenological basis, rigorous simulations could improve understanding of its quantitative behavior and physical underpinnings. A first-principles understanding of the Marangoni patterning process could allow for quantitative prediction and optimization of feature formation by varying factors such as material selection and the details of the surface energy gradient. Ultimately, this knowledge will enable precise control over topographic feature sizes and locations. Examples of related models include those developed to describe electrohydrodynamic patterning,[1-5] lithographically induced self-assembly,[6-8] and deformations of compliant gels by surface stresses.[9-11]

In this chapter, we aim to describe a theoretical model that allows quantitative prediction of various target metrics relevant to photochemical, Marangoni-driven patterning, such as the maximum achievable feature height and annealing times necessary to achieve it. We first outline equations describing the dynamics of the film as well as the numerical method employed to solve them, their scaling and an analytical solution based on linearization. This allows comparison of model predictions, based on numerical solutions of the non-linear governing equations, with experimental observations and consideration of the role that temperature exerts on the kinetics of feature development. Finally, we identify limits on the resolution and aspect ratio the process can achieve and address the issue of how materials and experimental parameters can be judiciously

---

This chapter reproduced in part from "Precision Marangoni-driven Patterning" Arshad, T. A.; Kim, C. B.; Prisco, N. A.; Katzenstein, J. M.; Janes, D. W.; Bonnecaze, R. T.; Ellison, C. J. *Soft Matter* **2014**, *10*, 8043-8050 with permission from the Royal Society of Chemistry, copyright 2014.

selected to achieve patterns with the highest resolution or aspect ratio as efficiently as possible.

2.2THEORETICAL MODEL

2.2.1 Model and Numerical Method

The dynamics of the film are defined by the interplay between Marangoni and capillary forces. The photochemically induced surface tension gradient drives flow from relatively low to high surface tension regions. This is counteracted by capillary forces, which act to minimize surface area by maintaining a flat film. These dynamics are described by the thin film equation:

$$\frac{\partial h}{\partial t} + \frac{\partial}{\partial x}\left[\left(\frac{1}{2\mu}\right) h^2 \frac{\partial \gamma}{\partial x} + \left(\frac{1}{3\mu}\right) h^3 \frac{\partial}{\partial x}\left\{\gamma \frac{\partial^2 h}{\partial x^2}\right\}\right] = 0 \quad (2.1)$$

where h is the thickness of the film at any given location, γ is local surface tension, μ viscosity, and x and t are the lateral distance and time, respectively.[12, 13] The first and second terms inside the square brackets account for Marangoni and capillary flux, respectively. Van der Waals and gravitational forces are neglected since they only become relevant at length scales much smaller or larger than those of interest here. Given that the films were thin and held isothermally on a large hot plate surface during experiment, gradients in temperature across the film were not considered. The programmed surface energy is uniform parallel to the mask lines (as in Chapter 1, a symmetric line and space mask was used in these experiments), but varies in the lateral direction perpendicular to them. Therefore, along with the thin-film condition, the equations reduce to one dimension. The local surface tension at any point is related to the concentration of the photochemically generated species which is assumed to be given by

$$\gamma = \gamma_0 + (\Delta\gamma)c \quad (2.2)$$

where c is the mole fraction of the photochemical product, γ_0 is the surface tension of the original PS, and $\Delta\gamma$ is the difference in surface tensions between neat PS and a PS with two backbone hydrogens removed per repeat unit (i.e. poly(phenyl acetylene)). $\Delta\gamma$ is defined to be positive when the photoexposed polymer exceeds the base polymer in surface tension. Local concentration is expressed in fractional (dimensionless) terms. The evolution of this concentration is described by:

$$\frac{\partial c}{\partial t} - \mathcal{D}\frac{\partial^2 c}{\partial x^2} + \frac{\partial}{\partial x}\left[\left(\frac{1}{\mu}\right) h \frac{\partial \gamma}{\partial x} + \left(\frac{1}{2\mu}\right) h^2 \frac{\partial}{\partial x}\left\{\gamma \frac{\partial^2 h}{\partial x^2}\right\}\right] c = 0 \qquad (2.3)$$

where $\mathcal{D}$ is the diffusivity. This is simply the convection-diffusion equation with fluid velocity being a sum of its Marangoni and capillary components (the first and second terms within the square brackets, respectively).[12, 13] For initial periodic variations in the surface energy, the symmetry boundary conditions applied at x = -λ and +λ, where the x = 0 is at the centerlines of the chrome lines on the mask under which the film is unexposed to light, are given by

$$\frac{\partial h}{\partial x} = 0 \qquad (2.4)$$

$$\frac{\partial p}{\partial x} = \frac{\partial}{\partial x}\left(-\gamma \frac{\partial^2 h}{\partial x^2}\right) = 0 \qquad (2.5)$$

$$\frac{\partial c}{\partial x} = 0 \qquad (2.6)$$

A smoothed step function was employed to generate the initial concentration profile for the simulations. (See Figure A.1 in Appendix A) This system was solved using a second-order finite difference method with explicit time stepping. 80 node points over a half periodicity of the mask pattern are found to be sufficient for convergence.

2.2.2 Scaling & Linearized Solution

The relative strength of Marangoni forcing and capillary dissipation, which determine the size of the resulting peak-to-valley heights as well as the time scale over which they are formed, depend upon a number of factors: geometry (pattern periodicity and film thickness), material properties (surface tension, diffusivity and viscosity) and experimental parameters (photochemical conversion and thermal annealing temperature). To gain insight into these interrelationships, we non-dimensionalized the governing equations, employing the scales $x \sim \lambda$ (mask half-periodicity), $h \sim h_0$ (initial film thickness), $c \sim c_0$ (peak fractional conversion), $\gamma \sim \gamma_0$ (surface tension of the neat PS) and $t \sim \mu\lambda^2/h_0\gamma_0$. Rescaling equations (2.1 and 2.3) to make them dimensionless but retaining the same symbols for clarity gives the following:

$$\frac{\partial h}{\partial t} + \frac{\partial}{\partial x}\left[\left(\frac{1}{3A}\right) h^3 \frac{\partial}{\partial x}\left\{\gamma \frac{\partial^2 h}{\partial x^2}\right\} + \left(\frac{1}{2}\right) h^2 \frac{\partial \gamma}{\partial x}\right] = 0 \qquad (2.7)$$

$$\frac{\partial c}{\partial t} = \left(\frac{1}{Pe}\right)\frac{\partial^2 c}{\partial x^2} - \frac{\partial}{\partial x}\left[c\left\{\left(\frac{1}{2A}\right) h^2 \frac{\partial}{\partial x}\left\{\gamma \frac{\partial^2 h}{\partial x^2}\right\} + h\frac{\partial \gamma}{\partial x}\right\}\right] \qquad (2.8)$$

where $A \equiv \lambda^2/{h_0}^2$ is the square of a geometric aspect ratio, and the Peclet number $Pe \equiv h_0\gamma_0/\mu D = (\lambda^2/D)/(\mu\lambda^2/h_0\gamma_0)$ is a ratio of the diffusive timescale to the convective timescale. The third relevant dimensionless group is $c_0\Delta\gamma$ which describes the initial surface tension difference between exposed and unexposed regions.

In order to develop analytical solutions leading to predictive capability for feature size and time scale for feature formation for any given system, the governing equations were linearized. For small perturbations from their initial values, the film height and concentration profile are assumed to be have the forms

$$h = 1 + \eta(x,t) = 1 + \hat{\eta}(t)\frac{\cos(\pi x)}{2} \qquad (2.9)$$

$$c = \frac{1}{2} + \xi(x,t) = \frac{1}{2} + \hat{\xi}(t)\frac{\cos(\pi x)}{2} \tag{2.10}$$

Here the initial concentration profile is taken to be sinusoidal: $c_{t=0} = 0.5(1+\cos(\pi x))$ as experimentally observed using fluorescence microscopy. (See Figure A.1 in Appendix A) $\eta(x,t)$ and $\xi(x,t)$ represent the deviation in film thickness and concentration, respectively, from their respective steady state values, 1 and ½. $\hat{\eta}$ and $\hat{\xi}$ are the purely time-dependent amplitudes of $\eta(x,t)$ and $\xi(x,t)$. Substituting these into the governing equations and neglecting higher order terms, the linearized equations are then

$$\frac{\partial\hat{\eta}}{\partial t} + \left[\left(\frac{1+\Delta\gamma c_0 c_f}{3A}\right)\pi^4\right]\hat{\eta} - \left[\left(\frac{\Delta\gamma c_0}{2}\right)\pi^2\right]\hat{\xi} = 0 \tag{2.11}$$

and
$$\frac{\partial\hat{\xi}}{\partial t} + \left[\left(\frac{\left(1+\Delta\gamma c_0 c_f\right)c_f}{2A}\right)\pi^4\right]\hat{\eta} - \left[\left(\Delta\gamma c_0 c_f - \frac{1}{Pe}\right)\pi^2\right]\hat{\xi} = 0 \tag{2.12}$$

with the initial conditions $\hat{\eta}(t=0) = 0$ and $\hat{\xi}(t=0) = 1$. These are solved to yield:

$$\hat{\eta} = \frac{\pi^2\frac{\Delta\gamma c_0}{2}}{\psi_1 - \psi_2}\left(e^{\psi_1 t} - e^{\psi_2 t}\right) \tag{2.13}$$

$$\hat{\xi} = \left(\frac{\frac{\pi^4}{3A}\left(1+\frac{\Delta\gamma c_0}{2}\right)+\psi_1}{\psi_1-\psi_2}\right)e^{\psi_1 t} - \left(\frac{\frac{\pi^4}{3A}\left(1+\frac{\Delta\gamma c_0}{2}\right)+\psi_2}{\psi_1-\psi_2}\right)e^{\psi_2 t} \tag{2.14}$$

Where

$$\psi_1,\psi_2 = \frac{\left[\left(1-\frac{\pi^2}{3A}\right)\pi^2\frac{\Delta\gamma c_0}{2} - \pi^2\left(\frac{1}{Pe}+\frac{\pi^2}{3A}\right)\right]}{2} \pm \frac{\sqrt{\left[\left(1-\frac{\pi^2}{3A}\right)\pi^2\frac{\Delta\gamma c_0}{2} - \pi^2\left(\frac{1}{Pe}+\frac{\pi^2}{3A}\right)\right]^2 - \frac{\pi^6}{3A}\left(\frac{4}{Pe}-\frac{\Delta\gamma c_0}{2}\right)\left(1+\frac{\Delta\gamma c_0}{2}\right)}}{2} \tag{2.15}$$

These describe the evolution of the film thickness and concentration profiles. The imposed surface tension profile results in the formation and growth of features when the film is thermally annealed above its glass transition temperature; the features eventually decay due to capillary forces and self-diffusion.[14] The maximum thickness attained and the thermal annealing periods after which it is achieved can be found from:

$$\hat{\eta}_{max} = \frac{\pi^2 \frac{\Delta\gamma c_0}{2}}{\psi_1 - \psi_2}\left\{\exp\left[\frac{\psi_1}{\psi_1 - \psi_2}\ln\left(\frac{\psi_2}{\psi_1}\right)\right] - \exp\left[\frac{\psi_2}{\psi_1 - \psi_2}\ln\left(\frac{\psi_2}{\psi_1}\right)\right]\right\} \quad (2.16)$$

$$t(\hat{\eta}_{max}) = \frac{\ln\left(\frac{\psi_2}{\psi_1}\right)}{\psi_1 - \psi_2} \quad (2.17)$$

Hence we arrive at analytical expressions for both the evolution of the film profile with time as well as the maximum feature size and associated time for any given choice of materials and experimental parameters. Equations 2.16 and 2.17 and the appropriate scaling factors can be used to find the dimensional maximum peak-to-valley height, $h_{max} = \hat{\eta}_{max} h_0$, and the heating time necessary to achieve it, $t_{max} = t(\hat{\eta}_{max}) \times \mu\lambda^2/h_0\gamma_0$. It should be noted that since higher order terms have been ignored, these expressions apply only to situations where the non-dimensional feature size and conversion are small. However, they serve as a useful tool to understand how the numerous independent variables and material properties affect quantities of primary interest, namely the feature size and time scale.

2.3 EXPERIMENTAL

2.3.1 Materials

Chemicals used in this study were purchased from Fisher Scientific or Sigma Aldrich and used as received unless otherwise noted. PS (M_n = 2900 g/mol, Đ = 1.2) was synthesized by activators regenerated by electron transfer atom transfer radical

polymerization (ARGET ATRP) and characterized as previously described.[15] This PS is atactic and completely amorphous exhibiting a glass transition of 61 ^{o}C.[15] (See Figure A.2 in Appendix A) High molecular weight atactic PS (M_n = 50,000 g/mol Đ = 1.06) was purchased from Pressure Chemical.

2.3.2 Sample Preparation

PS (4 wt%) was dissolved in either toluene or cyclopentanone and spin coated (Specialty Coating Systems Spincoat G3-8) onto glass or silicon substrates with approximately 2 nm thick native oxide layers. Spin speeds varied from 1000 – 2000 RPM to control the film thickness. The films were stabilized against dewetting by blending 1 wt% of high molecular weight PS (50 kDa) relative to the total PS film content. The spin coated films were placed in a vacuum chamber at room temperature overnight to get rid of residual solvents. Thicknesses were characterized using either a Veeco Dektak 6M stylus Profiler or a J.A. Woollam M-2000D Spectroscopic Ellipsometer.

2.3.3 UV Exposure

In order to prescribe the surface tension pattern in the glassy PS films, the spin coated films were UV exposed using an Optical Building Blocks ScopeLite 200 through a photo-mask with chromium line patterns on quartz. The typical intensity of this broadband light source at a typical exposure distance of 20 mm was measured to be 700 mW/cm^2 using a radiometer (Fieldmax TO, Coherent, Inc.). All experiments here used a 12.5 µm chrome line on a 25 µm pitch photo-mask (Edmunds Optics). The light exposure dose was 140 J/cm^2 for samples on silicon substrates and 840 J/cm^2 for samples on glass substrates, which yielded roughly the same photochemical conversion (~ 6.4 mol %) on each substrate as confirmed by Fourier transform infrared spectroscopy (FTIR) using a

Thermo Nicolet 6700 FTIR with liquid nitrogen cooled MCT-B detector. These exposure dose values were measured from the entire spectral output of the broadband light source (200 nm to 600 nm). Since PS absorbs only a fraction of the broadband output, significantly lower doses limited to effective wavelengths (i.e. < 300 nm), could give an equivalent result. During the UV exposure, the films were kept in the glassy state by holding the exposure stage temperature at 20 °C using an Instec mK 1000 temperature controller. To demonstrate that dehydrogenation occurs without adverse side reactions, such as coupling and crosslinking, size exclusion chromatography and spectroscopic ellipsometry were performed showing a typical patterning light exposure procedure does not affect the polymers' chain length distribution[15] or the film's glass transition temperature. (See Figure A.3 in Appendix A) Since the exact photochemical reaction leading to an associated surface energy gradient is unique to each polymer-light source system, the model equations were written in terms of photochemical conversion instead of light exposure dose.

2.3.4 Topography Creation and Characterization

After the UV exposure, the film was thermally annealed at various temperatures and annealing times to initiate the polymers' melt state flow. The annealing temperature used in experiments was confirmed by placing a type K surface thermocouple on the top surface of an uncoated substrate. The resulting topographic pattern was imaged using an optical microscope (Olympus BX 60 microscope with a Spot Insight QE camera). The evolution of topographic features at various temperatures was investigated by characterizing thickness profiles of patterned samples after sequential thermal annealing intervals. The average peak-to-valley height was determined after examining 10 half-periodicities near the center of the film.

2.4 RESULTS AND DISCUSSION

2.4.1 Physical Property Values

Material property values used as input for model predictions are summarized in Table 2.1 at the temperatures considered. The viscosity, μ, of the PS blend as used (see Section 2.3.2) was measured at 120 °C under steady shear. (See Figure A.4 in Appendix A) This viscosity was adjusted to lower values at higher temperatures using free-volume parameters obtained from literature $\mu(T)$ data.[16] A handbook value[17] was used for γ_0, the surface tension of PS, and was subsequently adjusted for smaller molecular weights and higher temperatures.[18]

The (dimensional) difference in surface tension between PS and poly(phenyl acetylene) (PPA), $\gamma_0\Delta\gamma$, was extracted from the experimentally observed feature height evolution at short times. (See Figure A.5 in Appendix A) While a literature value for the surface energy of PPA is not available for comparison, we previously estimated it using a group contribution method to determine $\gamma_0\Delta\gamma$; from this approach, the difference in surface tension between PS and PPA at 25 °C, is 6.8 dyne/cm.[15] Furthermore, note that an equimolar copolymer of ethylene and propylene possesses a surface tension 1 dyne/cm lower than its partially dehydrogenated form, poly(isoprene), at 20 °C.[18] We consider the values of $\gamma_0\Delta\gamma$ in Table 2.1 to be very reasonable because they agree in magnitude, and lie between, these examples. At the photochemical conversion typically used for patterning, c_0 = 6.4 mol%,[15] the surface energy difference between exposed and unexposed regions, $c_0\gamma_0\Delta\gamma$, is at most 0.2 dyne/cm. $c_0\gamma_0\Delta\gamma$ does not appear to have a strong temperature dependence within the relatively narrow temperature range explored in this initial work.

The effective polymer blend diffusivity, $\mathcal{D}$, was extracted from the feature height decay at 120 °C observed at long experimental times. (See Figure A.6 in Appendix A)

This value of $\mathcal{D}$ was adjusted to higher temperatures using an Arrhenius fit to bulk self-diffusion coefficient values measured by Fleischer[19] for PS with M_W = 2.1 kg/mol and M_W = 4.0 kg/mol at temperatures between 160 ^oC and 220 ^oC to obtain the values in Table 2.1. Note that Ediger and coworkers[20] described $\mathcal{D}$ (T > 84 ^oC) for a PS blend possessing M_w = 1.8 kg/mol and T_g = 59 ^oC using a WLF equation

$$\log_{10}\mathcal{D} = -14.48 + \frac{10.37\left(T - T_g - 16.6\ °\mathrm{C}\right)}{56.11\ °\mathrm{C} + \left(T - T_g - 16.6\ °\mathrm{C}\right)}. \tag{2.18}$$

Our PS blend possesses T_g = 61 ^oC and M_W = 3.98 kg/mol, the latter of which is a factor 2.2 higher than that determined by Ediger and coworkers. A direct comparison can be made between their values of $\mathcal{D}$ and the ones in Table 2.1 by using T_g = 61 ^oC in Equation 2.18 and dividing the $\mathcal{D}$ values it predicts by 2.2.[21] Since these values differ from ours by less than 50% at all 4 temperatures used in this work, we consider the values of $\mathcal{D}$ used in model predictions to be very reasonable. This agreement implies that this approach of extracting temperature dependent physical parameter values, such as the surface tension gradient and diffusivity, using the model with Marangoni experiments could be used to quickly characterize any polymer without sophisticated or specialized measurement methods.

Table 2.1: Physical property values used in model predictions.

Property	Value				Ref.
	120 °C	126 °C	136 °C	140 °C	
μ [Pa·s]	2550	1000	250	150	Appendix A, [16]
γ_0 [dyne/cm]	32.2	31.7	31.1	30.8	[17, 18]
$\gamma_0\Delta\gamma$ [dyne/cm]	2.0	3.0	3.1	3.1	Appendix A
$\mathcal{D}$ [cm^2/s]	3.63×10^{-11}	2.15×10^{-10}	4.49×10^{-10}	5.91×10^{-10}	Appendix A, [19]

2.4.2 Evolution of Topographical Features after Annealing above T_g

A schematic for topographical patterning of polymers is shown in Figure 2.1. UV irradiation through a photo-mask selectively dehydrogenates the PS backbone and increases the local surface energy in the UV exposed regions compared to the unexposed regions. This was predicted by a group contribution method and confirmed by a decrease in water contact angle. As a result, the polymer flows from low surface tension regions (unexposed to light) to high surface tension regions (exposed to light) upon subsequent thermal annealing above the glass transition temperature (i.e., in the liquid state) due to the Marangoni effect. This flow creates smooth, three dimensional topography reflective of the original light exposure pattern.

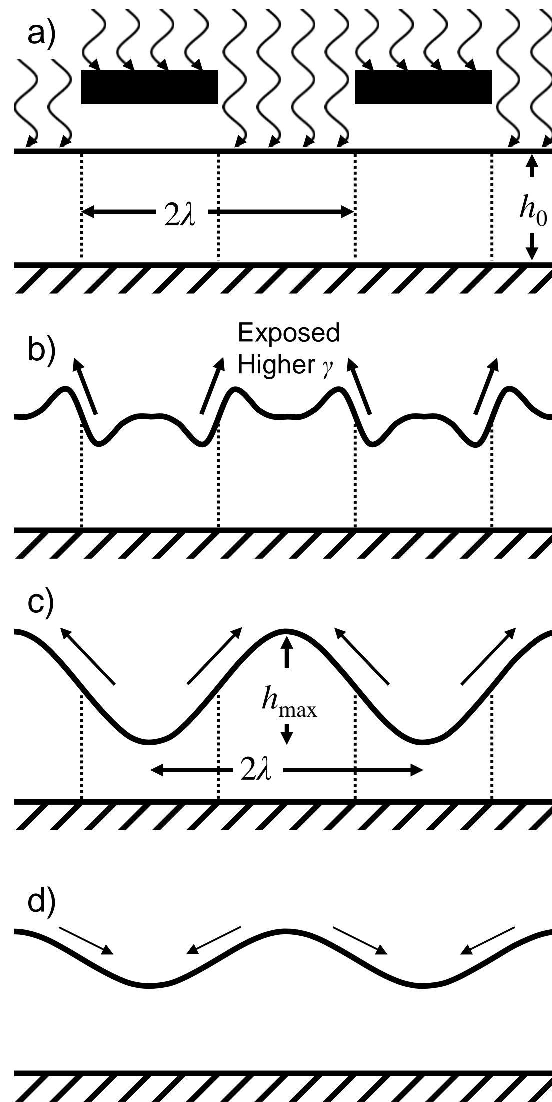

Figure 2.1: Patterning schematic. (a) UV illumination through a line-and-space photomask possessing a half-periodicity, λ, while the polymer film is in the solid state with an initial film thickness, h_0. (b) The topographical profile after a short period of thermal annealing above the glass transition temperature of the polymer shows its melt-state flow is first initiated near the boundary between UV exposed and unexposed regions. (c) Further annealing develops the topographical profile into a complete sinusoidal shape with the same periodicity as the mask reaching the maximum peak-to-valley height, h_{max}, then, (d) the topography dissipates after extended thermal annealing.

Figure 2.2 includes both experimental results and model predictions for the film thickness profile after short and long thermal annealing periods. Each different stage of topography development as illustrated in Figure 2.1 is revealed by experiments and theory. It is evident that the (non-linear) model reproduces both the formation of secondary minima observed at short periods of thermal annealing and that of the complete sinusoidal features at the extended annealing periods.

Both theory and experiment reveal that the appearance of secondary peaks at short thermal annealing times is related to the shape of the initial surface tension profile. Intuitively, one expects polymer transport to occur first at the interface between exposed and unexposed regions before it can reach the regions relatively far from that interface. This concept is verified by noting that Equation 2.1 shows that the Marangoni flux is proportional to the second derivative of surface tension. At very short times, the film is essentially flat and capillary dissipation is negligible, resulting in maximum accumulation (and depletion) at points where the second derivative of surface tension has its largest magnitude. At intermediate and long times, on the other hand, when capillary forces are also relevant, maxima and minima in film height coincide with the maxima and minima of the concentration profile at the centerlines of mask quartz spaces and chrome lines, respectively. When the points of maximum magnitude of the second derivative of the initial surface tension profile do not coincide with the centerlines of the mask lines and gaps, secondary peaks form at short times. As long as the surface tension profile is present, these peaks always form; however, they may be short-lived in many cases.[16] This finding is practically relevant because it represents a strategy, rooted in the physical nature of fluids, to double the areal density of topographic features from that present in the projected photo-mask pattern.

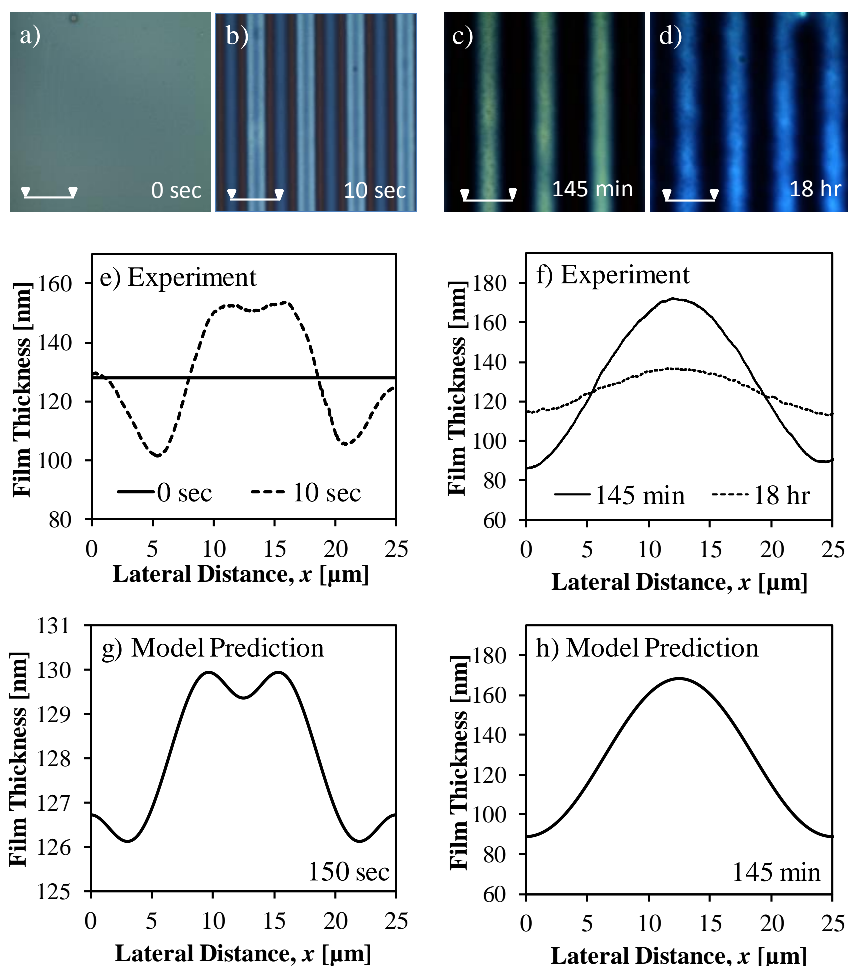

Figure 2.2: Representative 100 μm wide optical micrographs of one 128 nm thick PS film supported on a Si wafer after short (a,b) and long periods (c,d) of thermal annealing at120 °C. Prior to the heating, the PS film was exposed to UV light through a 25 μm pitch photo-mask. Different colors observed in the optical micrograph are light interference patterns resulting from the film thickness variations. Experimentally characterized height profiles for one periodicity from the same polymer film are shown in (e) and (f) after short and long periods of heating, respectively. Two different film thickness profiles were also theoretically predicted for a 128 nm thick film and are shown in (g) and (h), respectively.

It is also apt to note that the three distinct regimes of film topography evolution once heated above its glass transition temperature are strongly connected to the structure of the theoretical model. At very short times, secondary peaks form at points where the

second derivative of the initial surface tension profile has its largest magnitude. At intermediate times, features rise as Marangoni flux dominates over capillary dissipation. The Marangoni driving force decays with time as polymer self-diffusion makes the concentration/surface tension profile increasingly uniform while capillary dissipation intensifies as features grow. Eventually capillary forces dominate, features begin to decay and the film tends towards its original flat form.

2.4.3 Quantitative Comparison of the Model to Experimental Data

Figure 2.3 depicts both the experimentally observed and model predicted evolution of peak-to-valley height, $\hat{\eta}h_0$, as a function of cumulative annealing time at four different temperatures. Reasonable agreement between model predictions and experimental results are achieved for three of the four temperatures. The theoretical model quantitatively predicts both the height of features as well as the timescale associated with their growth and decay. The quality of agreement obtained at the two highest temperatures is especially encouraging since those model predictions were made with only one parameter, $c_0\Delta\gamma$, that was gleaned from the data itself. Unfortunately, as evident in Figure 2.4, the highest $\hat{\eta}h_0$ values measured at 126 ^{o}C are exceptionally large relative to the two neighboring datasets, and the model predictions do not closely match them.

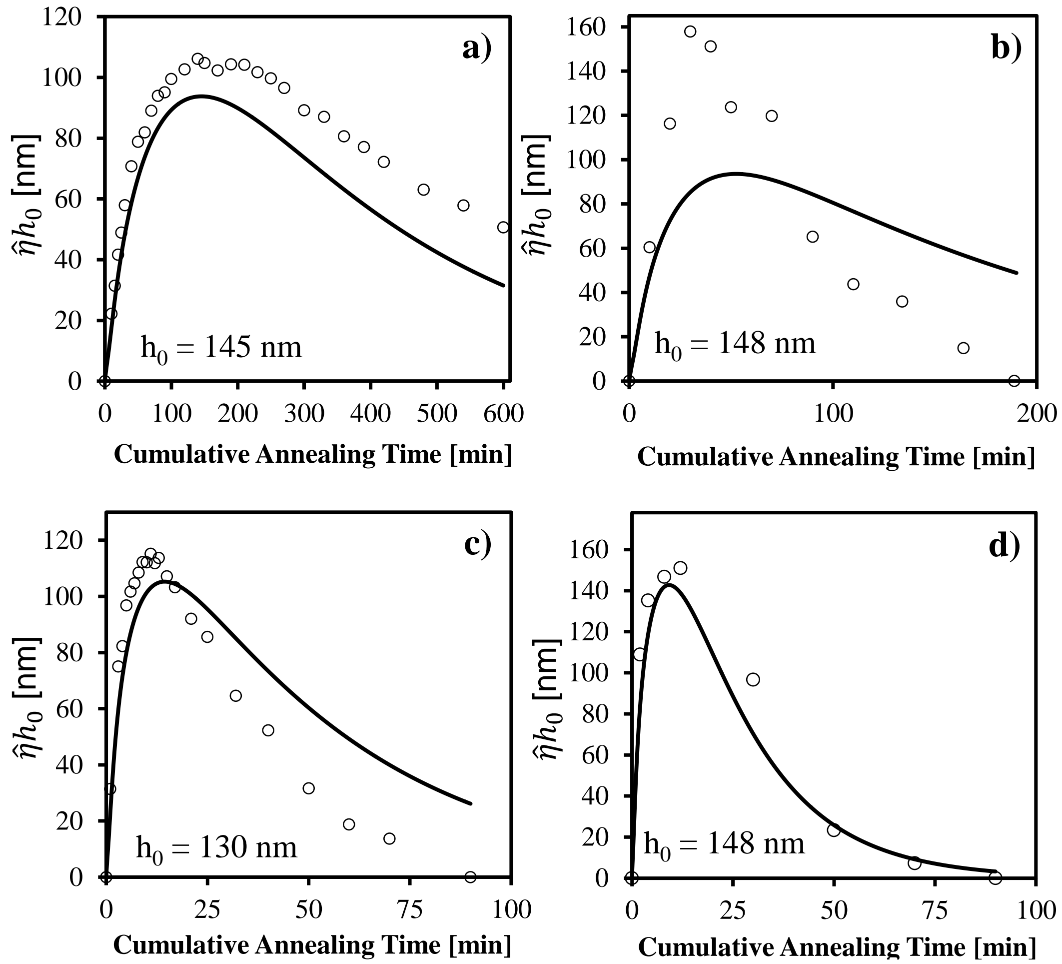

Figure 2.3: Comparison of peak-to-valley height evolution between experimental results (opened circle) and model predictions (solid line) at (a) 120 °C, (b) 126 °C, (c) 136 °C, and (d) 140 °C for PS films on glass.

Raising temperature reduces the viscosity of the film and increases its diffusivity. The former promotes the formation of larger features and more rapidly, while the latter hastens the onset of decay. Any change in the patterned surface tension gradient with temperature would also affect the process. Results show that overall, higher temperatures make larger features accessible while reducing the time needed to form them. Again, only the experimental data point for h_{max} collected at 126 °C lies outside this general trend. A 20 °C rise in temperature increases feature height by 50% while reducing the heating time

eleven-fold. Higher temperatures, within material constraints, are therefore preferable as long as the films are stable.

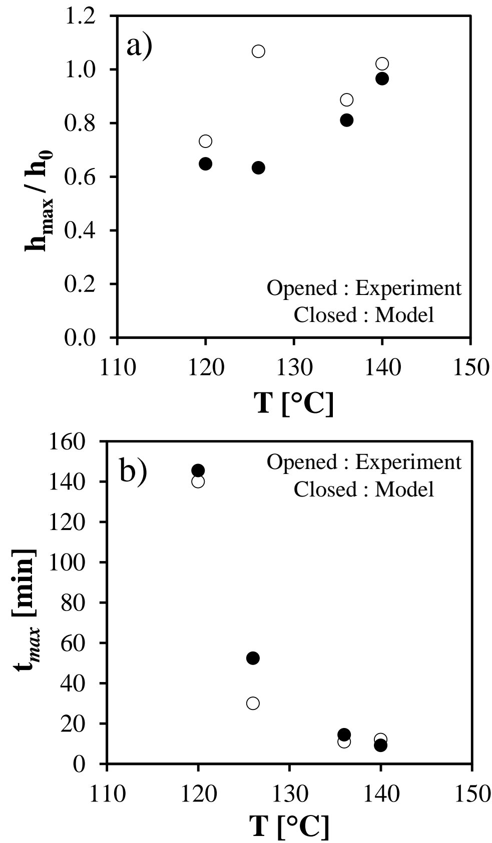

Figure 2.4: (a) Attainable maximum feature size and (b) associated thermal annealing time as a function of temperature.

2.4.4 Model Predictions of Marangoni-Driven Flow at Various Conditions

In the context of a patterning process targeting a specific feature size, it is prudent to engineer a process wherein the maximum height attained by features coincides with the target feature height. This ensures that the desired pattern is achieved in the most efficient way possible and is an important goal to enable rapid processing methods, such as roll-to-roll processing. Therefore, key variables for the application of this technique for various purposes are the maximum feature height attained and the heating time needed to

achieve it. In order to be able to design a process targeting a specific feature size with the desired resolution for a given application in the shortest possible heating time, an understanding of the limits of the process and the effects of each process variable on the two key quantities is necessary.

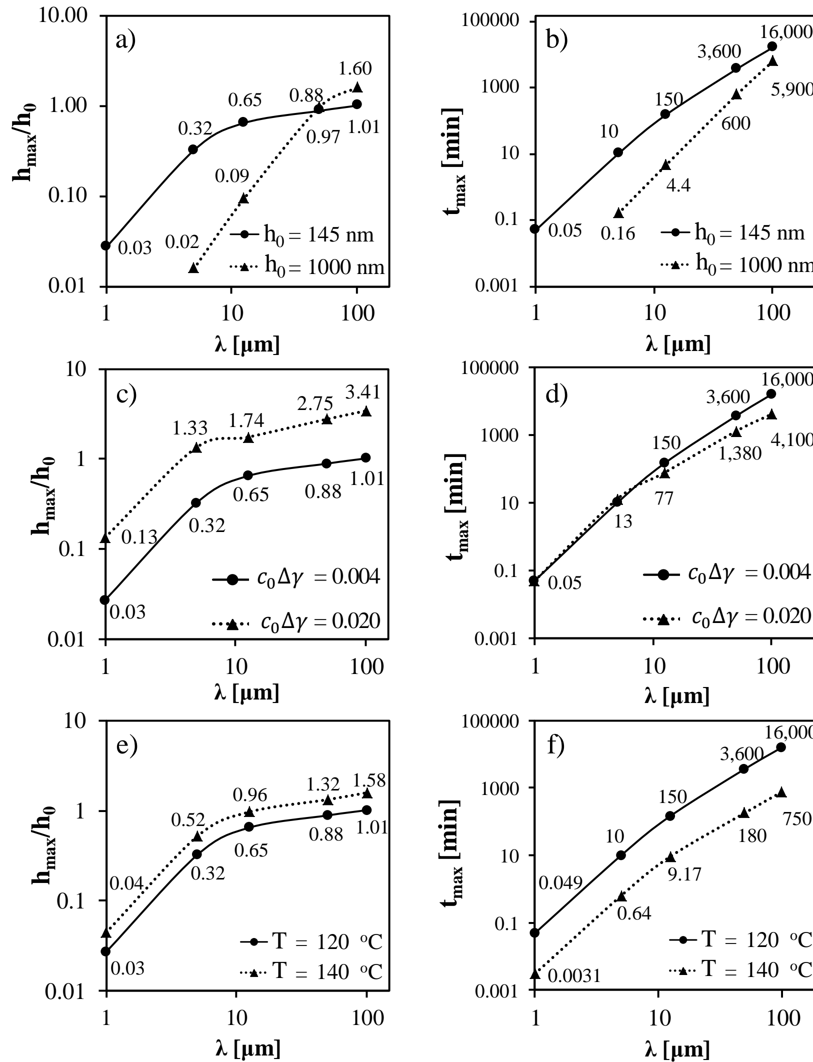

Figure 2.5: Normalized maximum peak-to-valley height, h_{max}/h_0, and heating time as a function of resolution (photo-mask half-periodicity) for different film thicknesses (a, b), surface tension differentials (c, d), and heating temperatures (e, f). Data points represent model predictions and lines are guides to the eye. All case studies are otherwise at identical conditions as a base condition with h_0 = 145 nm, $c_0\Delta\gamma$ = 0.004, and/or T = 120 °C.

Figure 2.5 shows how absolute feature height and thermal processing time vary as a function of the desired pattern periodicity, and how experimental parameters, namely thickness, the initial surface tension differential, and annealing temperature affect this relationship. An increase in pattern periodicity results in an enhancement in the accessible feature height but delays the achievable throughput time-scale. This is due to the fact that features farther apart can draw material from a larger region of low surface tension polymer. This effect has previously been seen in evaporative self-assembly of particles[22, 23] where reduced pitch results in smaller features. As seen in Figure 2.5, this feature height penalty worsens with decreasing periodicity whereas promotion in throughput time-scale is approximately linear on this log-log plot.

The feature height in normalized terms (i.e. relative to the initial film thickness) is larger for thinner films. However, the absolute height of the features above the residual layer is larger for thicker films. This means that in applications tolerant to thick residual layers, greater variations in film thickness can be achieved by using thicker films. On the other hand, for applications in which the residual layer thickness between the feature minima and substrate surface needs to be minimized, thinner films are preferable. The data in Figure 2.5a predict that for the thinner film, h_0 = 145 nm, the highest possible aspect ratio of features, $½h_{max}\lambda^{-1}$, is achieved for a mask with a periodicity between 10 and 25 μm. However, for the thicker film, h_0 = 1000 nm, the maximum achievable aspect ratio can be made with a mask possessing a periodicity between 100 and 200 μm.

The initial surface tension differential is set by the UV exposure time. A longer exposure time increases the surface tension differential and results in significantly larger features. The heating time necessary to reach the maximum feature height is not strongly affected by the surface tension difference. Figures 2.5c and 2.5d predicts that maximizing

the surface tension difference is the most effective way to manufacture films with the greatest variations in film thickness.

As noted above, higher temperature promotes the formation of larger features at faster rates. Figures 2.5e and 2.5f shows that while the increase in feature height resulting from a 20 degree rise in temperature to 140°C is relatively modest (~ 60%), the necessary thermal processing time shortens by well over an order of magnitude. These results for varying temperature also suggest the role the molecular weight of the polymer plays in determining feature size and heating time. Temperature affects the dynamics of the film through variation in viscosity and diffusivity. According to the Rouse model for unentangled polymer melts, the product of diffusivity and viscosity is directly proportional to temperature and inversely proportional to molecular weight.[21] Reduced molecular weight would therefore exert an effect on feature height and throughput time-scale as a function of pattern periodicity similar to that of increased temperature. The relatively modest rise in feature height with increased temperature is due to the fact that the viscosity of the polymer melt and the diffusivity of the photo-exposed polymers are coupled, as predicted by the Rouse model. With increasing temperature, a sharp decline in viscosity, which should promote the formation of larger features more rapidly, is accompanied by an increase in the polymers' self-diffusion, resulting in a more rapid dissipation of the surface tension gradient.

2.5 CONCLUSION

Here a model was introduced which accurately describes topography formation in thin polymer films which possess surface energy patterns. All of the stages of topography development (see Figure 2.2) are qualitatively predicted by a relatively simple, computationally efficient adaptation of the film equation. Strictly speaking, if a polymer film possesses a surface energy pattern, even one in which the variations are only 0.2

dyne/cm, Marangoni flow will result when it is heated to its liquid state. Only the size and longevity of the topographical features varies with the properties of the system. This, rather than a critical value of the Marangoni number, defines a criterion for feature formation.

Furthermore, the model is capable of quantitatively predicting the peak-to-valley heights of the smoothly varying thickness profile at different heating times and temperatures, using reasonable physical parameters as input (see Figure 2.3). The model was used to define process trends to guide future development of this patterning methodology. The highest feature aspect ratios, $½h_{max}\lambda^{-1}$, can be achieved for thinner films, high surface energy differences between exposed and unexposed regions, a mask periodicity that is optimized for film thickness, and systems which possess both low viscosity and low self-diffusion coefficients. The dissipation of film topography at excessively long heating times was used to extract a diffusion coefficient at 120 ^{o}C that matched a literature value within 50%. Therefore, this demonstration could motivate the application of this combined theory/experimental methodology as a measurement method for surface energy changes and diffusion coefficients of any polymer in thin films, using only inexpensive bench equipment and materials.

2.6 REFERENCES

1. Wu, N.; Pease, L. F.; Russel, W. B. *Langmuir* **2005**, 21, 12290-12302.
2. Amarandei, G.; Beltrame, P.; Clancy, I.; O'Dwyer, C.; Arshak, A.; Steiner, U.; Corcoran, D.; Thiele, U. *Soft Matter* **2012**, 8, 6333-6349.
3. Roberts, S. A.; Kumar, S. *J. Fluid Mech.* **2009**, 631, 255-279.
4. Verma, R.; Sharma, A.; Kargupta, K.; Bhaumik, J. *Langmuir* **2005**, 21, 3710-3721.
5. Dickey, M.; Raines, A.; Collister, E.; Bonnecaze, R.; Sreenivasan, S. V.; Willson, C. G. *J. Mater. Sci.* **2008**, 43, 117-122.
6. McLeod, E.; Liu, Y.; Troian, S. M. *Phys. Rev. Lett.* **2011**, 106, 175501.
7. Pease, L. F.; Russel, I. W. B. *J. Chem. Phys.* **2006**, 125, 184716.
8. Schäffer, E.; Harkema, S.; Roerdink, M.; Blossey, R.; Steiner, U. *Macromolecules* **2003**, 36, 1645-1655.

9. Kumar, S. *Langmuir* **2003**, 19, 2473-2478.
10. Paretkar, D.; Xu, X.; Hui, C.-Y.; Jagota, A. *Soft Matter* **2014**, 10, 4084-4090.
11. Casper, M. D.; Gozen, A. O.; Dickey, M. D.; Genzer, J.; Maria, J.-P. *Soft Matter* **2013**, 9, 7797-7803.
12. Jensen, O. E.; Grotberg, J. B. *J. Fluid Mech.* **1992**, 240, 259-288.
13. Gaver, D. P.; Grotberg, J. B. *J. Fluid Mech.* **1990**, 213, 127-148.
14. Janes, D. W.; Katzenstein, J. M.; Shanmuganathan, K.; Ellison, C. J. *J. Polym. Sci., Part B: Polym. Phys.* **2013**, 51, 535-545.
15. Katzenstein, J. M.; Janes, D. W.; Cushen, J. D.; Hira, N. B.; McGuffin, D. L.; Prisco, N. A.; Ellison, C. J. *ACS Macro Lett.* **2012**, 1, 1150-1154.
16. Williams, M. L. *J. Appl. Phys.* **1958**, 29, 1395-1398.
17. Brandrup, J.; Immergut, E. H.; Grulke, E. A.; Abe, A.; Bloch, D. R., *Polymer Handbook*. 4th ed.; John Wiley & Sons: Hoboken, 2005.
18. Bicerano, J., *Prediction of Polymer Properties*. 3rd ed.; Marcel Dekker, Inc.: New York, 2002.
19. Fleischer, G. *Polym. Bull.* **1984**, 11, 75-80.
20. Urakawa, O.; Swallen, S. F.; Ediger, M. D.; von Meerwall, E. D. *Macromolecules* **2004**, 37, 1558-1564.
21. Rouse, P. E. *J. Chem. Phys.* **1953**, 21, 1272-1280.
22. Harris, D. J.; Hu, H.; Conrad, J. C.; Lewis, J. A. *Phys. Rev. Lett.* **2007**, 98.
23. Arshad, T. A.; Bonnecaze, R. T. *Nanoscale* **2013**, 5, 624-633.

Chapter 3: Bidirectional Control of Flow in Thin Polymer Films by Photochemically Manipulating Surface Tension

3.1 INTRODUCTION

In previous chapters, it was demonstrated that photochemically directed Marangoni flow can create smooth, three dimensional topography reflective of the light exposure pattern in a polystyrene film. Moreover, a theoretical framework that gives a more thorough understanding of the physics of this process was presented along with a comparison between simulation predictions and experimental observations. This Marangoni-driven patterning may represent a practically useful route to manufacture topographically patterned surfaces. An especially versatile material for this application should be able to be spatially programmed to possess regions of higher or lower relative surface tension so that the direction of flow into or out of those areas could be directed with precision. To this end, we describe here a new photopolymer whose melt-state surface tension can be selectively raised or lowered in the light exposed regions depending on the wavelength and dose of applied light. Control of the directionality of melt-state surface tension changes is obtained by selecting irradiating wavelengths that activate different photochemistries in the solid state. The ability to control film convection into or out of exposed regions on-demand enables a greater diversity of accessible structures than if only flow in one direction was triggered. Relatively complex three-dimensional shapes and hierarchical assemblies are therefore achievable using very simple photomask patterns.

This chapter reproduced in part from "Bidirectional Control of Flow in Thin Polymer Films by Photochemically Manipulating Surface Tension" Kim, C. B.; Janes, D. W.; Zhou, S. X.; Dulaney, A. R.; Ellison, C. J. *Chemistry of Materials* **2015**, *27*, 4538-4545 with permission from the American Chemical Society, copyright 2015.

3.2 METHODS

3.2.1 Materials

A styrene-acrylic acid copolymer, Joncryl 611, was provided by BASF. Nifedipine was purchased from TCI America and used as a photo-base generator (PBG). Polished 4 in. diameter silicon wafers were purchased from University Wafer. All other chemicals used in this study were purchased from Fisher Scientific or Sigma Aldrich and used as received unless otherwise noted.

3.2.2 Film Preparation and Characterization

Films in this study were spin-coated (Specialty Coating Systems Spincoat G3-8) onto silicon substrates with ~ 2 nm thick native oxide layers. Spin coating solution concentrations were 1.5-15 wt% polymer in diglyme. Solid film compositions contained 30 wt% PBG. Spin speeds were varied from 1000 – 3000 RPM to control the film thickness. The thickness of films prepared on silicon substrates were characterized by ellipsometry using a J.A. Woollam M-2000D spectroscopic ellipsometer using wavelengths from 382 to 984 nm with a 65° angle of incidence.

3.2.3 Topography Formation and Characterization

Light exposures were performed with a 200 W metal-halide lamp with broadband output from 200 − 600 nm (Optical Building Blocks Scopelite 200). For the 365 nm UV exposure, a bandpass optical filter was employed (10 nm full-width/half-maximum, Edmund Optics). A 20 mm working distance was used with a light intensity of 50 mW/cm^2 as measured by a Coherent Field MaxII-TO radiometer with a PM10 sensor. A typical exposure dose for 365 nm exposure was 0.4 J/cm^2 (8 seconds) unless otherwise noted. Broadband light exposure was performed with the same metal halide lamp but without any optical filter. The broadband light intensity was 0.7 W/cm^2 at a 20 mm

working distance. The typical light exposure dose was 420 J/cm^2, which was measured from the entire spectral output of the broadband light source. Since the host polymer absorbs only a fraction of the broadband output, significantly lower doses limited to effective wavelengths (i.e. < 300 nm), could give an equivalent result. The exposure stage was held at 0 − 20 °C by an Instec mK 1000 temperature controller with a HCS-402 stage to retain a solid state film during exposure.

All exposed films were annealed at 150 °C on a heating plate to develop topographic features unless otherwise noted. Bright field optical micrographs were taken for all samples using an Olympus BX 60 microscope with a Spot Insight QE camera. The feature heights were characterized at ambient temperature and pressure using either a Veeco Dektak 6M stylus profiler with a stylus diameter of 25 μm and stylus force of 3 mg, a Veeco NT9100 optical profiler, or an AC mode atomic force microscope (AFM, Asylum Research). AFM tips with a resonant frequency of 320 kHz and a force constant of 42 N/m were purchased from Nanosensors.

3.2.4 Characterization of Properties and Composition

A carbon nuclear magnetic resonance (^{13}C-NMR) measurement was performed using a Varian Direct Drive 600 system using deuterated chloroform ($CDCl_3$) as the solvent. The relaxation delay was 10 seconds with a 1 second acquisition time using a 90 degree pulse.

Size exclusion chromatography (SEC) measurements were performed using a Viscotek VE 2001 triple-detector SEC module possessing two I-Series mixed bed low MW columns. It was equipped with a Viscotek Model 270 dual viscometer/light scattering detector, a Viscotek VE 3580 refractive index detector, and a Jasco FP-2020 Plus Intelligent Fluorescence Detector. Tetrahydrofuran (THF) was used as the eluent at a

flow rate of 1.0 mL/min. Samples were dissolved in THF and filtered through a 0.20 µm PTFE filter before injection.

Background-subtracted, transmission-mode Fourier transform infrared (FTIR) spectra were recorded on a Thermo Nicolet 6700 FTIR with a liquid nitrogen cooled MCT-B detector. Films spin-coated onto a double-side polished silicon wafer were used. Prior to the FTIR measurement, background spectra were collected using clean, identical silicon wafers to appropriately correct the polymer film data. 64 scans with a resolution of 4 cm^{-1} were averaged. For quantitative analysis, the areas under distinct absorption peaks were measured on the associated OMNIC software. The areas under the peaks of interest ($A_{interest}$) were normalized to the area under the invariant peaks ($A_{invariant}$) for quantitating the extent of reaction for each chemical transformation. The extent of each chemical transformation was calculated from

$$\text{Extent of reaction} = 1 - \left(\frac{A_{t,interest}}{A_{t,invariant}}\right)\left(\frac{A_{0,invariant}}{A_{0,interest}}\right) \tag{3.1}$$

Here, *t* refers to the cumulative exposure time while 0 refers to pre-exposure conditions.

UV/Vis spectra of films and solutions were acquired with a Thermo Scientific Evolution 220 UV-Visible Spectrophotometer. Films were characterized on background-subtracted quartz substrates using thicknesses measured on identically prepared films on silicon wafers. Solutions were measured in quartz cuvettes with background contributions from the solvent and cuvette subtracted. Fluorescence spectroscopy was performed for solutions in diglyme on a Photon Technology International Quanta Master 40 with a photomultiplier tube detection system, 4 nm excitation slits, and 2 nm emission slits.

Solution samples used for SEC, UV/Vis spectroscopy, and fluorescence spectroscopy were prepared first by casting films with an initial film thickness of 240 nm.

The film thickness reduced to 187 nm after 365 nm exposure and heating. Films were then re-dissolved and analyzed. UV/Vis measurements on 190 to 240 nm thick films are shown in Figure B.1 in Appendix B. The light dose is attenuated by at most ~ 25%; therefore, photochemical transformations were applied approximately uniformly through the film depth.

3.2.5 Predictive Estimates of Surface Energy Changes

Predictive estimates of the surface tension gradients imposed by each chemical transformation (see Table 3.1) were based on molar composition-weighted averages of homopolymer values. The melt-state surface tension change due to decarboxylation was based on handbook values[1] for PS (31.4 dyne/cm), poly(methacrylic acid) (31.2 dyne/cm, substituted for poly(acrylic acid)), and poly(ethylene) (29.4 dyne/cm) at 150 °C, the temperature used to drive flow in this study. Dehydrogenation of 6% of the repeat units in PS homopolymer results in a surface energy increase of 0.2 dyne/cm at 150 ^{o}C.[22] This value enabled prediction of the surface energy change for the dehydrogenated styrene-acrylic acid copolymer used in this work.

3.2.6 Contact Angle Analysis of Dewetted Polymer

Si wafer substrates were coated by crosslinked poly(cyclohexylethylene) (PCHE). This layer was crosslinked by co-casting it with 4 wt.% ethane-1,2-diyl bis(3-benzoylbenzoate) and exposing it to 900 J/cm^2 broadband light.[3] The crosslinked PCHE layer remained affixed with no change in film thickness (~ 110 nm) after repeated washings with a good solvent, toluene, and it was then thermally annealed at 120 °C in vacuum for 2 h. The static water contact angle of this surface was 92°. Styrene-acrylic acid copolymer films were spin-coated onto the crosslinked PCHE layers. 14 nm thick films of neat styrene-acrylic acid copolymer were used for the γ_0 and γ^+ films; a 17 nm

thick film containing 30 wt. % PBG was used for the γ^- film. The blanket exposure conditions were analogous to those used for patterning. To dewet the styrene-acrylic acid copolymer films, they were heated at 170 °C in vacuum for 30 minutes then in ambient air for 2 h to induce polymer film dewetting. The droplet height h and radius r were measured using atomic force microscopy (AFM) for 5 - 8 different droplets on each sample, and the contact angle was calculated by assuming a spherical cap shape (h << 2r, where h and r are cap height and radius) and using the formula $\cos\theta = 1 - 2(h/r)$[2,4,5] The fractional increase or decrease in surface energy, $\frac{\gamma_2}{\gamma_1}$, due to a contact angle shift from θ_1 to θ_2 can be estimated from

$$\left(\frac{\gamma_2}{\gamma_1}\right) \approx \left(\frac{\cos\theta_1 + 1}{\cos\theta_2 + 1}\right)^2 \tag{3.2}$$

This simplification of Young's Equation is based on a geometric mean rule taking into account dispersive interactions as discussed in Ref. 6; we consider our use of it reasonable because θ_1 and θ_2 differ only by a few degrees. We estimated the absolute change in surface energy, $\gamma_2 - \gamma_1$, using γ_1 = 31.3 dyne/cm as estimated for the styrene-acrylic acid copolymer at 150 ^{o}C.

3.3 RESULTS AND DISCUSSION

3.3.1 Photochemical Transformation Strategy

The sequential chemical transformations used to control Marangoni flow are shown in Figure 3.1. Each reaction changes the composition of the random copolymer chain, producing desired changes in surface energies. A styrene-acrylic acid copolymer was used as a host polymer. Carbon NMR (^{13}C-NMR) analysis of the copolymer suggests a composition ratio of 0.26 : 0.74 of acrylic acid to styrene groups, respectively (See Figure B.2 in Appendix B). Base-catalyzed thermal decarboxylation of polymers containing acrylic acid has been studied both in films[7,8] and in aqueous solution.[9] When

a film of the copolymer and a Nifedipine photo-base generator (PBG) is exposed to 365 nm UV light and heated, the exposed PBG decarboxylates the acrylic acid groups in the exposed regions.[7,8] This reaction yields poly(ethylene) subunits as shown as Film γ^- in Figure 3.1. This product possesses a relatively lower melt-state surface tension, γ^-, than the starting film, γ_0. We anticipate a decrease in melt-state surface tension because the surface energy of random copolymers containing ethylene and acrylic acid decreases from 59 to 41 dyne/cm at 20 °C as the ethylene fraction increases from 80 to 97 mol%.[1] A subsequent broadband UV exposure applied to the same film, denoted as Film γ^+ in Figure 3.1, dehydrogenates the styrenic backbone.[10] Due to an increased degree of unsaturation, the product of this reaction possesses a higher melt-state surface tension, denoted as γ^+. An increase in surface tension for exposed PS homopolymer is supported by both water contact angle measurements and group contribution estimations,[10] and a full theoretical analysis of Marangoni flow in this system indicated an increase of 0.2 dyne/cm due to dehydrogenation.[2] By convention in this work, we use the symbols γ_0, γ^-, and γ^+ to refer to both the film melt-state surface tension and the film regions themselves.

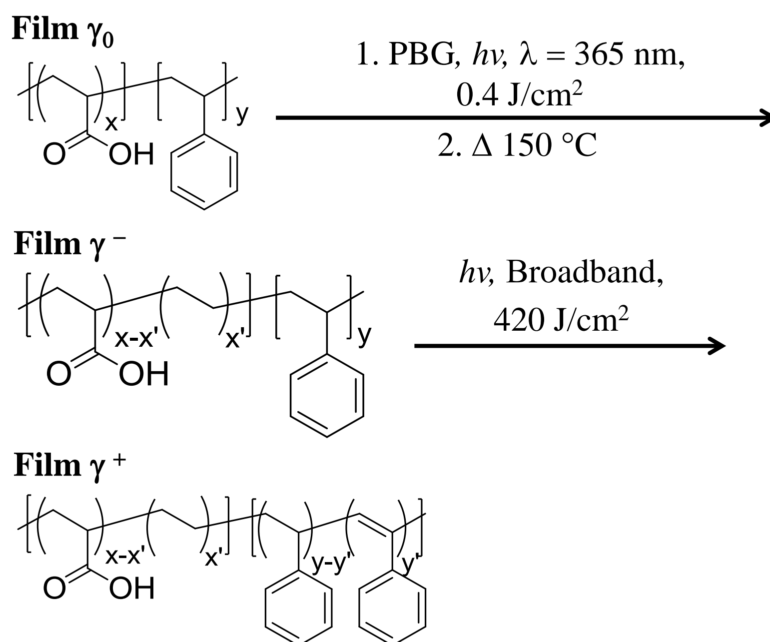

Figure 3.1: Chemical transformation scheme. The first chemical transformation, a decarboxylation, is shown from Film γ_0 to Film γ^-. The second chemical transformation, a dehydrogenation, is shown from Film γ^- to Film γ^+.

A schematic for patterning films by directing Marangoni flow is shown in Figure 3.2. Copolymer and PBG are co-cast by spin-coating onto a silicon wafer from diglyme solution. To direct flow out of the light exposed regions, a 365 nm light exposure was applied through a photomask to fully convert PBG to its basic form in the exposed regions. Melt-state flow is triggered by thermal annealing above the film's T_g and results in a topographic pattern that is *thinnest* at the center of the exposed regions. Alternatively, to direct flow into exposed regions, a different film can be first blanket exposed to 365 nm UV light without any masks and then thermally annealed at 150 °C to decarboxylate the polymer and uniformly lower the surface energy of the entire film. A second broadband UV exposure through a mask selectively raises the melt-state surface tension of the exposed regions from γ^- to γ^+ through dehydrogenation. Annealing at 150 °C triggers melt-state flow that creates a topographic pattern *thickest* at the center of the

exposed regions. In this sequential photochemical approach, the directionality of relative melt-state surface tension changes in UV exposed regions can be spatially programmed into a solid polymer film.

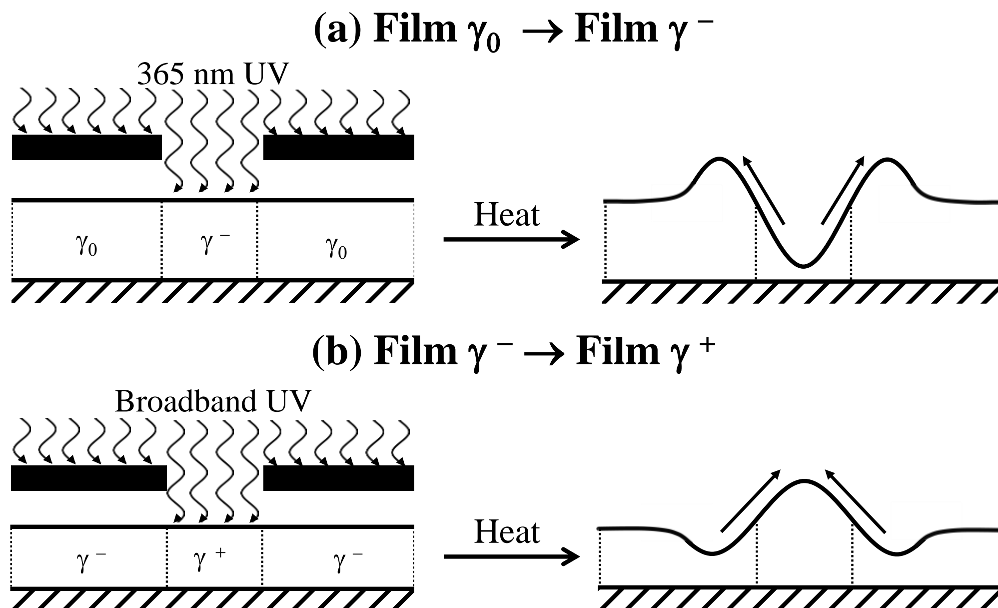

Figure 3.2: Patterning schematic. (a) 365 nm UV light exposed through a mask activates PBG in the exposed regions. Upon thermal annealing to liquefy the polymer, activated PBG also locally decarboxylates the polymer. This lowers the melt-state surface tension from γ_0 to γ^-, and polymer flows out of the exposed regions. Alternatively, after uniformly decarboxylating a film, (b) broadband UV exposure applied through a mask selectively increases the melt-state surface tension from γ^- to γ^+. Upon thermal annealing, polymer flows into the exposed regions.

3.3.2 Pattern Formation and Directionality

Representative optical and AFM images of the sample after the processes described above are shown in Figure 3.3. A mask with a regular array of hexagonally arranged hexagonal transparent regions was used in both cases. The different interference colors present in the optical micrographs are reflective of spatially-directed film thickness changes. Due to the different locally imposed photochemical transformations, increases

or decreases in thickness are present in the exposed regions after thermal annealing. Each example in Figure 3.3 demonstrates the topographic directionalities indicated by the schematic in Figure 3.2. The thickness reduction shown in the upper half of Figure 3.3 (240 nm) is well over twice the film thickness reduction that would be possible from polymer mass loss due to decarboxylation and/or evaporation of residual diglyme alone (See Figure B.7 in Appendix B that shows the initial film thickness loss due to these two factors). Therefore, the formed surface topography is due to Marangoni flow of polymer to higher surface tension (unexposed) regions. The thickness increases shown in the lower half of Figure 3.3 (210 nm) is similar to that in the upper half, suggestive that the photochemical surface tension changes are similar in magnitude. Note that in both cases thickness changes form against the influence of capillary forces, which favor a flat film.[11,12] Example feature development curves as a function of heating time are provided for both patterning directionalities as Supporting Information (see Figure B.3 in the Appendix B), which show how the film thickness variations can be easily tuned within 0 - 250 nm. The thickness profile of samples produced by this patterning methodology is always smoothly varying because it results from directed flow of liquid polymer.

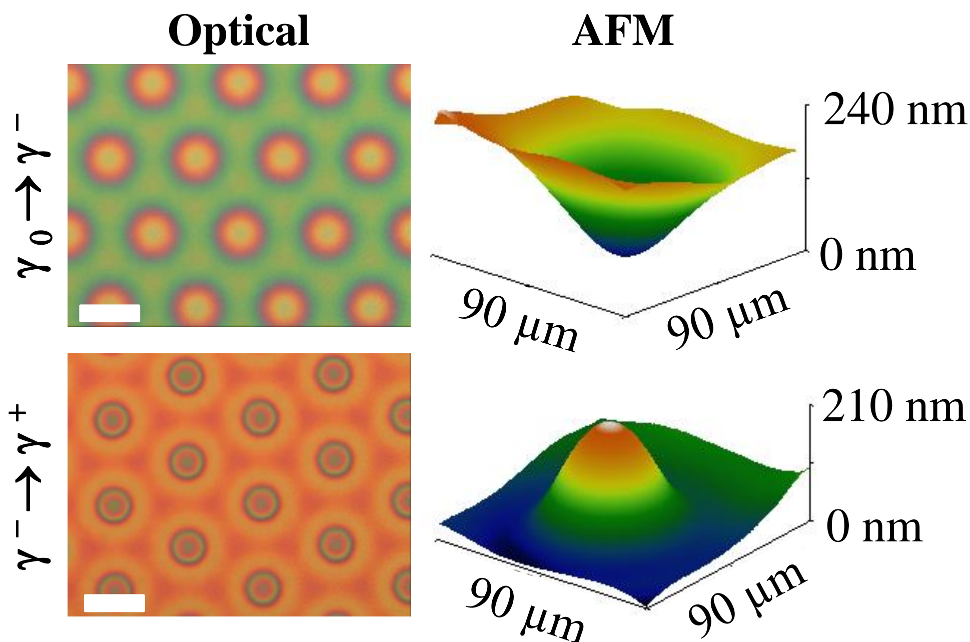

Figure 3.3: Representative optical and AFM images after heating the films with *lower* surface tension in the exposed regions (top row) and analogous images after heating the films with *higher* surface tension in the exposed regions (bottom row). Both samples were thermally annealed for 5 minutes at 150 °C after the patterned light illumination step. The initial film thicknesses were 530 nm. Scale bars in optical micrographs indicate 90 µm.

We note that Marangoni flow will always occur in polymer films as long as a surface tension gradient profile is present,[2] so the minimum feature size possible is most dependent on the resolution limit of the photopatterning methodology utilized. Once a specific surface tension profile has been patterned, the maximum film thickness variations and the heating time necessary to achieve them depend crucially on physical properties such as the film viscosity and component diffusivities. Generally, large film thickness variations are favored by large surface tension gradients, low diffusivities and low viscosities. Surface tension patterns are erased by diffusion of film components, so this parameter will critically limit feature height for a given surface energy pattern.

3.3.3 Molecular Characterization Upon Chemical Transformations

The composition and material properties of polymeric films after being subjected to typical processing conditions are summarized in Table 3.1. The subsequent sections provide details on how the values in Table 3.1 were obtained.

Table 3.1: Changes of a single film (γ_0) after sequential decarboxylation then dehydrogenation transformation procedures.

Film	Transformation	(x, y, x', y') in Figure 3.1	$\Delta\gamma$ [dyne/cm][c]
γ_0	-	(0.26,[a] 0.74,[a] 0, 0)	0
γ^-	Decarboxylation	(0.26,[a] 0.74,[a] 0.06,[b] 0)	- 0.1 dyne/cm
γ^+	Dehydrogenation	(0.26,[a] 0.74,[a] 0.06,[b] 0.04[b])	+ 0.1 dyne/cm

[a] ^{13}C-NMR, [b] Transmission-mode FTIR. [c] Estimation based on composition-weighted molar averages of homopolymer values relative to Film γ_0.

3.3.3.1 Composition Changes Due to Decarboxylation

Transmission mode FTIR spectroscopy was performed on blanket-irradiated films to quantify the extent of decarboxylation. Representative IR spectra of the C=O carbonyl stretch of acrylic acid (ν = 1725 cm^{-1}) after different heating times at 150 °C are shown in Figure 3.4a (full IR spectra are shown in Figure B.6 in Appendix B). Prior to heating, PBG was fully converted to its basic form by 0.4 J/cm^2 of 365 nm UV exposure (see Figure B.4 in Appendix B for evidence of this transformation). Because the spectra were normalized to the area under alkyl stretches (2850–3100 cm^{-1}), which are invariant signals during this chemical transformation, the decrease in the 1725 cm^{-1} peak area is due to decarboxylation. The extent of decarboxylation at different cumulative heating times is shown in Figure 3.4b. Our typical protocol for decarboxylation yields a 24% reduction in the area under the $\nu_{C=O}$ signals associated with acrylic acid, yielding x' =

0.06 for the structures in Figure 3.1. Other possible thermo-oxidative reactions that are often reported to form in carboxylic acid containing polymers, such as intramolecular anhydride[13] and intermolecular anhydride (potentially leading to crosslinking)[14] formation, were not detected by FTIR during our typical decarboxylation procedure (see Figure B.6 in Appendix B for full FTIR spectra).

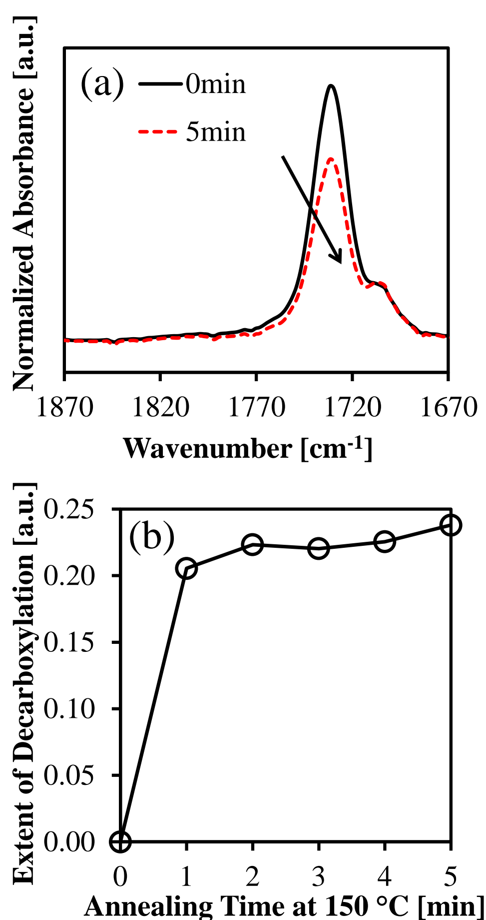

Figure 3.4: (a) Representative FTIR spectra for decarboxylation upon thermal annealing at 150 °C for 0 and 5 minutes. Spectra were normalized by the area under the alkyl stretches from 2850–3100 cm^{-1}. (b) The extent of decarboxylation at different cumulative heating times.

3.3.3.2 Composition Changes Due to Dehydrogenation

To investigate the dehydrogenation mechanism shown in Figure 3.1 from Film γ^- to Film γ^+, solution fluorescence measurements in diglyme were performed on re-dissolved films using $\lambda_{excitation}$ = 310 nm. Kabanov and coworkers[15] demonstrated that UV irradiation of polystyrene caused its backbone to dehydrogenate, creating a fluorescence center with an absorption band in the 280 – 460 nm region and a fluorescence band in the 330 – 550 nm region. Each solution sample was prepared at identical concentrations (~ 0.5 mg/mL). As shown in Figure 3.5, the solution fluorescence emission intensity increases after each chemical transformation. Some fluorescence originates from the basic form of PBG, as was confirmed by a measurement on an exposed PBG solution (see Figure B.4 in Appendix B). A further increase in fluorescence emission intensity was observed from Film γ^- to Film γ^+ in Figure 3.5, even though all PBG had been converted to its basic form, suggesting the creation of an additional fluorescence center.

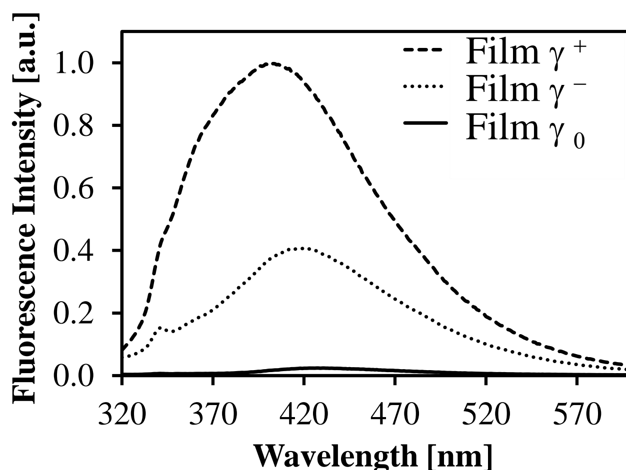

Figure 3.5: Solution fluorimetry using 310 nm wavelength excitation light. All signals were normalized to the fluorescence intensity of γ^+ at 404 nm. The concentration for all samples was 0.5 mg/mL.

To verify that the fluorescence center was located on the polymer chain, a size exclusion chromatography (SEC) setup equipped with fluorescence and refractive index (RI) detectors was employed to analyze re-dissolved film materials using $\lambda_{excitation}$ = 310 nm and $\lambda_{emission}$ = 400 nm. The corresponding fluorescence and RI chromatograms are shown in Figure 3.6 with higher molecular weight materials eluting at lower retention volume. As expected, the SEC fluorescence chromatogram does not indicate any florescence from the Film γ_0 materials. However, data for Film γ^- shows the light exposed PBG acts as a fluorophore at a retention volume of 21 mL, and Film γ^+ fluoresces both at polymeric and PBG retention volumes. Because a significant fluorescence signal is present at a polymeric retention volume (16 mL) in Film γ^+, the creation of stilbene-like structures via backbone dehydrogenation is strongly supported.[2,10,15] Furthermore, the chromatogram from the refractive index detector using SEC after being subjected to each chemical transformation is unchanged. Since the refractive index detector is linearly sensitive to mass concentration, this indicates that polymer molecular weight and chain length distribution were not changed within instrument resolution by the typical patterning process. This is also strong supporting evidence that anhydride formation is not present as this would lead to changes in the molecular weight distribution. This dehydrogenation was quantified using FTIR spectroscopy by measuring the decrease in alkyl peak area at 2850 – 3000 cm^{-1} and increase in alkenyl C=C peak area at 1580 – 1620 cm^{-1} (see Figure B.8 in Appendix B). The extent of dehydrogenation upon our typical light exposure dose was approximately 6 % of the styrenic portions of the backbone, giving y' = 0.04 (Figure 3.1).

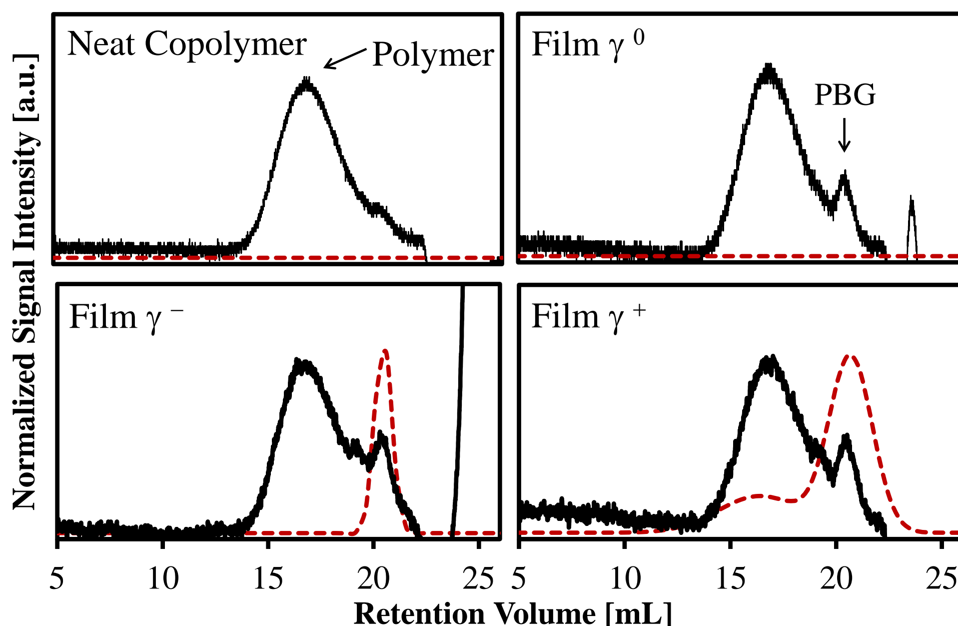

Figure 3.6: SEC chromatograms of re-dissolved films after being subjected to representative processing conditions. Solid black lines indicate normalized RI responses while dashed red lines represent normalized fluorescence responses. $\lambda_{excitation}$ = 310 nm and $\lambda_{emission}$ = 400 nm were used to detect the fluorescence signals in this study.

3.3.3.3 Surface Tension Changes

The bidirectional flow of the polymer film materials here are driven by melt-state surface tension gradients caused by photochemically-imposed chemical patterns. The magnitude of variations in surface tension needed to cause Marangoni flow are extremely small,[2] and are potentially below the uncertainty associated with conventional surface energy analysis from water contact angle or pendant drop measurements. To verify the surface tension changes beyond uncertainty, host polymer films subjected to both chemical transformations were dewetted from the top of a hydrophobic surface and the contact angles of the vitrified droplets were measured using AFM.[4,5] The contact angles at various degrees of decarboxylation or dehydrogenation are shown in Figure 3.7. Since the PCHE substrate has lower surface energy than the host polymer, reductions in the

contact angle of the dewetted host polymer atop PCHE indicate a decrease in its surface tension and vice versa. As shown in Figure 3.7, the contact angle of dewetted film materials on PCHE decreased by 3° after decarboxylating 6 % of the total polymer repeat units, suggesting that surface tension decreased ≈ 0.3 dyne/cm (Eq. 3.2). Conversely, the contact angle increased monotonically from 12.6 ± 0.5° to 14.0 ± 0.5° due to dehydrogenation of up to 12% of the host polymer repeat units, suggesting that surface tension increased ≈ 0.2 dyne/cm. Our typical exposures only dehydrogenate 4% of the repeat units, thus increasing surface energy by ~ 0.1 dyne/cm. These surface energy changes are the same or only slightly larger than the estimates based on composition changes shown in Table 3.1. For reference, representative line scans from which contact angles were extracted are shown in Figure B.9 of Appendix B.

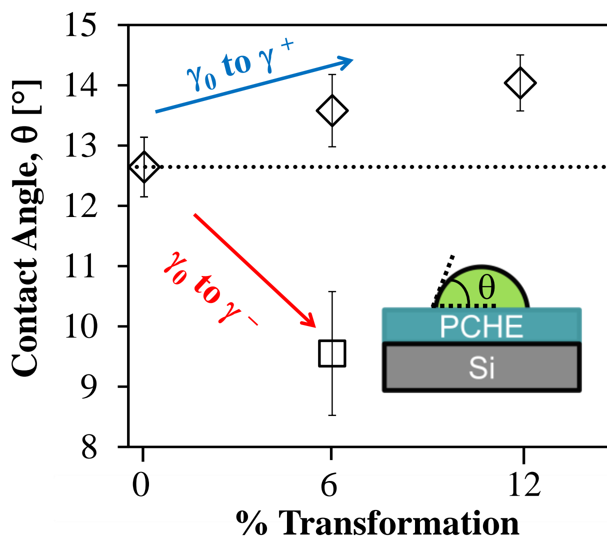

Figure 3.7: Contact angles for dewetted styrene-acrylic acid copolymers after chemical transformations. Data points represent polymer droplets whose volumes ranged from only 0.004 to 0.01 μm^3. Error bars represent 95 % confidence intervals based on 5 – 8 different droplets on each sample.

3.3.4 Bidirectional Flow in One Polymer Film

To further demonstrate the versatility of this method, we patterned discrete regions of higher and lower melt-state surface tension into the same film and developed the thickness profiles simultaneously in one heating step. The evolution of topographical patterns was monitored *in situ* on a heating stage by optical microscopy, and representative micrographs are shown in Figure 3.8. Exposure conditions causing decarboxylation (Film $\gamma_0 \rightarrow$ Film γ^-) were applied to isolated hexagonal regions and irradiation resulting in dehydrogenation (Film $\gamma^- \rightarrow$ Film γ^+) was applied to isolated triangular regions. The film remained flat after the exposure steps since the film was solid during all exposure steps. For the first 20 seconds of heating, film thickness reductions are present in both exposure regions, as evidenced by the presence of identical interference colors. However, at longer heating times, from 40 to 60 sec, the interference colors in the triangular (light green/yellow) and hexagonal (dark purple) regions differ from each other and also from the unexposed film, which appears only light green. The light yellow color present in the center of triangular regions is characteristic of a thickness near 370 nm and the dark purple color present in the center of the hexagonal regions is characteristic of a thickness of 290 nm. Approaching heating times of 90 sec, the triangular regions increase in thickness by drawing in material from outside their exposure regions creating nearby depletion regions. Those nearby depletion regions eventually merge with the sinking hexagonal regions. Synergistically, material flows out of hexagonal (Film γ^-) regions and directly into triangular (Film γ^+) regions. As a result, triangular "hills" adjacent to hexagonal "valleys" possess slightly higher thickness (dark orange at center, ~ 430 nm) than totally isolated triangular regions (light orange/yellow at center, ~ 380 nm). With improved registration between sequential exposures, this effect could be harnessed to produce even greater film thickness variations. The given film

thicknesses were estimated by cataloging the interference colors from copolymer films with various thicknesses on silicon substrates.

Photographs of the film after 0 and 90 sec of annealing are shown as insets in Figure 3.8. While the film initially had a light blue interference color when viewed from an oblique angle, no dominant interference color can be discerned by eye after feature formation due to the resulting film roughness. Topographically patterning films by this method can manipulate light reflection of polymer films. Also from the inset after the feature development, millimeter sized hexagonally packed spots are clearly observed by eye. This Moiré pattern resulted from micropatterned arrays being aligned at different rotation angles during the exposure steps.

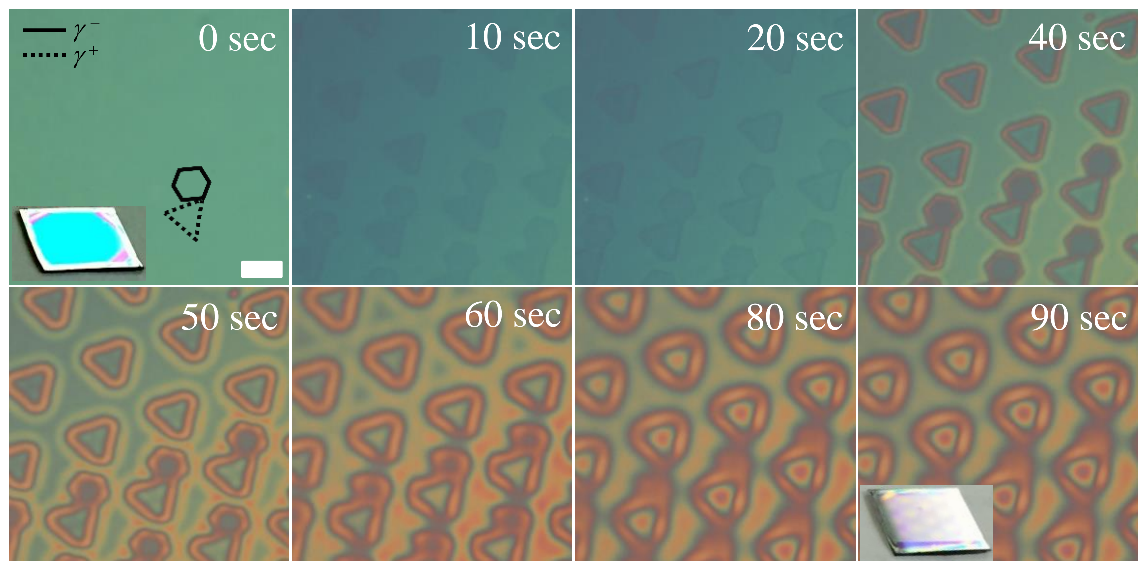

Figure 3.8: Representative optical micrographs of a single film possessing spatially programmed regions of lower (γ^-, hexagons) and higher (γ^+, triangular) surface energy at different heating times at 150 °C. Note that the hexagons are only patterned over half of the image. Scale bar indicates 50 μm. Photographs of the sample before and after thermal annealing are shown as insets in the initial and final optical micrographs. The initial film thickness was 360 nm.

A combination of spatial light exposures through relatively simple photomask patterns can create complex three-dimensional topographies that were not present in the any of the original light exposure patterns. To demonstrate this point, light exposure for decarboxylation was applied through a hexagonal mask then heated to direct the flow out of the hexagonal region, Figure 3.9a. From Figure 3.9c, the topographical profile after a short period of thermal annealing shows Marangoni flow is initiated near the boundary between light exposed and unexposed regions. Then, a subsequent light exposure for dehydrogenation was applied through a triangular mask onto the vitrified hexagonal features. Upon heating, polymer flows into the triangular regions. Investigation of this sample shows triangular "hills" located within the hexagonal "valleys" as shown in Figure 3.9b. The resulting "star" pattern was not originally present in any of the masks used. The directionality of the thickness changes can be ascertained by noting that the order of interference color changes present on the outer edge of the hexagonal regions reverses on the outer edge of the triangular regions. The height profile after each step was also characterized by an optical profiler. The maximum thickness variation is 240 nm, which corresponds to 45 % of the initial film thickness.

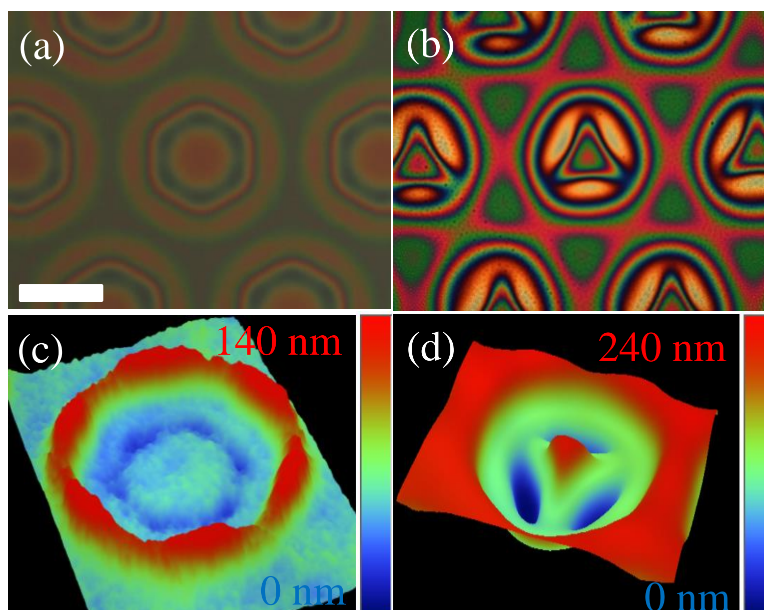

Figure 3.9: Top down optical micrographs (a) after decarboxylation was applied through hexagonal mask and annealing at 150 °C for one minute, and (b) after dehydrogenation was performed through triangular mask and annealing at 150 °C for one minute. Corresponding optical profilometer results are shown below each optical micrograph (c and d) showing directionality and height. The initial total film thickness was 530 nm. Scale bar indicates 50 μm.

3.4 CONCLUSIONS

A photopolymer was described whose melt-state surface tension can be selectively raised or lowered on-demand in the light exposed regions. Upon heating to the melt state, the spatially-defined pattern directs Marangoni flow from low-to-high surface tension regions to produce a film with a smoothly varying height profile. The versatile photochemistry enabled a greater diversity of topography to be accessed than if flow in only one direction was triggered. Directing polymer flow using light is an emerging area of interest in numerous groups,[10,16,17] yet we consider this to be the first example of bidirectional control in a single material. The phenomenologically-observed flow patterns have been strongly connected to well-defined photochemical transformations, adding to a physical understanding of how melt-state surface tension affects thin film morphologies.

3.5 REFERENCES

1. Brandrup, J.; Immergut, E. H.; Grulke, E. A. Eds. Polymer Handbook; Wiley and Sons: Hoboken, New Jersey, **1999**.
2. Arshad, T.; Kim, C. B.; Prisco, N. A.; Katzenstein, J. M.; Janes, D. W.; Bonnecaze, R. T.; Ellison, C. J. *Soft Matter* **2014**, 10, 8043–8050.
3. Katzenstein, J. M.; Kim, C. B.; Prisco, N. A.; Katsumata, R.; Li, Z.; Janes, D. W.; Blachut, G.; Ellison, C. J. *Macromolecules* **2014**, 47, 6804–6812.
4. Mansky, P.; Liu, Y.; Huang, E.; Russell, T. P.; Hawker, C. *Science* **1997**, 275, 1458−1460.
5. Vitt, E.; Shull, K. R. *Macromolecules* **1995**, 28, 6349–6353.
6. Balkeneende, A. R.; van de Boogaard, H. J. A. P.; Scholten, M.; Willard, N. P. *Langmuir* **1998**, 14, 5907–5912.
7. Song, S.; Yokoyama, S.; Takahara, S.; Yamaoka, T. *Polym. Adv. Technol.* **1998,** 9, 326–333.
8. Song, S.; Takahara, S.; Yamaoka, T. *J. Photopolym. Sci. Tech.* **1998,**11, 171–172.
9. Gurkaynak, A.; Tubert, F.; Yang, J.; Matyas, J.; Spencer, J. L.; Gryte, C. C. *J. Polym. Sci. Part A: Polym. Chem.* **1996**, 34, 349–355.
10. Katzenstein, J. M.; Janes, D. W.; Cushen, J. D.; Hira, N. B.; McGuffin, D. L.; Prisco, N. A.; Ellison, C. J. *ACS Macro Lett.* **2012,** 1, 1150–1154.
11. Benzaquen, M.; Fowler, P.; Jubin, L.; Salez, T.; Dalnoki-Veress, K.; Raphaël, E. *Soft Matter* **2014**, 10, 8608–8614.
12. Benzaquen, M.; Ilton, M.; Massa, M. V.; Salez, T.; Fowler, P.; Raphaël, E.; Dalnoki-Veress, K. 2015, arXiv:1503.08728 [cond-mat.soft]. arXiv.org e-Print archive. http://arxiv.org/abs/1503.08728 (accessed May 1, 2015).
13. Namasté, Y. M. N.; Obendorf, S. K.; Anderson, C. C.; Krasicky, P. D.; Rodriguez, F.; Tiberio, R. *J. Vac. Sci. Technol. B1* **1983**, 4, 1160−1165.
14. La, Y.; Edwards, E. W.; Park, S.; Nealey, P. F. *Nano Lett.* **2005**, 5, 1379−1384.
15. Nurmukhametov, R. N.; Volkova, L. V.; Kabanov, S. P. *J. Appl. Spectrosc.* **2006**, 73, 55−60.
16. Okada, K.; Tokudome, Y.; Makiura, R.; Konstas, K.; Malfatti, L.; Innocenzi, P.; Ogawa, H.; Kanaya, T.; Falcaro, P.; Takahashi, M. *Adv. Funct. Mater.* **2014**, 24, 2801–2809.
17. Ubukata, T.; Moriya, Y.; Yokoyama, Y. *Polym. J.* **2012**, 44, 966–972.

Chapter 4: Generating Large and Thermally Stable Marangoni-driven Topographical Patterns in Thin Polymer Films by Photochemically Stabilizing the Surface Energy Gradient

4.1 INTRODUCTION

A previously developed theoretical model (see Chapter 2) reveals that the maximum film thickness variations are favored by large surface tension gradients, low diffusivities, and low viscosities. A lower viscosity promotes a faster feature formation rate. However, as described by the Rouse model,[1] low viscosity generally results in high diffusivity, which rapidly dissipates the prescribed surface energy patterns. This coupling between film diffusivity and viscosity critically limits attainable feature heights for a given surface energy pattern.

To this end, in this chapter, a strategy was developed to decouple film diffusivity and viscosity to rapidly produce large and thermally stable features so that the patterned films can be used for a broader range of applications. This was achieved by blending a low molecular weight PS (M_n=2.6 kDa, Đ=1.1) with a higher molecular weight copolymer (M_n=42 kDa, Đ=1.01) that was miscible with PS. The high molecular weight copolymer is a random copolymer of *tert*-butoxystyrene and styrene. These two polymers were co-cast with a photoacid generator and exposed through a photomask, yielding a surface energy gradient between light exposed and unexposed regions via acid-catalyzed deprotection chemistry of the high molecular weight copolymer.

This strategy enabled the formation of ca. 500 nm high features (over three times taller compared to previous PS work) within only 30 mins of thermal annealing. Furthermore, the formed features were stable upon extensive thermal annealing up to one month. A scaling analysis using Marangoni and capillary terms indicated that these stable

features originated from the domination of the Marangoni forces over capillary forces due to the decoupled film viscosity and diffusivity.

4.2 Experimental Methods

4.2.1 Materials

HPCL-grade tetrahydrofuran (THF) was purchased from J.T. Baker. Triphenylsulfonium (TPS) nonaflate (AZ Clariant Corporation) was generously provided and used as a photoacid generator (PAG) as received. All other chemicals were purchased from Sigma Aldrich or Fisher Scientific. Polished 4 inch silicon wafers were purchased from University Wafer. Quartz glass substrates were purchased from Chemglass.

4.2.2 Polymer Synthesis and Characterization

PS (M_n=2.6 kDa, $Đ_M$=1.1) was synthesized by activators regenerated by electron transfer atom transfer radical polymerization (ARGET ATRP) and characterized as previously described.[2] The random copolymer, poly(*tert*-butoxystyrene-*ran*-styrene), P(tBOS-*ran*-S) (M_n=42 kDa, $Đ_M$=1.01), was synthesized using anionic polymerization. HPCL-grade THF was purified with an Innovative Technology Pure Solv MD-2 solvent purification system equipped with two activated alumina columns. Styrene and 4-*tert*-butoxystyrene were purified by distilling twice over di-*n*-butylmagnesium (1.0 M in heptane, dried on a Schlenk line before use). The purified monomers were brought into an Argon filled drybox, where appropriate amounts of each monomer were mixed to create a 70 mol % styrene, 30 mol % 4-*tert*-butoxystyrene monomer solution. The reactor vessel was flame dried five times, and then the appropriate amount of THF was added to the reactor vessel and cooled to -78 °C. The appropriate amount of *sec*-butyllithium was added to initiate the reaction. The monomer solution was added dropwise to the reactor vessel using an airtight glass syringe. Upon addition of the monomer solution, the

reaction solution turned a light yellow-orange color. After the reaction was allowed to proceed for 2 h at -78 °C, degassed methanol was used to terminate the reaction. The polymer was precipitated in methanol and dried.

The copolymer, poly(hydroxystyrene-*ran*-styrene),P(HOST-*ran*-S), was synthesized in bulk by acid deprotection of P(tBOS-*ran*-S) following a slightly modified procedure outlined in Tung et al.[3] P(tBOS-*ran*-S) was dissolved in a solution of dioxane and hydrochloric acid (20 ml dioxane: 3 ml HCl) and refluxed at 60°C for 12 h. The resulting polymer was precipitated in hexanes, and freeze dried before use.

Molecular weight and molecular weight dispersities were determined by gel permeation chromatography (GPC) or Matrix Assisted Laser Desorption Ionization (MALDI) for P(tBOS-*ran*-S and PS, respectively (Figures C.1 and C.2 in Appendix C). GPC measurements were obtained using a Viscotek GPC Max VE 2001 with a Viscotek Model 270 dual detector viscometer/light scattering detector and Viscotek VE 3580 refractive index detector with 2 I-Series mixed bed low molecular weight (MW) columns (with THF as the eluent). MALDI data were collected on an AB SCIEX Voyager-DE PRO MALDI-TOF using trans-2-[3-(4-tert-butylphenyl)-2-methyl-2-propenylidene] malononitrile as a matrix with silver trifluoroacetate as a counterion. The ratio of tBOS:S was confirmed by ^{1}H NMR (Figure C.3 in Appendix C). Glass transition temperatures (T_gs) were measured on second heat after erasing thermal history using differential scanning calorimetry (DSC; Mettler Toledo DSC 1) with a heating rate of 10°C/min under nitrogen. DSC was also used to characterize polymer miscibility of freeze-dried polymer blends using the procedure described above.

4.2.3 Thin Film Sample Preparation and Characterization

Polymer solutions (9-10 wt% solids in cyclohexanone) of PS, P(tBOS-*ran*-S), and PAG (varied amounts depending on the mol% of tBOS in P(tBOS-*ran*-S)) were spin

coated (Specialty Coating Systems G3-8) onto silicon substrates with an approximately 2 nm thick native oxide. Spin speeds were varied from 2000 to 3000 RPM to control film thickness. After preparation, film samples were annealed at 100°C for 1 min to remove residual solvent.

Film thicknesses were characterized using a J.A. Woollam M-2000D spectroscopic ellipsometer. Unless otherwise noted, all films were initially ca. 285 nm thick in this study. UV/Vis absorbance measurements were performed on a Thermo Scientific Evolution 220 UV/Vis spectrophotometer. Films for UV/Vis measurements were spin coated onto quartz plates and representative data showing high transmittance is given in Supporting Information (Figure C.4 in Appendix C). This UV/Vis transmittance data indicates that the light dose is attenuated by a negligible amount (~ 20 %) when passing through the film; therefore, the photochemical reaction takes place nearly homogeneously throughout the depth of the film. Background-subtracted, transmission-mode Fourier transform infrared (FTIR) spectra were recorded on a Thermo Nicolet 6700 FTIR with liquid nitrogen cooled MCT-B detector. Films spin-coated onto a double-side polished silicon wafer were used. Two hundred scans with a resolution of 4 cm^{-1} were averaged.

Static liquid contact angles on selected films were measured with a Ramé-Hart NRL C.A. goniometer (Model #100-00) at room temperature. Prior to the measurement, the film was rinsed thoroughly with deionized water and then blown dry with filtered air. Then, a 4 μL drop of glycerol was placed on the sample, and the stage was leveled, at which point the real-time image was captured and the contact angles on the left and right sides of the drop were determined. The image was paused within 10 s of placing the drop on the sample. Between measurements, samples were rinsed with deionized water and blown dry with filtered air.

4.2.4 Topography Formation and Characterization

A PAG, in combination with UV exposure and heat, was utilized to deprotect P(tBOS-*ran*-S) polymer films in order to produce P(HOST-*ran*-S) (see Figure C.5 in Appendix C).[3,4] In all film studies, the PAG TPS nonaflate was used for its relatively slow migration characteristics.[5] The percentage of PAG added varied depending on film composition and ranged from 5-25 wt% with respect to the percentage of tBOS in P(tBOS-*ran*-S), which converts to a maximum of 1.1% of incorporated PAG with respect to all film materials. Then, films were exposed using a 200 W metal-halide lamp with broadband output from 200-800 nm (Optical Building Blocks ScopeLite 200). Typical intensity of this broadband light source at an exposure distance of 20 mm was measured to be 0.56 W/cm^2 using a radiometer (Fieldmax TO, Coherent, Inc.). The light exposure dose was 34 J/cm^2 (1 min exposure) for all specimens in this study. Since the PAG used here absorbs only a fraction of the broadband output, much lower doses at a precise wavelength (254 nm) would likely give the same effect.

After exposure, samples were subsequently annealed at 120°C unless otherwise noted. Photochemical deprotection required both UV exposure and thermal annealing. Also, due to the isobutylene gas byproduct, the film thickness reduced by ca. 17% for unblended P(tBOS-*ran*-S) homopolymer. For blended systems, however, film thickness was only slightly reduced since the concentration of P(tBOS-*ran*-S) in PS was relatively small (Appendix C, Table C.1). Feature height as a function of annealing time was characterized using a Veeco Dektak 6 M stylus profiler with a stylus diameter of 25 µm and stylus force of 29.4 µN. Feature height is defined as the maximum height difference between the peaks and corresponding valleys. Bright field optical micrographs were taken for all samples using an Olympus BX 60 microscope with a Spot Insight QE camera.

4.3 RESULTS AND DISCUSSION

4.3.1 Polymer Design

The polymers used in this work were designed with the goal of reducing the dissipation rate of the pre-programmed surface energy pattern while retaining rapid feature formation, ultimately to form larger Marangoni-driven features. For this initial proof of concept, we separated the polymer that creates the surface energy gradient (i.e., the high MW tBOS containing copolymer) from the primary flow component (i.e., low MW PS) by blending two different polymers that are miscible with each other to form a homogeneous film. By using a high molecular weight surface energy gradient forming polymer, the rate of surface energy pattern dissipation through diffusion can be reduced. By blending this polymer with a low molecular weight PS with low viscosity and high diffusivity, the speed of feature formation was not significantly sacrificed. For the surface energy gradient creator, a high molecular weight *tert*-butoxystyrene (tBOS) containing copolymer was chosen since this component can undergo a deprotection reaction with the aid of an acid catalyst.[6] In thin films, the photochemical product of the deprotection is hydroxystyrene (HOST) units possessing significantly higher surface energy compared to unexposed, protected tBOS units, as demonstrated by liquid contact angle measurements.[4,7] Often times, this surface energy change is large enough to switch solubility of P(tBOS) and P(HOST) homopolymers towards a certain solvent.[8]

While a large shift in surface energy is advantageous for promoting high features by Marangoni flow, a large surface energy change may also result in immiscibility between blended polymers. This can cause phase segregation[9] between those polymers, which can additionally lead to polymer film dewetting. Although directed dewetting[10-12] can also be an alternative thin film patterning method, it represents a different patterning paradigm outside of the scope of the process used in this study. In order to prevent

immiscibility between P(tBOS) and PS, a random copolymer containing *tert*-butoxystyrene and styrene was synthesized (P(tBOS-*ran*-S)) as a surface energy gradient creator. The copolymer structure used in this work along with the deprotection chemistry scheme to generate the surface energy gradient is given in Figure 4.1.

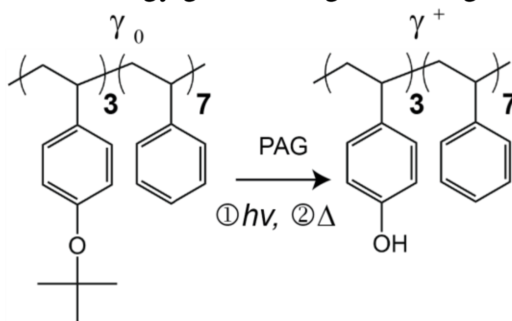

Figure 4.1: Photochemical transformation of P(tBOS-ran-S) to P(HOST-ran-S) with the aid of PAG. Thin films were exposed to UV light and subsequent heating led to the removal of the tert-butoxystyrene moiety in P(tBOS-ran-S).

Maintaining miscibility of all polymers while maximizing the surface energy gradient requires careful control of the monomer ratio in P(tBOS-*ran*-S). With the aid of miscibility predictions using the Flory-Huggins parameter, χ, the monomer molar ratio was fixed at 3:7 *tert*-butoxystyrene: styrene (see Figure 4.1). This ratio represents the highest percentage of *tert*-butoxystyrene that can be incorporated while ensuring miscibility between all polymers. As a result, the highest possible surface energy gradient can be imposed. A complete discussion of the calculations used to select this ratio is given in Supporting Information (Section C4 in Appendix C).

To confirm the miscibility of the polymer blends, glass transition temperatures (T_gs) of various blends of PS, P(tBOS-*ran*-S), and P(HOST-*ran*-S) were evaluated using DSC (Figure 4.2). Generally, the presence of one T_g from the blending of two polymers indicates miscible polymers, while the presence of two distinct T_gs indicates immiscibility. A 50:50 blend of P(tBOS-*ran*-S) and P(HOST-*ran*-S) was prepared and the resulting DSC curve shows two T_gs at 100°C and 120°C. Bulk P(HOST-*ran*-S) used

for DSC here was prepared by acid deprotection of P(tBOS-*ran*-S) in solution and full deprotection was confirmed by FTIR (Appendix C, Figure C.6). Both T_gs from DSC for the 50:50 blend of P(tBOS-*ran*-S) and P(HOST-*ran*-S) correspond to the T_gs measured for each homopolymer (Figure C.9 in Appendix C), and the corresponding values lie in between literature values for PS[13] and either P(tBOS) or P(HOST) homopolymers.[14,15] In contrast, DSC traces of 30 wt% P(tBOS-*ran*-S) or 30 wt% P(HOST-*ran*-S) in PS (the highest blend ratio with PS in this study) both show a single T_g, indicative of miscibility. Therefore, the carefully designed surface energy gradient forming polymer was miscible with the PS majority component, while the polymers that create the surface energy gradient were not miscible with each other. This immiscibility between P(tBOS-*ran*-S) and P(HOST-*ran*-S), in combination with the high molecular weight, was originally intended to synergistically impede dissipation of the surface energy gradient. For reference, a DSC trace of the low molecular weight PS is also given in Figure 4.2, which shows a T_g ca. 60°C.[2,15]

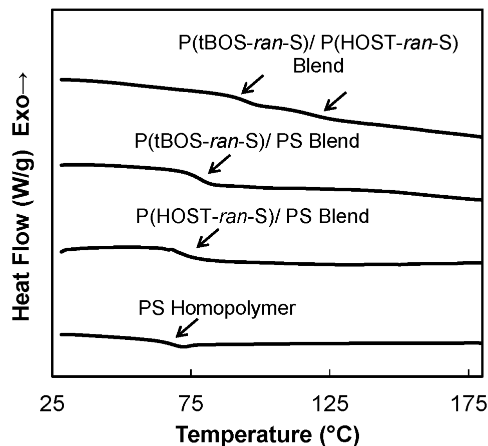

Figure 4.2: DSC traces showing immiscibility between bulk P(tBOS-ran-S) and P(HOST-ran-S) as indicated by two Tgs, but a single Tg for PS blended with either 30 wt% P(tBOS-ran-S) or 30 wt% P(HOST-ran-S) indicating miscibility. For reference the DSC trace for the low molecular weight PS homopolymer is also given.

4.3.2 Topography Formation

The patterning methodology using the aforementioned polymers is shown schematically in Figure 4.3. A thin film, comprised of a blend of PS and P(tBOS-*ran*-S) was co-cast with PAG onto a silicon substrate. These films were then exposed to UV light through a photomask possessing a 12.5 μm half-periodicity on equal-sized lines and spaces. Upon subsequent annealing at 120°C, photochemical transformation of the *tert*-butoxystyrene moiety into hydroxystyrene and simultaneous liquid-state flow of the film materials towards light exposed regions occurred. The surface energy gradient was controlled by varying blend ratios between P(tBOS-*ran*-S) and PS. While the molecular weight of the PS homopolymer was relatively small (2.6 kDa) to facilitate rapid flow, the molecular weight of the surface energy gradient former (P(tBOS-*ran*-S)) was large (42 kDa) in order to limit the relative mobility of the surface energy gradient forming polymer and thus stabilize the surface energy gradient. With extended annealing times, PS flowed towards regions of higher surface energy (light exposed) and these features decayed or persisted depending on whether the dominating force was capillary or Marangoni, respectively.

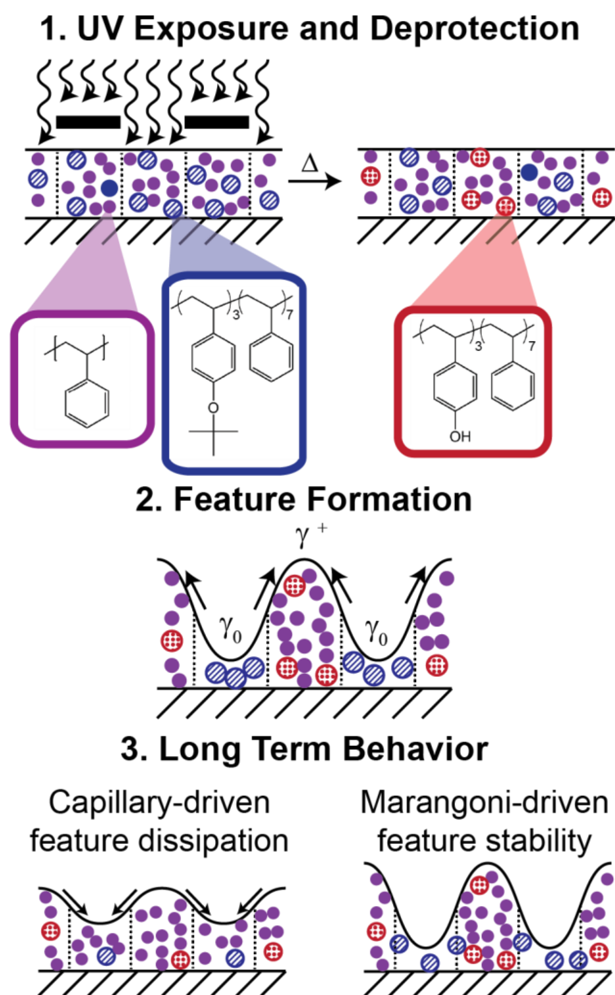

Figure 4.3: Polymer patterning methodology. (1) Schematic of the polymer blend which is comprised of a low molecular weight PS (solid purple) and a high molecular weight copolymer, P(tBOS-ran-S) (blue hashed circles). Spatial control of the surface energy gradient is achieved by exposing films through a photomask and the subsequent annealing of these films leads to a photochemical transformation of P(tBOS-ran-S) into P(HOST-ran-S) (red dotted circles) with the aid of a photoacid generator. (2) With extended annealing time, polymer flows from regions of low to high surface energy and (3) the long term behavior (dissipation or stability of topography) is determined by whether capillary or Marangoni forces dominate, respectively.

Representative profilometry traces and corresponding optical microscope images of the films processed as described in Figure 4.3 are shown in Figure 4.4. The uniform reflected interference color in the optical micrograph is evidence of uniform film

thickness for all films immediately after light exposure. The topographic features developed only upon subsequent thermal annealing at a temperature above the film's T_g. The first set of images (top row) shows the evolution of feature development for 30 wt% P(tBOS-*ran*-S) in PS at 120°C. At short annealing times (2 min), a double peak for a prescribed light pattern periodicity was observed, which later merged into a single peak forming the sinusoidal topography shown at the intermediate time scale of 40 min. The occurrence of a double peak is a unique feature of flow-driven patterning.[15] This finding is practically relevant because it represents a strategy to double the areal density of topographic features present for a given projected light exposure pattern. In contrast to prior work, however, here the sinusoidal features did not decay and remained stable for extended periods of annealing at 120°C. Additionally, the features formed in films possessing 30 wt% P(tBOS-*ran*-S) in PS were twice the initial film height, i.e. they achieved the maximum possible feature height. The fact that the film height was doubled is evidence that not only PS but also the unexposed surface energy gradient creator, P(tBOS-*ran*-S), flowed towards the higher surface energy regions. This indicates the low molecular weight PS matrix effectively compatibilized the originally immiscible P(tBOS-*ran*-S) and P(HOST-*ran*-S).[16]

For comparison, optical microscope images and corresponding profilometry traces for 10 wt% P(tBOS-*ran*-S) in PS are also included in Figure 4.4. In these films, feature development was faster with the largest features present after only 2 min of annealing at 120°C. This was attributed to the reduction in the film viscosity as a result of the lower content of high molecular weight polymer. Due to this rapid topography formation, the double peaks were not observed, though the peaks likely formed in the very initial stages of feature development (< 1 min). For this blend composition, after reaching the maximum feature height, features decayed upon extended heating as in prior

studies on pure PS films. Detailed discussion regarding these two different long term annealing behaviors follows in the subsequent sections. Directionality of the flow toward higher surface energy (light exposed) regions was confirmed using a photomask with isolated patterns and the corresponding results are shown in Figure C.10 in Appendix C.

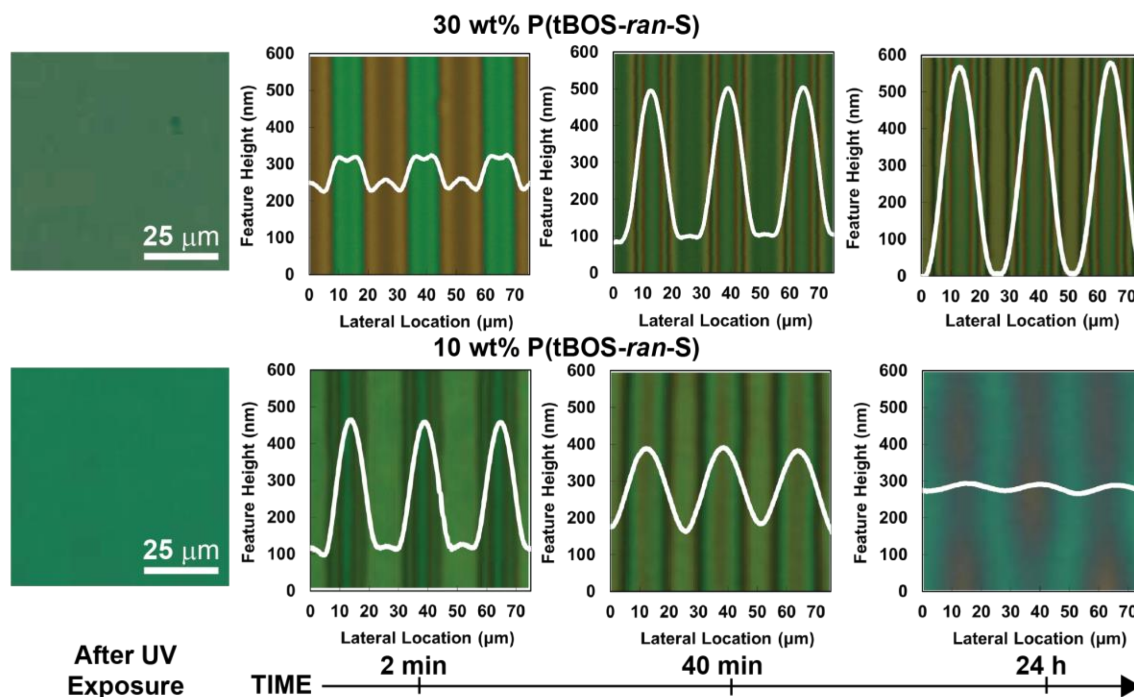

Figure 4.4: Representative profilometry traces and corresponding optical images of feature formation in a 30 and 10 wt% P(tBOS-ran-S) in PS blend (initial film thickness= 288 nm). All films were exposed to UV light for 1 min (34 J/cm2) and annealed at 120°C. Stable features with twice the initial film thickness are observed for 30 wt% P(tBOS-ran-S), while features decayed for 10 wt% P(tBOS-ran-S).

4.3.3 Photochemical Mechanism and Characterization

We believe that the transformation from P(tBOS-*ran*-S) to P(HOST-*ran*-S) shown in Figure 4.1 and the subsequent creation of a surface energy gradient in thin films is

responsible for the programmed polymer flow demonstrated in Figure 4.4. The following results in this section were obtained to quantitatively validate these claims.

First, the acid-catalyzed photo-transformation of the homopolymer from P(tBOS-*ran*-S) to P(HOST-*ran*-S) was confirmed by FTIR (Figure 4.5). Upon flood UV exposure and subsequent heating at 120°C for 10 minutes, the peak at 2980 cm^{-1} was significantly reduced while a broad peak at 3450 cm^{-1} formed, corresponding to C-H and hydroxyl stretching, respectively.[3,18] This behavior indicates deprotection of P(tBOS-*ran*-S) to P(HOST-*ran*-S). All spectra were normalized by the area under a light insensitive peak in the phenyl ring region at 2926 cm^{-1}. Full spectra are available in Supporting Information along with spectra confirming both UV and heat were required for deprotection to occur (Figure C.7 in Appendix C). Note that a slightly different amount of PAG was incorporated for samples with different blend ratios to ensure full deprotection from P(tBOS-*ran*-S) to P(HOST-*ran*-S) (see Figure C.12 in Appendix C). All data shown here are for full deprotection unless otherwise noted.

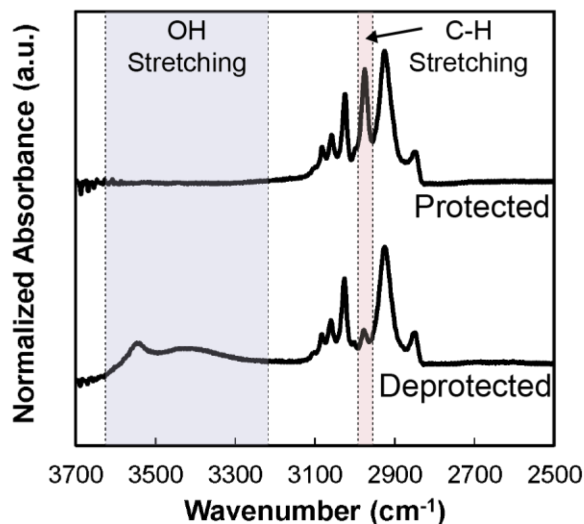

Figure 4.5: Excerpts from representative FTIR traces of both protected polymer (P(tBOS-ran-S)) and deprotected polymer (P(HOST-ran-S)). Deprotection was confirmed by the presence of OH-stretching between 3200-3600 cm^{-1} and the reduction of the peak at 2980 cm^{-1} due to C-H stretching. All spectra were normalized by a light insensitive peak in the phenyl ring region at 2926 cm^{-1}.

Furthermore, the change in surface energy under typical patterning procedures for different blend compositions was qualitatively evaluated using static glycerol contact angle measurements on solid polymer films. These results are shown in Figure 6. Before deprotection, the contact angle slightly increased (ca. 1°) as the amount of blended P(tBOS-ran-S) increased from 10 to 30 wt% in PS. Though slight, this is consistent with the lower surface energy predicted for P(tBOS-ran-S) compared to PS (Supporting Information, Section III). After deprotection, however, glycerol contact angles decreased for all samples, indicating the surface energy increases upon the deprotection of P(tBOS-ran-S) into P(HOST-ran-S). As more P(tBOS-ran-S) was incorporated, a larger change in surface energy was observed, suggesting the surface energy gradient of the films was dictated by the deprotection of P(tBOS-ran-S).

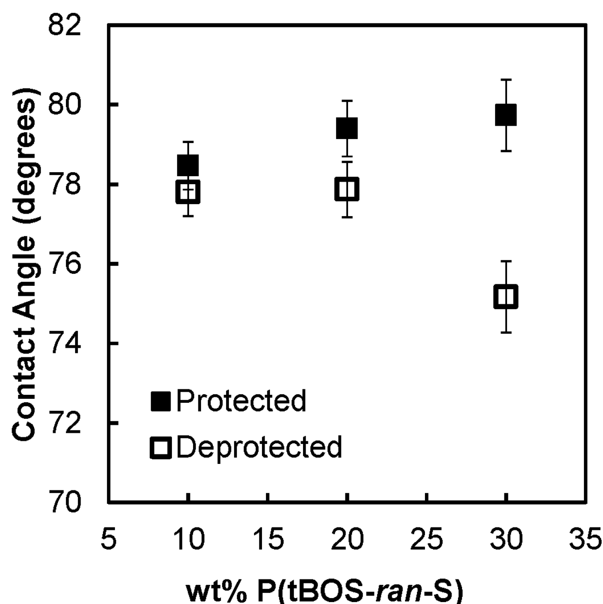

Figure 4.6: Effect of wt% P(tBOS-ran-S) in PS on contact angle measurements both before and after deprotection (exposure to UV and subsequent annealing). The wt% PAG for these measurements was 5 wt% with respect to tBOS in P(tBOS-ran-S). The test liquid used in this study was glycerol and error bars represent the standard deviation between three test droplets on the same sample. Films used here were exposed to UV light for 1 min and annealed 150°C for 1 min.

4.3.4 Physical Patterning Behavior

In Figure 4.4, different blend ratios between P(tBOS-*ran*-S) and PS showed different behaviors after extended annealing. For 10 wt% P(tBOS-*ran*-S) in PS, the features formed and then decayed while the formed features from 30 wt% P(tBOS-*ran*-S) in PS persisted upon extensive annealing at 120°C. In order to understand this contrasting behavior, a complete characterization of feature development with increasing annealing time for 10, 20, and 30 wt% P(tBOS-*ran*-S) in PS is given in Figure 4.7. The lowest concentration of P(tBOS-*ran*-S) (10 wt%) in PS was representative of the lowest surface energy gradient, and features formed with this blend always decayed. In contrast, blends with 20 wt% P(tBOS-*ran*-S) in PS were capable of producing stable features. Initial

feature formation rate was also relatively fast, reaching 500 nm in height in only 30 min. After the initial feature development, longer annealing times led to slow migration of the large molecular weight copolymer, allowing the maximum feature height (ca. 600 nm) to be achieved (double the initial thickness). For the final concentration (30 wt% in PS), thermally stable features were also observed. Higher concentrations of P(tBOS-*ran*-S) were not explored since with increasing P(tBOS-*ran*-S), the respective amount of the transport polymer PS would be reduced, leaving less available material for large feature formation.

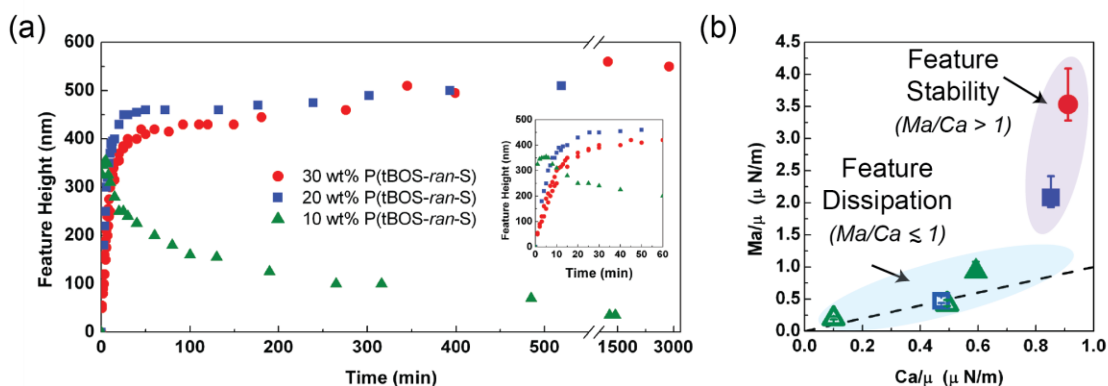

Figure 4.7: (a) Evolution of feature development for 10, 20, and 30 wt% P(tBOS-ran-S) for the case of full deprotection. Inset showing the short term annealing behavior. (b) Comparison of calculations of the Marangoni and capillary velocities for all blends tested (including incomplete deprotection which is marked by open symbols). Error bars represent minimum and maximum calculated values for surface energy. A full description of the calculations is given in Supporting Information, Section C6 in the Appendix C.

Feature dissipation/stability is a competition between Marangoni-driven flow and capillary-driven levelling.[15] However, the driving force behind the shift from decay to stability at a given polymer blend ratio remained unclear. To better understand the driving forces behind feature dissipation/stability, a scaling analysis based on the thin film equation was performed and a summary of these results (extended discussion available in Supporting Information, Section V) is given in Figure 4.7b. The analysis

utilizes the ratio between the Marangoni velocity, which drives flow towards regions of higher surface energy, to the capillary velocity, which acts to minimize surface area[19,20] by flattening the film. Due to the large molecular weight of P(tBOS-*ran*-S), diffusion of surface energy gradient creator, which represents the other mechanism responsible for feature dissipation, was assumed negligible.

We define the Marangoni velocity Equation (4.1) as:

$$Ma = \frac{\Delta\gamma h_0}{\lambda\mu} \tag{4.1}$$

where $\Delta\gamma$ is the surface energy gradient, h_0 is the initial film thickness, λ is the half-periodicity determined by the photomask (and confirmed with profilometry), and μ is the polymer blend viscosity. The surface energy gradient was estimated from contact angle measurements by fitting to a known value for PS of 39.3 dyne/cm[21] and using the Young-Dupré equation, while the initial film thickness was measured with ellipsometry. We similarly define a capillary velocity Equation (4.2) as:

$$Ca = \frac{\gamma\Delta h h_0^2}{\lambda^3\mu} \tag{4.2}$$

where γ is the average film surface energy (from contact angle measurements), Δh relates to the change in film height (measured by profilometry), and all other quantities are the same as defined for the Marangoni velocity. It is noteworthy that the scaling between the Marangoni and capillary forces suggests higher surface energy gradients relative to the initial value ($\Delta\gamma/\gamma$), combined with larger pattern periodicity are favorable for forming stable features. Meanwhile, the initial film thickness and perturbation height act against the Marangoni forces.

Here, we investigate the importance of surface energy by controlling the surface energy gradient with both the blend composition and also the degree of deprotection (from incorporation of PAG, See Appendix C, Figures C.11, C.12, and Table C.3). As mentioned previously, all data presented above was for full deprotection. Results for

incomplete deprotection are included only in Figure 4.7b (open symbols) to illustrate the effect of intermediate surface energy gradients. The degree of deprotection along with the associated surface energy gradient was approximated by quantitative FTIR analysis (Appendix C, Figure C.12) and liquid contact angle measurements. As Figure 4.7b indicates, once the magnitudes of the Marangoni velocities were smaller than or similar in magnitude to those of capillary velocities, the formed features always decayed upon a long period of heating. However, for the samples possessing ratios of Ma/Ca > 1, the formed features persisted upon extensive thermal annealing. Hence, whether the formed features dissipate or persist after long heating periods was governed by the domination of capillary or Marangoni forces, respectively.

Interestingly, estimations of the surface energy gradients using molar averaged values of each polymer (see Supporting Information, Table C.3) revealed the maximum magnitude of the surface energy gradient imposed here was similar in magnitude to prior work with PS (~ 0.2 dyne/cm).[2,15] This similarity implies that the observed significant improvement in feature aspect ratio along with formation of thermally stable features were both solely enabled by decoupling of the film viscosity and diffusivity. Thus, this decoupling strategy was demonstrated as an effective method for development of large features and future studies on systems with an even higher surface energy gradient are expected to further enhance the maximum attainable aspect ratio.

Lastly from the inset of Figure 4.7a, the feature development rate (seen by the initial slope of feature height over annealing time) was impacted by the blend composition. As the concentration of P(tBOS-*ran*-S) in PS increased, the slope decreased. The incorporation of higher molecular weight, surface energy gradient creating polymer increases not only the surface energy gradient, but also the film viscosities. Thus, this effect was shown through the timescale to achieve the maximum

feature height; features formed faster for films with lower viscosity. However, the scaling analysis above indicated that formation of stable features or dissipation of features did not rely on viscosity. Thus, viscosity dictated the flow timescale, but what governed feature stability upon extensive annealing was independent of the film viscosity. This is additional supporting evidence that the main driving force behind feature stability observed here was due to the Marangoni effect.

4.4 CONCLUSIONS

In summary, we have designed and demonstrated the viability of the use of a polymer blend, instead of a homopolymer, to produce Marangoni-driven sinusoidal topographies in polymer films. The blend was comprised of a low molecular weight PS and a relatively high molecular weight random copolymer, P(tBOS-*ran*-S). By using a blend, we removed the need for a single polymer to simultaneously produce a stable surface energy gradient (with low diffusivity), while also rapidly forming features (requiring low viscosity). The effects of blend composition on surface energy gradient magnitude, speed of feature formation, and feature stability were investigated. When sufficient surface energy gradient forming polymer was present, large features formed and the formed features were thermally stable up to one month. The stable features were formed after only 30 min of annealing. Because polymers have thermally accessible melt states with relatively low melt viscosities, the speed of feature formation can also be controlled by changing the annealing temperature. Lastly, a scaling analysis to investigate the underlying mechanism behind feature stability/dissipation was performed and key driving forces were identified for future tailoring of feature formation.

4.5 REFERENCES

1. Rouse, P. E. *J. Chem. Phys.* **1953,** *21*, 1272-1280.
2. Katzenstein, J. M.; Janes, D. W.; Cushen, J. D.; Hira, N. B.; McGuffin, D. L.; Prisco, N. A.; Ellison, C. J. *ACS Macro Lett.* **2012,** *1*, 1150-1154.

3. Tung, P. H.; Kuo, S. W.; Chan, S. C.; Hsu, C. H.; Wang, C. F.; Chang, F. C., *Macromol. Chem. Phys.* **2007,** *208*, 1823-1831.
4. Daugaard, A. E.; Hvilsted, S. *Macromol. Rapid Commun.* **2008,** *29*, 1119-1125.
5. Vogt, B. D.; Kang, S.; Prabhu, V. M.; Lin, E. K.; Satija, S. K.; Turnquest, K.; Wu, W. L. *Macromolecules* **2006,** *39*, 8311-8317.
6. Conlon, D. A.; Crivello, J. V.; Lee, J. L.; Obrien, M. J. *Macromolecules* **1989,** *22*, 509-516.
7. Augsburg, A.; Grundke, K.; Poschel, K.; Jacobasch, H. J.; Neumann, A. W., *Acta Polym.* **1998,** *49*, 417-426.
8. Willson, C. G.; Ito, H.; Frechet, J. M. J.; Tessier, T. G.; Houlihan, F. M. *J. Electrochem. Soc.* **1986,** *133*, 181-187.
9. Olabisi, O.; Robeson, L. M.; Shaw, M. T., *Polymer-Polymer Miscibility*. Academic Press: New York, 1979.
10. Sehgal, A.; Ferreiro, V.; Douglas, J. F.; Amis, E. J.; Karim, A. *Langmuir* **2002,** *18*, 7041-7048.
11. Zhang, Z. X.; Wang, Z.; Xing, R. B.; Han, Y. C. *Polymer* **2003,** *44*, 3737-3743.
12. Karim, A.; Slawecki, T. M.; Kumar, S. K.; Douglas, J. F.; Satija, S. K.; Han, C. C.; Russell, T. P.; Liu, Y.; Overney, R.; Sokolov, O.; Rafailovich, M. H. *Macromolecules* **1998,** *31*, 857-862.
13. Andrews, R. J.; Grulke, E. A., *Polymer Handbook*. 4th ed.; John Wiley & Sons: Hoboken, 1999; Vol. 1, p 209-213.
14. Rahman, S. S. A.; Kawaguchi, D.; Ito, D.; Takano, A.; Matsushita, Y. *J. Polym. Sci., Part B: Polym. Phys.* **2009,** *47*, 2272-2280.
15. Nakamura, K.; Hatakeyama, T.; Hatakeyama, H. *Polymer* **1981,** *22*, 473-476.
16. Arshad, T. A.; Bin Kim, C.; Prisco, N. A.; Katzenstein, J. M.; Janes, D. W.; Bonnecaze, R. T.; Ellison, C. J. *Soft Matter* **2014,** *10*, 8043-8050.
17. Koning, C.; van Duin, M.; Pagnoulle, C.; Jerome, R. *Prog. Polym. Sci.* **1998,** *23*, 707-757.
18. Hsu, C. H.; Kuo, S. W.; Chen, J. K.; Ko, F. H.; Liao, C. S.; Chang, F. C. *Langmuir* **2008,** *24*, 7727-7734.
19. Ardekani, A. M.; Sharma, V.; McKinley, G. H. *J. Fluid Mech.* **2010,** *665*, 46-56.
20. Zhang, Y. R.; Sharma, V. *Soft Matter* **2015,** *11*, 4408-4417.
21. Wu, S., *Polymer Handbook*. 4th ed.; John Wiley & Sons: Hoboken, 1999; Vol. 2, p 525.

Chapter 5: Patterning Thin Polymer Films by Photodirecting the Marangoni Effect using a Photosensitizer

5.1 INTRODUCTION

Up to this point in this thesis, the Marangoni-driven patterning technique had been applied by tailoring the intrinsic polymers' photochemistry. However, this technique could become a more broadly useful way to pattern polymer films if it could be adapted more generally to other classes of polymers. Since polymers undergo a variety of responses to absorbed light energy, it is challenging to exclusively create surface energy patterns by chemically modifying neat polymer. For example, PS can crosslink under certain exposure conditions[1] while poly(methyl methacrylate) undergoes chain scission due to exposure to UV light.[2] Consequently, the magnitude of the surface tension gradient that could be imparted into most polymers is often low, which in turn limits the achievable variations in film thickness.

In this chapter, a method is described to photochemically pattern surface energy gradients into an otherwise transparent solid-state film using doped sensitizers; upon activation with patterned light, these sensitizers later direct Marangoni instabilities in the liquid state. Poly(isobutyl methacrylate) (PiBMA) films containing 5 – 10 wt% 9,10-dibromoanthracene (DBA) were employed because they are much more sensitive to visible and near UV light (300 nm $< \lambda <$ 400 nm) than the other polymer films used previously. The PiBMA host polymer is relatively transparent at these wavelengths and does not interfere with the sensitizer photochemistry. At the same time, its relatively low glass transition temperature, (T_g = 55 °C for the bulk polymer) allows the feature

---

This chapter reproduced in part from "Surface Energy Gradient Driven Convection for Generating Nanoscale and Microscale Patterned Polymer Films using Photosensitizers" Kim, C. B.; Janes, D. W.; McGuffin, D. L.; Ellison, C. J. *Journal of Polymer Science Part B: Polymer Physics* **2014**, 52, 1195-1202 with permission from John Wiley and Sons, copyright 2014.

development to occur quickly at moderate temperatures while staying below its degradation temperature.

5.2 EXPERIMENTAL

5.2.1 Materials

Chemicals used in this study were purchased from Fisher Scientific or Sigma-Aldrich, and were used as received unless otherwise noted. PiBMA (M_n = 10.0 kg/mol, PDI = 1.06) was synthesized by activators regenerated by electron transfer atom transfer radical polymerization (ARGET ATRP) according to a previously described procedure.[3] Polished, 4 in. diameter silicon wafers were purchased from Silicon Quest International, Inc.

5.2.2 Film Preparation

PiBMA and DBA were dissolved in toluene on a hot plate held at 60 °C for an hour. Silicon substrates were prepared by soaking in a solution of ethanol, deionized water and potassium hydroxide (80/10/10 wt%) and then rinsed with deionized water and tetrahydrofuran. Films were spin-coated (Specialty Coating Systems Spincoat G3-8) onto the cleaned silicon wafers possessing approximately 2 nm native oxide layers. DBA concentrations were 5 wt% with respect to the host polymer unless otherwise noted. Solution concentrations ranged from 4 to 10 wt% with respect to the spin-coating solvent. The thickness of films prepared on silicon substrates were characterized by ellipsometry using a J.A. Woollam M-2000D spectroscopic ellipsometer using wavelengths from 382 to 984 nm with a 65° angle of incidence.

5.2.3 Light Exposure Conditions

Light exposures were performed with a 200 W metal-halide lamp with broadband output from 300−800 nm (Optical Building Blocks Scopelite 200) coupled with a 400 nm

bandpass optical filter (100 nm FWHM; Edmunds Optics). A 20 mm working distance was used with light intensity of 65.1 mW/cm^2 as measured by a Coherent Field MaxII-TO radiometer with a PM10 sensor. A typical exposure dose was 60 J/cm^2 (15 minutes) unless otherwise noted. The exposure stage was held at 20 °C by an Instec mK 1000 temperature controller with a HCS-402 stage to retain a solid state film during exposure. Alternatively, sunlight was focused with a plastic magnifying lens as a light source for some experiments. Samples were placed on a metal stage cooled by an ice bath and were exposed to sunlight for 10 to 30 minutes through various photomasks. The plastic lens filters light wavelengths less than 300 nm. The power density was measured and it was 832 mW/cm^2. An estimated effective dose of sunlight that is useful for activating DBA is about 3 – 5 percent of this value.

5.2.4 Feature Development

All light-exposed films were thermally annealed at 120 °C (bulk T_g + 65 °C) on a heating plate after exposure to light in the glassy state unless otherwise noted. Optical micrographs were taken for all samples showing feature development. The colors observed in the optical micrographs are due to interference patterns caused by differences in film height. The feature heights were characterized using either a Veeco Dektak 6M stylus profiler with a stylus diameter of 25 microns and stylus force of 7 mg or by AC mode atomic force microscopy (AFM, Asylum Research) at ambient temperature and pressure.

5.2.5 Characterization

Molecular weight and polydispersity data were measured using a Viscotek GPC Max VE 2001 size exclusion chromatography (SEC) solvent/sample module with a Viscotek Model 270 dual detector viscometer/light scattering detector and Viscotek VE

3580 refractive index detector with 2 I-Series mixed bed low MW columns. Fluorophore attachment was verified by an in-line Jasco FP-2020 Plus Intelligent Fluorescence Detector ($\lambda_{excitation}$ = 380 nm, $\lambda_{emission}$ = 405 nm, 18 nm bandpass). All SEC samples were prepared by first casting on the substrate and re-dissolving into tetrahydrofuran (THF) after the desired procedure was performed on the films. The solution was then filtered before the injection. All films were completely dissolved in THF which indicates that they were not crosslinked under typical patterning procedures (See Figure D.1 and Table D.1 of the Appendix D) Molecular weights reported are relative to a conventional calibration curve created using PiBMA standards synthesized in house and absolutely characterized by Viscotek Triple Detect software combining light scattering, refractive index detection, and viscometry. The glass transition temperature of the bulk polymer sample (onset T_g = 51 °C, mid-point T_g= 55 °C) was measured by differential scanning calorimetry (DSC) using a Mettler-Toledo DSC-1 with a 10 °C/min heating rate upon second heating. UV-Visible absorbance (UV-vis) measurements were performed on a Thermo Scientific Evolution 220 UV-Visible Spectrophotometer. Films for UV-vis measurements were spin-coated from toluene onto quartz plates. Background-subtracted, transmission-mode Fourier transform infrared (FTIR) spectra were recorded on a Thermo Nicolet 6700 FTIR with liquid nitrogen cooled MCT-B detector. Films spin-coated onto a double-side polished silicon wafer were used. Prior to the FTIR measurement, background spectra were collected using clean, identical silicon wafers to appropriately correct the polymer film data. Water contact angles were measured with a Ramé-Hart, inc. NRL C.A. goniometer (Model #100-00). Prior to the measurement, the film was rinsed thoroughly with deionized water then blown dry with filtered air. Then, a 4 μL drop of deionized water was placed on the sample, and the stage was leveled, at which point the real-time image was frozen and the contact angles on the left and right side of

the drop were determined. The final image was collected within 10 s of placing the drop on the sample. Between measurements the sample was blown dry with filtered air.

5.3 RESULTS AND DISCUSSION

A schematic that describes the patterning procedure is shown in Figure 5.1. First, a PiBMA film containing 5 wt. % DBA was spincoated from a toluene solution onto a silicon wafer. A light exposure dose of 60 J/cm^2 was applied through a photomask. During this step, the DBA sensitizer was photochemically oxidized in the exposed regions. Upon thermal annealing above the T_g, thermolysis of the oxidized DBA causes chemical changes to the PiBMA that raise the surface tension in the exposed regions. Due to the Marangoni effect, polymer flows into the exposed regions from the unexposed regions. This results in a film with a smoothly varying thickness profile reflective of the photomask pattern.

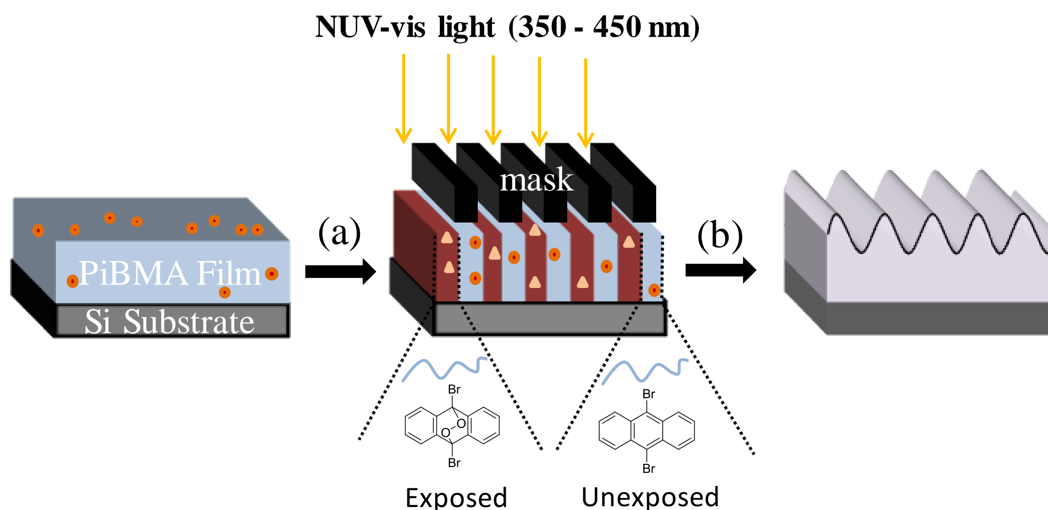

Figure 5.1: Patterning schematic of (a) NUV-vis light exposure in ambient air atmosphere, and (b) subsequent thermal annealing. Exposed regions (higher surface energy) rise while the unexposed regions (lower surface energy) sink upon thermal annealing.

Representative optical micrographs and AFM images of samples possessing 12.5 μm, 5 μm and 800 nm half-pitch are shown in Figure 5.2. The periodicity of the topographical pattern matches that of the “line and space” mask used during exposure. The resulting film thickness variations exhibit color differences in optical micrographs due to interference patterns. The AFM results show that the sinusoidal film thickness variations for these samples are 580, 140, and 12 nm, respectively. 60, 30, and 5 minutes of cumulative annealing time at 120 °C were applied to achieve these features, respectively, to produce roughly the maximum feature height. Note that commercial “I-line” contact lithography tools such as those used as mask aligners apply pressure to minimize the air gap between the mask and film and optimize patterning resolution. Nevertheless, the minimum feature size typically accessible by these I-line systems is near 500 nm.[4] That our results approach this limit despite using a more crude approach suggest that the pattern resolution is inhibited primarily by our lack of sophisticated tools, and not by any underlying chemical or physical limitations.

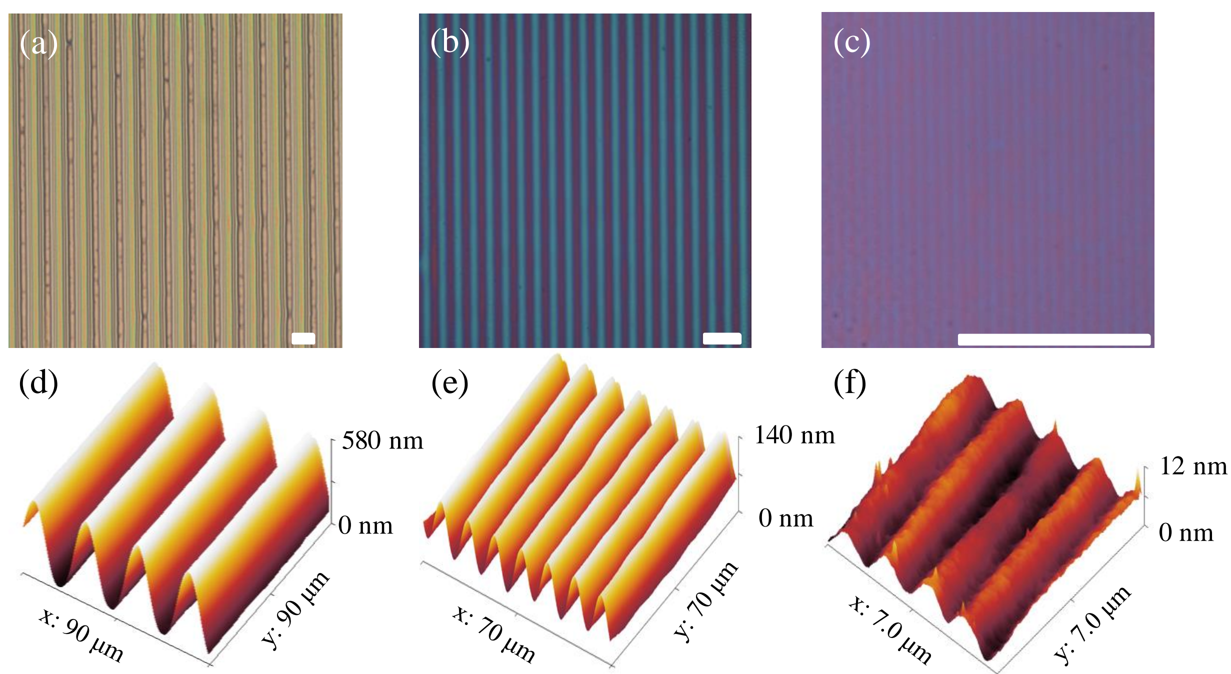

Figure 5.2: Optical micrographs of the patterned samples using (a) 12.5 µm, (b) 5 µm, and (c) 800 nm half-pitch "line and space" masks. All scale bars indicate 25 µm. AFM images of the corresponding patterned samples are shown below. Initial film thicknesses were 300 nm. All samples were light exposed for 15 minutes.

Because PiBMA films containing 5 wt% DBA absorb light broadly ($\lambda \leq 420$ nm, see Figure D.2 of Appendix D) and well within the solar output spectrum (i.e., from the UV to infrared range), we show here that sunlight can be used as a patterning stimulus. Optical micrographs of samples patterned by solar irradiation are shown in Figure 5.3.

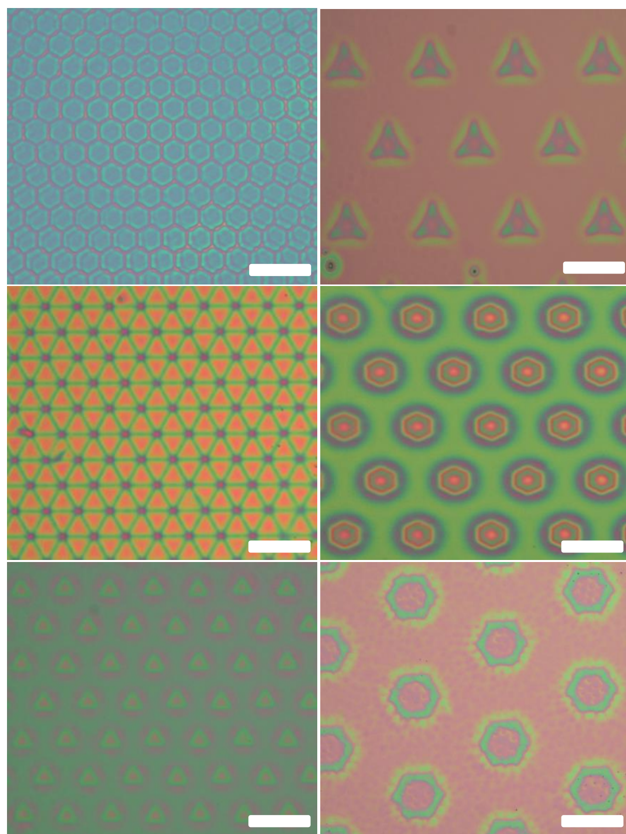

Figure 5.3: Optical micrographs of samples patterned using sunlight through various photo-masks. Scale bars indicate 100 μm. Samples were subsequently annealed for 30 minutes at 120 °C.

5.3.1 Chemical Patterning Mechanism

It is hypothesized that thermolysis of photo-oxidized DBA is responsible for the programmed polymer flow demonstrated in Figures 5.2 and 5.3. The chemical mechanism is shown in Figure 5.4. Light exposure in the presence of ambient O_2 produces an endoperoxide form of DBA by (4π+2π) cycloaddition with singlet oxygen.[5-10] Subsequent heating yields free radicals that chemically modify the PiBMA film in a number of potential ways. One pathway, shown in Figure 5.4, results in the fluorophore being covalently bound to polymer chains. The following results in this section were obtained to quantitatively validate these claims.

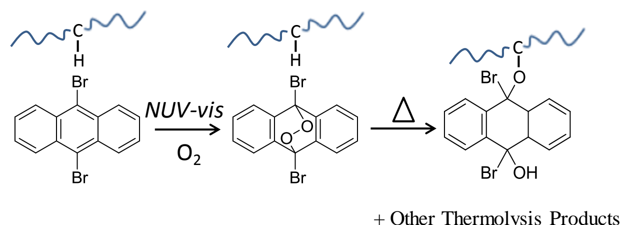

Figure 5.4: Proposed reaction scheme for DBA doped into a polymer matrix with extractable hydrogens.

Control experiments were conducted to show that patterning could not be performed if DBA was omitted from the film composition or if oxygen was nearly absent during light exposure. Optical micrographs of these conditions following otherwise identical procedures are shown in Figure 5.5. First, all of the films remain flat after light exposure because the patterning was performed in the glassy state. After thermal annealing, only the film containing 5 wt% DBA and exposed under ambient atmosphere contains significant film thickness variations similar in magnitude to the one shown in Figure 5.2a. The neat PiBMA patterned by the same procedure remains flat after annealing, confirming the importance of sensitizer in this process. The sample that was irradiated in a small chamber purged with argon gas shows only faint features ~10 nm in total height. (See Figure D.3 of Appendix D) Invariably, trace oxygen not removed by the purge protocol has a small effect. This illustrates the fact that the air atmosphere is the preferential atmospheric condition during the light exposure step.

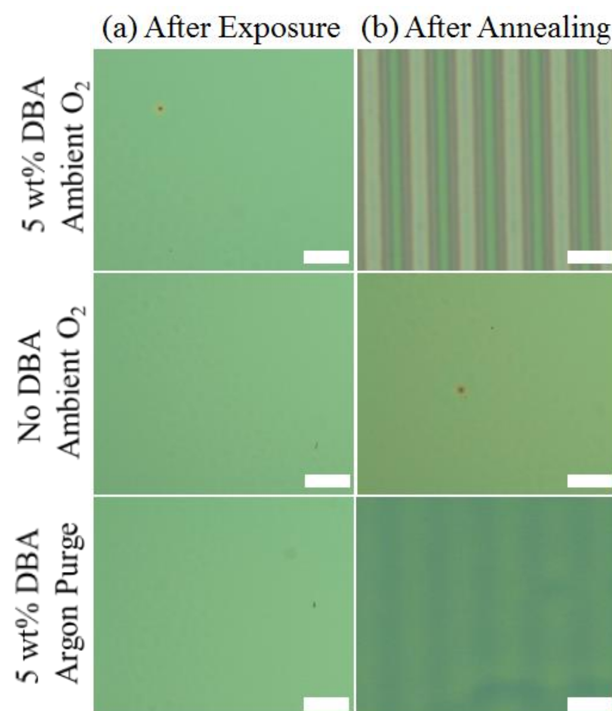

Figure 5.5: Optical micrographs of polymer films (a) after patterned light exposure, and (b) after subsequent thermal annealing at 120 °C for 60 minutes. PiBMA containing 5 wt% DBA exposed in ambient atmosphere (top row), neat PiBMA exposed in ambient atmosphere (middle row), and PiBMA containing 5 wt% DBA exposed in an argon purged atmosphere (bottom row). The scale bars indicate 25 μm. The films were exposed to light through a 12.5 μm half-pitch line and space photomask. Initial film thicknesses were 250 nm.

The formation of DBA endoperoxide shown in Figure 5.4 disrupts the conjugated π-electron system of the central benzene ring in DBA. This step is anticipated to result in bleaching of the higher absorbing wavelengths in the UV-vis absorbance spectra. For this reason, UV-vis absorbance spectra were obtained for PiBMA films containing 5 wt% DBA subjected to blanket light exposure and are shown in Figure 5.6. In the presence of oxygen, UV-vis absorbance wavelengths characteristic of DBA (340 nm $\leq \lambda \leq$ 420 nm) reduce in size with varying exposure times 0 - 5 minutes. However, when the same photo-exposure times were tested in a chamber purged with argon, the spectra are nearly

identical. This provides spectral evidence that DBA endoperoxide forms during typical ambient exposure conditions. Fullerenes, another highly conjugated and strongly light absorbing compound, exhibit a similar photo-oxidative mechanism if exposed simultaneously to oxygen and UV light.[11] This corroborates the conclusion drawn from Figure 5.5 that the DBA endoperoxide is a critical reaction intermediate. Note that the absorbance ($A_{405,t}$) at λ = 405 nm after an exposure time t, relative to that of the unexposed film, $A_{405,0}$, is directly related to the fraction of DBA converted to another form. The converted fraction of DBA can be calculated from

$$\textit{Converted Fraction} = 1 - \left(\frac{A_{405,t}}{A_{405,0}}\right) \tag{5.1}$$

because $A_{405,t}$ tends towards zero at long exposure times. After 5 minutes of exposure in ambient atmosphere, 98 % of DBA is converted; but less than 1 % is converted for an identical exposure performed in a chamber purged with argon gas. This result is similar to the one obtained by Lee et al. for a solution-irradiated, coumarin-containing polyester.[12] Note this UV-vis absorbance data also indicates that the light dose is attenuated by a negligible amount (∼ 10%) as it passes through the film; therefore, the photochemical reaction takes place homogeneously throughout the depth of the film.

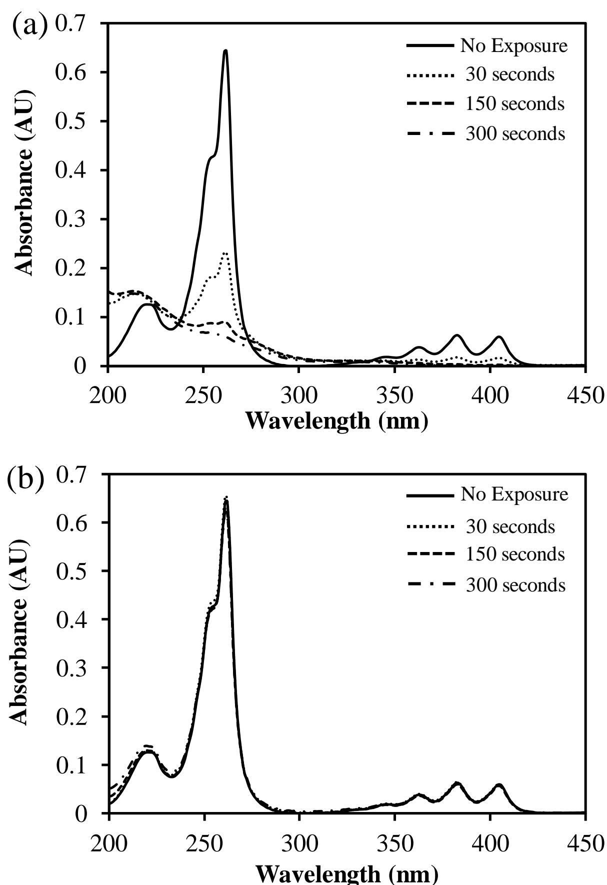

Figure 5.6: UV-vis absorption spectra of a PiBMA film containing 5 wt% DBA with varying light exposure time from 0 to 5 minutes in (a) ambient air atmosphere, and in (b) argon atmosphere. Films were all approximately 250 nm thick on quartz. One sample was used for each plot.

SEC was performed on re-dissolved film materials to determine if covalent grafting of DBA sensitizer to PiBMA occurred. A fluorescence detector was used to distinguish sensitizer from polymer so that the sample's characteristic elution time could confirm covalent attachment. SEC elution curves for PiBMA films containing 5 wt% DBA after being subjected to representative processing conditions are shown in Figure 5.7. The films after spin-coating and after blanket irradiation do not fluoresce significantly at the polymer's elution time scale. Fluorescence signals for the samples

irradiated but not annealed were only detected at the elution time characteristic of small molecules, which clearly indicates that irradiation alone does not promote covalent grafting reactions. However, the exposed and thermally annealed polymer films clearly possess bound fluorophore because a detector response is observed at the polymer elution time. Furthermore, output from the refractive index detector (See Figure D.1 of Appendix D) is unchanged after these typical processing conditions. Since the refractive index detector is most sensitive to PiBMA concentration, this indicates that polymer molecular weight and PDI is not altered within the resolution of SEC during the patterning process.

A mechanism for anthracene endoperoxide radical intermediate formation by either thermal or photochemical decomposition was previously investigated by other groups.[13,14] Based on their findings for our system, the photo-exposure first produced DBA endoperoxide, which then decomposed to generate a biradical intermediate upon thermal annealing. Figure 5.7 confirms that DBA is not grafted directly during the photo-exposure step in the glassy state PiBMA. This could be due to the fact that the radicals are confined and immobilized in the glassy polymer matrix, hence, there is little opportunity to undergo grafting reactions for attaching to polymer.

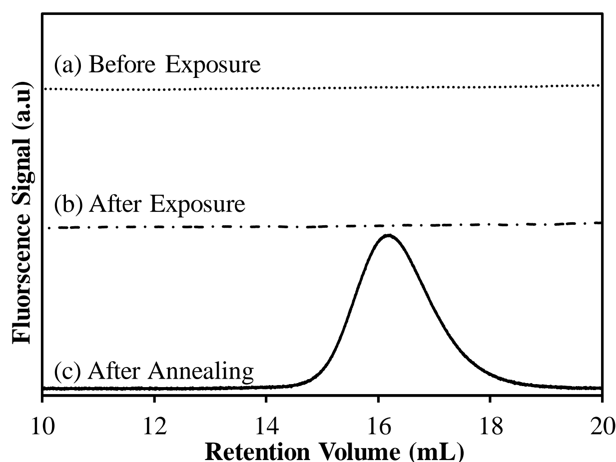

Figure 5.7: SEC fluorescence detector responses near the host polymer retention volume (a) before light exposure, (b) after light exposure and (c) after light exposure and subsequent thermal annealing. $\lambda_{excitation}$ = 380 nm and $\lambda_{emission}$ = 405 nm were used to detect the fluorescence signals in this study. Total polymer concentration for each plot was approximately constant.

The oxidative grafting reaction is further supported by FTIR (Figure D.4 of Appendix D). There is no difference in the spectra taken after photo-exposure compared to the one taken before the exposure. This result agrees with the Hargreave's statement that there is no difference between IR spectra of light exposed and unexposed anthracene if only endoperixde formation has occurred because of the weak influence of O-O on any dipole moment.[15,16] Once the photo-exposed sample has been thermally annealed, two new peaks start appearing at 1650 – 1700 cm^{-1} and 3250 – 3620 cm^{-1}, which correspond to a ketone stretch and hydroxyl stretch, respectively. Both the ketone and hydroxyl groups are common functional groups resulting from polymer oxidation. It is noteworthy that the ketone stretch signals are not from the ester signals at 1700 – 1775 cm^{-1} that are present in PiBMA. The hydroxyl signals are appearing since the di-functional and symmetric DBA radical intermediate abstracts hydrogen from the polymer chain forming hydroxyl at one end, then, the other end immediately covalently bonds to the abstraction site. (See reaction scheme in Figure 5.4) An analogous mechanism could result with

further oxidized DBA, yielding a ketone functional group instead of a hydroxyl group. Such grafting was also previously reported with 9-methyl-10-oxymethyl anthracene and poly(methyl methacrylate).[17] It is noteworthy that we were also able to use DBA to activate Marangoni flow and topography formation in other host polymers such as polystyrene and poly(methyl methacrylate) (See Figure D.5 of Appendix D). Because many polymers have thermally accessible melt states with relatively low melt viscosities (viscosity can always be lowered by decreasing molecular weight) and are chemically modified by thermolyzed peroxides, we anticipate that this methodology is applicable to other systems as well.

5.3.2 Physical Patterning Mechanism

We believe that film flow from unexposed to exposed regions is driven by surface energy gradients imposed by photochemical patterning. Generally, oxidation reactions that impart alcohol (see Figure 5.4) and/or carboxyl, ketone, hydroperoxy functionalities to hydrophobic polymers such as PiBMA are anticipated to result in an increase in surface energy.[18-21] To confirm this qualitatively, the water contact angle of PiBMA films containing 10 wt% DBA was measured after various processing steps and the results are shown in Figure 5.8. These films possess a static water contact angle of 85.3 ° (± 0.8), and this value is unchanged after blanket photo-exposure times typically used for patterning. However, films which are irradiated and then annealed at 120 °C for 30 minutes possess a static water contact angle that decreases monotonically with increasing exposure time. This increase in film hydrophilicity, however slight, is consistent with a higher surface energy for PiBMA in exposed regions under typical patterning conditions.

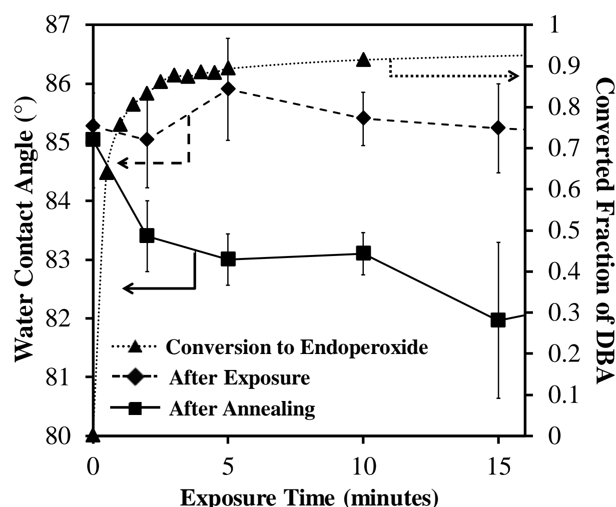

Figure 5.8: Water contact angle goniometry results: diamonds are the water contact angle measurements after NUV-vis blanket exposures, and squares are the measurements after post exposure thermal annealing for 30 minutes at 120 °C. Error bars are standard deviation calculated from three water contact angle measurements on the same sample. Between measurements the sample was blown dry with filtered dry air. The triangles represent the relative amount of DBA endoperoxide based on UV-Vis absorption peak changes along with photo exposure in ambient air atmosphere. 10 wt% of DBA dopant was used.

To clearly illustrate the connection between surface energy changes and the photochemical stimulus, Figure 5.8 includes DBA conversion data calculated from Eq. 5.1 and plotted on a secondary axis. DBA conversion increases monotonically at a rate commensurate with the decrease in water contact angle observed for the exposed and annealed samples. As DBA conversion nears unity, the water contact angles after thermal annealing remain roughly constant with increasing photo-exposure time. This is consistent with the presence of surface energy gradients in the patterned samples resulting from polymer oxidation by thermolysis of DBA endoperoxide.

To gain further insight into the physical effects that result in film thickness variations, height profiles of patterned samples were measured after a series of short thermal annealing intervals. Samples were exposed for one minute through a 12.5 µm

half-pitch line and space photo-mask. The peak to valley height observed during the study at each temperature as a function of cumulative annealing time at 120 °C and 130 °C is shown in Figure 5.9. The cumulative annealing time, t, was normalized by the characteristic self-diffusion time of the neat PiBMA ($\tau_{diff} = L^2/4D$) at both temperatures. The τ_{diff} was estimated based on a known characteristic diffusion length, L, in this case the half-pitch of the photo-mask being used, and the estimated diffusivity, D, using the Rouse model for unentangled polymer diffusion.[3,22] The zero shear viscosity of the polymer used in the Rouse model was characterized using a TA Instruments AR-2000ex rheometer. This value agreed with previous values[3] by linear scaling with molecular weight, the correct scaling factor for unentangled polymers. The estimated τ_{diff} of the neat PiBMA at 120 °C and 130 °C are 167 and 86 minutes, respectively; hence, unity on the time axis indicates τ_{diff} of the polymer at each temperature.

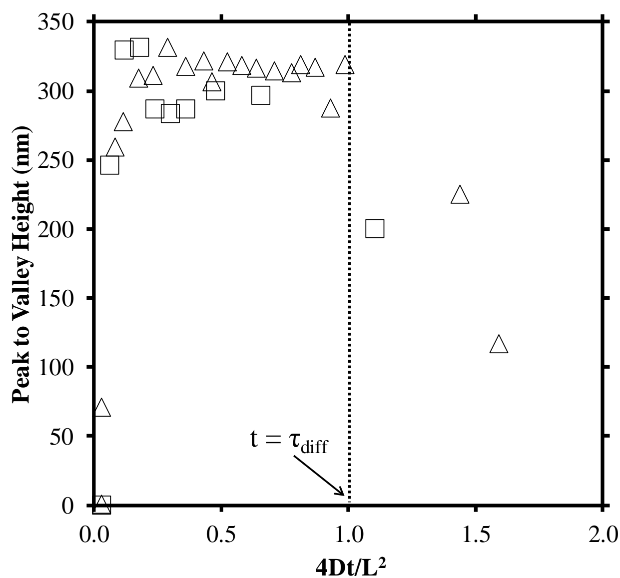

Figure 5.9: Peak to valley height at 120 °C (squares) and 130 °C (triangles), respectively, as a function of cumulative heating time after 60 seconds of photo-exposure. The initial film thicknesses were 250 nm.

Figure 5.9 shows that the patterned features increase in size with post exposure thermal annealing, reach a maximum, and then decrease. The cumulative annealing times to reach the maximum feature height for both temperatures were about a quarter of the estimated τ_{diff} at each annealing temperature. Additional annealing reveals a plateau-like region where there is only a slight reduction in feature height until the cumulative time is τ_{diff}. Once, the annealing time has exceeded τ_{diff}, the features start decaying dramatically. We believe this is because the polymer chains within the exposed and unexposed regions begin to interdiffuse significantly. Since interdiffusion weakens the surface energy pattern that drives Marangoni flow, capillary forces favoring a flat film surface eventually dominate and the height variations start dissipating.[23] This study strengthens the argument that the feature formation mechanism is from Marangoni convection that occurs on a shorter time scale than self-diffusion, with features decaying at longer annealing times as the surface energy gradient diminishes with polymer self-diffusion.

5.4 CONCLUSIONS

In this study, we photochemically directed surface energy driven Marangoni convection using a DBA photosensitizer doped into PiBMA thin films. By light exposure to near UV-visible light through a photomask, DBA is selectively oxidized in glassy state films. Following subsequent thermal annealing to convert the film to a liquid, nano- and micro-scale three dimensional topographical features can be formed due to the Marangoni effect that are reflective of the original light exposure pattern. A mechanistic investigation elucidated that the surface energy gradient originates from a thermally activated grafting reaction between DBA endoperoxide and the PiBMA chain, without a change in the polymer chain length distribution. Since many polymers are susceptible to chemical modification by DBA radical intermediates, this method could be considered very general and versatile for many polymers. In addition, judicious selection of the

photosensitizing compound in an otherwise transparent polymer expands the use of this method to more readily available light sources. For example, the broadband absorbance spectra of DBA enabled use of sunlight in this study, an unconventional light source for patterning films.

5.5 REFERENCES

1. Palacios, M.; Garcia, O.; Hernandez, J. R. *Langmuir*, **2013**, 29, 2756-2763.
2. Wochnowski, C.; Eldin, M. A. S.; Metev, S. *Polym. Degrad. Stab.*, **2005**, 89, 252-264.
3. Katzenstein, J. M.; Janes, D. W.; Hocker, H. E.; Chandler. J. K.; Ellison, C. J. *Macromolecules*, **2012**, 45, 1544-1552.
4. Suzuki, K.; Matsui, S.; Ochiai, Y.; Eds. Sub-Half-Micron Lithography for ULSIs; Cambridge University Press: New York, 2000.
5. Bratschkov, C.; Karpuzova, P.; Mullen, K.; Klapper, M.; Schopov, I. *Polym. Bull.*, **2001**, 46, 345-349.
6. Lapouyade, R.; Desvergne, J. P; Laurent, H. B. *Bull. Soc. Chim. Fr.*, **1975**, 9-10, 2137-2142.
7. Popov, A. P.; Shelekhov, N. S.; Bandyuk, O. V.; Ratner, O. B.; Vember, T. M.; Rebezov, A. O.; Lashkov, G. I. *Teor. Eksp. Khim*., **1986**, 22, 235-240.
8. DeRosa, M. C.; Crutchley, R. J. *Coord. Chem. Rev.*, **2002**, 233-234, 351-371.
9. Fudickar, W. Linker, T. *Chem. Eur. J*., **2006**, 12, 9276-9283.
10. Sheats, J. R. *J. Phys. Chem*., **1990**, 94, 7194-7200.
11. Wong, H. C.; Higgins, A. M.; Wildes, A. R.; Douglas, J. F.; Cabral, J. T. *Adv. Mater*., **2013**, 25, 985-991.
12. Lee, J.; Maddipatla, M. V. S. N.; Joy, A.; Vogt, B. D.; *Macromolecules,* **2014**, 47, 2891–2898.
13. Balta, D. K.; Arsu, N.; Yagci, Y.; Sundaresan, A. K.; Jockusch, S.; Turro, N. J. *Macromolcules*, **2011**, 44, 2531-2535.
14. Lauer, A.; Dobryakov, A. L.; Kovalenko, S. A.; Fidder, H.; Heyne, K. *Phys. Chem. Chem. Phys*. **2011**, 13, 8723-8732.
15. Bratschkov, C. *Eur. Polym. J.,* **2001,** 37, 1145-1149.
16. Hargreaves, J. S. *J. Polym. Sci., Part A: Polym. Chem.,* **1989,** 27, 203-216.
17. Popov, A. P.; Veniaminov, A. V.; Goncharov, V. F. *SPIE*, **1994**, 2215, 113-124.
18. Cui, L.; Ranade, A. N.; Matos, M. A.; Dubois, G.; Dauskardt, R. H. *ACS Appl. Mater. Interfaces*, **2013**, 5, 8495-8504.
19. Yang, P.; Yang, W.; *ACS Appl. Mater. Interfaces*, **2014**, 6 , 3759–3770.
20. Gonzalez, E.; Hicks, R. F. *Langmuir*, **2010**, 26, 3710−3719.
21. Gonzalez, E.; Barankin, M. D.; Guschl, P. C.; Hicks, R. F. *Langmuir*, **2008**, 24, 12636−12643.
22. Doi, M.; Edwards, S. F. The Theory of Polymer Dynamics; Clarendon Press: Oxford, **1986**.

23. Janes, D. W.; Katzenstein, J. M.; Shanmuganathan, K.; Ellison, C. J. *J. Polym. Sci., Part B: Polym. Phys.* **2013**, 51, 535–545.

Chapter 6: A Photochemical Approach to Stabilizing Marangoni-driven Patterned Polymer Films using Photosensitizers

6.1 INTRODUCTION

Coatings and substrates with topographically patterned features will play an important role in efficient technologies such as for harvesting and transmitting light energy[1-4] among other applications.[5-8] Such real world applications typically require that the coatings are stable at elevated temperatures and solvent-rich conditions. In order to address these important applications, a methodology for prescribing height profiles in polymer films and stabilizing them to subsequent solvent and/or heat treatments using two different photosensitizers is presented in this Chapter. The sensitizers used here are derivatives of benzophenone, and differ on the basis of their absorption spectra and functionalities. The structures of Michler's ketone (MK) and ethane-1,2-diyl bis(3-benzoylbenzoate), (bis-benzophenone, BB) are shown in Figure 6.1. Benzophenone and its derivatives are classic polymer photosensitizers,[9] and Carroll et al. have shown BB to crosslink polymer films after photoexposure *via* covalent grafting reactions.[10-12] It is shown here that a fraction of both MK and BB absorb UV light and are reduced by an initial exposure through a photomask, and the resulting chemical pattern directs melt-state transport, resulting in 3-dimensional topographies reflective of the mask pattern.[13] A second blanket exposure further photo-reduces remaining BB to crosslink the film and stabilize the topographic features.[10]

This chapter reproduced in part from "A Photochemical Approach to Directing Flow and Stabilizing Topography in Polymer Films" Katzenstein, J. M.; Kim, C. B.; Prisco, N. A.; Katsumata, R.; Li, Z.; Janes, D. W.; Blachut, G.; Ellison, C. J. *Macromolecules* **2014**, 47, 6804-6812 with permission from American Chemical Society, copyright 2014.

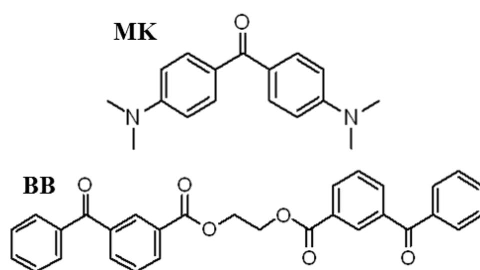

Figure 6.1: Structures of Michler's ketone (MK) and bis-benzophenone (BB).

6.2 EXPERIMENTAL

6.2.1 Materials

Chemicals used in this study were purchased from Fisher Scientific or Sigma Aldrich and used as received unless otherwise noted. Poly(isobutyl methacrylate) (PiBMA, M_n = 10 kg/mol, $Đ$ = 1.1) was synthesized and characterized using protocols and equipment described in previous work.[14] Bis-benzophenone (BB) was synthesized according to a published procedure.[10] The supporting information contains details of its synthesis. The poly(styrene-*block*-trimethylsilylstyrene) (PS-b-PTMSS) used in this study self-assembled into a lamellar structure with a periodicity of 27 nm. Its synthesis and characterization were described in other work.[15] Molecular weight and polydispersity data were measured using a Viscotek GPCMax VE 2001 size exclusion chromatography (SEC) module possessing 2 I-Series mixed bed low MW columns. It was equipped with a Viscotek Model 270 dual detector viscometer/light scattering detector, a Viscotek VE 3580 refractive index detector, and a Jasco FP-2020 Plus Intelligent Fluorescence Detector.

6.2.2 Film Preparation and Characterization

Films in this study were spin-coated (Specialty Coating Systems Spincoat G3-8) onto silicon substrates with native oxide layers. 2 wt. % MK was used in the films

because it sensitized the host polymer and directed melt-state flow in the absence of polymer scission or coupling. 10 wt. % BB was added because this amount was sufficient to stabilize the features without depressing the film T_g below room temperature. Substrates were prepared by soaking in a solution of ethanol, deionized water and potassium hydroxide (80/10/10 wt%) and then rinsed with deionized water and tetrahydrofuran at least three times. Spin coating solution concentrations were 4-8 wt% polymer in amyl acetate and spin speeds varied from 800 – 1500 RPM to control the film thickness.[16] Residual solvent was removed from the films by placing them on a hot plate at 150 °C for 20 minutes; longer annealing times did not alter the film thickness.

Film thicknesses were characterized using a J.A. Woollam M-2000D Spectroscopic Ellipsometer. Height profiles were measured using a Veeco Dektak 6M Stylus Profiler with a stylus force of 7 mg and a tip radius of 12.5 μm. Bright field microscopy was performed on an Olympus BX 60 microscope with a Spot Insight QE camera.

6.2.3 UV/Vis Spectroscopy

UV/Vis spectra of films and solutions were acquired with a Thermo Scientific Evolution 220 UV-Visible Spectrophotometer. Films were characterized on background-subtracted quartz substrates using thicknesses measured on identically prepared films on silicon wafers. Solutions were measured in quartz cuvettes with background contributions from the solvent and cuvette subtracted from the solution absorbances. Absorbances were divided by the molar concentration and path length to determine the molar absorptivity, ε. For PiBMA films we used a mass density of 1.05 g/cm^3 and a (repeat unit) molecular weight of 142.2 g/mol. For MK and BB, the molecular weight was expressed relative to benzophenone groups, 268.36 and 239.25 g/mol, respectively.

6.2.4 Topography Formation and Characterization

In order to pattern the film, the spin coated films were exposed to light from an Optical Building Blocks ScopeLite 200, a broadband microscope illuminator. Unfiltered doses are very large because the UV output useful for patterning is relatively low compared to the total spectral intensity supplied by this source. The initial photopatterning exposure utilized a 365 nm bandpass filter (10 nm full-width/half-maximum, Edmund Optics). Masks used in this work were evenly spaced chrome lines on a quartz substrate (Edmund Optics), although more complex patterns have been generated with alternate mask designs and/or sequential exposures.[17] During exposure, films were cooled to 15 °C to ensure they remained glassy during photo exposure (see Appendix E, Table E.1 for T_g of various compositions). An Instec mK 1000 temperature controller and HCS 402 stage connected to a liquid nitrogen pump was used for this step. Crosslinking was performed using the same light source and a UVB/UVC bandpass filter (maximum transmission at λ = 260 nm, 40 nm full-width/half-maximum, Edmund Optics) or a broadband exposure without any filter. Light intensity was measured using a Fieldmax TO (Coherent) radiometer capable of a wavelength range 250 nm to 11,000 nm. All photoexposure doses were measured through the bandpass filter used for the exposure step described. As shown in Figure E.1 in Appendix E, UV/vis spectra of a 110 nm thick PiBMA film containing 10 wt. % BB and 2 wt. % MK exhibit ~95% transmission at λ = 365 nm and ~92% transmission at λ = 260 nm. For a 400 nm thick film these transmissions would be ~85% and ~53%, respectively. Therefore, the light doses applied in this work for patterning and crosslinking thin films were applied nearly uniformly through the depth of the films.

6.2.5 Fourier Transform Infrared Spectroscopy (FTIR)

Samples for transmission FTIR analysis were made by spin coating films onto a double side polished silicon wafer. Background-subtracted spectra were acquired on a Nicolet 6700 FTIR spectrometer (Thermo Fisher Scientific). 64 scans with a resolution of 4 cm^{-1} were averaged. The area under distinct absorption peaks,[18] $\boldsymbol{A_{i,j}}$, characteristic of BB (C=O, 1666 cm^{-1}), MK (C=O, 1600 cm^{-1}), and esters present in PiBMA and BB (C=O, 1730 cm^{-1}) were measured on the associated OMNIC software. The areas under photochemically active peaks (BB and MK) were normalized to the area under the light insensitive ester peak. The fraction of MK and BB groups photochemically converted was calculated from

$$\text{Converted Fraction} = \mathbf{1} - \left(\frac{A_{i,j}}{A_{i,ester}}\right)\left(\frac{A_{0,ester}}{A_{0,j}}\right) \tag{6.1}$$

Here, i refers to the cumulative exposure dose (in J/cm^2), and j refers to the peak of interest (BB or MK).

6.2.6 Sol Fraction Measurements

Sol fractions (i.e. the fraction of the film soluble in solvent) were determined for PiBMA films with 10 wt% BB after exposure to UVB/UVC light. The film thicknesses were measured by ellipsometry after exposure, soaking in tetrahydrofuran (THF), and drying at 80 °C for ten minutes. The sol fraction was calculated by comparison to the film thickness prior to exposure, which was between 150 and 165 nm for all films. We ascribed 5% uncertainty to the data because about 5% of the intitial film thickness was strongly absorbed to the wafer even for conditions not possessing a gel fraction.

6.3 RESULTS AND DISCUSSION

6.3.1 Patterning of Topographic Features

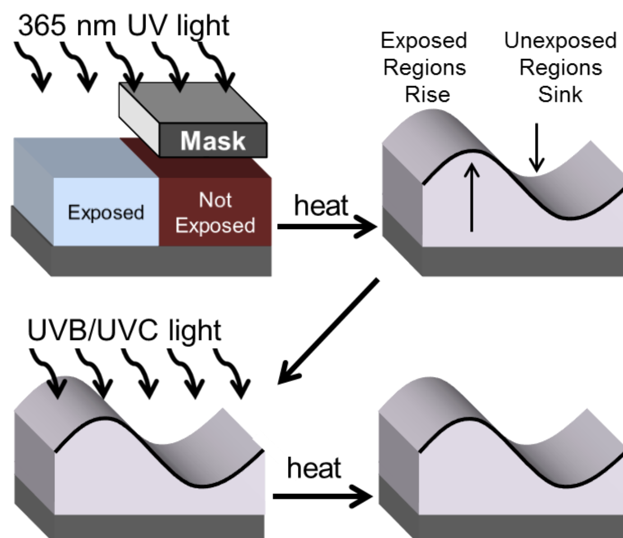

Figure 6.2: Schematic of process for forming and stabilizing topographic features in a polymer film. 365 nm UV light exposed through a mask photo-reduces a fraction of blended sensitizers to prescribe melt-state flow into the exposed regions. Features dissipate or distort after excessive heating. However, a second exposure to UVB/UVC light fully activates a crosslinker, bis-benzophenone, which stabilizes the topographic features.

A schematic of the process used is shown in Figure 6.2. Poly(isobutyl methacrylate) (PiBMA, M_n = 10.6 kg/mol, $Đ$ = 1.16) doped with 2 wt. % MK and 10 wt. % BB is spin coated from amyl acetate (7 wt.% total solids) onto a silicon wafer, forming a blend with a glass transition temperature of T_g = 27 ^{o}C. Irradiation of the film by UV light (λ = 365 nm, 10 J/cm^2) through a mask generates a chemical pattern by photo-reducing a fraction of benzophenone groups present in MK and BB. The exposed regions have higher relative surface energies and lower mobility due to the photochemical reactions in the sensitized polymer film. Upon heating the film at 125 ^{o}C for 1 h, polymer moves from unexposed to exposed regions, creating three-dimensional topography reflective of the photomask pattern. By blanket exposure to higher energy UV light

(UVB/UVC, λ ≈ 225-325 nm, 16 J/cm^2), benzophenone groups in BB graft to polymer chains and promote network formation by covalently linking together PiBMA chains.[10,19] The features do not dissipate after additional heating.

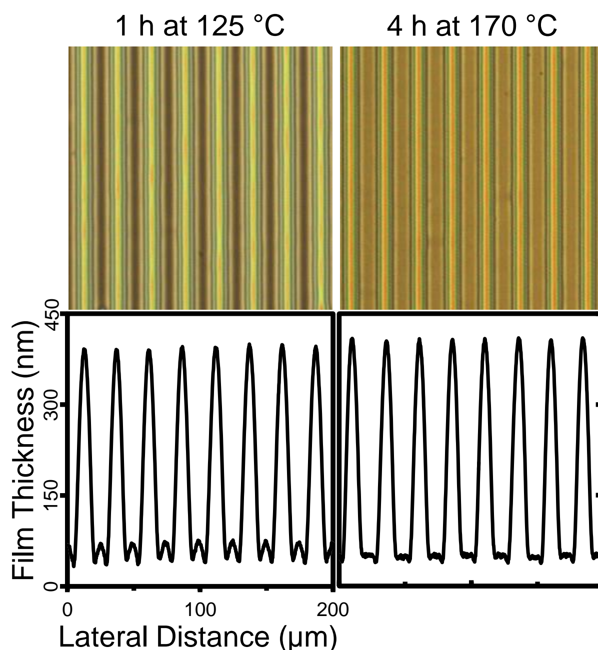

Figure 6.3: Representative 200 μm wide optical micrographs and height profiles of topographically patterned films prepared by the procedure defined by Figure 6.2. The left column depicts the samples after thermal development of photopatterned features. The right column depicts the samples after extensive thermal annealing. A crosslinking exposure was applied between these heating steps. The film thickness values have been set so that their mean matches the initial film thickness, 167 nm.

An example of a film processed this way using a photomask possessing a 25 μm pitch "line and space" pattern is shown in Figure 6.3. The various colors present in the optical micrograph are a consequence of the thickness variations constructively interfering with different wavelengths of reflected light. The exposed regions of the PiBMA blend film are a maximum of 350 nm thicker than the thinnest part of the unexposed regions, which greatly exceeds the thickness variations reported previously

using polystyrene films (< 120 nm).[17,20] Furthermore, the periodic height profile is not sinusoidal as it was in earlier work,[17,20] suggesting that different physical phenomena (i.e. not solely surface energy gradients) underlies its creation. Close inspection of this film with the optical microscope reveals no evidence of macroscopically large aggregates of BB being present in this film.[19] After the crosslinking photoexposure was applied, extended heating only resulted in a flattening of the thinnest regions and slight increase in peak film thicknesses. Dewetting is not present in these samples.

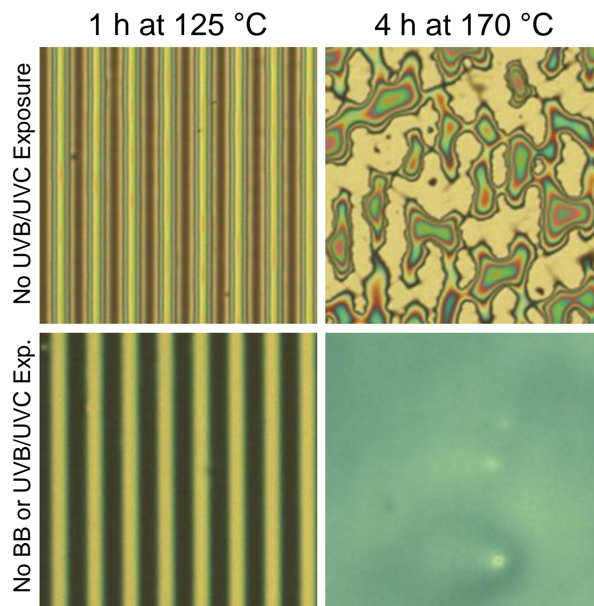

Figure 6.4: Representative 200 μm wide optical micrographs of PiBMA films prepared by procedure described by Figure 6.2, but with the crosslinking exposure step omitted. The upper row contained 10 wt. % BB and 2 wt. % MK and the lower row contained only 2 wt. % MK.

This result is contrasted by the films shown in Figure 6.4, which were not crosslinked after developing topographical features. A PiBMA film containing 10 wt. % BB and 2 wt. % MK becomes distorted due to uncontrolled dewetting after high

temperature annealing, and a PiBMA film containing only 2 wt. % MK dissipated back to its original thickness of 138 nm. The maximum thickness variations present in the latter film prior to dissipation are smaller (80 nm) than those in Figure 6.3.

6.3.2 Patterning Throughput and Aspect Ratio

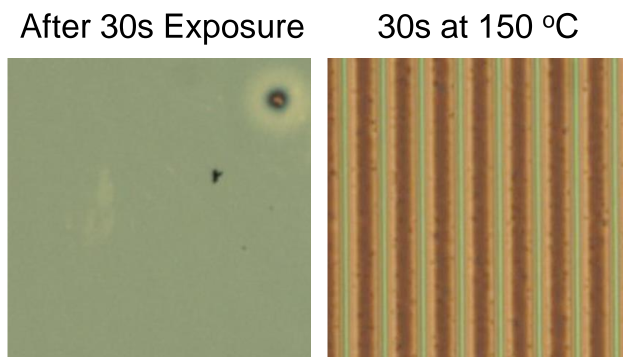

Figure 6.5: Representative 200 μm wide optical micrographs of a PiBMA film containing 2 wt. % MK and 10 wt. % BB after 30 seconds of photoexposure at an elevated intensity and b) after 30 seconds of subsequent heating at 150 °C.

Since this work is motivated in part by the need for more efficient light harvesting/transmitting devices, UV/Vis spectroscopy was performed on a 110 nm thick PiBMA film containing 10 wt. % BB and 2 wt. % MK. As shown in Figure E.1 of Appendix E, the light-absorbing dopants are bleached by photoexposure. After typical exposure conditions of 10 J/cm^2 (λ = 365 nm) and 16 J/cm^2 (UVB/UVC), film transmittance was higher than 99% for all light wavelengths greater than 345 nm. To show that the process throughput of this technique is potentially faster than the heating time used in Figure 6.3, a 142 nm thick PiBMA film containing 10 wt. % BB and 2 wt. % MK was processed at more aggressive conditions and the results are shown in Figure 6.5. Light was applied without any external filter with the smallest exposure distance

possible, such that a broadband dose of about 31 J/cm^2 was applied in 30 s of exposure time. The film was annealed at 150 ^oC for 30 s to yield a film possessing maximum film thickness variations of 260 nm.

Note that the feature height (350 nm) and periodicity (25 μm) demonstrated in Figure 6.3 differs from surfaces employed so far to improve solar cells and lighting. For example, the wrinkles in substrates employed by Loo and coworkers[1] had a periodicity of 1.8 μm and maximum thickness variation of 180 nm. The ridges of Bay et al.[2], defined by direct-writing laser lithography, had a 10 μm periodicity and a sharp 3 μm change in thickness. While different exposure conditions and film sensitivity could be employed to more closely duplicate their results, we note that the device properties of the films constructed here have yet to be measured.

6.3.3 Photochemical Conversion of Benzophenone Groups

It is well-established that irradiated benzophenones present in BB and MK can abstract hydrogen from polymer, generating a free-radical on each component, and graft to the abstraction site by radical-radical recombination.[10,19,21,22] This process of forming a polymer-benzophenone adduct is depicted in Figure 6.6. We anticipate this reaction to increase the surface energy of the PiBMA by replacing a ketone and C-H bond with a tertiary alcohol, a more polar group. Since BB contains two benzophenone groups, it is capable of two grafting reactions and can crosslink the host polymer by linking together many individual chains.[10,19] In contrast, MK possesses only one benzophenone group, and at low loadings does not crosslink PiBMA. Grafting of BB and MK to the PiBMA chain is also expected to raise its surface energy because these additives are more polar than the host polymer.

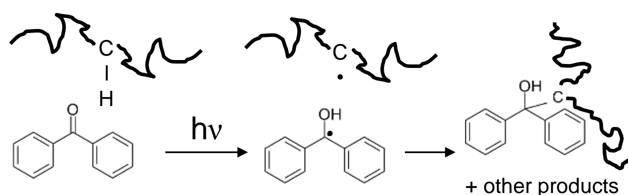

Figure 6.6: Grafting benzophenones to polymers by light irradiation.[11, 18-20]

UV/vis spectra of PiBMA, BB, and MK are shown in Figure 6.7. MK possesses a much stronger absorption (ε_{MK} = 2.9 × 10^3 m^2/mol) than BB (ε_{BB} = 7 m^2/mol) at the wavelength used for patterning, λ = 365 nm. At the wavelengths used for crosslinking (UVB/UVC), BB and MK absorb similarly. PiBMA is transparent relative to the two photosensitizers at all wavelengths as shown in Figure 6.7.

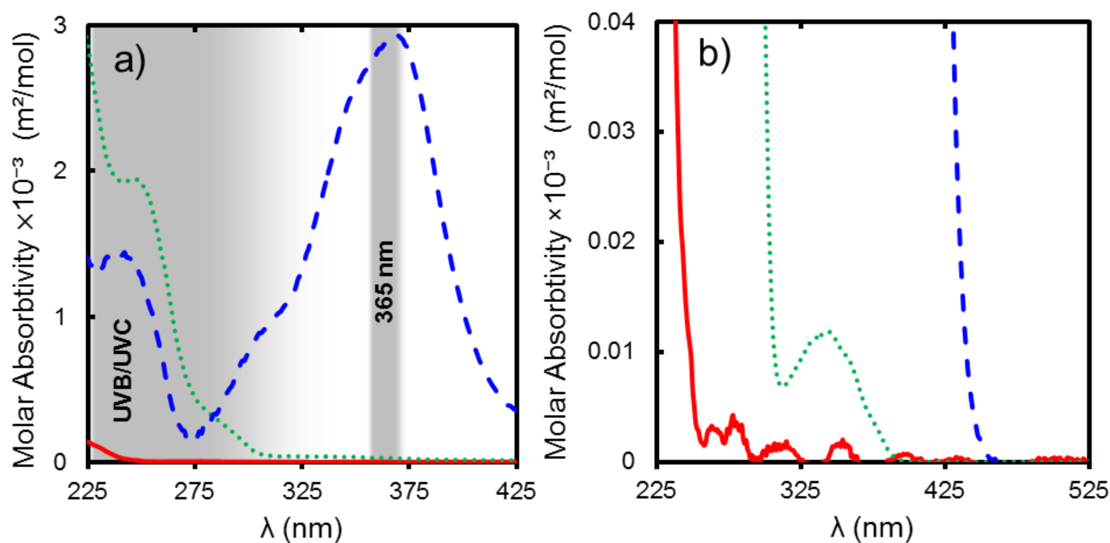

Figure 6.7: UV/Vis absorption spectra of PiBMA (solid line), MK (dashed line), BB (dotted line). ε was calculated on the basis of repeat unit molecular weight (PiBMA) or molecular weight per benzophenone group (MK and BB). PiBMA data represents an average of 3 films on quartz (thicknesses 1211, 990, and 781 nm). MK and BB were measured from methanol and tetrahydrofuran solutions, respectively, held in quartz cuvettes. The MK concentration was 4.6 × 10^{-4} mg/mL in a) and 2.345 × 10^{-2} mg/mL in b). The BB concentration was 3.6 × 10^{-3} mg/mL in a) and 1.65 mg/mL in b). Shaded regions in a) depict transmission bands of optical filters used to photopattern (365 nm) and crosslink (UVB/UVC).

Covalent grafting between MK and PiBMA was confirmed here by exposing films containing 2 wt.% MK to 20 J/cm^2 of light with λ = 365 nm, and passing an aliquot of redissolved films through a size exclusion chromatography column equipped with a fluorescence detector. As shown in Figure 6.8, material with excitation and emission characteristics possessed by MK, but not PiBMA, elutes at the same time as PiBMA, which confirms the presence of an MK/PiBMA adduct. Unexposed mixtures do not possess any fluorescence characteristic of MK at the elution time characteristic of PiBMA. Furthermore, the peak measured by the refractive index detector does not become broadened nor do new peaks appear due to exposure, indicating that PiBMA does not dimerize or undergo scission under these conditions.

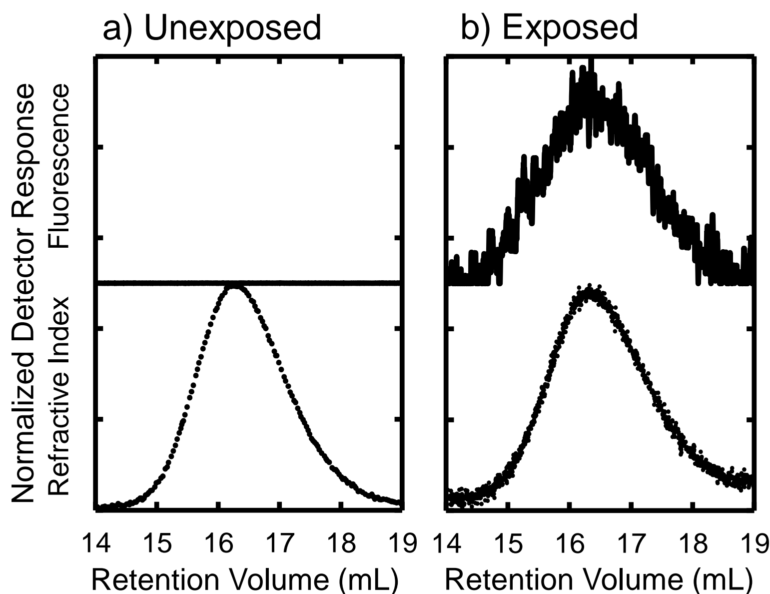

Figure 6.8: SEC chromatograms for PiBMA with 2 wt. % MK. a) is a directly injected solution and b) is composed of films that were exposed to 20 J/cm^2 of light with λ = 365 nm and re-dissolved. The fluorescence detector was operated with an excitation wavelength of 386 nm, and detected fluorescence emitted at λ = 457 nm.

In this section we seek to estimate how much MK and BB covalently grafts to PiBMA at the typical exposure conditions used for patterning, with the goal of learning how polymer molecular weight changes due to exposure. This exercise does not represent a comprehensive study of photogelation in benzophenone-containing polymer films; those efforts can be found in Refs. 19 and 22. A limited set of photochemical conversion and sol fraction data was collected using transmission FTIR spectroscopy and spectroscopic ellipsometry, respectively. It is shown in Figure 6.9 that conversion of benzophenone groups, p_{BB}, in films containing 10 wt. % BB increases monotonically with exposure to UVB/UVC light. A gel results after an exposure dose of 8 J/cm^2 UVB/UVC light; longer exposure times decrease the sol fraction, ω_s, as BB is more fully converted. Note that no coupling of PiBMA results from this exposure step in the absence of BB (see Figure E.2 of Appendix E).

In the glassy state, the dynamics of the spatial arrangement of polymer and benzophenone to configurations amenable to hydrogen abstraction and subsequent reaction steps are coupled to relaxations not well-described by a single exponential decay.[23,24] Unsurprisingly then, the rate of hydrogen abstraction in organic glasses is often not well described by first-order reaction kinetics possessing a single rate constant,[25] and neither are the photochemical conversion data in this work. Therefore to predict p_{BB} at higher and intermediate exposure doses (D_{UV}) we employed the dispersive kinetics model of Albery et al.,[26] which has been used before to describe the kinetics of triplet-state and ketyl radical decays of benzophenone in glassy polymers.[27] This model assumes that a ln-normal distribution of rate constants exists. The expression we used is

$$\boldsymbol{p_i = 1 - (\pi)^{-1/2} \int_{-\infty}^{+\infty} exp(-x^2)\, exp[-k_i \varepsilon_i D_{UV} exp(\gamma_i x)] dx}. \qquad (6.2)$$

where i refers to the species of interest, ε_i is its molar absorptivity, x is a transform variable, k_i is an average conversion efficiency, and γ_i describes the spread of its

distribution. A system possessing a broader rate constant distribution is described by higher γ and the conventional first order reaction kinetics possessing a single exponential decay is recovered for γ = 0. A quantum yield, defined as the molar ratio of reacted benzophenones to absorbed photons, can be determined by converting the units of k_i. By regressing Equation 6.2 to the experimental data $\varepsilon_{\mathrm{BB}}k_{BB}$ = 0.28 cm^2J^{-1} and γ_{BB} = 1.47 was found. We did not calculate k_{BB} here because $\varepsilon_{\mathrm{BB}}$ varies greatly over the broad transmission range of the UVB/UVC filter. This methodology provided good agreement with the data and was used to predict p_{BB} at higher and intermediate exposure doses.

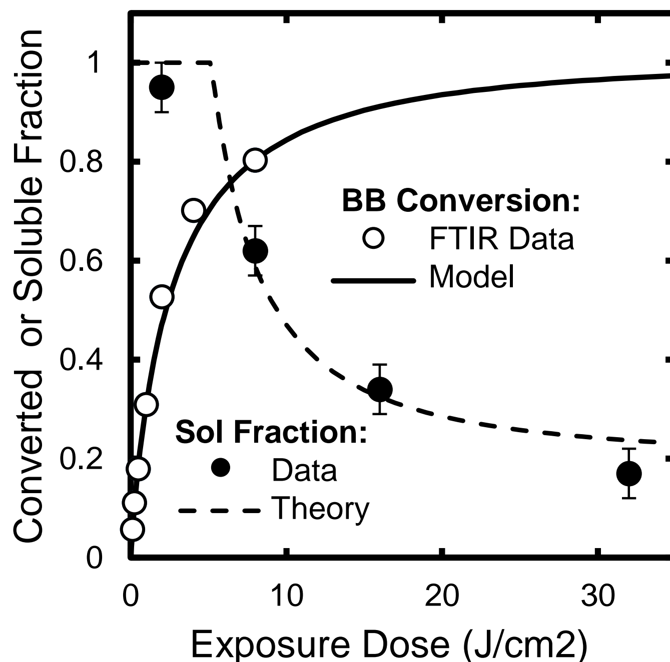

Figure 6.9: Benzophenone converted fraction and sol fraction for a PiBMA film containing 10 wt.% BB at different cumulative exposure doses of UVB/UVC light. The solid line depicts Equation 6.2 with $\varepsilon k_{\mathrm{BB}}$ = 0.28 cm^2J^{-1} and γ = 1.47 found by a regression. The dashed line depicts sol fraction predictions from an adaptation of Miller-Macosko theory[28,29] that includes a grafting efficiency, η_{eff} = 0.64, for photochemically activated benzophenone groups.

The sol data from Figure 6.9 is correlated to sol fractions predicted by the mean-field Miller-Macosko gelation theory.[28,29] The benzophenone conversions used in the gel theory were modified by a grafting efficiency prefactor, η_{eff}, which represents the likelihood of a converted benzophenone group grafting to a polymer chain. The result valid for stepwise coupling of BB possessing a functionality of 2 to PiBMA with a functionality of $N = 75$ is

$$\boldsymbol{\omega_s = (1 - \omega_{BB}) P(F_A^{out})^N + \omega_{BB}\left[\eta_{eff} p_{BB} P(F_A^{out})^{N-1}\right]^2}, \qquad (6.3)$$

where ω_{BB} is the weight fraction of BB in the film. The probabilistic parameter $P(F_A^{out})$ is determined as the root of

$$r\left(\frac{\eta_{eff} p_{BB}}{r}\right)^2 P(F_A^{out})^{N-1} - P(F_A^{out}) - r\left(\frac{\eta_{eff} p_{BB}}{r}\right)^2 + 1 = 0 \qquad (6.4)$$

where r = 15.2 is the initial ratio of PiBMA functional groups to BB functional groups. As shown in Figure 6.9, reasonable agreement between data and theory is achieved with only one adjusted parameter, $\eta_{\mathrm{eff}} = 0.64$. This value is slightly higher than the value of 0.5 ± 0.1 reported by Hayward and coworkers by a mean-field gelation model for PiBMA.[22] This analysis neglected chain scission because recent work has determined them to be low for reactions between benzophenone and alkyl methacrylates.[19,22] For example, Hayward and coworkers have reported grafting rates to be 100 times higher than chain scission for PiBMA possessing a fraction of benzophenone copolymerized into the chain as pendant groups.[22]

The decrease in characteristic IR absorbance peaks of BB and MK after exposure to λ = 365 nm light is shown in Figure 6.10a. Appendix E contains the full spectra and that for PiBMA films containing only BB or MK (see Figure E.3). Even in a ternary blend containing both BB and MK, each peak is clearly resolvable. The converted fraction of benzophenone in BB and MK at different cumulative exposure times is shown in Figure 6.10b. Similar conversion of MK is achieved whether BB is present or not. The

most interesting feature of Figure 6.9b is that, at the typical patterning dose of 10 J/cm^2, 66% of BB groups are converted despite its molar absorptivity being much lower than that of MK at this wavelength. Regression of Equation 6.2 to the two data points at 10 J/cm^2 using γ_{BB} = 1.47 and γ_{MK} = 3.42 suggest that the average quantum yield for benzophenone conversion of BB in PiBMA (0.56) is over 600 times greater than that for MK (8.7×10^{-4}) , overwhelmingly due to the similar conversions possessing an absorbance mismatch ($\varepsilon_{MK} = 414\varepsilon_{BB}$ at λ = 365 nm). While we think this work represents the first comparison of benzophenone conversion rates for BB and MK in a PiBMA host polymer, note that Brown and Porter reported the hydrogen abstraction rate constant in cyclohexane of benzophenone to be over 400 fold higher than that of MK.[30] Also, Deeg et al. reported quantum yields for hydrogen abstraction of 0.41 ± 0.14 and 0.89 ± 0.09, acquired by different methods, for benzophenone co-cast with PiBMA.[31] Note that the high conversion of BB at λ = 365 nm could also be rationalized by electron-transfer from MK to BB, a process that would require close proximity of the two components. That effect was neglected in the above discussion because MK and BB are relatively dilute and assumed to be distributed nearly homogeneously in the spin-coated, vitrified film.

The most important conclusion from Figure 6.10 is that the BB conversion lies very near the threshold of gelation at the typical patterning dose. This undoubtedly contributes to the features in the upper row of Figure 6.4 becoming distorted and not dissipating after extended heating. The film regions that were exposed to λ = 365 nm light contain highly branched and entangled PiBMA into which unexposed PiBMA can flow or diffuse into, but not readily relax back to a flat film.

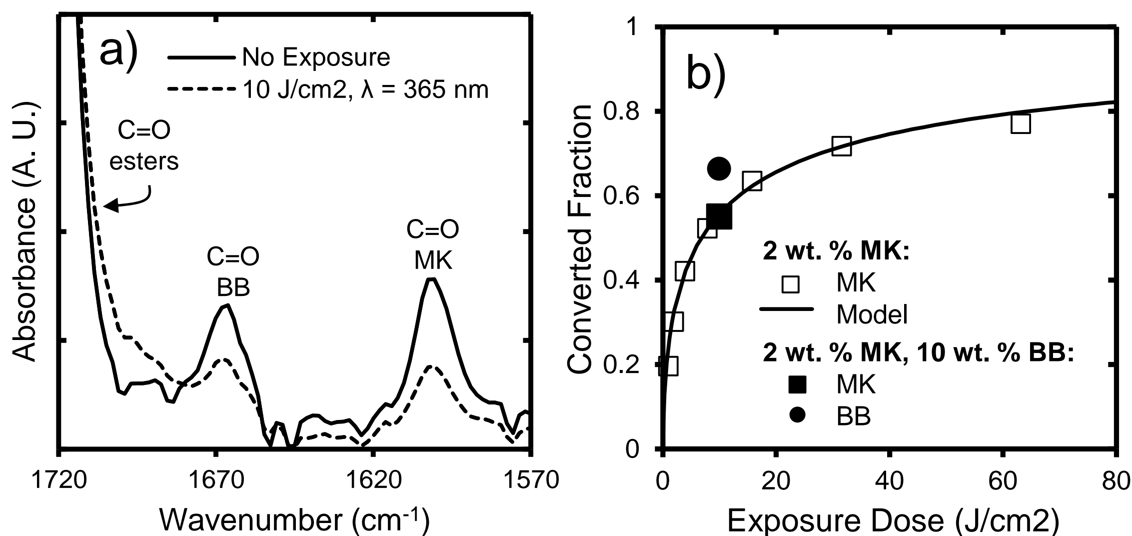

Figure 6.10: Conversion of BB and MK by exposure to λ = 365 nm light. a) Representative IR absorbance spectra for a PiBMA film containing 2 wt. % MK and 10 wt. % BB and b) converted fraction of BB and MK at different cumulative doses. The solid line depicts Equation 6.2 with k_{MK} = 3 × 10^{-9} mol/J and γ = 3.42 found by a regression.

6.3.4 Factors Contributing to Feature Formation

It is clear from the above analysis that molecular weight increases due to exposure contribute to the thickness profile shown in Figure 6.3. Like the process described by Ubukata and coworkers,[13,32] film thickness variations could result from unexposed, low molecular weight polymer diffusing into the exposed regions much faster than the exposed, high molecular weight polymer redistributes back into the unexposed regions.[32] To further investigate key mechanistic characteristics that cause topography to develop, a film composition in which molecular weight does not increase significantly due to exposure was investigated (No BB).

A 324 nm thick PiBMA film containing 2 wt. % MK was patterned according to the same conditions in Figure 6.4. The film thickness variations were examined at different cumulative heating times at 125 ^{o}C and are shown in Figure 6.11. At all heating times the examined thickness profile was sinusoidal and the feature periodicity matched

that of the photomask. The maximum variation in film thickness, 168 nm, is reached after 35 min of annealing. This corresponds to transport of 33% of the volume of unexposed regions into the exposed regions. It is possible to estimate a characteristic timescale for diffusion between exposed and unexposed regions, $\tau = H^2(4D)^{-1}$, based on the half-pitch of the photomask, H = 12.5 µm, and a self-diffusion coefficient, $D = 5 \times 10^{-11}\ cm^2s^{-1}$. As described in Appendix E, D is estimated using the Rouse model for unentangled polymers and rheology data (see Figure E.5). D estimated by this method compares well to directly measured values.[14] Based on these values, τ = 130 min is obtained, which is a factor 3.7 times greater than the annealing time necessary to develop maximum features. The characteristic diffusion timescale is commensurate with the decay of film thickness variations, which suggests that diffusion is not the physical transport mechanism that creates them.

It is also difficult to ascribe the movement of 33% of film volume in photopatterned PiBMA films containing 2 wt. % MK to differences in diffusivity because changes to molecular weight and T_g are vanishingly small or non-existent relative to the experimentally observed magnitude of melt state transport. Recall from Figure 6.8 that PiBMA films containing 2 wt. % MK do not undergo scission or coupling due to exposure to 10 J/cm^2 of light with λ = 365 nm. Furthermore, only a 0.05 % increase in average molecular weight for the blend can be anticipated due to grafting of MK to PiBMA under these conditions. To probe for potential changes to polymer mobility that could lead to differences in diffusivity, the T_g of a PiBMA film containing 2 wt. % MK was measured before and after exposure to 10 J/cm^2 of light with λ = 365 nm by variable-temperature spectroscopic ellipsometry. As shown in Figure E.4 in Appendix E, these values are identical within uncertainty, and they agree with the bulk DSC value within 2 ^oC.

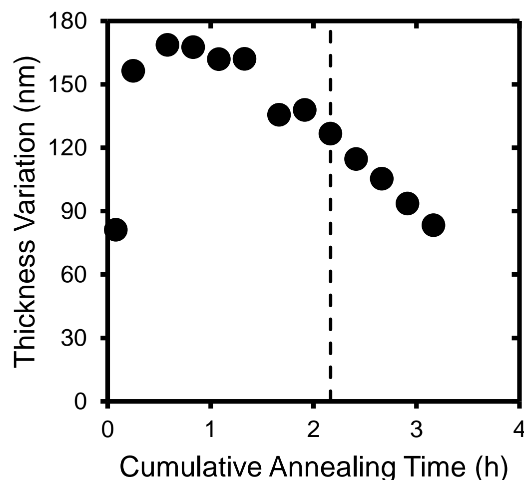

Figure 6.11: Thickness variations of a PiBMA film containing 2 wt. % MK at different cumulative heating times. The samples were photopatterned by the same conditions used in Figure 6.4 and then heated at 125 ^{o}C. The dashed line indicates τ = 130 min.

An additional, distinct factor is that variations in surface energy due to exposure could contribute to feature formation due to the Marangoni effect, a transport mechanism based on convection due to surface energy gradients.[17] The grafting reaction shown in Figure 6.6 as well as potential side products like hydroperoxides are expected to raise the surface energy of the exposed regions.[33] To demonstrate broadly that hydrophobic polymers possessing grafted MK have higher surface energies relative to their unmodified counterparts, polystyrene, poly(cyclohexylethylene), and poly(vinylidene fluoride-*co*-trifluoroethylene) films were coated with MK and irradiated with λ = 365 nm light. After stripping ungrafted MK, all polymers that had been coated by MK and irradiated possessed significantly lower water contact angles (10° – 29°) than did uncoated films that had been irradiated under identical conditions. Also, films which had been coated by MK, but not exposed before removing MK, possessed the same water contact angle as the neat polymer films. The decrease in water contact angle for coated

and exposed films demonstrates an increase in polarity and hydrophilicity that is consistent with an increase in surface energy for these hydrophobic polymers. Complete experimental details, micrographs of the films, and full water contact results are provided as Appendix E (see Figure E.6).

At exceedingly long annealing times, film features dissipate due to the photochemically directed surface energy gradient being erased by interdiffusion. The need to elucidate the complex relationship between Marangoni flow, interdiffusion, and thermo-capillary forces beyond this qualitative description has motivated an ongoing collaborative effort to develop and validate a quantitative theoretical model.[34] Note that while the film thickness variations possessed by the film used in Figure 6.3 are about twice as large as those shown in the lower row of Figure 6.4, the former film possesses about a six-fold higher total photosensitizer content.

6.3.5 Directing the Morphology of a Structured Overlayer

Because light harvesting/emitting devices are multilayered in construction, we spin coated and thermally annealed a polymer overlayer onto a topographically patterned film to demonstrate its thermochemical stability. A 300 nm thick PiBMA film containing 5% MK and 10% BB was exposed (16 J/cm^2, 365 nm) through a 200 μm pitch line and space mask and annealed at 120 ^{o}C for 1 h to yield a regular array of ridges. A 1250 J/cm^2 blanket exposure using broadband light (no external filter) crosslinked the film, which remained affixed to the substrate after repeated washings with a good solvent, tetrahydrofuran. A representative micrograph of the film region that had been exposed during patterning is shown in Figure 6.12a and a representative height profile is shown in Figure 6.12c. In the height profile, the thickness in the middle of the exposed regions has been set to 130 nm.

An overlayer of block copolymer was spin coated from amyl acetate onto the topographical pattern under the same conditions that yielded a thickness of 66 nm on a bare silicon wafer (3 wt. %, 3000 RPM). The overlayer is a lamella-forming, symmetric poly(styrene-*block*-trimethylsilylstyrene) (PS-b-PTMSS) with a bulk domain periodicity, L_0, of 27 nm. A representative optical micrograph of this film is shown in Figure 6.12b and a representative height profile is shown in Figure 6.12c. The topographically patterned height profile of the underlayer obstructs centrifugal thinning near ridges during spin coating and thus introduces significant local increases in the overlayer thickness, ℓ_{BCP}. In the height profile, all thickness values have been shifted equally upward such that $\ell_{BCP} = 66$ nm in the middle of the exposed regions. Nearer to the ridges, ℓ_{BCP} is significantly thicker. This film was annealed at 160 ^{o}C for 1 h, and a representative micrograph is shown in Figure 6.12d. Quantized height variations develop after annealing, which are unambiguously visible as sharp changes in the optical interference color. Their significance is described below within the context of block copolymer self-assembly.

Lamella-forming block copolymers placed atop substrates preferentially wetted by one block self-assemble during annealing to form μm-scale structures with distinct morphologies prescribed by the initial film thickness. This "hole and island" phenomenon was discovered by Russell and coworkers,[35] and its practical utility is discussed in depth within Refs.[36-38] Experiments on flat films confirmed that the PS block of the PS-b-PTMSS overlayer preferentially wets the crosslinked PiBMA substrate, and we assume that the low surface energy PTMSS block segregates to the air interface. As a consequence, PS-b-PTMSS will self-assemble into half-integer ($n + ½$) multiples of L_0. To accommodate this constraint, sample regions where $(n + ½)L_0 < \ell_{BCP} < nL_0$ will form small "islands" L_0 thicker than its surroundings after annealing; sample regions where

$nL_0 < \ell_{BCP} < (n + ½)L_0$ will form small "holes" L_0 thinner than its surroundings after annealing. For reference, this concept is represented graphically in Figure E.7 of the Appendix E.

Hole/Island morphologies are present in Figure 6.12d, where the dark orange interference color represents an overall film thickness L_0 thicker than the light orange interference color. Dark orange islands are labeled within regions that possessed $3.5L_0 < \ell_{BCP} < 4.0L_0$ prior to self-assembly; light orange holes are labeled within regions that possessed $4.0L_0 < \ell_{BCP} < 4.5L_0$ prior to self-assembly. In contrast to the holes *or* islands which are generated uniformly across flat, chemically homogeneous substrates, the photochemically directed surface topology of the crosslinked underlayer has prescribed the placement of regions containing islands *and* regions containing holes simply by modulating ℓ_{BCP}. While this example was not commercially-motivated, it demonstrates clearly that the methodology described in this work can produce a robust and stable underlayer onto which overlayers can be deposited via established process steps.

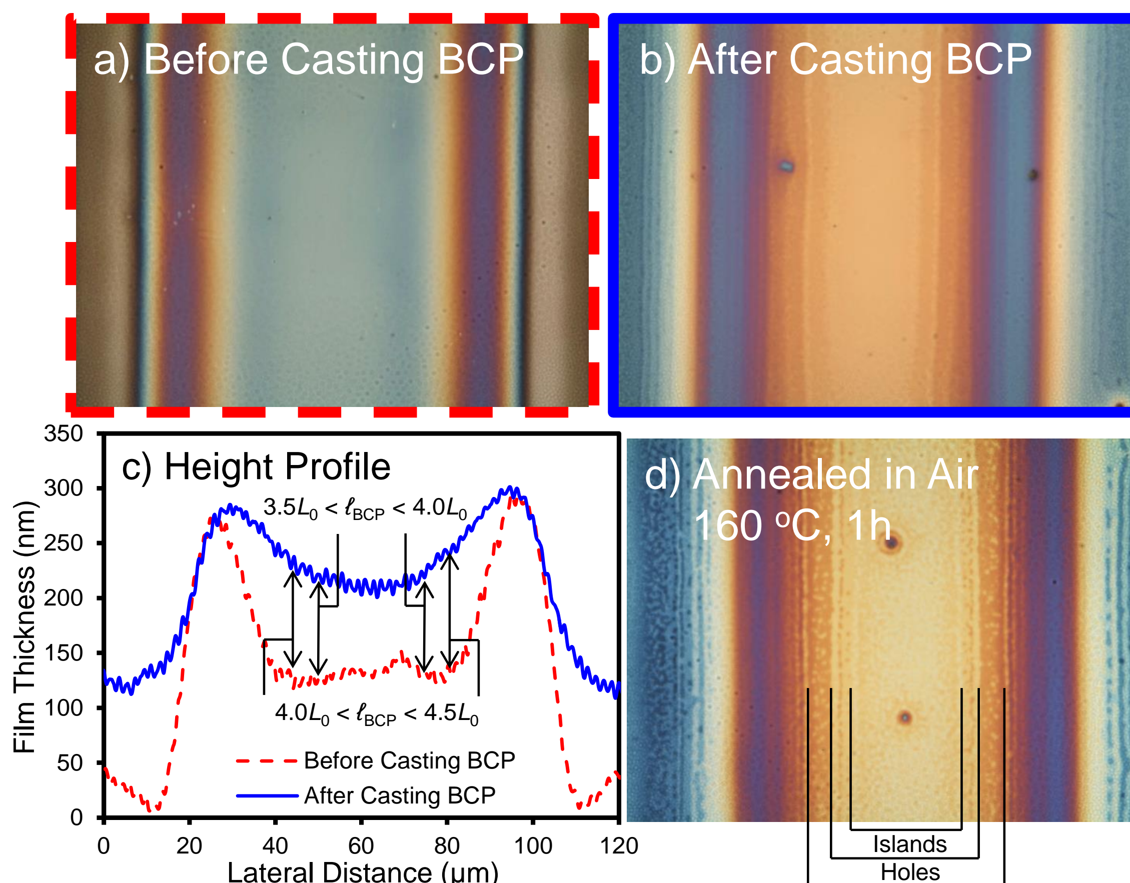

Figure 6.12: Thermochemically stable topographical features directed the morphology of an inherently structured overlayer. 120 μm wide optical micgrographs of the starting topography, the film after coating with a block copolymer (BCP) overlayer, and the film after annealing are shown in parts a), b), and d), respectively. The thickness profile of the film before and after coating with BCP is shown in part c). All data is representative and does not correspond to identical sample regions.

6.4 CONCLUSIONS

Here a method of prescribing melt-state transport in a thin polymer film using photosensitizers was described, which generates a smoothly varying thickness profile. These films were made thermochemically stable by completely activating a photosensitive crosslinker. While BB was added to PiBMA films to stabilize the features generated by MK, the results in this work clearly demonstrate that it is challenging to

independently activate these photosensitizers even when their absorption spectra differ significantly, due to the much higher quantum yield of BB. Because the films possess good transparency and the ability to serve as an underlayer in a multilayered film, we think the process complements emerging strategies to improve the efficiency of light harvesting/transmitting devices by employing topographical features.[1-3] It is likely that the generic procedure could be tailored to specific applications by substituting other polymers and photosensitizers for PiBMA and BB, if necessary. A block copolymer overlayer was spin coated directly onto crosslinked topographical features to provide a demonstration of their stability. The thickness variations in the annealed BCP overlayer caused the parallel-oriented microdomains to self-assemble into discrete regions containing macroscopic "islands" and regions containing macroscopic "holes".

6.5 REFERENCES

1. Kim, J. B.; Kim, P.; Pegard, N. C.; Oh, S. J.; Kagan, C. R.; Fleischer, J. W.; Stone, H. A.; Loo, Y.-L. *Nat. Photon.* **2012,** 6, 327-332.
2. Bay, A.; André, N.; Sarrazin, M.; Belarouci, A.; Aimez, V.; Francis, L. A.; Vigneron, J. P. *Opt. Express* **2013,** 21, A179-A189.
3. Koo, W. H.; Jeong, S. M.; Araoka, F.; Ishikawa, K.; Nishimura, S.; Toyooka, T.; Takezoe, H. *Nat. Photon.* **2010,** 4, 222-226.
4. Park, B.; Jeon, H. G. *Opt. Express* **2011,** 19, A1117-A1125.
5. Carman, M. L.; Estes, T. G.; Feinberg, A. W.; Schumacher, J. F.; Wilkerson, W.; Wilson, L. H.; Callow, M. E.; Callow, J. A.; Brennan, A. B. *Biofouling* **2006,** 22, 11-21.
6. Zhao, Y.; Xie, Z.; Gu, H.; Zhu, C.; Gu, Z. *Chem. Soc. Rev.* **2012,** 41, 3297-3317.
7. Aubin, H.; Nichol, J. W.; Hutson, C. B.; Bae, H.; Sieminski, A. L.; Cropek, D. M.; Akhyari, P.; Khademhosseini, A. *Biomaterials* **2010,** 31, 6941-6951.
8. Perera-Costa, D.; Bruque, J. M.; González-Martín, M. L.; Gómez-García, A. C.; Vadillo-Rodríguez, V. *Langmuir* **2014**.
9. Oster, G.; Oster, G. K.; Moroson, H. *J. Polym. Sci.* **1959,** 34, 671-684.
10. Carroll, G. T.; Sojka, M. E.; Lei, X.; Turro, N. J.; Koberstein, J. T. *Langmuir* **2006,** 22, 7748-7754.
11. Carroll, G. T.; Turro, N. J.; Koberstein, J. T. *J. Colloid Interface Sci.* **2010,** 351, 556-560.
12. Carroll, G. T.; Devon Triplett, L.; Moscatelli, A.; Koberstein, J. T.; Turro, N. J. *J. Appl. Polym. Sci.* **2011,** 122, 168-174.

13. Ubukata, T.; Yamamoto, S.; Moriya, Y.; Fujii, S.; Yokoyama, Y. *J. Photopolym. Sci. Technol.* **2012,** 25, 675-678.
14. Katzenstein, J. M.; Janes, D. W.; Hocker, H. E.; Chandler, J. K.; Ellison, C. J. *Macromolecules* **2012,** 45, 1544-1552.
15. Maher, M. J.; Bates, C. M.; Blachut, G.; Sirard, S.; Self, J. L.; Carlson, M. C.; Dean, L. M.; Cushen, J. D.; Durand, W. J.; Hayes, C. O.; Ellison, C. J.; Willson, C. G. *Chem. Mater.* **2014,** 26, 1471-1479.
16. Hall, D. B.; Underhill, P.; Torkelson, J. M. *Polym. Eng. Sci.* **1998,** 38, 2039-2045.
17. Katzenstein, J. M.; Janes, D. W.; Cushen, J. D.; Hira, N. B.; McGuffin, D. L.; Prisco, N. A.; Ellison, C. J. *ACS Macro Lett.* **2012,** 1, 1150-1154.
18. National Institute of Advanced Industrial Science and Technology. Spectral Database for Organic Compounds. http://sdbs.riodb.aist.go.jp/sdbs/
19. Carbone, N. D.; Ene, M.; Lancaster, J. R.; Koberstein, J. T. *Macromolecules* **2013**.
20. Janes, D. W.; Katzenstein, J. M.; Shanmuganathan, K.; Ellison, C. J. *J. Polym. Sci., Part B: Polym. Phys.* **2013,** 51, 535-545.
21. Prucker, O.; Naumann, C. A.; Rühe, J.; Knoll, W.; Frank, C. W. *J. Am. Chem. Soc.* **1999,** 121, 8766-8770.
22. Christensen, S. K.; Chiappelli, M. C.; Hayward, R. C. *Macromolecules* **2012,** 45, 5237-5246.
23. Inoue, T.; Cicerone, M. T.; Ediger, M. D. *Macromolecules* **1995,** 28, 3425-3433.
24. Cicerone, M. T.; Blackburn, F. R.; Ediger, M. D. *Macromolecules* **1995,** 28, 8224-8232.
25. Siebrand, W.; Wildman, T. A. *Acc. Chem. Res.* **1986,** 19, 238-243.
26. Albery, W. J.; Bartlett, P. N.; Wilde, C. P.; Darwent, J. R. *J. Am. Chem. Soc.* **1985,** 107, 1854-1858.
27. Levin, P. P.; Khudyakov, I. V. *J. Phys. Chem. A* **2011,** 115, 10996-11000.
28. Macosko, C. W.; Miller, D. R. *Macromolecules* **1976,** 9, 199-206.
29. Miller, D. R.; Macosko, C. W. *Macromolecules* **1976,** 9, 206-211.
30. Brown, R. G.; Porter, G. *J. Chem. Soc., Faraday Trans. 1* **1977,** 73, 1569-1573.
31. Deeg, F. W.; Pinsl, J.; Braeuchle, C. *J. Phys. Chem.* **1986,** 90, 5715-5719.
32. Ubukata, T.; Moriya, Y.; Yokoyama, Y. *Polym. J.* **2012,** 44, 966-972.
33. Millan, M. D.; Locklin, J.; Fulghum, T.; Baba, A.; Advincula, R. C. *Polymer* **2005,** 46, 5556-5568.
34. Arshad, T.; Kim, C. B.; Prisco, N. A.; Katzenstein, J. M.; Janes, D. W.; Bonnecaze, R. T.; Ellison, C. J. *Soft Matter* **2014**, 10, 8043-8050.
35. Russell, T. P.; Coulon, G.; Deline, V. R.; Miller, D. C. *Macromolecules* **1989,** 22, 4600-4606.
36. Mansky, P.; Russell, T. P.; Hawker, C. J.; Pitsikalis, M.; Mays, J. *Macromolecules* **1997,** 30, 6810-6813.
37. Peters, R. D.; Yang, X. M.; Kim, T. K.; Sohn, B. H.; Nealey, P. F. *Langmuir* **2000,** 16, 4625-4631.
38. Janes, D. W.; Thode, C. J.; Willson, C. G.; Nealey, P. F.; Ellison, C. J. *Macromolecules* **2013,** 46, 4510-4519.

Chapter 7: Marangoni Instability Driven Surface Relief Grating in an Azobenzene Containing Polymer Film

7.1 INTRODUCTION

A potentially related phenomenon that various research groups have reported independently is that azo-benzene containing polymers (azo-polymers), either linked to a polymeric chain or as part of azobenzene dye doped in a polymer matrix, can generate topography during light irradiation in the form of a crossed laser interference pattern.[1,2] The hypothesis tested in this chapter is that the underlying physio-chemical mechanism of this topography generation is due to migration of azo-benzene containing polymers by the Marangoni effect.

In 1995, the Natansohn[1] and Kumar[2] groups independently demonstrated that irradiating azobenzene-containing polymer (azo-polymer) films with a visible-light interference pattern can generate sinusoidal surface topography (also known as a surface relief grating; SRG). Such SRGs spontaneously form upon continuous light irradiation;[3] thus, the features constantly increase in height. Often times, the achievable feature heights in these systems are limited by the penetration depth of the pattern inscription light[4] or the total amount of available material in the polymer film.[5] The resulting pattern periodicities, typically 500-1000 nm, match the initial interference patterns[1] and height differences of 100-1000s nm have been produced,[1,2,5] corresponding to feature aspect ratios greater than 1 in some cases. Their findings generated worldwide research interest as a single step submicron-resolution patterning method not dependent on developing solvents, contact with masks, or etch procedures, which are generally required by other patterning methods such as photolithography or imprint lithography. Due to these advantageous processing characteristics, SRGs have been utilized for numerous target applications including directing block copolymer self-assemblies,[6,7] aligning colloidal

nanoparticles,[8] transferring patterns to different substrates,[9] rewritable holographic data storage,[10] photonic crystals,[11] among others.[12,13]

Despite the widespread success of a variety of applications, the SRG community has not yet accepted a general explanation of the underlying mechanism that produces these topographical patterns, which is discussed at length in several review articles.[3,14,15] Without a convincing description of the phenomena that enable SRG formation, researchers have been guided by empirical design principles. A shortcoming of many proposed explanations is that they cannot explain a relationship between a pattern inscription light field and the resulting flow directionality (i.e. either material accumulates in the illuminated regions or in the dark regions).[16]

Generally, it is accepted that light absorption produces a "photo-softened" transition in the film that allows for a macroscopic flow of polymer even at temperatures well below the glass transition temperature in some cases. Also, the interference pattern created by impinging light waves produces a maskless exposure pattern on the sample, causing some regions to be irradiated more intensely than others. A well-known photochemical transition of azo-polymers is the reversible *trans-cis* isomerization reaction. Importantly, the azobenzene isomerization in films can reversibly change liquid contact angles, consistent with altering surface energy, by changing the molecular orientation of different chemical substituents within and/or linked-to azobenzene.[17-20] One consequence of the patterned light irradiation is that a spatially patterned isomerization reaction can be anticipated to occur in the film, and thus there is the possibility for an associated spatially patterned surface tension.

Our study here aims to verify that azo-polymers flow towards regions of higher surface tension as dictated by the Marangoni effect, and by extension we propose that such surface tension-driven flow generally underlies the formation of SRGs in azo-

polymers. To critically assess our hypothesis, we synthesized and studied an amorphous poly(4-(acryloyloxyhexyloxy)-4'-pentylazobenzene) model polymer. In order to increase the rate of mass migration of the film materials (i.e. rate of SRG topography formation), azo-polymer with hexyl acrylate monomer was chosen to enhance translational mobility of the resulting azo-polymer with modest heating (i.e., this polymer has a low glass transition temperature). In addition, various studies have revealed that alkyl-substituted azobenzene side chains orient perpendicularly with respect to the substrate.[21-24] Intuitively, a uniformly oriented hydrophobic pendant substituent in a perpendicular orientation causes the maximum surface tension change upon photo-isomerization of azobenzene from *trans-* to the *cis*-form as molecular substituents are reoriented during isomerization. Thus, polymers possessing a pentyl substituted azobenzene side chain were chosen.

7.2 EXPERIMENTAL

7.2.1 Materials

4-Pentylaniline, phenol, acryloyl chloride, 6-chlorohexanol, hexyl acrylate and 2,2′-Azobis(2-methylpropionitrile) (AIBN) were purchased from Sigma-Aldrich. Polished 4 in. diameter silicon wafers were purchased from University Wafer and quartz plates were purchased from Chemglass. All other chemicals used in this study were purchased from Fisher Scientific or Sigma-Aldrich, and used as received unless otherwise noted.

7.2.2 Synthesis of 4-(acryloyloxyhexyloxy)-4′-pentylazobenzene (5Az6A)

4-(Acryloyloxyhexyloxy)-4′-pentylazobenzene (5Az6A) was prepared following a previously published procedure.[25] Briefly, diazotization of *p*-pentylaniline occurred through reaction with sodium nitrite under acidic conditions, generating a diazonium salt

which was immediately added to phenoxide (Figure 7.1). This generated, after acidification, 4′-pentylphenylazophenol **1**. Chain extension was then accomplished by addition of 6-chlorohexan-1-ol under basic conditions. Reaction of 4-(hexyloxy)-4′-pentylazobenzene **2** with acryloyl chloride allowed for the formation of the targeted monomer 4-(acryloyloxyhexyloxy)-4′-pentylazobenzene (5Az6A).

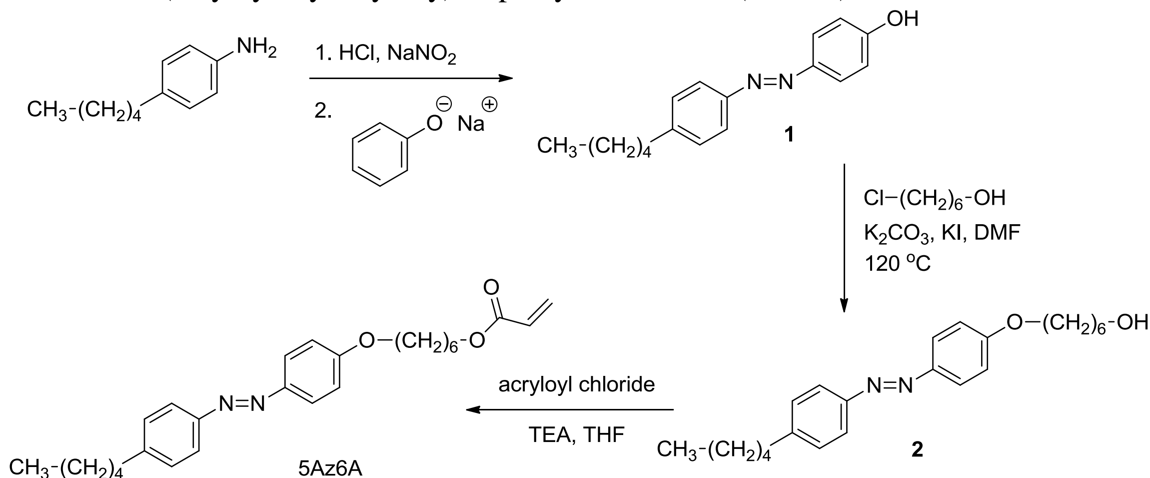

Figure 7.1: Synthesis of 5Az6A monomer.

7.2.3 Polymerization and Polymer Characterization

A conventioanl free radical polymerization was adapted to synthesize the poly(4-(acryloyloxyhexyloxy)-4’-pentylazobenzene) (P5Az6A) as shown in Figure 7.2. 5Az6A (2.0 g, 4.7 mmol) and AIBN (100 mg, 0.5 wt % of the total monomer) were dissolved in dry anisole (10 mL) in a round-bottomed flask. After the flask was sealed and sparged with dry argon for 30 min, the reaction was allowed to proceed for 16 h at 80 °C. The resulting polymer (P5Az6A) was precipitated from methanol and then dried at 40 °C under vacuum to remove residual solvents. The dried polymer was then redissolved and freeze-dried out of benzene.

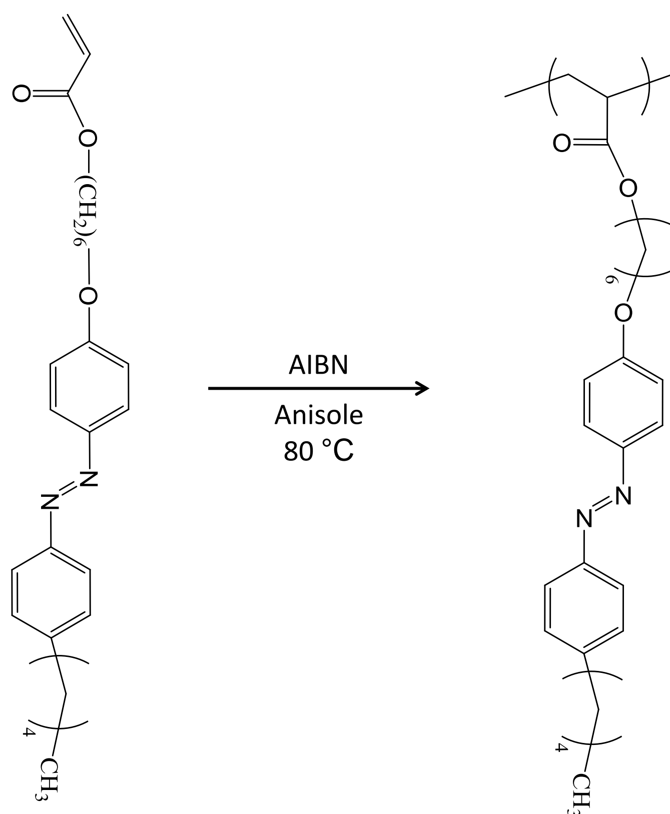

Figure 7.2: Synthesis of poly(4-(acryloyloxyhexyloxy)-4'-pentylazobenzene).

The dried polymer, P5Az6A (Mn = 12.8 kDa, Đ = 1.2, relative to PS standards), was characterized by size exclusion chromatography and ^{13}C NMR spectroscopy. Size exclusion chromatography (SEC) measurements were performed using a Viscotek VE 2001 triple-detector SEC module possessing two I-Series mixed bed low MW columns. Tetrahydrofuran (THF) was used as the eluent at a flow rate of 1.0 mL/min. Samples were dissolved in THF and filtered through a 0.20 μm PTFE filter before injection. ^{13}C-NMR was used to confirm the structure of the azobenzene side chain in the synthesized polymer, P5Az6A. Approximately 100 mg/mL of the azobenzene polymer was dissolved in deuterated chloroform ($CDCl_3$), and the data was collected on an Agilent INOVA-500 NMR. The sample was run with a 15 second relaxation delay at a 90 degree pulse angle for 1000 repetitions. The spectrum is shown in Figure 7.3. All 26 carbons in the repeat

unit are accounted for, and the integration is shown where possible. The ester carbon and the tertiary backbone carbon were not integrated because of low signal-to-noise ratio, but they are indicated on the spectrum.

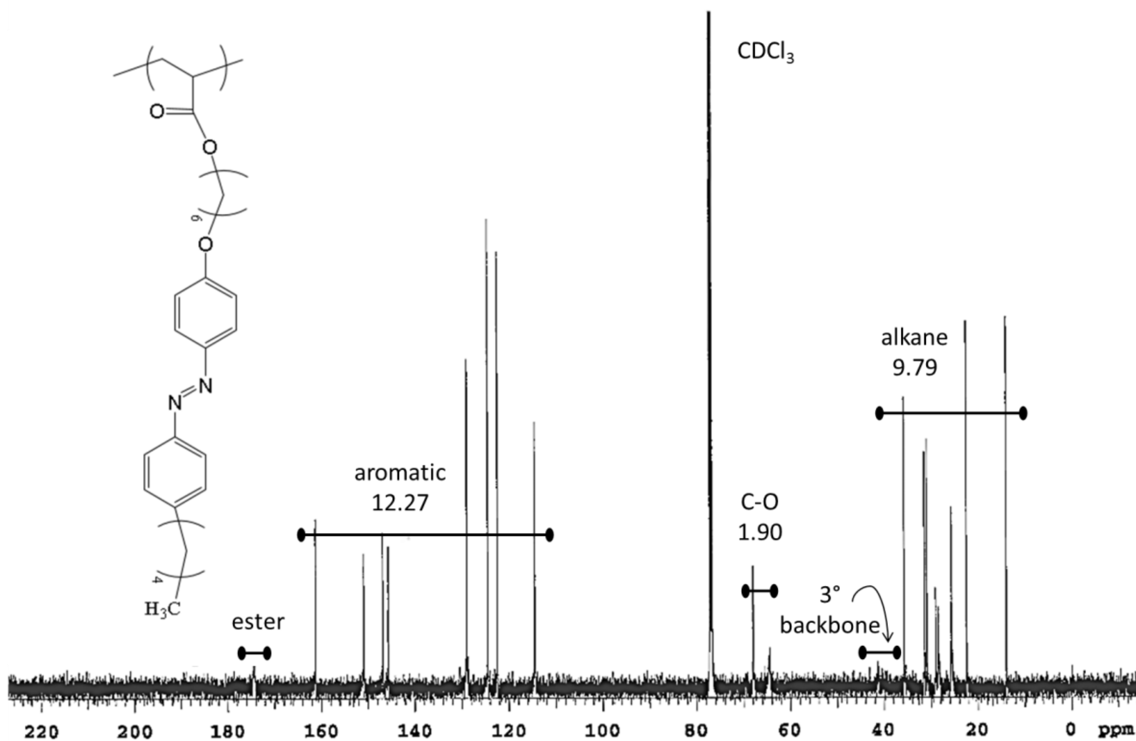

Figure 7.3: ^{13}C-NMR of the dried P5Az6A.

The glass transition temperature of the bulk polymer sample was measured by differential scanning calorimetry (DSC) using a Mettler-Toledo DSC-1 with a 10 °C/min heating rate upon second heating. The polymer used here is completely amorphous as confirmed by DSC and cross-polarized optical micrographs.

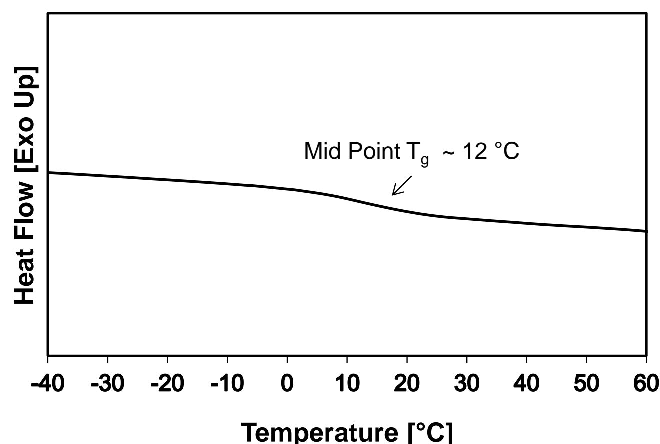

Figure 7.4: DSC thermogram of P5Az6A taken upon the second heating at a rate of 10 °C/min showing a Tg of 12 °C.

7.2.4 Film Preparation

Films in this study were spin-coated (Specialty Coating Systems Spincoat G3-8) onto silicon or quartz substrates. Spin coating solutions (3 - 5 wt% polymer in THF) and spin speeds (1000 – 1500 RPM) were varied to control the film thickness. Residual solvent was removed from the films by placing them in a vacuum chamber at 25 °C for at least 90 minutes; longer annealing times did not further reduce the film thickness. The thicknesses of films prepared on silicon substrates were measured using a J.A. Woollam M-2000D spectroscopic ellipsometer using wavelengths from 500 to 984 nm with a 65° angle of incidence. The thicknesses of films prepared on quartz substrates were assumed to be equal to identically prepared films on silicon wafers.

7.2.5 Topography Formation and Characterization

In order to prescribe patterned light exposure onto the polymer film surface, the spin coated films were exposed to light through various photomasks (Edmunds Optics). A broadband microscope illuminator (Optical Building Blocks ScopeLite 200) with output wavelength ranges from 300 − 800 nm was used. The optical bandpass filters

(Edmund Optics) used to select wavelengths of 365 and 450 nm both possessed 10 nm full-width/half-maximum. The exposure stage was held at - 20 °C by an Instec mK 1000 temperature controller with a HCS-402 stage to retain a solid, glassy state film during exposure, unless otherwise noted. Light exposures were conducted through a quartz topped chamber purged continuously by dry N_2 gas to prevent water condensation from the cryogenic temperatures. To prevent pattern transfer from the mask onto the liquid polymer film, a spacer between the polymer film surface and the photomask was set to maintain ca. 200 nm gaps between them. The spacer used here was prepared by spincoating PS film (200 nm thick) on a silicon substrate. Light intensity was measured using a Radiometer Fieldmax TO (Coherent) thermopile. A 20 mm working distance was used with a light intensity of 41 mW/cm^2 and 10 mW/cm^2 for 365 and 450 nm filters, respectively. The typical light exposure time was 30 sec for both optical filters. Topographic features were developed by a room-temperature annealing step performed in the absence of light.

7.2.6 Film Characterization

Background-subtracted UV/Vis absorbance spectra of quartz-supported films were acquired with a Thermo Scientific Evolution 220 UV-Visible Spectrophotometer. Background-subtracted transmission mode FTIR absorbance spectra were acquired on a Nicolet 6700 FTIR spectrometer (Thermo Fisher Scientific) using the associated OMNIC software. These films were supported by a double-side polished, high-resistivity Si wafer. 200 scans with a resolution of 4 cm^{-1} were averaged. All spectra were normalized by the ester peak areas (1720 – 1770 cm^{-1}) since these are only present in the polymer repeat units.

Bright field optical micrographs were taken using an Olympus BX 60 microscope with a Spot Insight QE camera. The feature heights were characterized at ambient

temperature and pressure using an AC mode atomic force microscope (AFM, Asylum Research). AFM tips with a resonant frequency of 320 kHz and a force constant of 42 N/m were purchased from Nanosensors.

Static water contact angles were measured on a Rame-Hart Model 100-00 goniometer and the accompanying DROPimage software. Samples were thoroughly rinsed with deionized water and blown dry with filtered air. A 6 µL drop of deionized water was placed on the sample, and the stage was leveled, at which point the real-time image was frozen and the contact angles on the left and right side of the drop were determined. The image was collected within 5 s of placing the drop on the sample. Between measurements the sample was blown dry with filtered air.

7.3 RESULTS AND DISCUSSION

Amorphous poly(4-(acryloyloxyhexyloxy)-4’-pentylazobenzene) (P5Az6A, M_n = 12.8 kDa, Đ = 1.2, relative to PS standards) was synthesized via conventional free radical polymerization using azobisisobutyronitrile (AIBN) as the initiator (see Figures 7.1-7.3). The polymer was then spin-coated from tetrahydrofuran (4 wt % total solids) onto a Si wafer. Since the polymer is a liquid at room temperature (T_g =12 °C, differential scanning calorimetry (DSC); see Figure 7.4), the polymer spontaneously rearranges into the preferred conformation after sufficient room temperature annealing (ca. 1 hr at 25 °C; see Figures F.1 and F.2 in Appendix F). Upon annealing, the azobenzene side chain adopted a homeotropic orientation (i.e. perpendicular to the substrate), causing the side chain pentyl groups to wet the free interface.[21-24] A discussion and spectral evidence of perpendicular side-chain orientation of the polymer used in this study is provided in Supporting Information (see Figures F.1 and F.2 in Appendix F).

A schematic describing how the side chain orientation affected the surface tension is shown in Figure 7.5. A water droplet on top of the *trans*-azo-polymer surface yields a

contact angle of 95°, corresponding to a hydrophobic surface. A 365 nm UV exposure photoisomerized the azo bonds from the *trans*- to the *cis*-form, greatly reducing the water contact angle by 12°, indicating the film possessed higher surface tension. A subsequent 450 nm light exposure (or thermal annealing) reverts *cis*-isomers back to *trans*-isomers, with reversibility over at least 4 cycles (see Figure F.3 in Appendix F).

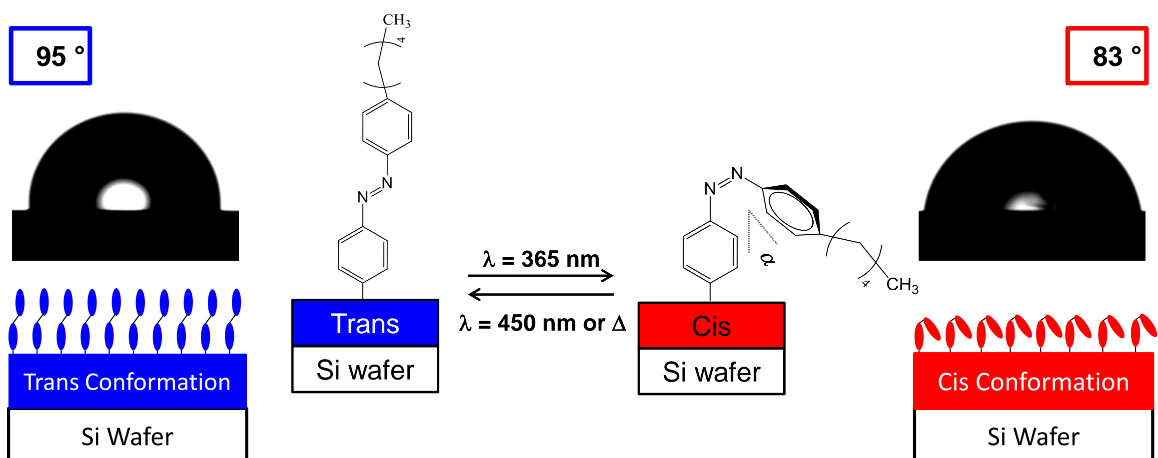

Figure 7.5: Schematic describing photochemical conformation changes and corresponding changes in the films' water contact angle (boxed values). A lower contact angle corresponds to a higher surface tension. α indicates the molecular angle of the cis-isomer.

Flood irradiation of the film with UV light (λ = 365 nm, 1.2 J/cm^2) converted *trans*-isomers to the *cis*-form. This photo-isomerization was confirmed using UV-vis and Fourier transform infrared (FTIR) spectroscopy. As Figure 7.6a illustrates, the characteristic absorption of the *trans*-isomer at a wavelength of 347 nm was reduced while the characteristic absorption for the *cis*-isomer increased at a wavelength of 444 nm upon 365 nm UV exposure. Longer exposure times (at 365 nm) did not alter the absorbance further (See Figure F.4 in Appendix F), indicating the photo-isomerization was complete after only 30 sec of UV exposure. A subsequent 450 nm light exposure (30 secs; 0.3 J/cm^2) on the same film resulted in the identical absorbance spectra taken prior

to the initial 365 nm UV exposure, indicating a return to the *trans*-isomer. This indicates that the polymer conformation, thus the surface tension, can be controlled by these two different light exposures.

FTIR spectra shown in Figure 7.6b and 6c further revealed the conformational shift upon photo-isomerization. Peaks between 1605-1585 cm^{-1} and near 840 cm^{-1} were used for this study. The former peak (A_{1w}) describes ring vibrations in plane with the polarization along the long axis of azobenzene[26] while the latter peak (C_{1w}) describes the out-of-plane wagging of the aryl C–H with polarization perpendicular to the aromatic plane.[27,28] After exposing the film with 365 nm UV light for 30 sec, the A_{1w} peak area intensified while the C_{1w} peak diminished. Since transmission mode FTIR spectroscopy measures the dipole moment projected on to the substrate, this behavior corresponded to the shift of the aromatic plane toward the substrate by isomerization. Various molecular orbital calculations[29] and experimental evidence[30,31] have determined the flip angle, α in Figure 7.5, to be $< 60°$. As a result, the pentyl functional group is likely far below the film interface after isomerization to the *cis*-form. Thus, the water contact angle shift upon light exposures shown in Figure 7.5 can be attributed to different uppermost wetting chemistries (i.e. pentyl- vs azo-).

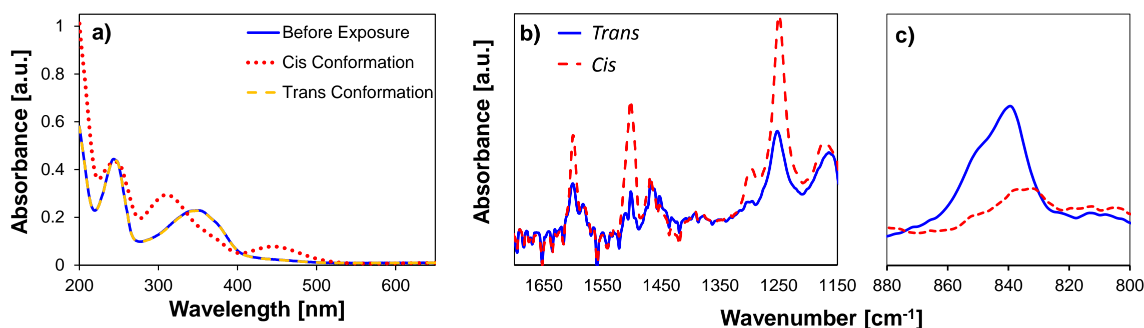

Figure 7.6: (a) UV–vis absorption spectra of a film (141 nm thick) after annealing for 1 hr at room temperature (solid), 365 nm UV exposure for 30 sec (dotted), and 450 nm light exposure for 30 sec (dashed). (b,c) FTIR spectra of a film (183 nm thick) demonstrating the dipole moment of azobenzene changes before (solid) and after (dashed) 365 nm UV exposure.

In this section, we show that flow in azo-polymer films is fully decoupled into separate exposure and heating steps, which unequivocally demonstrates that polymer flow into *cis*-isomer regions is explained by the Marangoni effect. During the light exposure step, the exposure stage was held at - 20 °C to retain a solid, glassy state film in a N_2 purged quartz chamber. Directionality of flow was controlled using photomasks with isolated transparent regions, and a schematic of the approach is shown in Figure 7.7. To direct flow *into* the light exposed regions, a 365 nm light exposure was applied through the photomask to create *cis*-isomers in the exposed regions. After light exposure, the film was warmed to room temperature in which a liquid state polymer flow was triggered from unexposed (*trans*) to exposed (*cis*) regions, forming a topographic pattern thicker in the exposed region. Alternatively, to direct flow out of the exposed regions, the film was first flood exposed with 365 nm UV light without any masks to photoisomerize the entire film, generating only the *cis*-isomers. A second 450 nm exposure through a photomask selectively yielded *trans*-isomers in the exposed regions. In this case, annealing triggered flow that created a topographic pattern thinner in the exposed region. Both of the directionalities demonstrated here flow from low to high surface tension

regions, as described by the Marangoni effect.

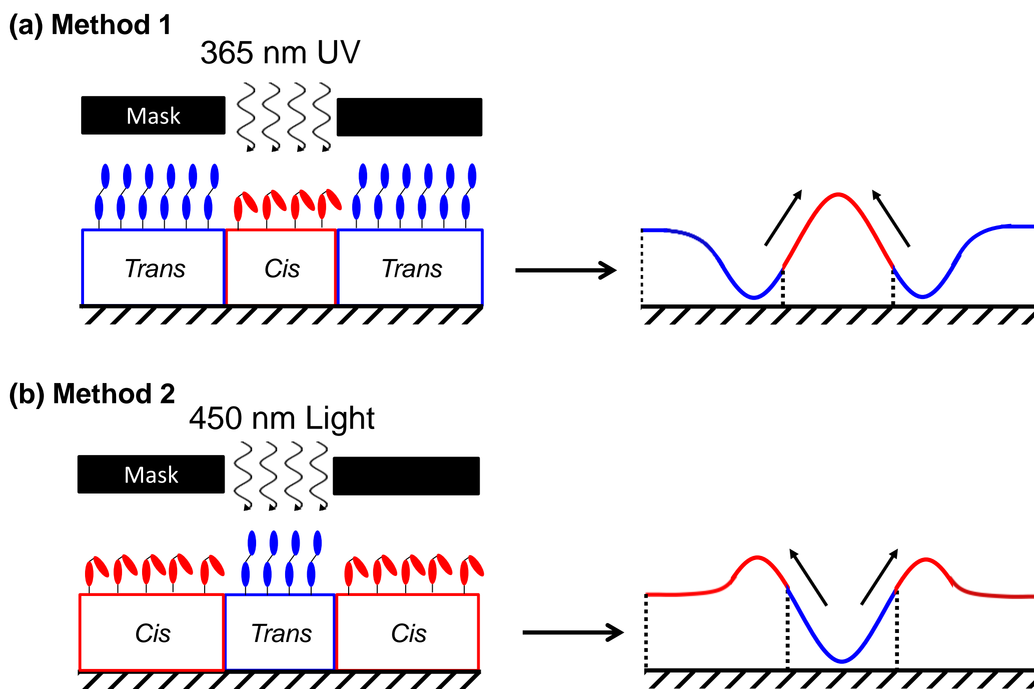

Figure 7.7: Patterning schematic. (a) 365 nm UV light exposed through a photomask selectively yields cis-rich domains in the exposed regions (i.e. relatively higher surface tension) with trans-rich surroundings (i.e. lower surface tension). Due to the prescribed surface tension gradient between exposed and unexposed regions, polymer flowed into the exposed regions, as described by the Marangoni effect. Alternatively, after uniformly converting a film into cis-rich isomers, (b) 450 nm light exposure applied through a photomask selectively yielded trans-rich regions in the exposed regions. Therefore, the polymer flowed out of the exposed regions.

Representative optical and atomic force microscope (AFM) images of a polymer film after the processes described above are shown in Figure 7.8. A mask with a regular array of hexagonal transparent regions was used in both cases. The optical micrographs taken right after light exposure are representative of a flat film because they have consistent, uniform interference color. After annealing at room temperature for 1 hr, the optical micrographs clearly show hexagonally-shaped, spatially directed thickness

variations based on those regions having different interference colors. Due to the different local surface tensions, increases or decreases in thickness are present in the exposed regions after annealing at room temperature. Each example in Figure 7.8 demonstrates the topographic directionalities indicated by the schematic in Figure 7.7. The thickness profile of samples produced by this patterning methodology is always smoothly varying as a result of continuous flow of liquid polymer.

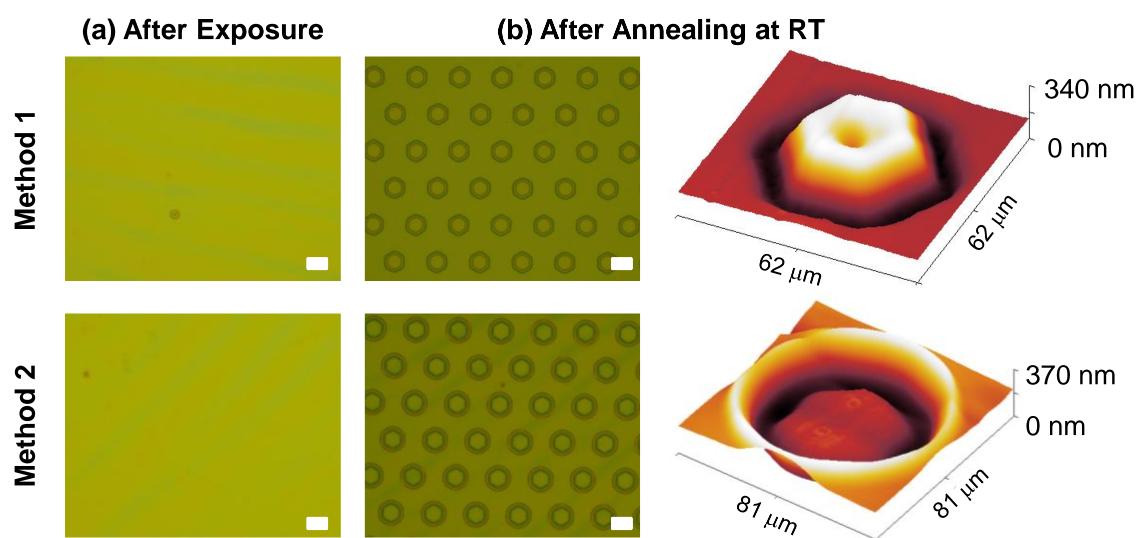

Figure 7.8: Representative optical and AFM images (a) before and (b) after room temperature annealing the films with higher surface tension in the exposed hexagonal regions (Method 1, top row) and analogous images of the films with lower surface tension in the exposed hexagonal regions (Method 2, bottom row). Both samples were annealed for 1 hr at room temperature after the patterned light illumination step. The initial film thicknesses were 183 nm. Scale bars in optical micrographs indicate 60 μm.

It is noteworthy that the thickness variations due to both methods were similar to each other, consistent with the surface tension gradient imposed by both methods described in Figure 7.7 being identical but opposite in direction. The topographical profiles in Figure 7.8 show local maxima/minima in film thickness variations at the

boundary between light exposed and unexposed regions, indicating the flow was initiated at the boundary. A previously developed thin film equation governing thin film dynamics with a Marangoni stress revealed that Marangoni flux is proportional to the second derivative of surface tension (or isomer concentration in this study) with respect to distance. [32] Thus, the formed local maxima/minima in film thickness variations at initial stages implies the Marangoni flow dominated at the boundary between light exposed and unexposed regions where the second derivative of surface tension has the largest magnitude.

Above all else, it is noteworthy that the flow-driven pattern formation process was decoupled into two completely separate stages, meaning that constant irradiation was not by any means a prerequisite to molecular migration of azo-polymers. A latent isomer pattern (with corresponding surface tension pattern) can be written into the solid, glassy polymer film, and subsequently activated at any future time to drive flow of the film materials in a liquid state. Since we have shown here that azo-polymers can translationally move µm-scale distances (many times their molecular size) in the absence of light, we argue that the light applied in SRG patterning does not directly influence topography formation. In our view, the continuous light exposure heats the film above its thermal transition and simultaneously induces a *trans* to *cis* isomerization pattern. Additionally, isomerization generally enhances the chain mobility in the *cis*-rich regions,[33-35] which has been attributed to created free volume upon *trans* to *cis* photo-isomerization.[36,37] Accordingly, the surface tension changes and simultaneous flow into *cis*-rich regions via the Marangoni effect is an indirect consequence of those photochemical transformations.

While surface tension driven flow was our initial hypothesis, other mechanisms to drive liquid polymer flow have been demonstrated. For example, a spatially defined

molecular weight[38]/viscosity[39] gradient could drive polymer flow from low to high viscosity regions. In this study, the polymer viscosity was actually reduced upon UV irradiation (see Figure F.5 in Appendix F). Hence, the flow directionality shown in Figure 7.8 goes against a viscosity gradient driven flow.[38,39] In another example, Seki and coworkers have demonstrated that a polymer phase change from crystalline to amorphous upon light exposure can drive flow.[24,40] Since our polymer is completely amorphous (as confirmed by DSC Figure 7.4 and cross polarized optical microscopy), the polymer flow in this study was clearly not driven by a phase transition. Although some studies suggest phase change, viscosity, and/or surface tension gradients can be combinatorial and synergistic to drive even more flow,[41,42] here, careful selection of our model polymer allowed elimination of these alternative mechanisms.

So far, it has been demonstrated that the reversible photo-isomerization reaction of azobenzene side chains produces a surface tension gradient, which later triggers macroscopic flow of the polymer film, forming topographic features. This non-destructive, reversible photo-isomerization effect, therefore, enables the SRG strategy to be fully 'recyclable'. This means the topographic patterns can be formed repeatedly after erasing the pre-formed features by thermal annealing and/or cyclic exposure of the film to UV light. Therefore, understanding the SRG dissipation mechanism is also critical for efficiently tailoring the reversibility of SRG formation. To this end, height profiles describing the decay of film thickness perturbations were characterized using AC mode AFM after a series of annealing intervals at room temperature. Samples were exposed to 365 nm light through a 12.5 μm half-pitch line and space photomask. Figure 7.9 shows the decrease in sinusoidal feature size (peak to valley height, $\hat{\eta}$) upon post exposure annealing. The feature size was normalized by its maximum value (~ 220 nm). The features decayed exponentially upon annealing at two different rates. Initially, the

features dissipated relatively quickly, but with extended annealing time the feature decay rate slowed considerably.

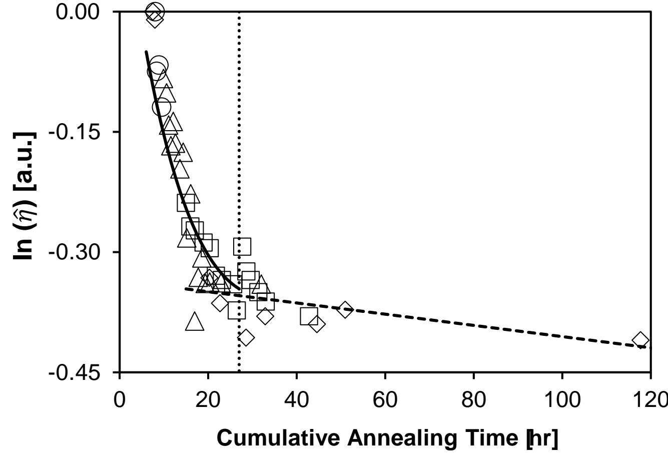

Figure 7.9: Peak to valley height measured by AFM upon annealing at room temperature as a function of cumulative annealing time. Different symbols indicate identically prepared samples. The initial film thicknesses were ca. 135 nm. Samples were exposed for 30 sec through a 12.5 μm (λ) half-pitch line and space photo-mask. The data set shown here are averaged height values of four different periodicities. The vertical dotted line indicates the relaxation time of the corresponding cis-isomer, τ, at room temperature. Two fits are provided corresponding to different decaying behaviors of the features as a result of capillary levelling with different capillary velocities (solid line, Equation 7.7 and dashed line, Equation 7.4).

Often topographical features in liquid films decay due to the presence of capillary forces, which is often referred to as capillary levelling.[43,44] This behavior can be described by the thin film equation:

$$\frac{\partial h}{\partial t} + \frac{\partial}{\partial x}\left[\left(\frac{1}{3\mu}\right) h^3 \frac{\partial}{\partial x}\left\{\gamma \frac{\partial^2 h}{\partial x^2}\right\}\right] = 0 \tag{7.1}$$

where h is the thickness of the film at any given location, γ is local surface tension, μ viscosity, and x and t are the lateral distance and time, respectively. The governing equation shown as Equation 7.1 is the one-dimensional form since the programmed surface energy varies only in the in-plane direction, x, perpendicular to the mask lines.

Since h is much smaller than the pattern half-periodicity, λ, a lubrication approximation is valid.

The above governing equation was linearized by first assuming that for small perturbations in film height, changes in height take a sinusoidal form as seen from AFM scans (Equation 7.2).

$$h/h_0 = 1 + \eta(x,t) = 1 + \hat{\eta}(t)\cos(\pi x) \tag{7.2}$$

Here, h_0 indicates the initial film thickness and $\eta(x,t)$ represents the deviation in film thickness from its steady state value, 1. The purely time-dependent amplitude of $\eta(x,t)$ is defined as $\hat{\eta}$. Rescaling Equation 7.1 with $x \sim \lambda$ and $h \sim h_0$, the complete linearized version of Equation 7.1 is:

$$\frac{\partial \hat{\eta}}{\partial t} + \frac{\gamma {h_0}^3}{\mu \lambda^4}\hat{\eta} = 0 \tag{7.3}$$

Then, solving for $\hat{\eta}$ one obtains:

$$\hat{\eta}(t) \sim exp\left\{-\frac{{h_0}^3}{\lambda^4}\left(\frac{\gamma}{\mu}\right)t\right\} \tag{7.4}$$

The relationship in Equation 7.4 describes the exponential decay of sinusoidal features with annealing time with a time constant proportional to the capillary velocity, γ/μ. Since both the surface tension and viscosity vary as a function of isomer concentration (see Figure 7.5 and Figure F.5 in Appendix F), we first characterized how the concentration of *cis* isomer reverts to *trans* isomer upon annealing at room temperature after light exposure by using UV-vis spectroscopy (Figure F.6 in Appendix F). Consistent with the literature,[45] the concentration of *cis*-isomer decayed exponentially in the form of

$$[C_{cis,t}] = [C_{cis,0}]exp\left(-\frac{t}{\tau}\right), \tag{7.5}$$

where τ is the *cis* to *trans* relaxation time scale at room temperature, and $[C_{cis,t}]$ describes the concentration of *cis*-isomer at time *t* after the 365 nm light exposure. The

characteristic relaxation time scale, τ, was 27 hrs which was extracted by fitting the UV-vis data with Equation 7.5 (Figure F.7 in Appendix F).

Since the surface tension, γ, decreases while viscosity, μ, increases as the prescribed *cis* isomers relax back to *trans* form, the rate of feature dissipation, γ/μ, continuously decreases during the initial annealing period. Therefore, the capillary velocity, γ/μ, is assumed to decay according to the isomer concentration changes with a pre-factor, β.

$$\frac{\gamma}{\mu} = \beta\, exp\left(-\frac{t}{\tau}\right) \;\; at \;\; t < \tau \tag{7.6}$$

By substituting Equation 7.6 into Equation 7.4,

$$\hat{\eta}(t) \sim exp\left\{-\frac{\beta {h_0}^3}{\lambda^4}\, exp\left(-\frac{t}{\tau}\right) t\right\} \;\;\; at \;\; t < \tau \tag{7.7}$$

Equation 7.7 now predicts the feature height at short time scales (t < τ) decays exponentially with the exponentially decaying capillary velocity. This equation is plotted in Figure 7.9 as a solid line and agreed well with experimental observations. However, since there are only *trans* isomers left at longer annealing times (t > τ ~ 27 hrs), the remaining features decayed with a constant capillary velocity, $\gamma_{trans}/\mu_{trans}$. By fitting Equation 7.4 with the data at this later annealing period, $(h_0^3\,\gamma)\,/\,(\mu\lambda^4\,)$ ~ 0.0007 hr^{-1} could be extracted. This fitted slope then yielded a capillary velocity of 2.2 μm/s, which agreed with an estimated value (~ 1.0 μm/s). For this estimation, γ_{trans} was calculated by fitting the water contact angle measurements shown in Figure 7.5 to the Young's equation[46] while μ_{trans} was measured using rheology. Figure 7.9 shows that the time for thermal relaxation of *cis*-isomers back to *trans*-form is in good agreement with feature decay at early times (t < τ) but it is possible that the feature dissipation at early times is also partially caused by interdiffusion of the surface energy gradient creator.[32]

7.4 CONCLUSIONS

In summary, an amorphous model azo-polymer, poly(4-(acryloyloxyhexyloxy)-4'-pentylazobenzene), was synthesized and studied to verify that the underlying mechanism of the feature formation is due to the Marangoni effect. The phenomenologically-observed flow patterns originated from spatially defined azobenzene photo-isomerization. This photo-isomerization generated a surface tension gradient between *cis*-rich and *trans*-rich regions. This surface tension gradient triggered migration of liquid polymers, forming smoothly varying thickness profiles. Additionally, the polymer flow direction was controlled with precision by inducing different surface tension changes in the exposed regions consistent with the Marangoni effect. By comparison with experimental observations, a scaling analysis was performed to verify that the mechanism for the feature dissipation was capillary levelling. The features decayed upon thermal annealing with two distinct rate regimes, which were attributed to dissimilar capillary velocities associated with different azobenzene isomers. We envision this study will help guide future materials design and process development in this area.

7.5 REFERENCES

1. Rochon, P.; Batalla, E.; Natansohn, A. *Appl. Phys. Lett.* **1995**, 66, 136.
2. Kim, D.Y.; Tripathy, S.K.; Li, L.; Kumar, J. *Appl. Phys. Lett.* **1995**, 66, 1166.
3. Viswanathan, N. K.; Kim, D. Y.; Bian, S.; Williams, J.; Liu, W.; Li, L.; Samuelson, L.; Kumar, J.; Tripathy, S. K. *J. Mater. Chem.* **1999**, 9, 1941–1955.
4. Fukuda, T.; Matsuda, H.; Shiraga, T.; Kimura, T.; Kato, M.; Viswanathan, N. K.; Kumar, J.; Tripathy, S. K. *Macromolecules* **2000**, 33, 4220–4225.
5. Lagugne-Labarthet, F.; Buffeteau, T.; Sourisseau, C. *Phys. Chem. Chem. Phys.* **2002**, 4, 4020–4029.
6. Aissou, K.; Shaver, J.; Fleury, G.; Pecastaings, G.; Brochon, C.; Navarro, C.; Grauby, S.; Rampnoux, J.; Dilhaire, S.; Hadziioannou, G. *Adv. Mater.* **2013**, 25, 213–217.
7. Rho, Y.; Aissou, K.; Mumtaz, M.; Kwon, W.; Pecastaings, G.; Mocuta, C.; Stanecu, S.; Cloutet, E.; Brochon, C.; Fleury, G.; Hadziioannou, G. *Small* **2015**, 11, 6377–6383.
8. Snell, K. E.; Stéphant, N.; Pansu, R. B.; Audibert, J.; Lagugné-Labarthet, F.; Ishow, E. *Langmuir* **2014**, 30, 2926–2935.

9. Lee, S.; Jeong, Y.-C.; Park, J.-K. *Opt. Express* **2007**, 15, 14550–14559.
10. Ishow, E.; Brosseau, A.; Clavier, G.; Nakatani, K.; Pansu, R. B.; Vachon, J.; Tauc, P.; Chauvat, D.; Mendonça, C. R.; Piovesan, E. *J. Am. Chem. Soc.* **2007**, 129, 8970–8971.
11. Gritsai, Y.; Goldenberg, L. M.; Kulikovska, O.; Stumpe, J. *J. Opt. A Pure Appl. Opt.* **2008**, 10, 125304.
12. Priimagi, A.; Shevchenko, A. *J. Polym. Sci., Part B: Polym. Phys.* **2014**, 52, 163–182.
13. Lee, S.; Kang, H.S.; Park, J. *Adv. Mater.* **2012**, 24, 2069–2103.
14. Yager, K.G.; Barrett, C.J. *Curr. Opin. Solid State Mater. Sci.* **2001**, 5, 487–494.
15. Yager, K.G.; Barrett, C.J. *J. Photochem. Photobiol. A* **2006**, 182, 250–261.
16. Yager, K.G.; Barrett, C.J. *Macromolecules* **2006**, 39, 9320-9326.
17. Lim, H. S.; Han, J. T.; Kwak, D.; Jin, M.; Cho, K. *J. Am. Chem. Soc.* **2006**, 128, 14458-14459.
18. Ichimura, K.; Oh, S. K.; Nakagawa, M. *Science*, **2000**, 288, 1624-1626.
19. Delorme, N.; Bardeau, J. F.; Bulou, A.; Poncin-Epaillard, F. *Langmuir* **2005,** *21,* 12278-12282.
20. Ahmad, N. M.; Lu, X.; Barrett, C. J. *J. Mater. Chem.*, **2010**, 20, 244–247.
21. Yamashita, N.; Watanabe, S.; Nagai, K.; Komura, M.; Iyoda, T.; Aida, K.; Tadac, Y.; Yoshida, H. *J. Mater. Chem. C,* **2015**, 3, 2837 -2847.
22. Nakai, T.; Tanaka, D.; Hara, M.; Nagano, S.; Seki, T. *Langmuir* **2016**, *32*, 909–914.
23. Zettsu, N.; Seki, T. *Macromolecules* **2004**, 37, 8692-8698.
24. Isayama, J.; Nagano, S.; Seki, T. *Macromolecules* **2010**, 43, 4105–4112.
25. Hayata, Y.; Nagano, S.; Takeoka, Y.; Seki, T. *ACS Macro Lett.* **2012**, *1*, 1357-1361.
26. Nakahara, H.; Fukuda, K. *J. Colloid Interface Sci*, **1983**, 93, 530-539.
27. Lin-Vien, D.; Colthup, N.B.; Fateley, W.G.; Grasselli, J.G.The Handbook of Infrared and Raman Characteristic Frequencies of Organic Molecules, Academic Press, Boston, 1991.
28. Ihs, A.; Uvdal, K.; Liedberg, B. *Langmuir* **1993**, 9, 733-739.
29. Kurita, N.; Tanaka, S.; Itoh, S. *J. Phys. Chem. A* **2000**, 104, 8114-8120.
30. Bouwstra, J. A.; Schouten, A.; Kroon, J. *Acta Crystallogr.* **1983**, C39, 1121.
31. Traetteberg, M.; Hilmo, I.; Hagen, K. *J. Mol. Struct.* **1977**, 39, 231.
32. Arshad, T. A.; Kim, C. B.; Prisco, N. A.; Katzenstein, J. M.; Janes, D. W.; Bonnecaze, R. T.; Ellison, C. J. *Soft Matter* **2014**, 10, 8043−8050.
33. Hurduc, N.; Donose, B. C.; Macovei, A.; Paius, C.; Ibanescu, C.; Scutaru, D.; Hamel, M.; Branza-Nichita, N.; Rocha, L. *Soft Matter*, **2014**, 10, 4640–4647.
34. Fang, G. J.; Maclennan, J. E.; Yi, Y.; Glaser, M. A.; Farrow, M.; Korblova, E.; Walba, D. M.; Furtak, T. E.; Clark, N. A. *Nat. Commun*., **2013**, 4, 1521.
35. Karageorgiev, P.; Neher, D.; Schulz, B.; Stiller, B.; Pietsch, U.; Giersig M.; Brehmer, L. *Nat. Mater.*, **2005**, 4, 699–703.
36. Yager, K. G.; Tanchak, O. M.; Godbout, C.; Fritzsche, H.; Barrett, C. J. *Macromolecules* **2006**, 39, 9311-9319.

37. Tanchak, O. M; Barrett, C. J. *Macromolecules* **2005,** 38, 10566-10570.
38. Ubukata, T.; Moriya, Y.; Yokoyama, Y. *Polym. J.* **2012**, 44, 966–972.
39. Sachan, P.; Kulkarni, M.; Sharma, A. *Langmuir*, **2015**, 31, 12505–12511.
40. Li, W.; Dohi, T.; Hara, M.; Nagano, S.; Haba, O.; Yonetake, K.; Seki, T. *Macromolecules* **2012**, 45, 6618−6627.
41. Zettsu, N.; Ogasawara, T.; Arakawa, R; Nagano, S.; Ubukata, T.; Seki, T. *Macromolecules* **2007**, 40, 4607−4613.
42. Katzenstein, J. M.; Kim, C. B.; Prisco, N. A.; Katsumata, R.; Li, Z.; Janes, D. W.; Blachut, G.; Ellison, C. J. *Macromolecules* **2014**, 47, 6804−6812.
43. Benzaquen, M.; Fowler, P.; Jubin, L.; Salez, T.; Dalnoki-Veress, K.; Raphael, E. *Soft Matter*, **2014**, 10, 8608–8614.
44. Benzaquen, M.; Ilton, M.; Massa, M. V.; Salez, T.; Fowler, P.; Raphael, E.; Dalnoki-Veress, K. *Appl. Phys. Lett.* **2015**, 107, 053103.
45. Garcia-Amoros, J.; Sanchez-Ferrerz, A.; Massad, W. A.; Nonell, S.; Velasco, D. *Phys. Chem. Chem. Phys.* **2010**, 12, 13238–13242.
46. Balkeneende, A. R.; van de Boogaard, H. J. A. P.; Scholten, M.; Willard, N. P. *Langmuir* **1998**, 14, 5907-5912.

Chapter 8: Future Work

The previous chapters in this dissertation focused on the work completed during my graduate studies involving polymer synthesis, solid-state photochemistry, and processing of polymer thin films to demonstrate that Marangoni-driven topographic patterning has significant and broad utility. In order to direct further advances in this technology, specifically towards more practical issues, future work related to Marangoni-driven patterning is provided in this chapter.

8.1 BCP/LCP DIRECTED SELF-ASSEMBLY

While Marangoni-driven patterning itself could be used as a powerful patterning method for some applications, an even greater variety of applications could be realized if the Marangoni strategy can be used to align other structured materials. Directed self-assembly (DSA) using chemical or topographical directing templates (and combinations thereof) has been implemented to successfully align block copolymer (BCP) and/or liquid crystalline polymer (LCP) micro-domains, enabling their use in microelectronic devices,[1-3] barrier films for packaging,[4,5] optics,[6] etc.

In particular, BCPs offer an attractive alternative patterning technology since they can yield smaller features than possible with conventional photolithography while potentially retaining high throughput and low defect density. Unfortunately, thin film BCP line (from lamellae forming BCP) and dot patterns (from cylinder forming BCP) exhibit placement defects unless alignment techniques are implemented during the annealing process. For example, line patterns tend to adopt a “fingerprint” with significant curvature within the BCP domains and dot patterns typically have good short-range but poor long-range hexagonal order. A crucial step toward the arrangement of BCP micro-domains into proper device structures requires long-range order and specified

domain placement of BCP micro-domains.[7] Both long-range order and domain placement can be improved by DSA, most often with sparse lithographically pre-defined directing patterns. These prepatterns either promote alignment of the BCP domains within a confined topographic relief structure (graphoepitaxy)[8] or by using chemically distinct surface regions that align the BCP on top of them by inducing block domains to selectively contact certain regions on the surface (chemoepitaxy).[9,10] Even though the BCP domains that can be formed are far smaller than those accessible from conventional photolithography tools, the DSA of BCPs is still necessarily linked to either an e-beam or 193 nm immersion lithography step due to the need for a lithographically pre-defined directing pattern. To that end, alternative non-conventional methods for inducing long range order of BCP domains without or with less use of high-resolution photolithography steps could be attractive.[11,12] The following proposed strategies, which is the subject of the next few sections, focus mainly on inducing long-range order of BCP micro-domains, but may not be able to define placement of them. Although the placement of the BCP micro-domains is required for the microelectronics industry,[7] BCP films possessing only long-range ordered micro-domains can be utilized for other applications[4-6] unrelated to the microelectronics industry.

8.1.1 Shear Alignment

Extensive studies have shown that directional shear stress, often applied by film extrusion or moving plates contacting the film, can improve large scale (micron or larger length scale) micro-domain alignment of BCP[13,14] or LCP[15,16] films. Simultaneous alignment of the domain structures of BCPs or LCPs on top of the Marangoni feature forming layer during the Marangoni flow process could be an impactful capability. When topography is formed via the Marangoni effect, deformation of the polymer surface clearly has an associated local shear stress because the surface area is increased compared

to the flat film precursor. Therefore, it is possible that by placing an unaligned BCP or LCP film on top of the photoactive polymer layer, the shear stress/strain imparted by the topography formation may be sufficient to align micro-domains. A potential challenge for this approach is a viscosity mismatch between the BCP layer and the Marangoni feature forming layer. Since the viscosity mismatch in multilayer films may promote layer breakup and other defects during processing, careful control of processing conditions along with judicious material selection of both the BCP and the Marangoni feature forming polymers will be required for obtaining high quality structurally-aligned films.

8.1.2 Direct Marangoni Flow on BCP

A second area of future work involves directly programming Marangoni flow into the BCP material itself to obtain aligned BCPs. In this approach, the photochemically induced Marangoni stress in the BCP films could be directly translated to a shear force in the system, potentially at the maximum possible level. This approach also requires less care in material selection than is needed in the multilayer approach outlined above (e.g., viscosity mismatch is not a concern). One could envision employing a BCP that has intrinsic photochemically active groups (e.g., a polystyrene block as outlined in several chapters of this thesis) or one that is designed with more specific functionalities that undergo large polarity switches (e.g., *tert*-butoxy styrene units in one block). As an initial proof of concept, a cylinder forming BCP would be used to form parallel cylinders, thus simplifying the process by excluding the need for neutral interfaces that would be required for most lamellae-forming BCPs.

8.1.3 Surface Roughening

An alternative strategy and possibly the simplest way to align BPCs using Marangoni flow is by placing the BCP on top of a periodic roughened substrate.

Previously, Russell and coworkers demonstrated a substrate possessing nanometer apart scale roughness can induce highly ordered ultradense arrays in BCP films over macroscopic distances.[17] Furthermore, Kim and coworkers reported a micron scale thickness-modulated neutral substrate can create a highly aligned lamellar morphology on top of it.[18] Spontaneous alignment occurs through the directional growth of well-ordered domains along the thickness gradient with vertical linear defects moving from thicker parts of the film towards the thinner ones. The mechanism underlying this interesting self-aligning behavior is proven to be a 'geometric anchoring' phenomenon,[18] originally envisioned to account for the alignment of liquid crystals in a curved but confined film geometry.

Since it was already demonstrated multiple times in this thesis that Marangoni-driven patterning can effectively produce micron and sub-micron scale patterns, we believe that the Marangoni-driven thickness-modulated films could serve as a periodic roughened substrate to induce alignment of BCP domains on top. To meet this outcome, the crosslinking strategy detailed in Chapter 6 along with designing a proper neutral layer for the perpendicular orientation of a lamellae-forming BCP may be required. The process flow would consist of first fabricating the crosslinked Marangoni features, then applying the crosslinkable neutral layer on top, and finally depositing the BCP films on top of this roughened and neutral substrate. A final thermal annealing step would yield the aligned BCPs on top of the roughened and neutral bilayer substrates. A symmetric poly(styrene-*block*-methyl methacrylate) block copolymer can be a good starting model polymer to demonstrate this hypothesis because of its unique processing characteristic that does not require additional neutral top interface materials when thermally annealed.

8.2 IMPROVING FEAUTRE ASPECT RATIO

Although the DSA strategies suggested in Section 8.1 might seem straight-

forward and easily achievable, there are some additional features that may be required to meet these goals. For example, the largest currently achievable pattern aspect ratio using the Marangoni-driven patterning method may not be sufficiently large to align BCP micro-domains. For the shear alignment approach in Section 8.1.1, it is simplest to think in terms of the strain caused by increased surface area of the film after topographic features are formed. In existing shear alignment literature, strain amplitudes of 50-100% were imparted to the film for several hours in order to observe high degrees of both BCP[14] and LCP[16] alignment. However, in the case where ~ 600 nm features are created with a 25 μm pitch, the highest aspect ratio we have observed so far using Marangoni flow (as detailed in Chapter 5) corresponds to only 0.12 % strain. Moreover, the roughness required to align the BCP outlined in Section 8.1.3 is only possible when the critical contact angle between the roughed surface and the BCP film is over 3°,[18] which is also slightly higher than the largest achievable angle using the current Marangoni method described in Chapter 5 (~ 2°). This is a significant challenge to overcome to successfully align BCPs or LCPs. The simplest way to increase the amount of strain applied or the sample roughness would be to significantly increase the aspect ratio of the Marangoni features; therefore, these objectives will have to be considered alongside the strategies to improve Marangoni feature aspect ratio.

One might imagine that applying light exposure through a smaller pitch size photomask would improve the feature resolution. One of the limiting factors for this approach is the resolution limit for proximity (shadow) printing as shown below[19]

$$b_{min} = \frac{3}{2}\sqrt{\lambda\left(S + \frac{z}{2}\right)} \qquad (8.1)$$

Where b_{min} is the minimum feature size, S is the distance between the film surface and the mask, λ is the wavelength of light, and z is the film thickness. This shows that the

resolution for this process is strongly dependent on the size of the gap between the polymer and the photomask. Since the films are glassy and are on substrates that are not perfectly smooth, ensuring intimate contact over the entire area of the film is very challenging. It is also noteworthy that our results shown in Chapter 5 approach the resolution limit for proximity printing despite using crude experimental setups. This suggests that the Marangoni-driven pattern resolution is inhibited primarily by our lack of sophisticated tools, and not by any underlying chemical or physical limitations. Therefore, we strongly believe that adapting more sophisticated tools in the Marangoni-driven patterning method would possibly further improve the pattern resolution and aspect ratio.

Although simply adapting sophisticated tools would improve the pattern aspect ratios, here we propose three additional non-conventional approaches to improve the Marangoni feature aspect ratios without adapting new and complex tools. In Chapter 4, we have already demonstrated that careful material selection can increase feature heights for a given pattern periodicity, improving the pattern aspect ratio. Hence, we suggest here other strategies to improve the pattern aspect ratio by reducing pattern periodicity without adapting more sophisticated and complex equipment. Each approach is described in detail in the following sections and they are written from the viewpoint that enhancing the resolution (e.g., decreasing feature sizes or decreasing periodicities) will be helpful in increasing aspect ratio at equivalent feature height.

8.2.1 Exploiting Secondary Peak Formation

In Chapters 2 and 5, the formation of secondary peaks during short periods of thermal annealing was observed. A theoretical framework described in Chapter 2 demonstrated that the formation of the secondary peaks originated from the thin film dynamics. The Marangoni flux is at a maximum where the second derivative of surface

energy with respect to the characteristic distance has its largest magnitude. This finding is practically relevant because it represents a strategy, rooted in the physical nature of fluids, to double the areal density of topographic features from that present in the projected photo-mask pattern. Further research investigation to optimize this phenomenon will be a promising method to enhance the pattern resolution and aspect ratio.

8.2.2 Controlled PAG/PBG Diffusion Method to Reduce the Critical Dimension of the Surface Energy Gradient

Strictly speaking, the final pattern periodicity of the Marangoni-driven features matches that of the initially prescribed surface energy pattern. So far, this surface energy gradient pattern was purely dictated by the mask dimensions used during the patterned light irradiation steps. To achieve greater resolution than the original light exposure pattern, tailoring the diffusion of small molecule catalysts to "trim" the surface energy pattern inscription could be an interesting pathway to developing even smaller periodicity than the original light exposure pattern. As demonstrated in Chapters 3 and 4, a photo-resist type polymer possessing acid or base labile protecting groups can first be co-cast with photo-acid generator (PAG) or photo-base generator (PBG) into a film, respectively. A subsequent light exposure followed by post exposure soft bake can facilitate diffusion of PAG/PBG in the polymer matrix. As the diffusion of PAG/PBG proceeds the critical dimension is "trimmed" and chemical transformations of the polymer will occur along the diffusion pathway, which would potentially reduce the surface energy gradient pattern periodicity from the original light exposure pattern periodicity.

8.2.3 Smaller Periodicity using Shrinking Substrates

To get a smaller lateral resolution without adapting more sophisticated and complex equipment for the Marangoni process, a shrinking substrate could "contract or

densify" the features along the substrate plane. A pre-strained polymer film (in-plane) could be used as such a substrate which can be easily purchased. The Marangoni feature forming polymer layer could be coated on top of this pre-strained film. Then, light exposure through a photomask with dimensions close to the resolution limit for proximity printing as described by Equation 8.1 will be applied to impose a surface energy gradient onto the Marangoni feature forming layer. Once these films are heated above the glass transition temperature of both layers, the pre-strained substrate will shrink while the Marangoni flow process occurs. This will result in 3-dimensional topographies with smaller resolution than the resolution limit for proximity printing.

This strategy will only work for the Marangoni patterning method when the feature forming layer is in the liquid state during substrate shrinking. Otherwise, with the presence of a *solid* film on top of the shrinking substrate, the film would be more likely to wrinkle or buckle due to modulus mismatch.[20-23] Due to the no-slip condition between the shrinking substrate and the polymer melt, the spatial lateral surface energy pattern programmed in the Marangoni feature forming layer should shrink with the substrate upon heating. By keeping the films thin and by tuning the viscosity of the Marangoni layer (e.g., through molecular weight and annealing temperature), most of the in-plane shrinkage rate from the substrate may be imparted to the Marangoni feature-forming layer, thus allowing patterning beyond the resolution limit of proximity printing, yielding higher aspect ratio features.

8.3 REFERENCES

1. Park, S. M.; Stoykovich, M. P.; Ruiz, R.; Zhang, Y.; Black, C. T.; Nealey, P. E., *Adv. Mater.* **2007,** 19, 607-611.
2. Bita, I.; Yang, J. K. W.; Jung, Y. S.; Ross, C. A.; Thomas, E. L.; Berggren, K. K., *Science* **2008,** 321, 939-943.
3. Segalman, R. A.; Yokoyama, H.; Kramer, E. J., *Adv. Mater.* **2001,** 13, 1152-1155.
4. Weinkauf, D. H.; Kim, H. D.; Paul, D. R. *Macromolecules* **1992**, 25,788-796.

5. Park, J. Y.; Paul, D. R.; Haider, I.; Jaffe, M. *J. Polym. Sci., Part B: Polym. Phys.***1998**, 34,1741-1745.
6. Grell, M.; Bradley, D. D. C.; Inbasekaran, M.; Woo, E. P. *Adv Mater.* **1997**, 9, 798-802.
7. Koren, I.; Koren, Z. *Proceedings of the IEEE* **1998,** *86*, 1819-1838.
8. Park, S. M.; Stoykovich, M. P.; Ruiz, R.; Zhang, Y.; Black, C. T.; Nealey, P. E. *Adv. Mater.* **2007**, 19, 607-611.
9. Ruiz, R.; Kang, H. M.; Detcheverry, F. A.; Dobisz, E.; Kercher, D. S.; Albrecht, T. R.; de Pablo, J. J.; Nealey, P. F. *Science* **2008**, 321, 936-939.
10. Cheng, J. Y.; Rettner, C. T.; Sanders, D. P.; Kim, H.-C.; Hinsberg, W. D. *Adv. Mater.* **2008**, 20, 3155-3158.
11. Janes, D. W.; Thode, C. J.; Willson, C. G.; Nealey, P. F.; Ellison, C. J. *Macromolecules* **2013**, 46, 4510–4519.
12. Inoue, T.; Janes, D. W.; Ren, J.; Suh, H. S.; Chen, X.; Ellsion, C. J.; Neaely, P. F. *Adv. Mater. Interfaces* **2015**, 2, 1500133.
13. Pujari, S.; Keaton, M. A.; Chaikin, P. M.; Register, R. A. *Soft Matter* **2012**, *8*, 5358-5363.
14. Gupta, V. K.; Krishnamoorti, R.; Chen, Z. R.; Kornfield, J. A.; Smith, S. D.; Satkowski, M. M.; Grothaus, J. T. *Macromolecules* **1996**, *29*, 875-884.
15. Alt. D. J.; Hudson, S. D.; Garay, R. O.; Fujishiro, K. *Macromolecules* **1995**, 28, 1575-1579.
16. Geary, J. M.; Goodby, J. W.; Kmetz, A. R.; Patel, J. S. *J. Appl. Phys.* **1987**, 62, 4100-4108.
17. Park, S.; Lee, D. H.; Xu, J.; Kim, B.; Hong, S. W.; Jeong, U.; Xu, T.; Russell, T. P. *Science* **2009,** *323*, 1030-1033.
18. Kim, B. H.; Lee, H. M.; Lee, J-H.; Son, S-W.; Jeong, S-J.; Lee, S.; Lee, D. I.; Kwak, S. U.; Jeong, H.; Shin, H.; Yoon, J-B.; Lavrentovich, O. D.; Kim, S. O. *Adv. Funct. Mater*. **2009**, 19, 2584-2591.
19. Madou, M. J. *Fundamentals of Microfabrication: The Science of Miniaturization*; Second Edition ed.; CRC Press: Boca Raton, Florida, **2002**.
20. Ma, S. J.; Mannino, S. J.; Wagner, N. J.; Kloxin, C. J. *ACS Macro Lett.* **2013**, 2, 474−477.
21. Chiche, A.; Stafford, C. M.; Cabral, J. T. *Soft Matter* **2008**, 4, 2360−2364.
22. Chung, J. Y.; Nolte, A. J.; Stafford, C. M. *Adv. Mater*. **2009**, 21, 1358−1362.
23. Chandra, D.; Crosby, A. J. *Adv. Mater*. **2011**, 23, 3441−3445.

Appendices

APPENDIX A: THEORETICAL FRAMEWORK TO PREDICT MARANGONI PATTERNING FOR PS

A1: Initial Concentration Profile

For fluorescence microscopy experiments, a nitrobenzofurazan (NBD) fluorophore attached to polystyrene (PS) was synthesized as described earlier.[1] Toluene or cylcopentanone solutions containing NBD-labeled PS (M_n = 2900 g/mol, Đ = 1.2) and dye-unlabeled PS possessing identical molecular weight were spin coated onto quartz substrates. To prevent fluorophore self-quenching, the amount of fluorophore content was limited to 0.18 wt. % of the total dry film mass.[2] The UV exposure dose typically used for patterning, 840 J/cm^2, was applied to the films through a line-and-space photo-mask possessing 25 μm pattern periodicity. The fluorescence intensity profile after photobleaching the NBD dye was obtained by imaging with a Hamamatsu Orca R2 camera with μManager software for camera control[3] on an Olympus BX 51 epifluorescence microscope coupled to a Photon Technologies Quanta Master 40 fluorimeter. The excitation wavelength used was 465 nm with a 4 nm bandpass and an emission filter selected for all wavelengths greater than 520 nm. Because the NBD-labeled PS content has been set below the threshold for self-quenching, this intensity is linearly proportional to the concentration of NBD. The depth of focus of the microscope was 2.9 μm, which is much larger than the typical thicknesses of films used in this study; therefore, fluorescence of the film is captured from the entire depth. Informed by the

---

This appendix reproduced in part from "Precision Marangoni-driven Patterning" Arshad, T. A.; Kim, C. B.; Prisco, N. A.; Katzenstein, J. M.; Janes, D. W.; Bonnecaze, R. T.; Ellison, C. J. *Soft Matter* **2014**, *10*, 8043-8050 with permission from the Royal Society of Chemistry, copyright 2014.

NBD concentration profile of the bleached NBD-labeled PS after light exposure through the mask, the solid line in Figure A.1 represents a smoothed step function,

$$\frac{c}{c_0}\left({}^{x}/_{\lambda}, t = 0\right) = 6\left({}^{x}/_{\lambda}\right)^5 - 15\left({}^{x}/_{\lambda}\right)^4 + 10\left({}^{x}/_{\lambda}\right)^3 \tag{A1}$$

which was used to generate the initial concentration profile for simulations, scaled to range between 0 and the peak conversion, c_0.

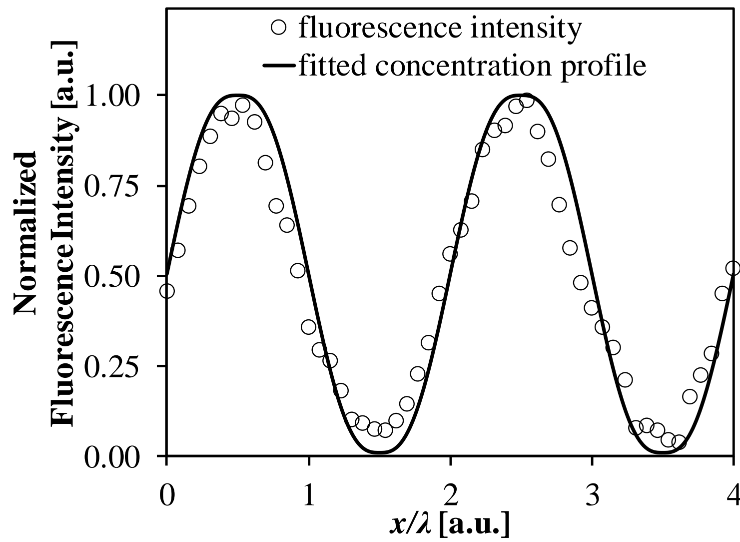

Figure A.1: Normalized fluorescence intensity profile obtained experimentally from fluorescence microscopy using NBD labeled PS after typical exposure protocol for patterning was performed. Solid line represents the initial concentration profile used in the model prediction.

A2: Glass Transition Temperature of PS

The glass transition temperature, T_g, of a bulk PS used in this study was determined by differential scanning calorimetry (DSC) using a Mettler-Toledo DSC-1. The sample was heated to 150 ˚C at a rate of 20 ˚C/min for the first 2 cycles then was heated to 300 ˚C of 15 ˚C/min for the last 2 cycles. All of the heating thermograms showed no T_g shifts between each cycle. The DSC thermogram shown in Figure A.2

corresponds the last heating step up to 300 ˚C which displays the PS possesses a bulk T_g of 61 °C. No melting temperature was detected during any of the DSC thermograms.

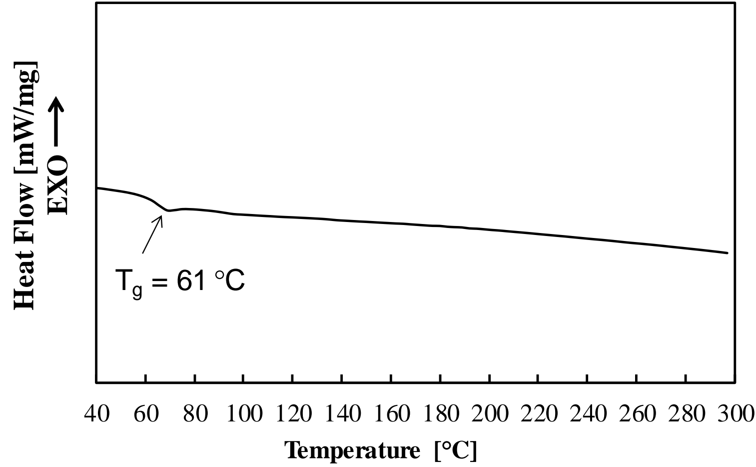

Figure A.2: DSC thermogram of PS taken upon the last heating cycle at a rate of 15 °C/min to 300 °C.

The glass transition temperature, T_g, of a thin PS film before and after a typical patterning light exposure procedure was determined by spectroscopic ellipsometry. The results are shown in Figure A.3. The film was heated at 120 °C for 5 min, and then cooled at 2 °C/min to -20 °C. The film's thickness, $h(\mathrm{T})$, was determined at each sample temperature, T, using a layered model that fitted the optical constants and film thickness. The T_g was found by regressing the equation[4]

$$h(\mathrm{T}) = w\left(\frac{\mathrm{M}-\mathrm{G}}{2}\right)\ln\left[\cosh\left(\frac{\mathrm{T}-\mathrm{T_g}}{w}\right)\right] + \left(\mathrm{T}-\mathrm{T_g}\right)\left(\frac{\mathrm{M}+\mathrm{G}}{2}\right) + \mathrm{c} \qquad \text{(A2)}$$

to the data. The parameters M, G, T_g, and c were fit and the glass transition width was set as w = 10 °C. Using larger or smaller values of w did not change the extracted value of T_g more than 1 °C.

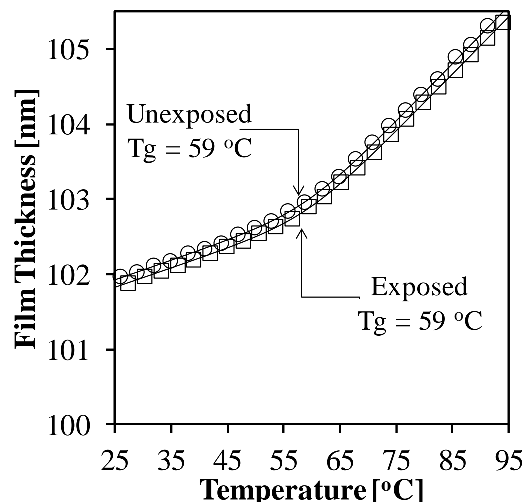

Figure A.3: Effect of 140 J/cm^2 blanket exposure to broadband light on the glass transition of a PS film supported by a Si substrate as determined by spectroscopic ellipsometry. For clarity, only every 100th data point is displayed. The solid lines represent regressions of Eq. A1 to the data.

A3: Viscosity of PS blend at 120 ^{o}C

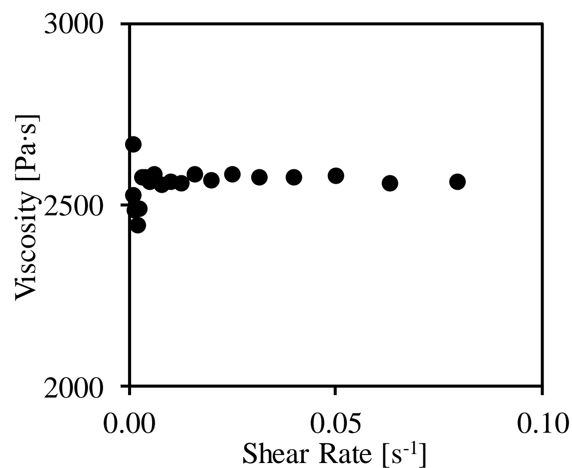

Figure A.4: Viscosity of the polystyrene blend (99 wt.% M_n = 2.9 kDa PS, 1 wt.% M_n = 50 kDa PS) was measured at 120 ^{o}C using a TA Instruments AR-2000ex rheometer under steady shear.

A4: Extracting Surface Tension Gradients and Diffusivities

The linearized solution gives the following for the peak to valley height in dimensionless form:

$$\hat{\eta} = \frac{\pi^2 \frac{\Delta\gamma c_0}{2}}{\psi_1 - \psi_2}\left(e^{\psi_1 t} - e^{\psi_2 t}\right) \tag{A3}$$

Substituting in the Taylor series expansion for the exponential function and retaining terms only up to first order yields the evolution of peak-to-valley height at short times:

$$\hat{\eta} \approx \left(\pi^2 \frac{\Delta\gamma c_0}{2}\right) t \quad \forall \quad t \ll 1 \tag{A4}$$

Comparing this to short-time experimental results, the difference in surface tension between the exposed and unexposed polymer ($\Delta\gamma$) can be extracted from the slope of the line.

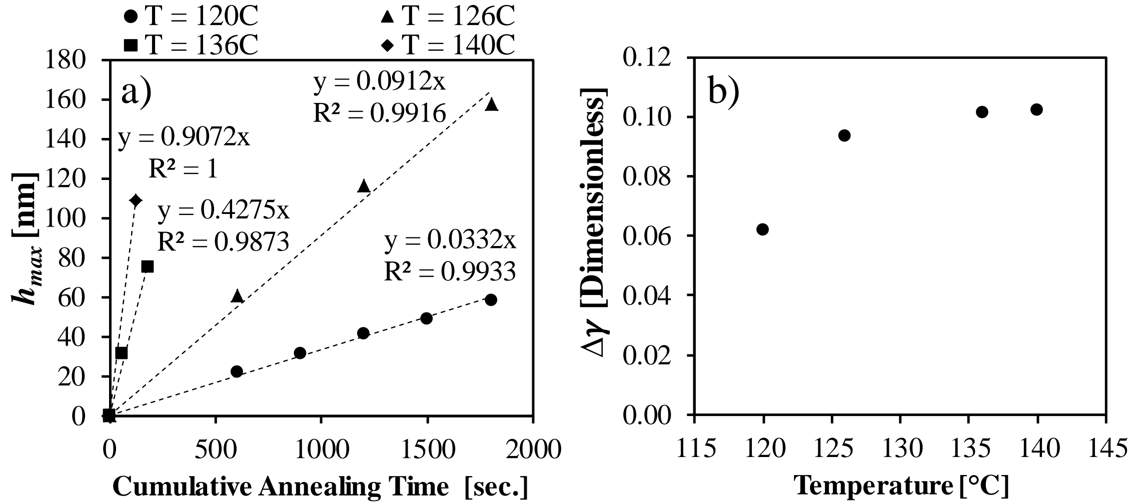

Figure A.5: (a) Experimental results at short times (b) Non-dimensional surface tension difference values extracted from experimental data at four different temperatures.

At long times, peak-to-valley height reduces to

$$\hat{\eta} \approx \frac{\pi^2 \frac{\Delta\gamma c_0}{2}}{|\psi_1 - \psi_2|} e^{\psi_{max} t} \quad \forall \quad t \gg 1 \tag{A5}$$

where $\psi_{max} \equiv \max(\psi_1, \psi_2)$. This can be re-written as

$$ln(\hat{\eta}) \approx ln\left(\frac{\pi^2 \frac{\Delta\gamma c_0}{2}}{|\psi_1 - \psi_2|}\right) + (\psi_{max})t \tag{A6}$$

Since the eigenvalues ψ_1 and ψ_2 are a function of diffusivity, it can be extracted by comparing this expression with experimental observations for peak-to-valley height at long times. As noted in the main text, the linearized solution is valid for cases where the features are small compared to the thickness of the unperturbed film. This is always true at short times, but applies at long times only for low temperatures or small initial conversions. For this reason diffusivity was extracted using experimental results at 120 °C and extrapolated to higher temperatures using correlations from literature (after shifting them to agree with the extrapolated value).

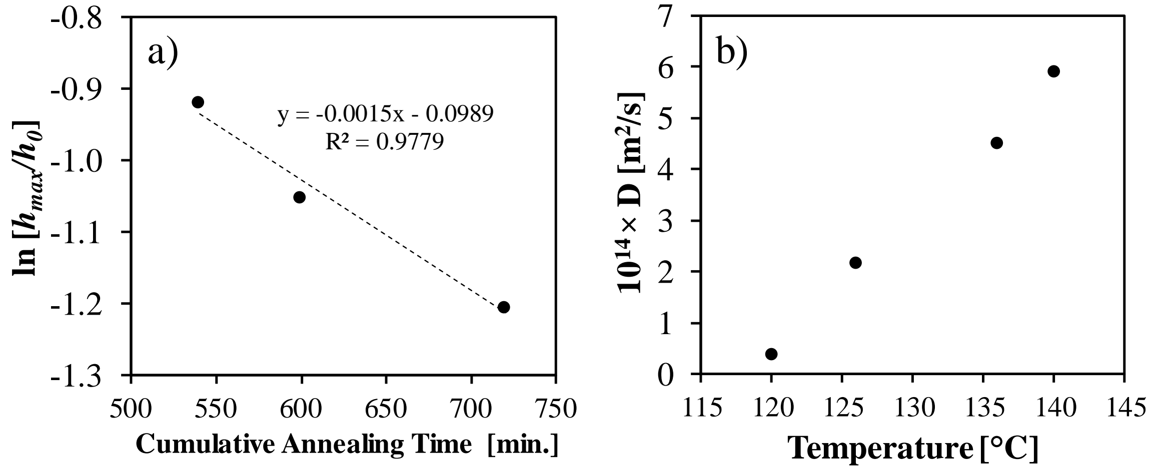

Figure A.6: (a) Experimental results at 120°C for long times (b) Diffusivity values extracted from experimental data at 120°C and extrapolated to higher temperatures as in Ref. 5.

A5: Secondary Peaks at Short Times

Simulations show that secondary peaks always form when a surface tension profile is present, but their longevity varies. When the mask periodicity is relatively small, short annealing times are necessary to observe them experimentally.

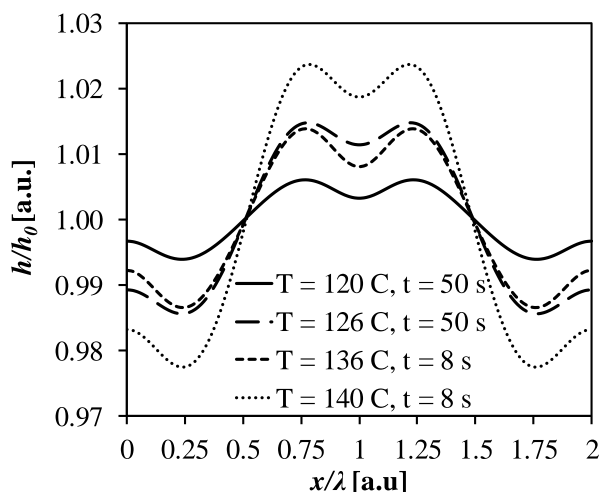

Figure A.7: Simulated film height profiles at short times clearly depict secondary peaks at four different annealing temperatures. Thicknesses of the film at each annealing temperature are identical to those used in Figure 2.3.

REFERENCES

1. Katzenstein, J. M.; Janes, D. W.; Cushen, J. D.; Hira, N. B.; McGuffin, D. L.; Prisco, N. A.; Ellison, C. J. *ACS Macro Lett.* **2012**, 1, 1150-1154.
2. Katzenstein, J. M.; Janes, D. W.; Hocker, H. E.; Chandler, J. K.; Ellison, C. J. *Macromolecules* **2012,** 45, 1544-1552.
3. Edelstein, A.; Amodaj, N.; Hoover, K.; Vale, R.; Stuurman, N. Computer Control of Microscopes Using µManager; John Wiley & Sons, Inc., 2001.
4. Dalnoki-Veress, K.; Forrest, J. A.; Murray, C.; Gigault, C.; Dutcher, J. R. *Phys. Rev. E* **2001,** 63, 031801.
5. Fleischer, G. *Polym. Bull.* **1984**, 11, 75-80.

APPENDIX B: BIDIRECTIONAL CONTROL OF FLOW IN THIN POLYMER FILMS BY PHOTOCHEMICALLY MANIPULATING SURFACE TENSION

B1. UV/Vis Spectra after Chemical Transformations

UV/Vis measurements were performed for films on quartz substrates after the typical protocol for each chemical transformation was performed. The initial film thickness of Film γ_0 was 240 nm. The film thickness reduced to 190 nm after the decarboxylation protocol and was unchanged after dehydrogenation. UV/Vis measurements on these films with the corresponding thicknesses are shown in Figure B.1. The light dose is attenuated by at most ~ 25% as it passes through the film for all photochemical reactions; therefore, the reactions take place throughout the depth of the films.

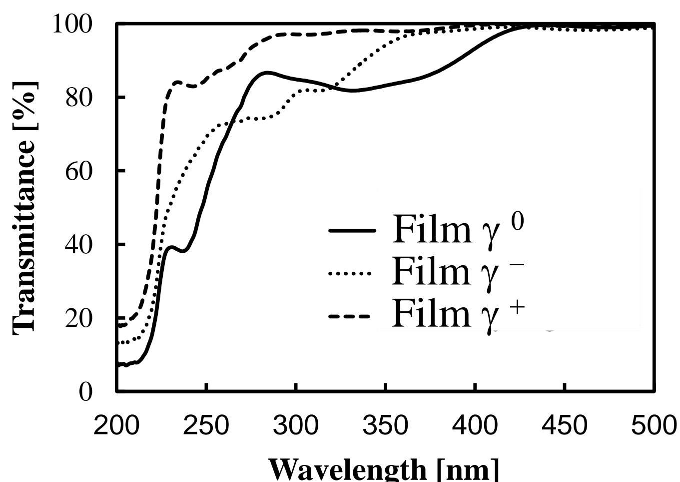

Figure B.1: UV/Vis spectra of films γ_0, γ^-, and γ^+.

This appendix reproduced in part from “Bidirectional Control of Flow in Thin Polymer Films by Photochemically Manipulating Surface Tension” Kim, C. B.; Janes, D. W.; Zhou, S. X.; Dulaney, A. R.; Ellison, C. J. *Chemistry of Materials* **2015**, *27*, 4538-4545 with permission from the American Chemical Society, copyright 2015.

B2. Carbon NMR Analysis

Carbon (^{13}C) NMR was used to determine the relative amount of monomers in the random copolymer. Approximately 100 mg/ml of Joncryl 611 was prepared in deuterated chloroform ($CDCl_3$), and the data was collected on a Varian Direct Drive 600. The sample was run with a 10 second relaxation delay at a 90 degree pulse angle for 512 repetitions. The spectra are shown in Figure B.2.

To estimate the composition of the random copolymer, the carbons were normalized by the benzylic ring (carbons C_B and C_C in Figure B.2). The values of x, and y were then determined to be 26, and 0.74, respectively. Several assumptions were made to estimate the composition. First, it was assumed that all non-hydrogenated carbons were from copolymer carbons C_A, and C_B in Figure B.2. The spectrum also contains end group effects and the possible presence of additives or residual small molecules/monomers in the as-received sample. Only very unambiguous peaks, such as the benzylic ring at 124-130 ppm, were used in the calculation to avoid including contaminants in the calculation.

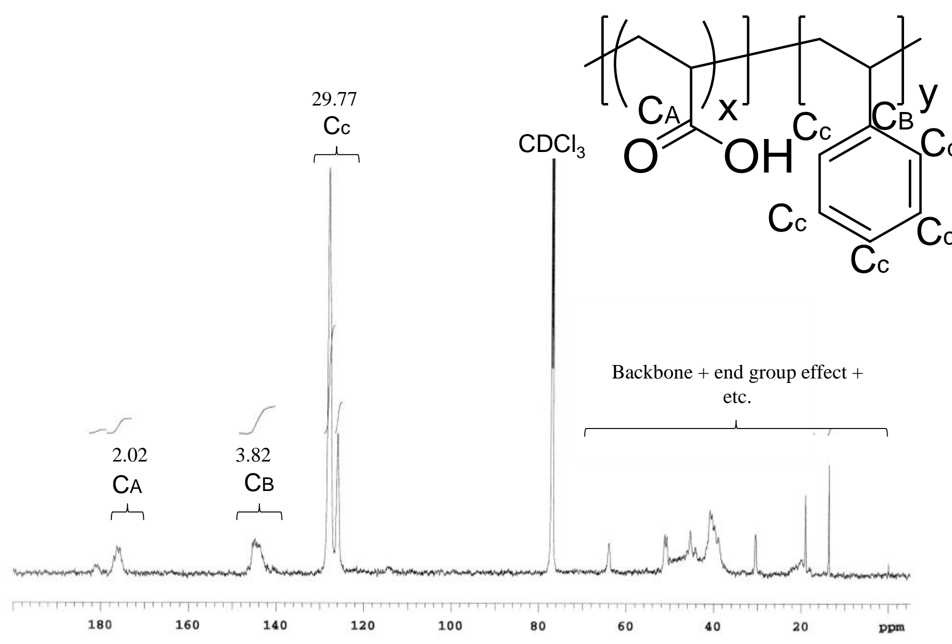

Figure B.2: ^{13}C-NMR of neat Joncryl as received.

B3. Example Feature Development Curves at 150 °C.

To provide an example of how film thickness variations develop over annealing time for both chemical transformations, the peak-to-valley film thickness variations were determined by profilometry as a function of cumulative annealing time at 150 °C and are shown in Figure B.3. During each light exposure step, the films were kept in the solid state and remained flat. Once these polymer films containing surface energy gradients were heated above T_g, the features formed due to Marangoni flow. While the features initially grow with heating time, long heating times result in dissipation of film thickness variations due to interdiffusion of film components erasing the surface tension pattern and capillary forces flattening the film.

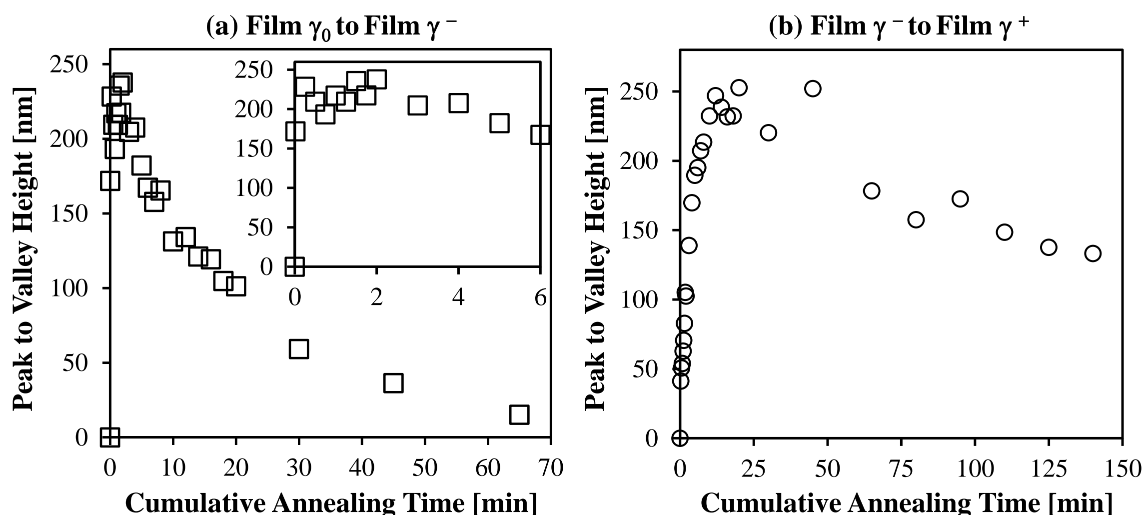

Figure B.3: Variation in film thickness as a function of cumulative heating time at 150 °C. An identical photomask used for Figure 3.3 in the main manuscript was used for this study. Each data point was characterized using a Veeco Dektak 6M stylus profiler with a stylus diameter of 25 microns and stylus force of 3 mg.

B4. Photochemical Mechanism of PBG

Under irradiation of a 365 nm light, a nifedipine photo-base generator, (4-(o-nitrophenyl)-2,6-dimethyl-1,4-dihydro-3,5-pyridinedicarboxylate), is converted to dimethyl 4-(o-nitrosophenyl)-2,6-dimehtyl-3,5-pyridinedicarboxtylate. A scheme showing this reaction is given in Figure B4a. The light exposed PBG can act as a base catalyst for the thermal decarboxylation of a copolymers containing an acrylic acid group.[1,2] The conversion of the PBG as a function of 365 nm exposure dose was characterized using FTIR. The normalized FTIR spectra can be seen in Figure B4b. All peaks were normalized by areas under the alkyl stretches from 2850 – 3100 cm^{-1}. As 365 nm exposure dose increases, the absorbance peak characteristic of N-H, at 3400 cm^{-1}, decreases. The area under the υ(N-H) peaks were used for quantitating the conversion of PBG, Figure B4c. As the FTIR data indicate, 0.4 J/cm^2 of 365 nm light fully converts the PBG to its basic form. To further confirm this conversion qualitatively, UV/Vis

absorption and fluorescence emission spectra of solutions containing PBG were acquired. These data are shown in Figure B4d and B4e, respectively. Upon light irradiation, the PBG creates a new π-conjugation center, blue-shifts its absorption, and fluoresces more strongly at 360 - 570 nm with λ_{ex} = 310 nm.

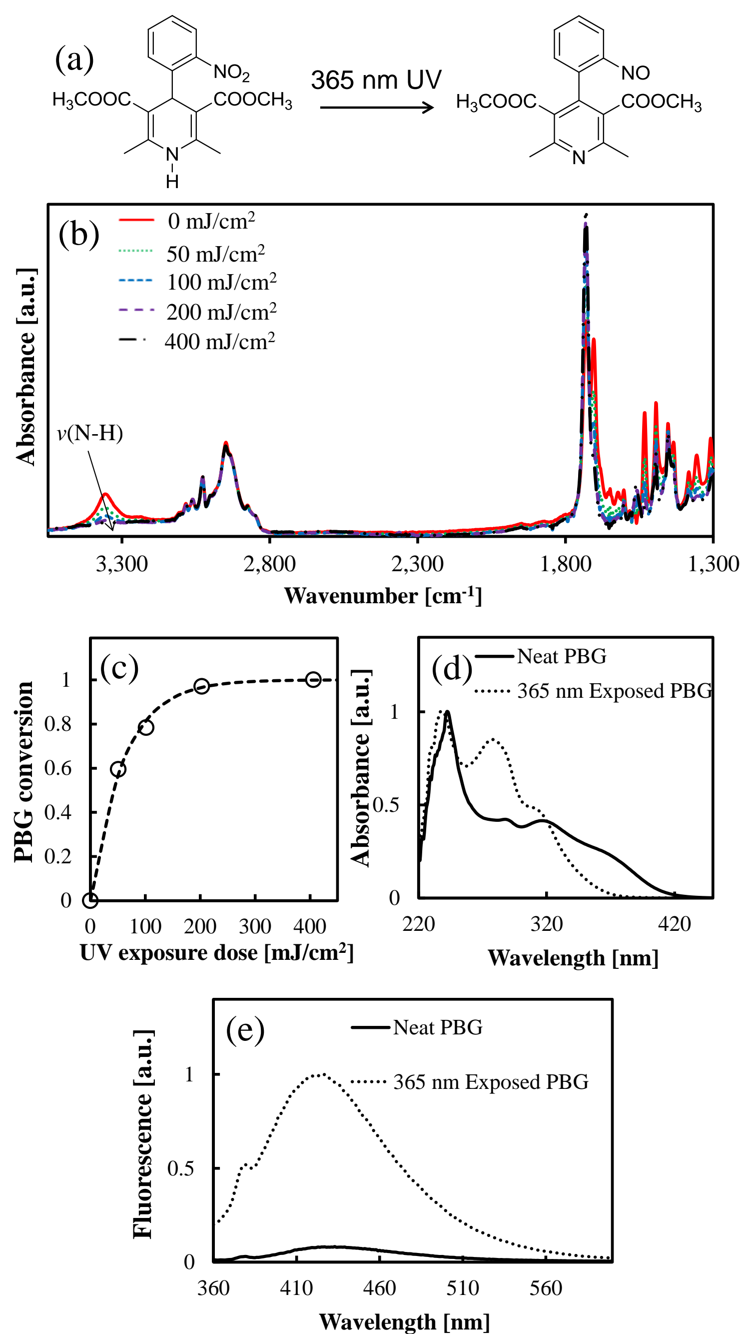

Figure B.4: (a) illustrates a reaction scheme of PBG upon 365 nm UV exposures. (b) shows representative IR peak changes upon light exposures. All peaks were normalized by the area under the alkyl stretches from 2850 – 3100 cm^{-1}. (c) is conversion data characterized by the area under IR peaks, *v*(N-H), as exposure dose increases. (d) UV/Vis and (e) fluorescence emission spectra using a solution sample containing only PBG in diglyme (0.15 mg/ml). For the fluorescence spectra, $\lambda_{excitation}$ = 310 nm was used.

B5. Glass Transition Temperatures of Films

The glass transition temperature, Tg, of polymer films after being subjected to representative processing conditions were determined by spectroscopic ellipsometry. The film was heated at 120 °C for 5 min then cooled at 2 °C/min to - 20 °C. The film's thickness, h(T), was determined at each sample temperature, T, using a model that fit the optical constants and film thickness. The Tg was found by regressing the equation B1[3]

$$h(T) = w\left(\frac{M-G}{2}\right)\ln\left[cosh\left(\frac{T-T_g}{w}\right)\right] + \left(T-T_g\right)\left(\frac{M+G}{2}\right) + C \tag{B1}$$

to the data. The parameters M (related to liquid state thermal expansivity), G (related to glass state thermal expansivity), Tg, and C (the film thickness at T=Tg) were fit and the glass transition width was set as w = 10 °C. Using larger or smaller values of w did not change the extracted value of Tg by more than 1 °C. The starting film containing PBG, γ_0, exhibits a glass transition 5 °C lower than neat copolymer due to the plasticizing effect of PBG. The film T_g increased up to 7 °C after all chemical transformations.

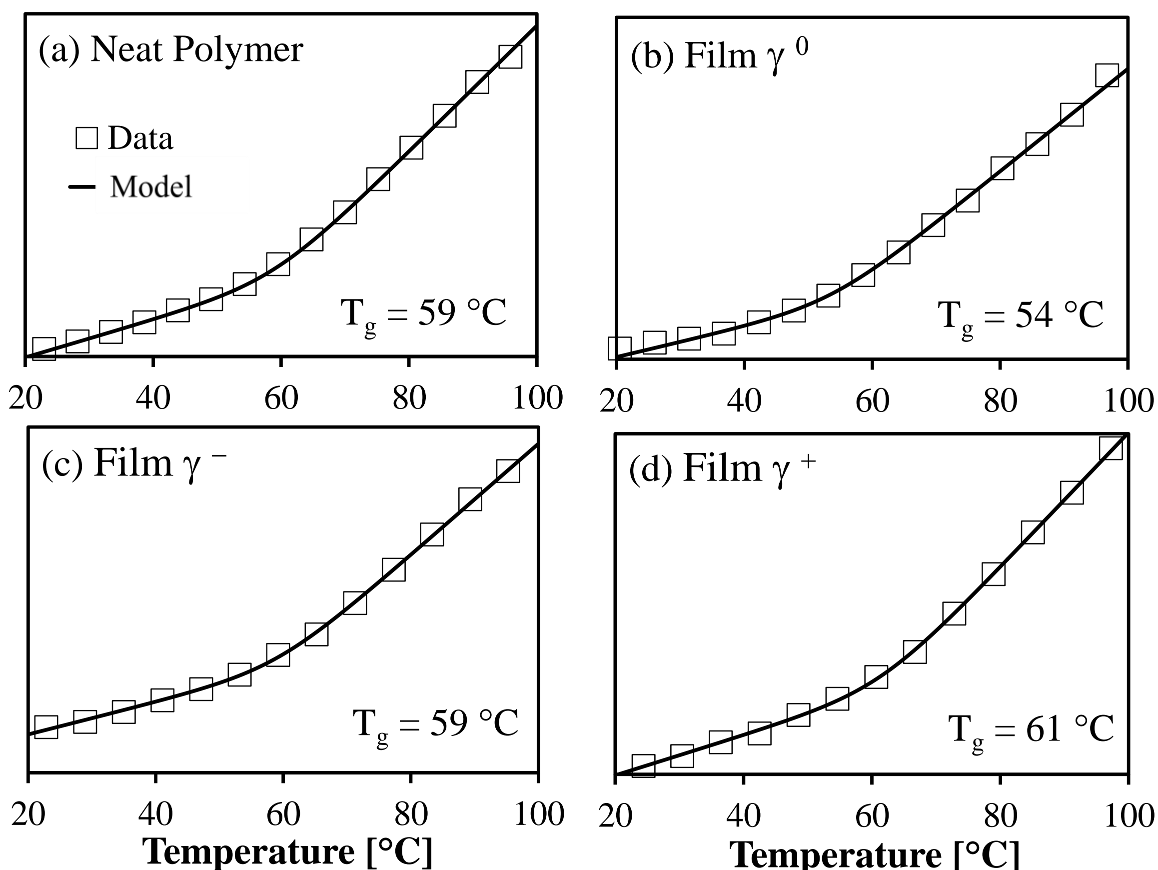

Figure B.5: The glass transitions of a Joncryl films as determined by spectroscopic ellipsometry after being subjected to representative processing conditions: (a) neat Joncryl without PBG, (b) Joncryl with 30 wt% PBG, (c) after decarboxylation, and (d) after dehydrogenation. For clarity only every 100th data point is displayed. The solid lines represent regressions of Eq. 1 in the main manuscript to the full data set.

B6. Chemical Characterization of Film γ^-

FTIR was used to quantify the extent of decarboxylation. After 0.4 J/cm^2 of 365 nm light exposure to fully convert PBG to its basic form, the film was thermally annealed at 150 °C from 0 to 5 minutes and the corresponding FTIR spectra of the films are shown in Figure B.6. All peaks were normalized by areas under the alkyl stretches from 2850 – 3100 cm^{-1}. Also, we noted that residual diglyme (spin-coating solvent, boiling point = 162 °C) was present before heating, but soon after the heating, the diglyme evaporated (at

wavenumber ~ 1560 cm^{-1}.)[4] The normalized film thickness reduction of the same film used for FTIR can be seen in Figure B.7. Additional controlled experiments were performed which indicate the thickness reduction was mainly due to the evaporation of residual diglyme in the polymer film.

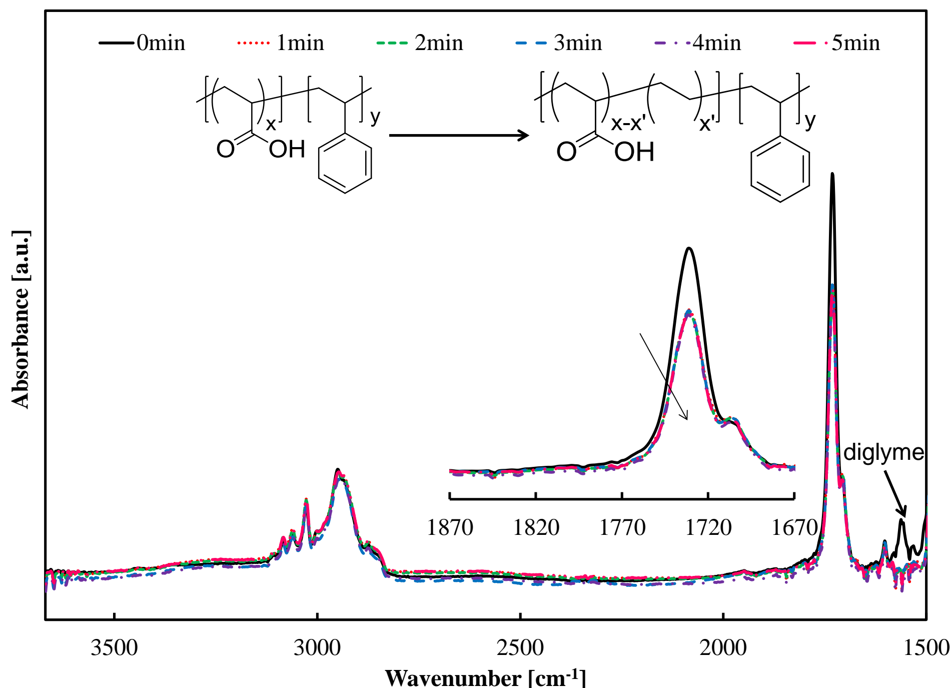

Figure B.6: FTIR for decarboxylation upon thermal annealing at 150 °C from 0 to 5 minutes. Prior to the thermal annealing, PBG was fully activated by exposing 365 nm UV light with dose of 0.4 J/cm^2. All spectra were normalized by area under the alkyl stretches (insensitive through this chemical transformation) from 2850–3100 cm^{-1}. Inset shows magnified region showing carbonyl peak reductions before and after thermal annealing for 5 minutes.

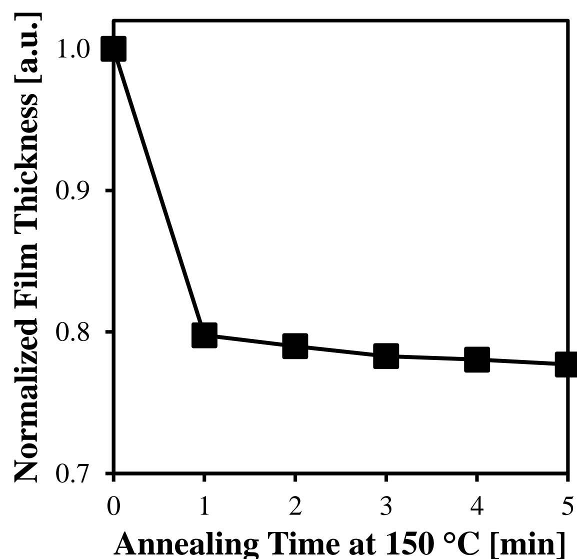

Figure B.7: Normalized film thickness upon thermal annealing. Prior to this heating the 365 nm UV exposure was given with a dose of 0.4 J/cm^2.

B7. Chemical Characterization of Film γ^+

FTIR was used to quantify the extent of dehydrogenation and spectra are shown in Figure B.8. All peaks were normalized by area under the carbonyl from 1670 – 1870 cm^{-1} because the carbonyl is insensitive to this chemical transformation. Alkyl C-H stretch signals (2850–3000 cm^{-1}) diminish while the alkenyl C=C stretch (1580 – 1620 cm^{-1}) signals intensify upon broadband UV exposure, consistent with dehydrogenation converting alkane to alkene backbone bonds.[5,6] To quantify the degree of dehydrogenation, the area under dissipating alkyl C-H stretch signals (2850–3000 cm^{-1}) was measured. Because the area under these peaks decreases by 6 % under typical exposure conditions, we estimate that 6 % of the styrene subunits have been dehydrogenated in Film γ^+.

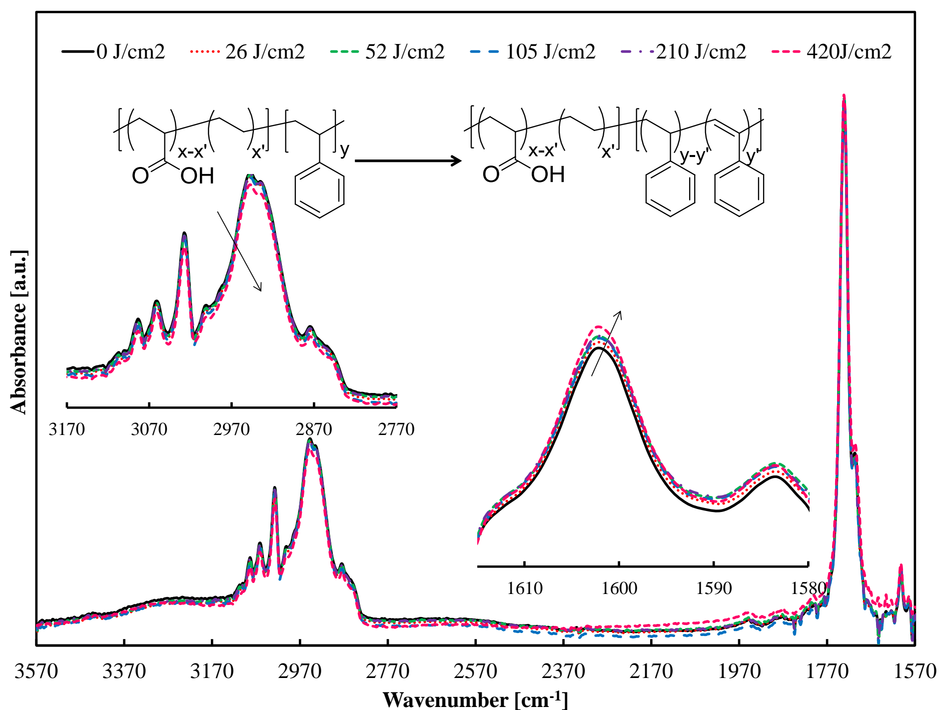

Figure B.8: FTIR for dehydrogenation upon broadband UV exposure from 0 to 420 J/cm^2. All spectra were normalized by area under the carbonyl from 1670 – 1870 cm^{-1} since the carbonyl is insensitive through this chemical transformation. A left hand side inset is a magnified region showing alkyl C-H stretch reductions while the right hand side inset shows alkenyl C=C signal intensifies upon broadband UV exposures.

B8. AFM of Dewetted Host Polymer Film on Crosslinked PCHE

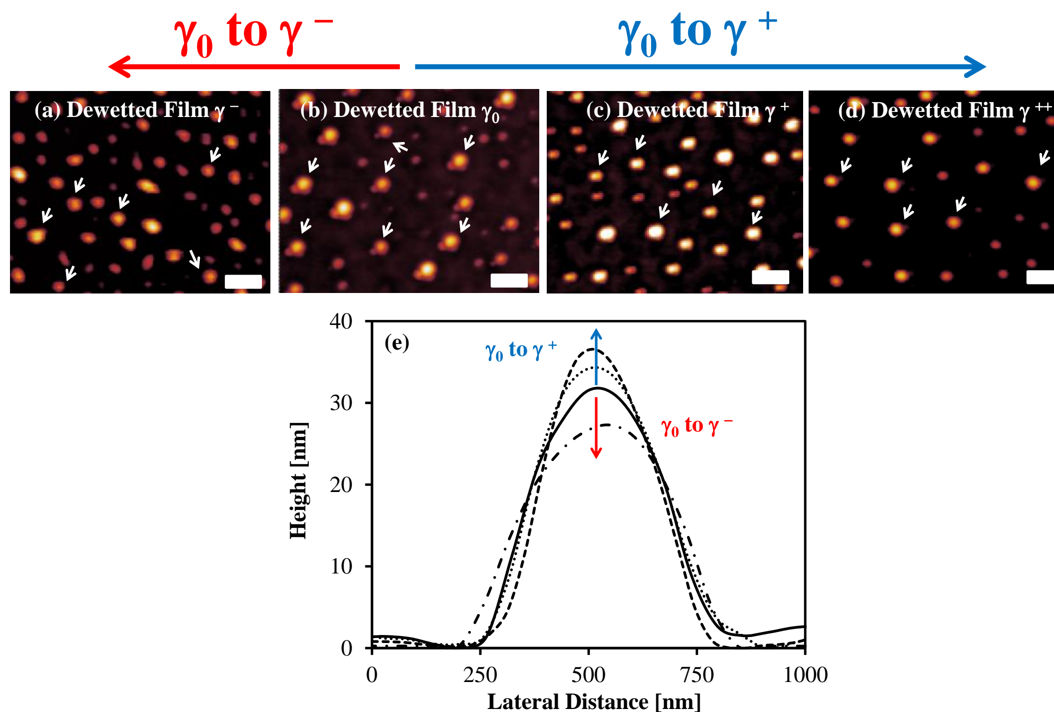

Figure B.9: AFM height profile of dewetted host polymer (a) after decarboxylation, (b) neat, (c) after dehydrogenation and (d) after even further dehydrogenation. Scale bars indicate 1 μm. Arrows on each image indicate the droplet used for measuring contact angle. (e) Representative height profile of one droplet on each sample. The droplet for this comparison has identical volume of 0.004 μm^3.

REFERENCES

1. Song, S.; Yokoyama, S.; Takahara, S.; Yamaoka, T. Novel Dual-mode Photoresist Based on Decarboxylation by Photogenerated Base Compound. *Polym. Adv. Technol.* **1998,** 9, 326–333.
2 Song, S.; Takahara, S.; Yamaoka, T. Photogenerated Base Catalyzed Decarboxylation in Polymers with an Aliphatic or an Aromatic Carboxyl Group. *J. Photopolym. Sci. Tech.* **1998,**11, 171–172.
3. Dalnoki-Veress, K.; Forrest, J. A.; Murray, C.; Gigault, C.; Dutcher, J. R. Molecular Weight Dependence of Reductions in the Glass Transition Temperature of Thin, Freely Standing Polymer Films. *Phys. Rev. E* **2001,**63, 031801.
4. National Institute of Advanced Industrial Science and Technology. Spectral Database for Organic Compounds. http://sdbs.riodb.aist.go.jp/sdbs/

5. Arshad, T.; Kim, C. B.; Prisco, N. A.; Katzenstein, J. M.; Janes, D. W.; Bonnecaze, R. T.; Ellison, C. J. Precision Marangoni-driven Patterning. *Soft Matter* **2014**, 10, 8043–8050.
6. Katzenstein, J. M.; Janes, D. W.; Cushen, J. D.; Hira, N. B.; McGuffin, D. L.; Prisco, N. A.; Ellison, C. J. Patterning by Photochemically Directing the Marangoni Effect. *ACS Macro Lett.* **2012,** 1, 1150–1154.

APPENDIX C: GENERATING LARGE AND THERMALLY STABLE MARANGONI-DRIVEN TOPOGRAPHICAL PATTERNS IN THIN POLYMER FILMS BY PHOTOCHEMICALLY STABILIZING THE SURFACE ENERGY GRADIENT

C1. Polymer characterization

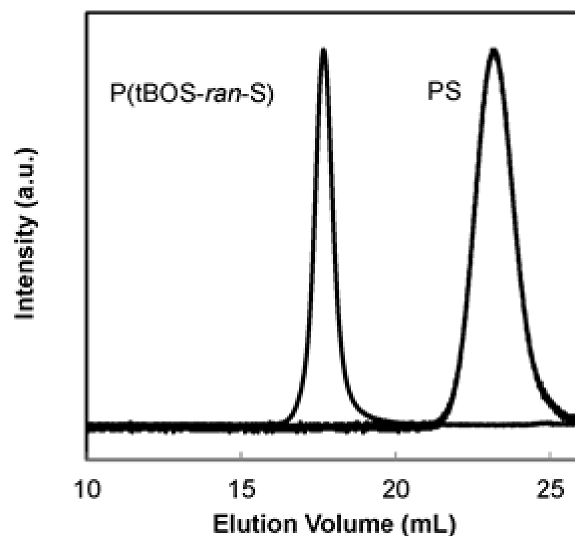

Figure C.1: Gel permeation chromatography of synthesized PS (M_n=2.6 kDa, Đ=1.1) and P(tBOS-*ran*-S) (M_n=42 kDa, Đ =1.01) in tetrahydrofuran (THF).

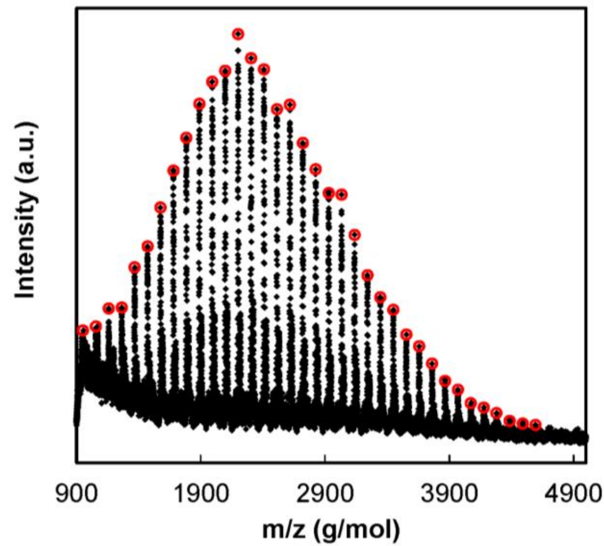

Figure C.2: Molecular weight distribution of the low molecular weight PS (M_n=2.6 kDa, Đ =1.1) by MALDI.

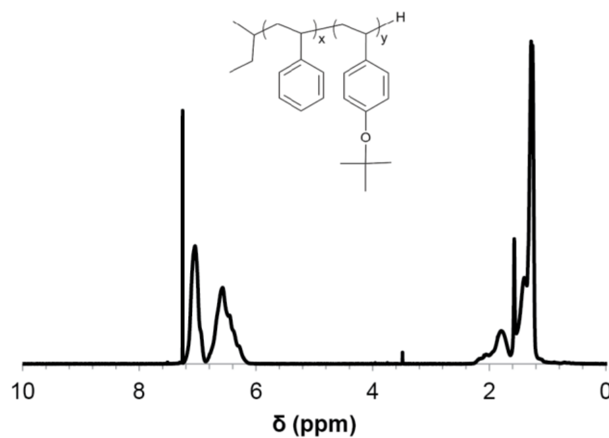

Figure C.3: ^{1}H NMR of P(tBOS-*ran*-S) used to calculate the molar ratio of *tert*-butoxystyrene: styrene.

C2. POLYMER THIN FILM CHARACTERIZATION

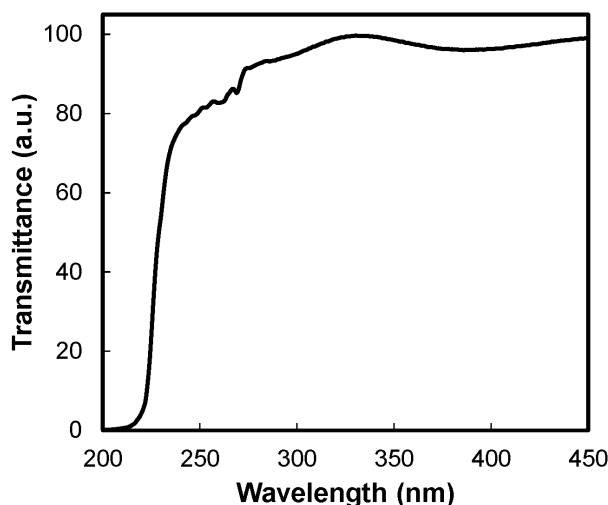

Figure C.4: UV/Vis spectrum of a 30 wt% P(tBOS-*ran*-S) in PS film showing high transmittance in the mid-UV range.

C3. CONTROL EXPERIMENTS FOR FEATURE DEVELOPMENT

To confirm that the deprotection chemistry was required for development of large stable features, a control film was prepared without PAG. As seen in Figure C.5, films exposed to 1 min UV and annealed for 10 min at 120°C showed no deprotection of P(tBOS-*ran*-S). Similar films were also exposed through a photomask (12.5 μm half periodicity). While feature development was expected due to the dehydrogenation of PS,[1] the low dose compared to prior studies (34 J/cm^2 in the present work vs. 140 J/cm^2 in prior work) led to a reduction in the magnitude of the surface tension gradient. Thus, only a maximum of 60 nm (compared to the initial thickness of 285 nm) in feature height was observed and these features decayed over 24 h (as with PS).

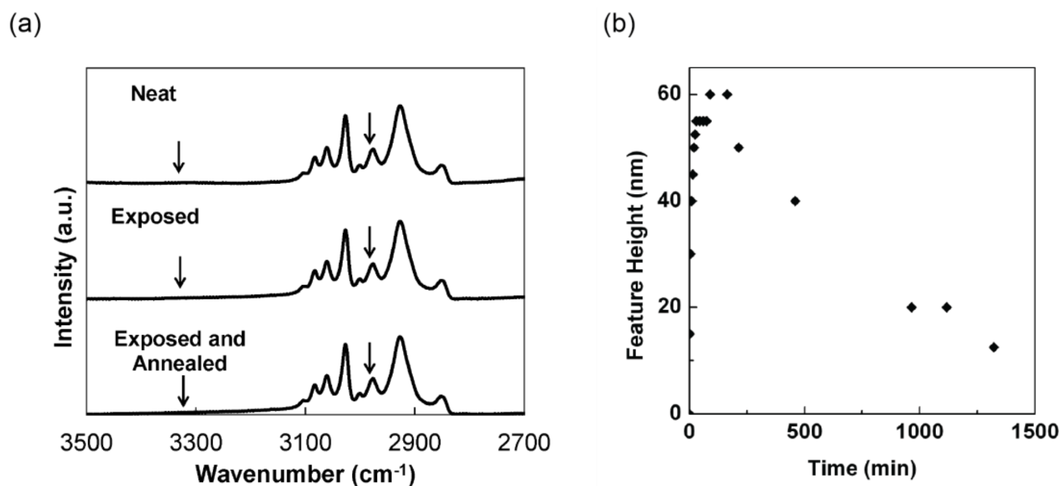

Figure C.5: FTIR (a) and feature development (b) for a 30 wt% P(tBOS-*ran*-S) film without PAG. Exposure (1 min UV, 34 J/cm^2) and annealing at 120°C for 10 minutes shows no deprotection. Feature height, for a film exposed and annealed through a line-and-space photomask, increased to a maximum of 60 nm and slowly decayed over 24 h.

Table C.1: Effect of full deprotection on film thickness of all blends

Wt% P(tBOS-*ran*-S)	% Loss of initial film thickness[a]
10	1.4
20	4.9
30	7.6
100	17

[a]All films were exposed to 1 min UV and annealed at 120°C until the film thickness remained constant. The PAG concentration was 5 wt% with respect to the percentage of tBOS in P(tBOS-*ran*-S).

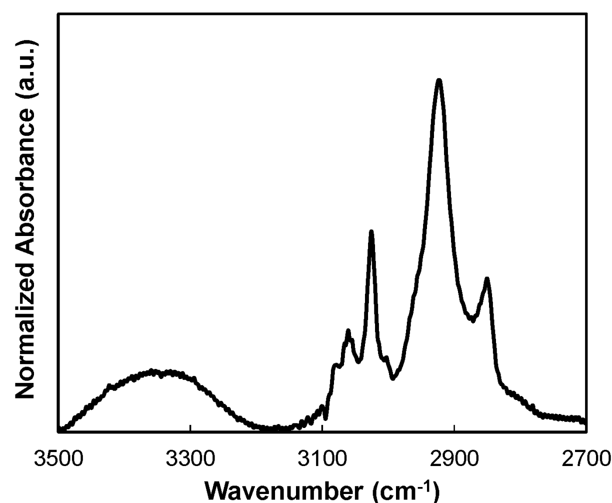

Figure C.6: FTIR spectra of P(HOST-*ran*-S) synthesized in a solution of hydrochloric acid and dioxane as described in the experimental methods section.

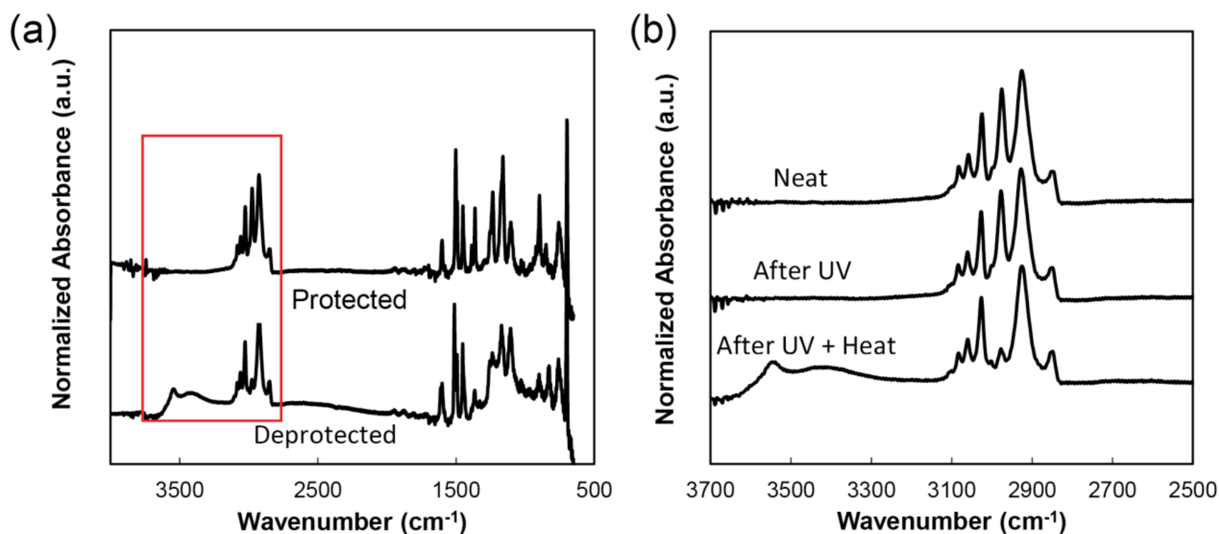

Figure C.7: (a) Full FTIR spectra of protected (neat P(tBOS-*ran*-S)) and deprotected polymer (P(HOST-*ran*-S)). (b) Selected spectra for neat P(tBOS-*ran*-S), after only UV, and after UV and annealing at 120°C for 10 min demonstrating that both UV and heat were required for deprotection to occur. All spectra were normalized to the light insensitive phenyl peak at 2926 cm^{-1}.

C4. Polymer miscibility calculations

The monomer ratio of 3:7 in P(tBOS-*ran*-S) was selected based on miscibility predictions using the Flory-Huggins Parameter, and the following relationship:

$$\chi - \chi_{critical} = \frac{V_1(\delta_1 - \delta_2)^2}{RT} - \frac{1}{2}\left(\frac{1}{\phi_1 N_1} + \frac{1}{\phi_2 N_2}\right) \quad \text{(C1)}$$

where V_1 is the molar volume, and $\delta_{1,2}$ represent the Hansen solubility parameters of each polymer and $N_{1,2}$ represent the degree of polymerization for each polymer. Hansen solubility parameters were estimated using group contribution methods according to van Krevelen and Hoy[2-3] and corresponding estimated values for surface tension are given in Table C.2.

Table C.2: Parameters used in miscibility calculations

Parameter	PS	P(tBOS-*ran*-S)	P(HOST-*ran*-S)
M_0 (g/mol)	104	127	109
ρ (g/ml)	1.05	1.03	1.08
V (ml/mol)	99	123	101
N^a	25	333	333
δ ($MPa^{1/2}$)	18.0	17.7	19.4

[a] Calculated from the molecular weight from GPC (for P(tBOS-*ran*-S)) and MALDI for PS

As seen in Figure C.8, as the percentage of tBOS incorporated into the P(tBOS-*ran*-S) copolymer was increased, the deprotected polymer P(HOST-*ran*-S) became increasingly more immiscible (χ-$\chi_{critical}$>0) with P(tBOS-*ran*-S). Since surface energy (γ) and the Hansen solubility parameters are related Equation (C2),[3] a large difference in Hansen solubility parameters, i.e. immiscibility, is advantageous for formation of a high

surface tension gradient, but Marangoni flow could be inhibited due to incompatibility of the two polymer phases.

$$\gamma = 0.75(\delta^2)^{\frac{2}{3}} \quad \text{(C2)}$$

Furthermore, the use of a transport polymer, PS, with a solubility parameter in between the upper and lower bounds (δ of P(HOST-*ran*-S) and P(tBOS-*ran*-S) respectively) removes the need for the two surface energy forming phases to be compatible. PS was found to be always miscible with P(tBOS-*ran*-S); however, at ratios above ca. 30 mol% tBOS, miscibility of PS in P(HOST-*ran*-S) trends towards immiscible. These estimations vary largely depending on the selected method for calculation of the Hansen solubility parameters and are included not as absolute values, but as a means to motivate selection of an appropriate monomer composition.

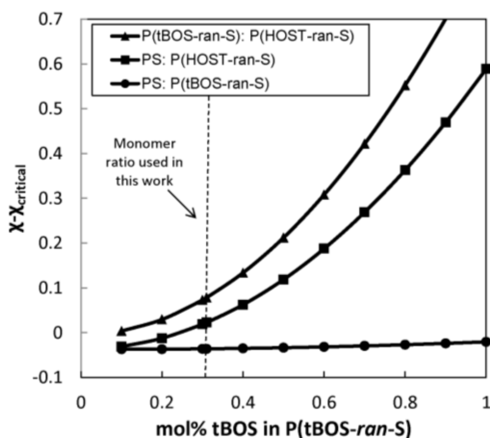

Figure C.8: Predictions of the mol% tBOS required to ensure miscibility of P(tBOS-*ran*-S) and P(HOST-*ran*-S) with PS (χ-$\chi_{critical}$<0), while maximizing immiscibility between P(tBOS-*ran*-S) and P(HOST-*ran*-S) (χ-$\chi_{critical}$>0). Predictions shown are calculated based on the molecular weights of polymers used in this study and the ratio of PS to P(tBOS-*ran*-S) or P(HOST-*ran*-S) of 30wt%.

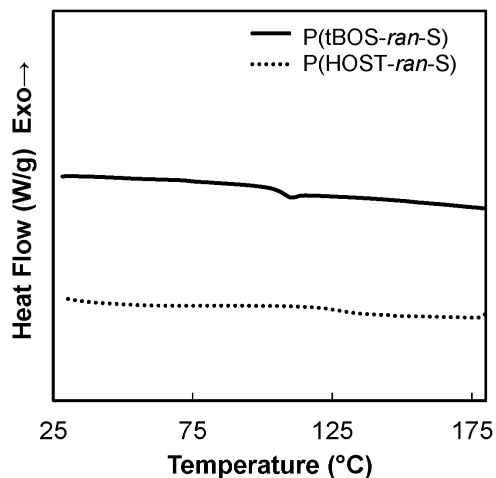

Figure C.9: DSC traces of homopolymers P(tBOS-*ran*-S) and P(HOST-*ran*-S).

C5.DIRECTIONALITY OF FLOW

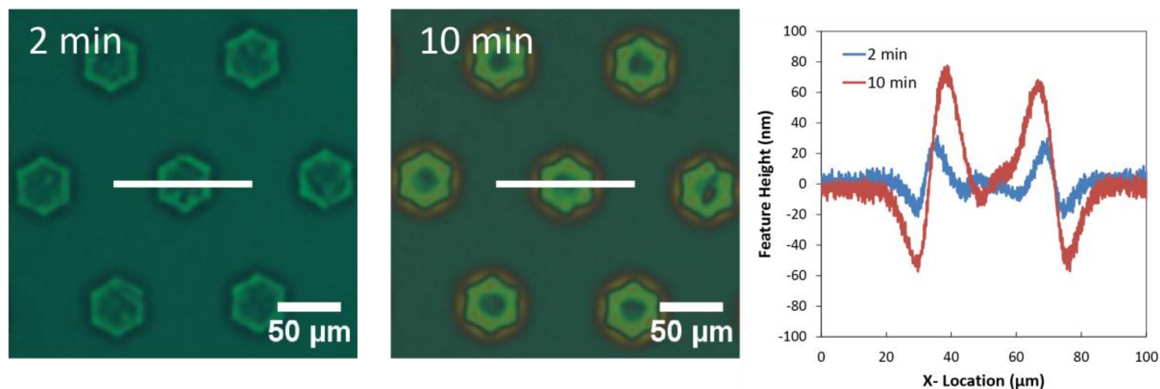

Figure C.10: Directionality of flow as confirmed using a photomask patterned with isolated hexagons. Here, regions of exposure were hexagonal in shape and subsequent annealing produced hexagonal regions of P(HOST-*ran*-S). Thus, polymer flowed towards the hexagonal regions with increasing time. Lines represent the direction of the corresponding profilometry traces.

C6. MARANGONI AND CAPILLARY VELOCITY CALCULATIONS

The effect of PAG concentration on feature evolution is shown below in Figure C.11. The different feature heights are a result of incomplete deprotection, which was confirmed by FTIR (Figure C.12).

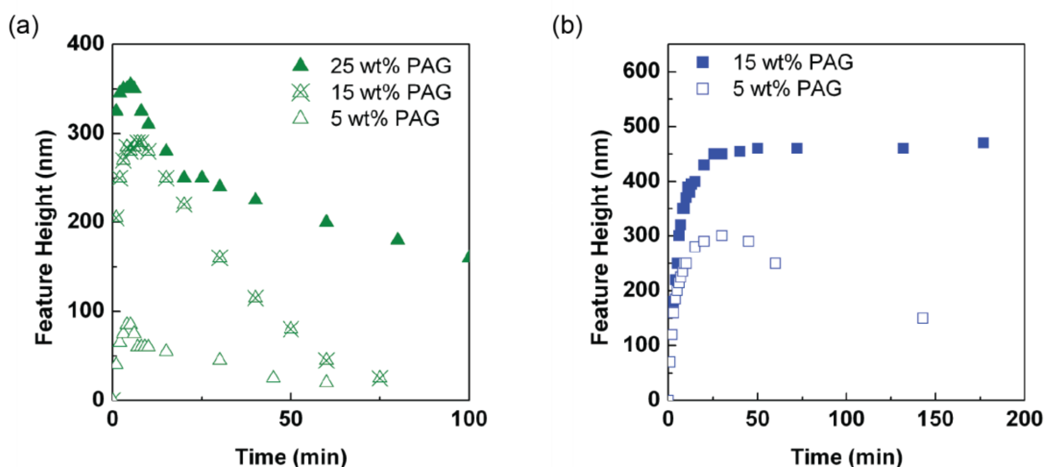

Figure C.11: Effect of PAG concentration on evolution of features for (a) 10 wt% P(tBOS-*ran*-S) and (b) 20 wt% P(tBOS-*ran*-S). All PAG concentrations were calculated based on the percentage of tBOS incorporated in P(tBOS-*ran*-S).

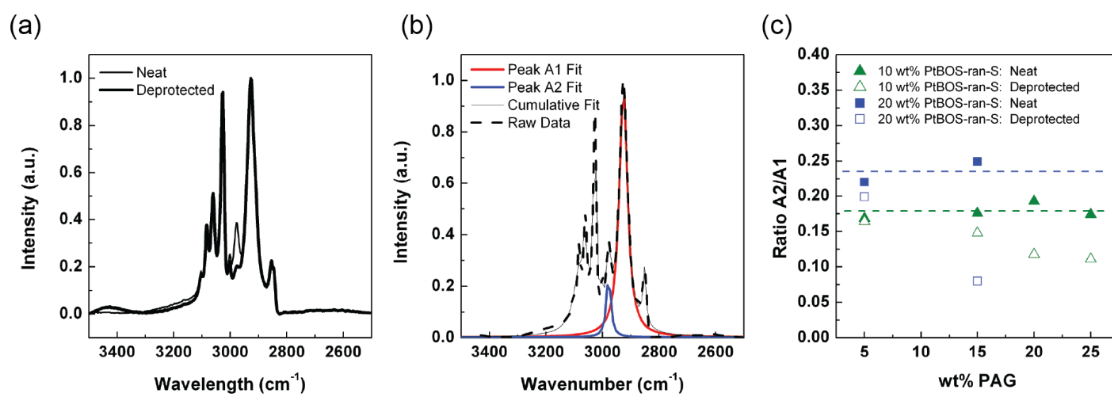

Figure C.12: Calculation of % deprotection from FTIR. (a) Representative FTIR spectra showing a decrease in the peak at 2900 cm^{-1} due to deprotection. (b) FTIR trace for a neat 20 wt% P(tBOS-*ran*-S) blend after peak deconvolution showing the area for peak A1, area for peak A2, and cumulative fit which includes all peaks that were fitted. (c) Ratios of A2/A1 before (neat) and after deprotection (deprotected) for increasing PAG concentration. Dashed lines show average neat values used to represent 0% deprotection.

The relative change in the peak area (A2/A1 in Figure C.12) was used to calculate a percentage of deprotection, which was in turn used to estimate a surface tension

gradient. Estimations of the surface tension values for homopolymers were obtained by fitting contact angle measurements for each homopolymer to a known value for poly(styrene) of 39.3 dyne/cm[4] using the Young-Dupré equation Equation (C3).

$$\gamma_{polymer} = \gamma_{PS} \left[\frac{\cos \vartheta_{polymer} + 1}{\cos \vartheta_{PS} + 1} \right]^2 \quad (C3)$$

The surface energy of each blend could then be calculated by weighting the contribution of each homopolymer by the corresponding molecular weight. A summary of the results is given in Table C.3.

Table C.3: Calculations of Marangoni and capillary velocities

Wt% P(tBOS-*ran*-S)	Wt% PAG[a]	% Deprotection	Δγ (dyne/cm)	Ma/μ (μN/m)	Ca/μ (μN/m)
10	5	21	0.008	0.20	0.10
10	15	45	0.02	0.42	0.49
10	25	100	0.04	0.93	0.59
20	5	20	0.02	0.47	0.47
20	15	100	0.09	2.1	0.85
30	5	100	0.2	3.5	0.91

[a]All PAG concentrations were calculated based on the percentage of tBOS incorporated in P(tBOS-*ran*-S).

References

1. Katzenstein, J. M.; Janes, D. W.; Cushen, J. D.; Hira, N. B.; McGuffin, D. L.; Prisco, N. A.; Ellison, C. J. *ACS Macro Lett.* **2012,** *1* (10), 1150-1154.
2. Grulke, E. A., *Polymer Handbook*. 4th ed.; John Wiley & Sons: Hoboken, 1999; Vol. 2, p 675-688.
3. Bicerano, J., *Prediction of Polymer Properties*. 3rd ed.; CRC Press: New York, 2002.
4. Wu, S., *Polymer Handbook*. 4th ed.; John Wiley & Sons: Hoboken, 1999; Vol. 2, p 525.

APPENDIX D: PATTERNING THIN POLYMER FILMS BY PHOTODIRECTING THE MARANGONI EFFECT USING PHOTOSENSITIZERS

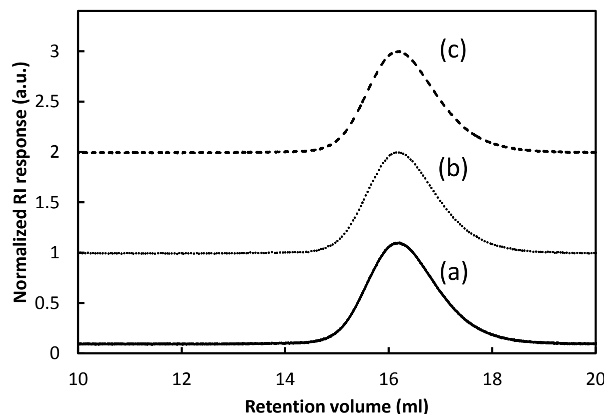

Figure D.1: Normalized SEC RI response plot: (a) before UV exposure, (b) after 400 (± 50) nm light exposure (for 15 minutes), and (c) after thermal annealing at 120 °C for 30 minutes.

Table D.1: Percent of polymer film that remained as characterized by spectroscopy ellipsometry after the described procedure was performed on the film (5 wt% DBA) followed by soaking the film in THF and drying. Photo-exposure with 400 (± 50) nm wavelength light was used.

Exposure Duration	5 minutes	15 minutes
Film thickness remaining after THF wash after photo-exposure	0.3 %	0.2 %
Film thickness remaining after THF wash after post exposure thermal annealing	0.5 %	0.5 %

This appendix reproduced in part from "Surface Energy Gradient Driven Convection for Generating Nanoscale and Microscale Patterned Polymer Films using Photosensitizers" Kim, C. B.; Janes, D. W.; McGuffin, D. L.; Ellison, C. J. *Journal of Polymer Science Part B: Polymer Physics* **2014**, 52, 1195-1202 with permission from John Wiley and Sons, copyright 2014.

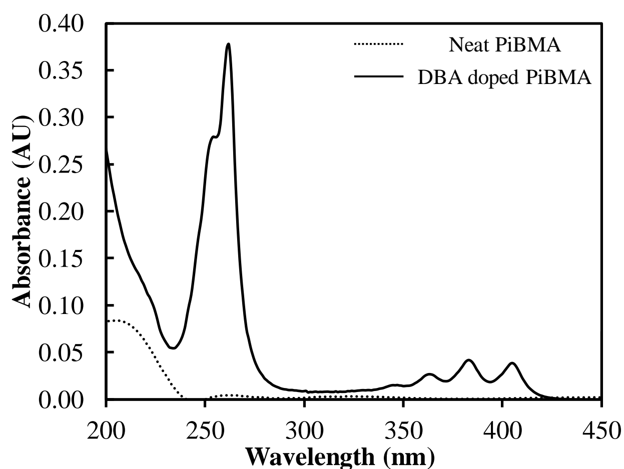

Figure D.2: UV-vis absorption spectra of neat PiBMA and 5 wt% DBA dopant in the PiBMA matrix. Initial film thickness was 150 nm on quartz. The wavelength range from 350 to 450 nm was used only during the photo-exposure.

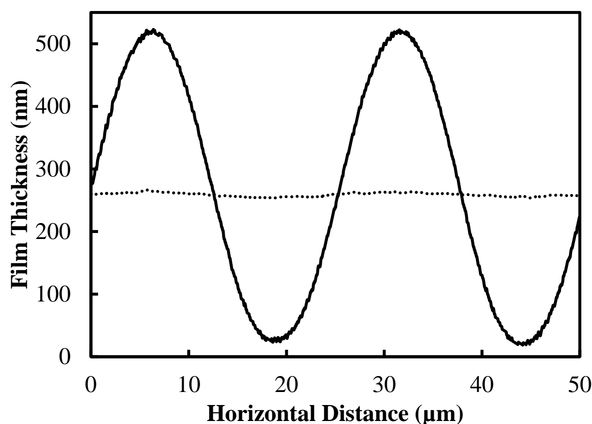

Figure D.3: Comparison of feature formations resulting from photo-exposure in air (solid line) and argon (dotted line) atmospheres. The representative topographical film thickness variations for two periodicities of each sample are shown which were collected with profilometry. Both samples were exposed to light for five minutes and annealed at 120 °C for 60 minutes.

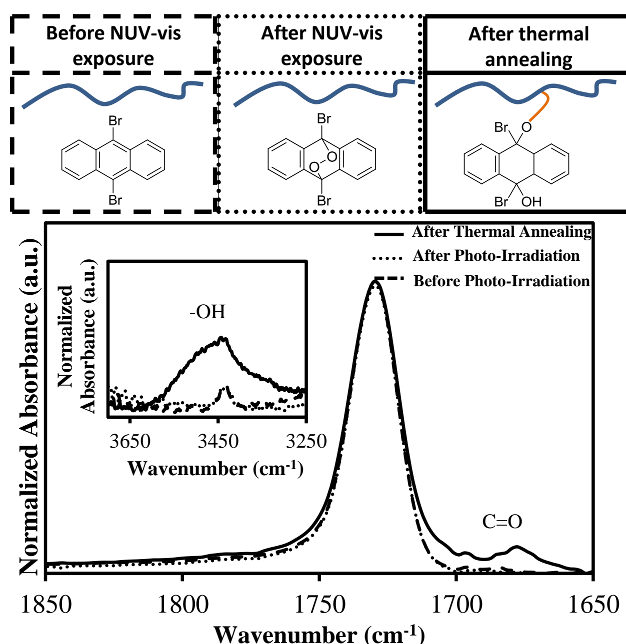

Figure D.4: FTIR spectra of the same DBA (10 wt%) doped PiBMA film: before photo-exposure, after 15 minutes of irradiation, and after 30 minutes of subsequent thermal annealing at 120 °C. Inset is a magnified window showing the hydroxyl signal. All spectra are normalized to the tallest ester peak at 1730 cm^{-1} corresponding to the ester on PiBMA which is a constant during the experiment. Films were all approximately 250 nm thick on double side polished silicon substrates.

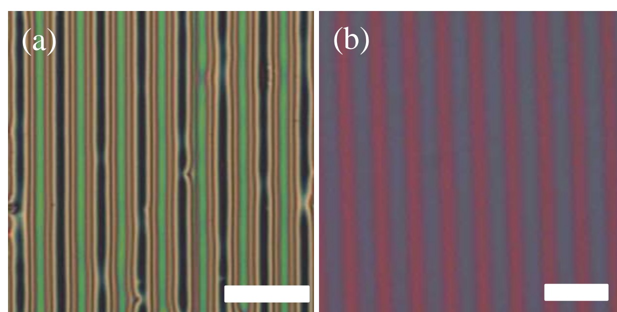

Figure D.5: Optical micrographs of patterned films with DBA in different host polymers: (a) polystyrene (PS) (M_n = 2.9 kDa, PDI = 1.36, T_g = 61 ^oC), and (b) poly(methyl methacrylate) (PMMA) (M_n = 9.6 kDa, PDI = 1.43). Scale bars indicate 50 μm. Both films contain 5 wt% DBA. 60 J/cm^2 of NUV-vis light exposure (15 minutes) was applied through a 25 μm pitch photomask for both samples. The PS film was heated at 126 ^oC for 30 min, and the PMMA film was heated at 176 ^oC for 30 min. The sinusoidal thickness profiles possessed peak-to-valley heights of 450 nm and 40 nm, respectively.

APPENDIX E: A PHOTOCHEMICAL APPROACH TO STABILIZING MARANGONI-DRIVEN PATTERNED POLYMER FILMS USING PHOTOSENSITIZERS

E1. Synthesis of Bis-Benzophenone

3-benzoyl-benzoic acid (6.7 g) was dissolved in a three neck flask fitted with a reflux condenser in 250 mL methylene chloride and 50 mL diethyl ether along with 4-pyrrolidinopyridine (0.4 g) and dicyclohexylcarbodiimide (6.1 g) and the reaction was sparged with dry argon for 30 mins. Ethylene glycol (0.93 g) was separately dissolved in about 20 mL of methylene chloride and sparged with dry argon for 10 minutes and then cannulated into the reaction vessel. The reaction was allowed to proceed at room temperature overnight and then refluxed for five hours. The reaction mixture was then filtered and washed with fresh methylene chloride. The solution was then liquid/liquid extracted with deionized water (3 x 100mL), 5% acetic acid (3 x 100 mL), deionized water (2 x 100 mL) and concentrated sodium chloride solution (1 x 100 mL). The organic layer was then dried with magnesium sulfate and the solvent removed by rotary evaporator and the solids were recrystallized twice out of ethanol and collected as a white powder (yield 36%, pure within NMR limits of detection).

E2. T_g of PiBMA Blends

DSC samples were prepared by dissolving spin-coated films in tetrahydrofuran and depositing a few drops of the solution in an aluminum DSC pan, which was initially dried at 55 ^{o}C. Using a Mettler-Toledo DSC-1, the samples were further annealed at 150 ^{o}C for 20 minutes to drive off residual solvent. Midpoint T_g values of PiBMA blends

---

This appendix reproduced in part from "A Photochemical Approach to Directing Flow and Stabilizing Topography in Polymer Films" Katzenstein, J. M.; Kim, C. B.; Prisco, N. A.; Katsumata, R.; Li, Z.; Janes, D. W.; Blachut, G.; Ellison, C. J. *Macromolecules* **2014**, 47, 6804-6812 with permission from American Chemical Society, copyright 2014.

were measured from a second heating cycle with a 10 °C/min heating rate. Table E.1 contains the T_g of several compositions. Blends of PiBMA and small molecule dopants have lower overall T_g than the neat homopolymer.

Table E.1: T_g of various compositions showing the plasticization effect of small molecules on PiBMA.

PiBMA(wt%)	MK (wt%)	BB (wt%)	T_g Midpoint (^oC)
100	0	0	55
98	2	0	48
97	2	1	46
93	2	5	39
90	0	10	34
88	2	10	27

E3. UV/Vis Spectra After Exposure

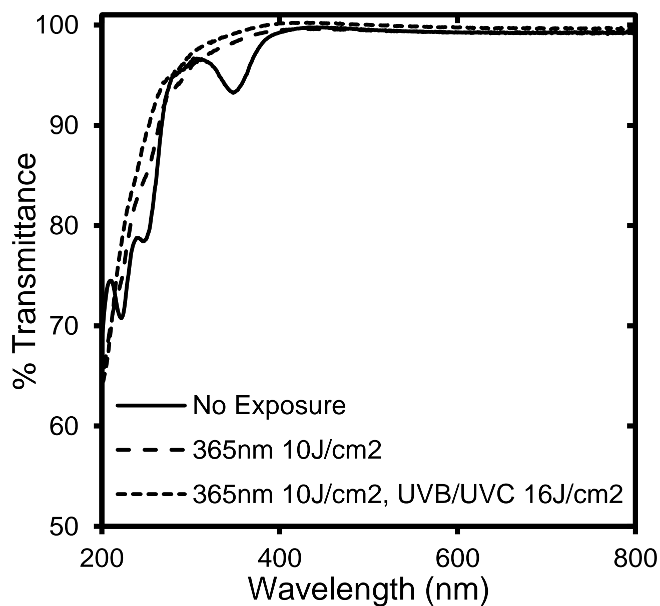

Figure E.1: UV/Vis spectra of a 110 nm thick PiBMA film containing 10 wt. % BB and 2 wt. % MK (solid line) after blanket exposures typical for patterning (long-dashed line) and crosslinking (short-dashed line).

E4. SEC of Exposed PiBMA Films

Neat PiBMA films less than 500 nm thick were exposed to 32 J/cm^2 of UVB/UVC nm light, redissolved, and passed through a SEC column. Unexposed PiBMA was dissolved and injected into the SEC column. Output from the refractive index detector is shown in Figure E.2. The peak corresponding to polymer does not become broadened nor do new peaks appear due to exposure, indicating that the molecular weight of neat PiBMA is unchanged under these exposure conditions.

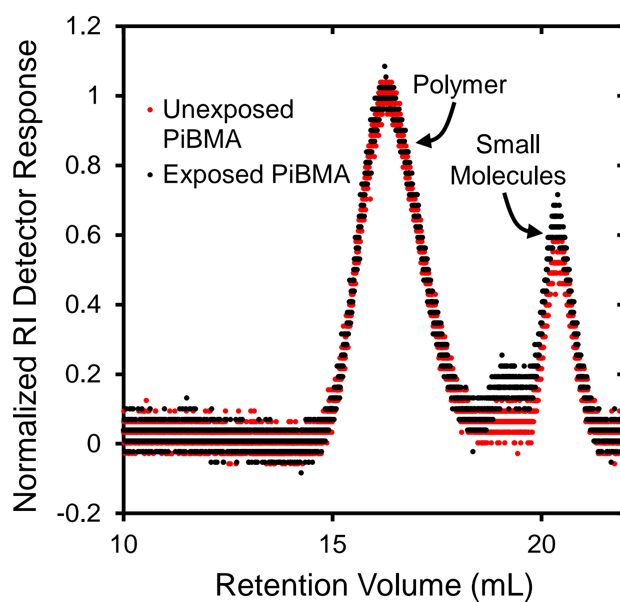

Figure E.2: SEC chromatograms for unexposed PiBMA and redissolved PiBMA films that were exposed to 32 J/cm^2 of UVB/UVC light.

E5. Supporting IR Absorbance Spectra

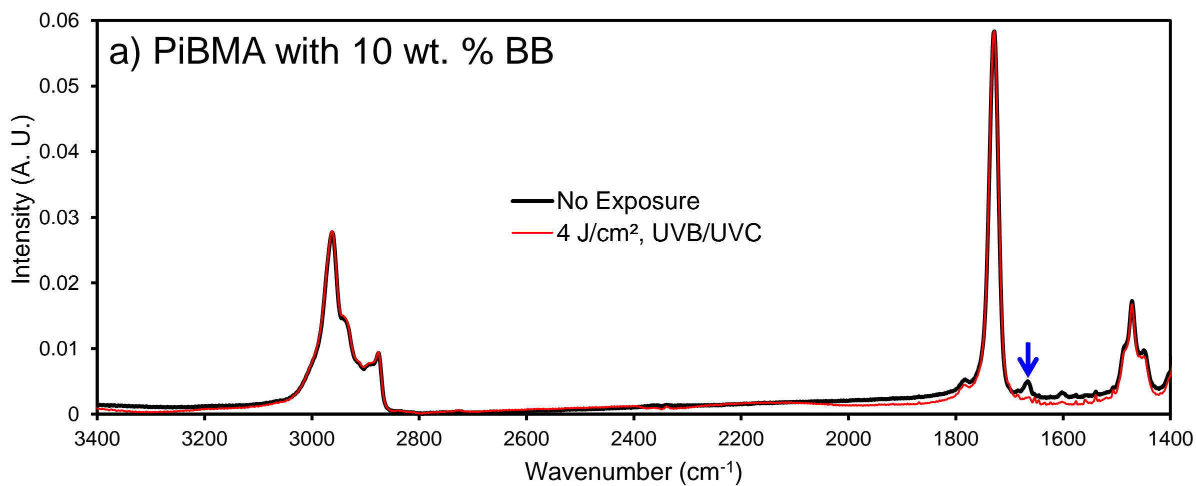

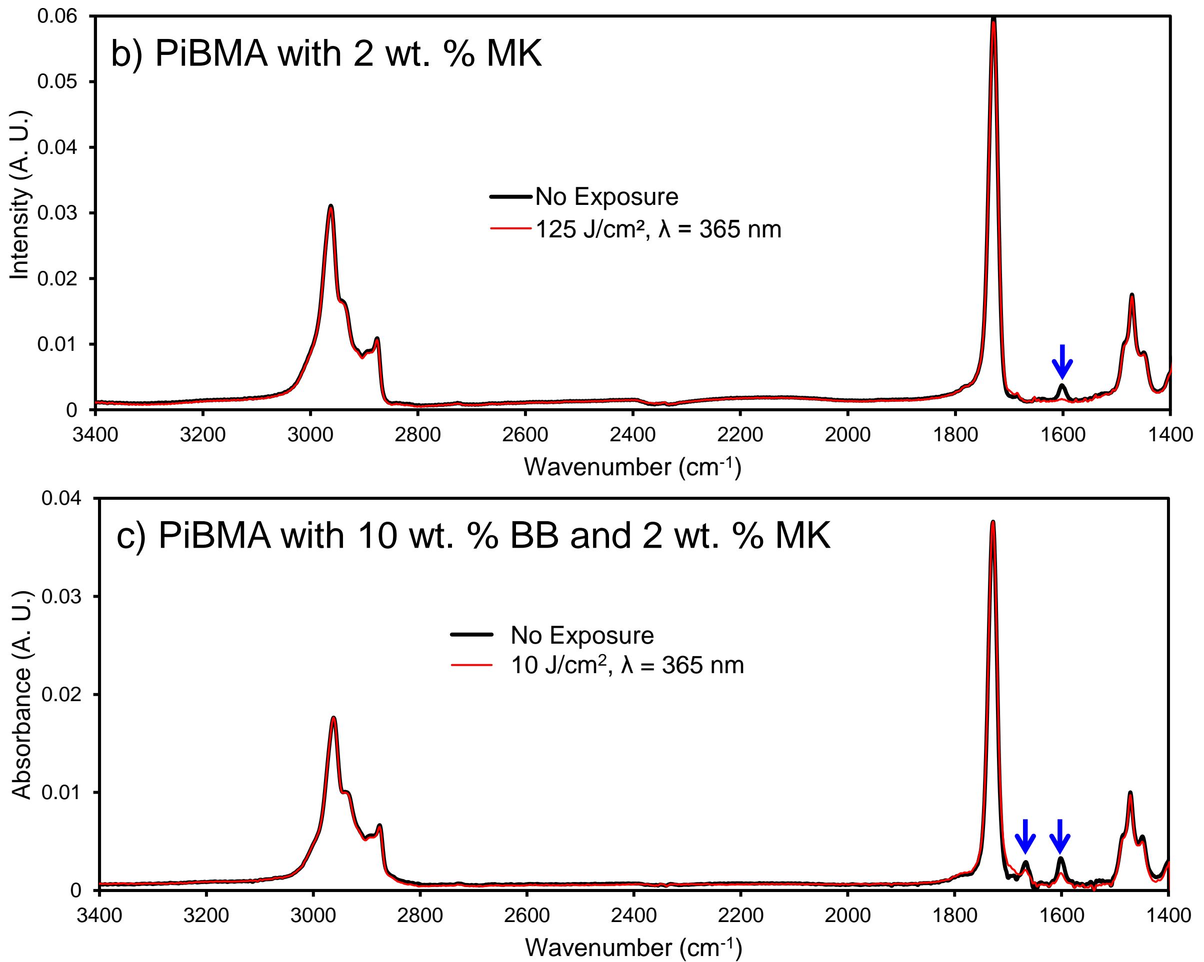

Figure E.3: Representative IR absorbance spectra for a PiBMA film containing MK and/or BB, before and after exposure to UV light.

E6. T_g of PiBMA/MK Film

The glass transition temperature, T_g, of a thin PiBMA film containing 2 wt. % MK was determined by spectroscopic ellipsometry. The results are shown in Figure E.4. The film was heated at 120 °C for 5 min, and then cooled at 2 °C/min to -20 °C. The film's thickness, h(T), was determined at each sample temperature, T, using a layered model that fitted the optical constants and film thickness. The T_g was found by regressing the equation[1]

$$h(T) = w\left(\frac{M-G}{2}\right) ln\left[cosh\left(\frac{T-T_g}{w}\right)\right] + (T - T_g)\left(\frac{M+G}{2}\right) + c \qquad (E1)$$

to the data. The parameters M, G, T_g, and c were fitted and the glass transition width was set as w = 10 °C. Using larger or smaller values of w did not change the extracted value of T_g more than 1 °C.

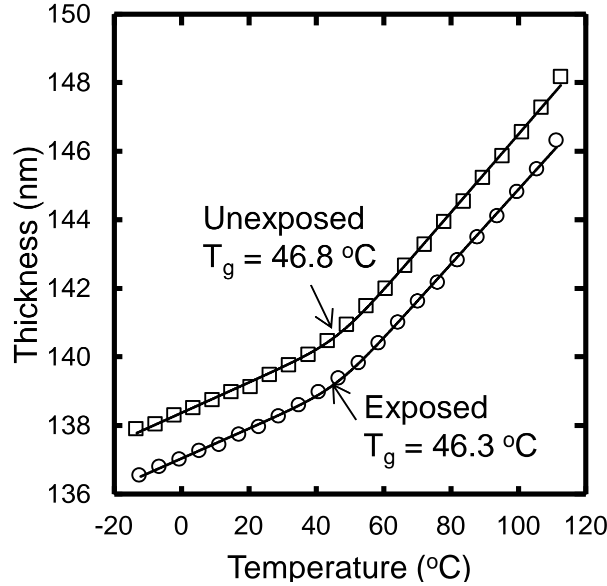

Figure E.4: Effect of blanket exposure to 10 J/cm^2 of light with λ = 365 nm on the glass transition of a PiBMA film containing 2 wt. % MK, as determined by spectroscopic ellipsometry. For clarity only every 100th data point is displayed. The solid lines represent regressions of Eq. D1 to the data.

E7. Viscosity and Self-Diffusion Coefficient of PiBMA

To predict values of the self-diffusion coefficient D for PiBMA using the Rouse model,[2] valid for unentangled polymer melts, the viscosity of PiBMA was measured on a TA instruments AR-2000ex rheometer under steady shear. These results are shown in Figure E.5. To interpolate within the measured values and predict a viscosity at 125 °C, the WLF equation was used,[3]

$$\mu = \mu_0 \exp\left(-\frac{C_1(T-T_r)}{C_2+(T-T_r)}\right), \quad \text{(E2)}$$

where μ_0 = 153.5 Pa·s, $T_r = T_g + 45$ °C, C_1 = 8.4, and C_2 = 73 °C. Equation E2 yields a value of μ = 18 Pa·s. The Rouse model equation is

$$D = \frac{\rho RT\langle R^2\rangle}{36M_w\mu}, \tag{E3}$$

where $\rho = 1000$ kg/m^3 is the polymer mass density estimated for 125 ^{o}C,[4] T = 398.15 K is the absolute temperature, R is the ideal gas constant, M_w = 10.58 kDa, and $\langle R^2\rangle$ = 10.371 nm^2 is the estimated unperturbed mean squared end-to-end distance estimated for 125 ^{o}C.[5] This effort predicts D = 5 × 10^{-11} cm^{2}s^{-1}. A previous work experimentally measured values of D in PiBMA films by a method based on direct visualization of polymer interdiffusion and found that they agree well with values of D predicted by the method described above.[6]

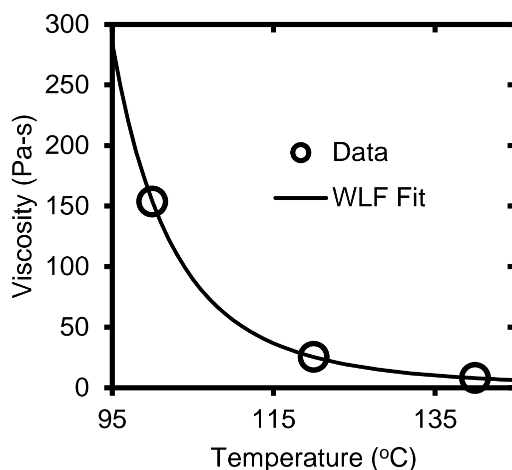

Figure E.5: Viscosity of M_n = 10 kDa PiBMA at varying temperature.

E8. Photochemical Modification of Polymer Surfaces Using Michler's Ketone

Polystyrene (PS, M_n = 170 kDa, Đ = 2.05) was purchased from Sigma-Aldrich. Poly(cyclohexylethylene) (PCHE) was the same as described previously.[7] Poly(vinylidene fluoride-*co*-trifluoroethylene) (PVDF-TrFE, 30 mol. % TrFE) was provided by Solvay. PS and PCHE were spin-coated from toluene solutions; PVDF-TrFE from a cyclopentanone solution. The films were placed on a 180 ^{o}C hot plate for 30s after spin coating to drive off solvent. A solution of Michler's Ketone (MK, 0.3 wt. % in methanol) was spin coated onto some of the polymer films and others were uncoated.

Afterwards, they were irradiated under the same conditions as described in the manuscript by λ = 365 nm light. All films, whether they were coated by MK or not, were then thoroughly rinsed by methanol. Unfortunately, this test could not be performed on the PiBMA used in the main manuscript because the films are not stable to methanol rinsing.

Static water contact angles (θ_W) were measured on a Ramé-Hart Model 100-00 goniometer and the accompanying DROPimage software were used to measure static water contact angles. After thoroughly rinsing the samples with deionized water they were blown dry with filtered air. A 6 μL drop volume of deionized water was used. Within 15 s, the stage was leveled and the real-time image was frozen and the contact angles on the left and right side of the drop were determined. The contact angle results represent the average value found from 3 drops and the error bar represents the standard deviation of those 6 values.

The results of this test are shown in Figure E.6. In all cases, exposure to λ = 365 nm light does not change the θ_W of the polymers not coated with MK. Also, samples coated with MK but not exposed possess the same θ_W as the neat polymer, indicating that the rinsing procedure is effective at removing ungrafted MK. All 3 polymers showed a decrease in θ_W if they were exposed while coated in MK. The θ_W of PS and PCHE coated in MK dropped 14° and 19°, respectively, after a dose of 20 J/cm^2. A dose of 200 J/cm^2 was necessary to make the θ_W of PVDF-TrFE decrease 10°, suggesting it was less susceptible to hydrogen abstraction by MK. This result is unsurprising because its molecular structure is primarily composed of C-F bonds, which are unabstractable by photoexcited MK.

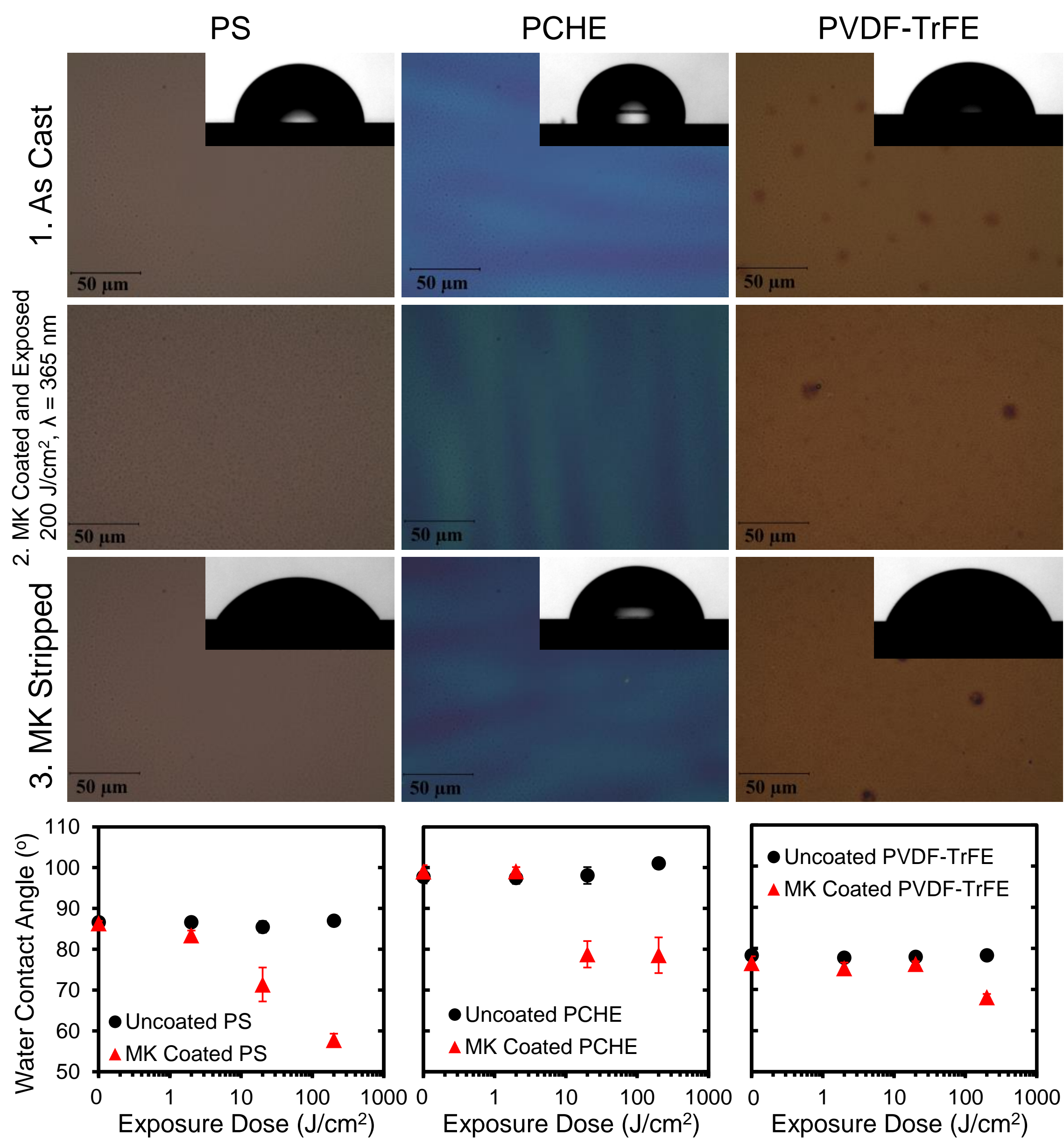

Figure E.6: Representative optical micrographs of film morphologies and water contact angles after different processing steps. Water contact angles of polymer films after various exposure times are plotted below.

E9. Graphical Representation of Hole/Island Morphologies

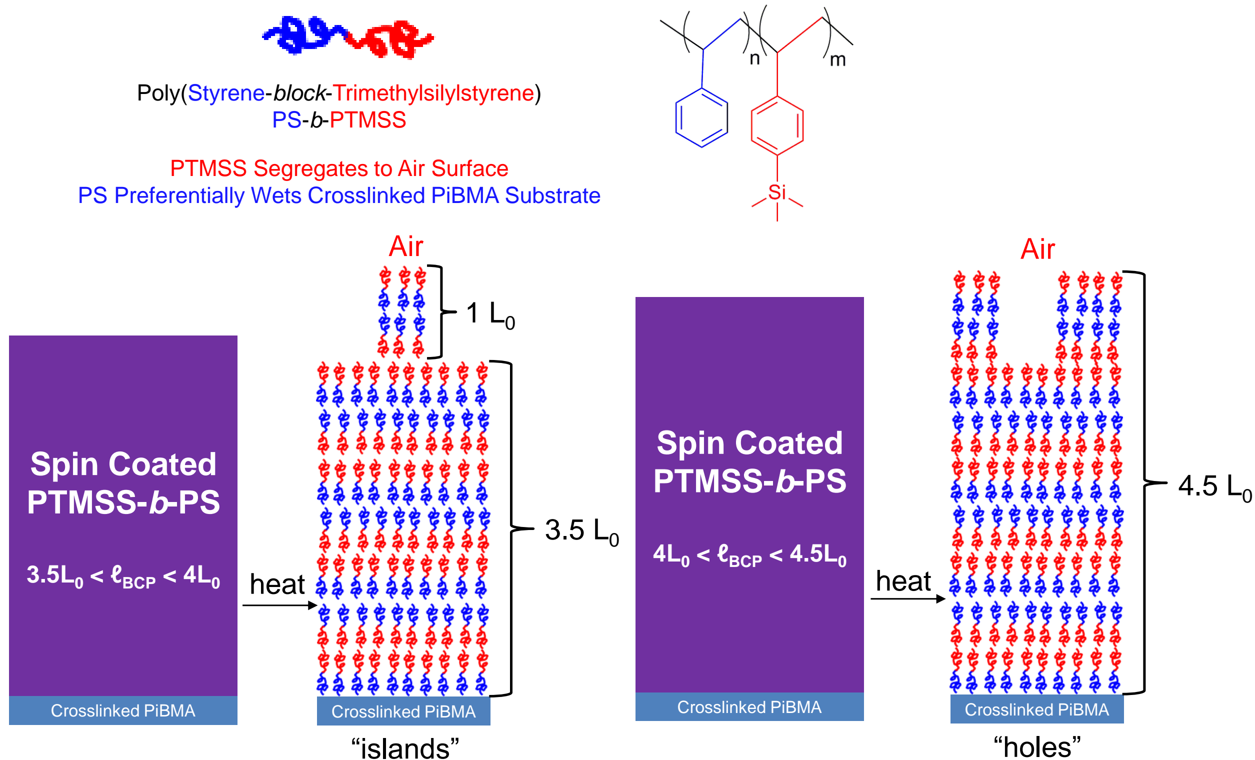

Figure E.7: Graphical representation of hole/island morphologies.

REFERENCES

1. Dalnoki-Veress, K.; Forrest, J. A.; Murray, C.; Gigault, C.; Dutcher, J. R. *Phys. Rev. E* **2001,** 63, 031801.
2. Rouse, P. E. *J. Chem. Phys.* **1953,** 21, 1272-1280.
3. Williams, M. L.; Landel, R. F.; Ferry, J. D. *J. Am. Chem. Soc.* **1955,** 77, 3701-3707.
4. Bicerano, J., *Prediction of Polymer Properties*. 3rd ed.; Marcel Dekker, Inc.: New York, 2002.
5. Brandrup, J.; Immergut, E. H.; Grulke, E. A., *Polymer Handbook*. Wiley and Sons: Hoboken, New Jersey, 1999.
6. Katzenstein, J. M.; Janes, D. W.; Hocker, H. E.; Chandler, J. K.; Ellison, C. J. *Macromolecules* **2012,** 45, 1544-1552.
7. Janes, D. W.; Thode, C. J.; Willson, C. G.; Nealey, P. F.; Ellison, C. J. *Macromolecules* **2013,** 46, 4510-4519.

APPENDIX F: MARANGONI INSTABILITY DRIVEN SURFACE RELIEF GRATING IN AN AZOBENZENE CONTAINING POLYMER FILM

F1. Orientation of P5Az6A in Supported Thin Films

Numerous studies have investigated the azobenzene side chain orientation behavior in polymer thin films. In general, surface wettability[1-4] and excluded free volume of the rod like molecules[5-8] affect the specific orientation of the azobenzene side chain. For example, polymer films with hydrophobic groups containing rod-like side chains such as pentyl-phenyl benzoate,[1] and butyl,[9] pentyl,[10] and hexyl[11] substituted azobenzene all adopted a perpendicular orientation to the substrate. Furthermore, Li and coworkers[12] have previously estimated a tilt angle between small azobenzene molecules (that were self-assembled on the substrate) and the normal surface using reflectance absorption polarized infrared spectroscopy. By systematically varying the para-substituted alkyl chain length from butyl (4 carbons) to dedocyl (12 carbons), they also found that small azobenzene molecules with shorter than octyl-substituents follow a perpendicular orientation. In order to confirm that our P5Az6A also follows this perpendicular orientation, a series of UV-Vis spectra were recorded on a film after various annealing intervals at room temperature, and the corresponding spectra are shown as Figure F.1. As cast film possesses an absorbance of ca. 0.31 at a wavelength of 347 nm, which is the characteristic absorbance of the π–π* transition of the *trans*-azobenzene moiety. Upon annealing up to one hour, this peak reduced in intensity to 0.23. Since the transition moment of the π–π* band at 347 nm is parallel to the long axis of the azobenzene, reduction in absorbance in these regions reflects that the azobenzene orientation follows a more perpendicular direction with respect to the substrate.

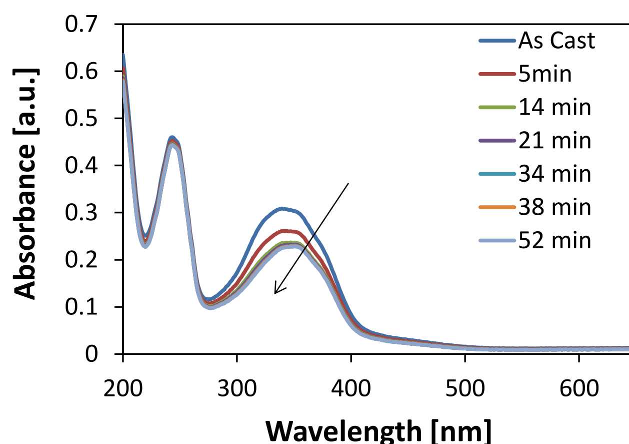

Figure F.1: UV–vis absorption spectra of a film (141 nm thick) after various annealing intervals at room temperature. The arrow indicates the effect of increasing time on the UV-vis spectra.

To further confirm this orientation, transmission mode Fourier transformed infrared spectroscopy (FTIR) was conducted on annealed films supported on double side polished silicon wafers. The corresponding FTIR results are shown in Figure F.2. Peaks between 1605-1585 cm^{-1} and one near 840 cm^{-1} were used for this study. The former peak (A_{1w}) describes ring vibrations in plane with polarization along the long axis of azobenzene[13] while the latter peak (C_{1w}) describes the out-of-plane wagging of aryl C–H which possesses polarization perpendicular to the aromatic plane.[14,15] These dipole moment directions for each IR peak are also shown in Figure F.2. Upon annealing for ca. 1 hr at room temperature, the area under A_{1w} peak decreases while the area under C_{1w} increases monotonically. Since the transmission mode FTIR measures dipole moment projected on to the substrate, this behavior corresponds to a change in the side chain orientation to a perpendicular direction with respect to the substrate, which also agrees with the aforementioned UV-vis results.

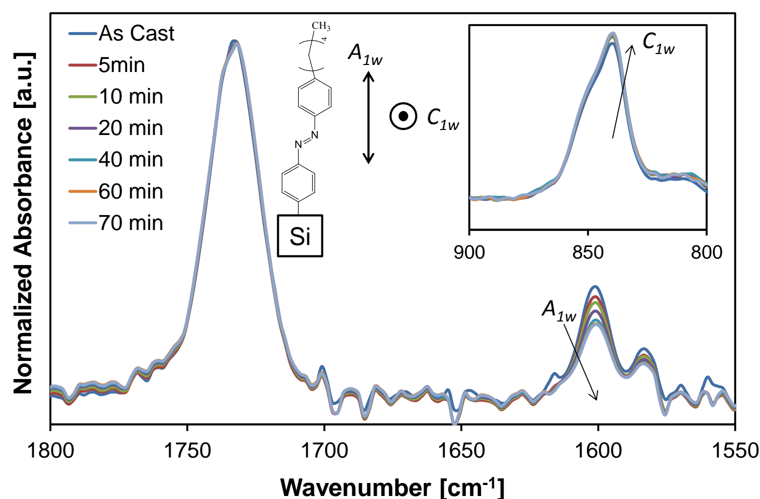

Figure F.2: FTIR spectra of the film (183 nm thick) after various annealing intervals at room temperature. Arrows show the effect of increasing annealing time on the spectra. All spectra in this study were normalized by the ester peak areas (1720 – 1770 cm^{-1}) (measured on the associated OMNIC software) which represent the peaks present in the polymer repeat units.

F2. Surface Tension Changes

To illustrate that surface tension can be controlled by two different light exposures, water contact angle measurements on the same film after a series of light exposure cycles were performed and the results are shown in Figure F.3. Water contact angles measured after 450 nm light exposure ranged from 94 – 96°, while the angles reduced to 82 – 83 ° after 365 nm UV exposure.

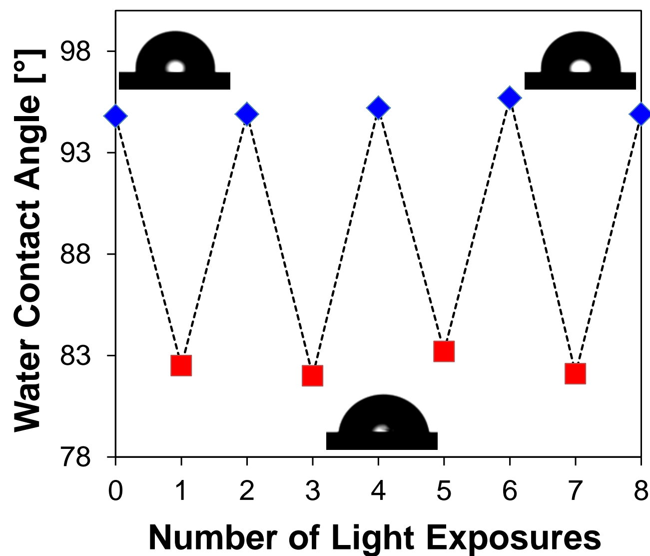

Figure F.3: Water contact angle goniometry results. Diamonds represent the water contact angle measurements on a film after 450 nm light exposure, and squares are the measurements after 365 nm UV exposure. The exposure time was kept constant at 30 sec. In-between measurements, the sample was blown dry with filtered dry air.

F3. 365 nm UV Exposure to Isomerize Trans to Cis

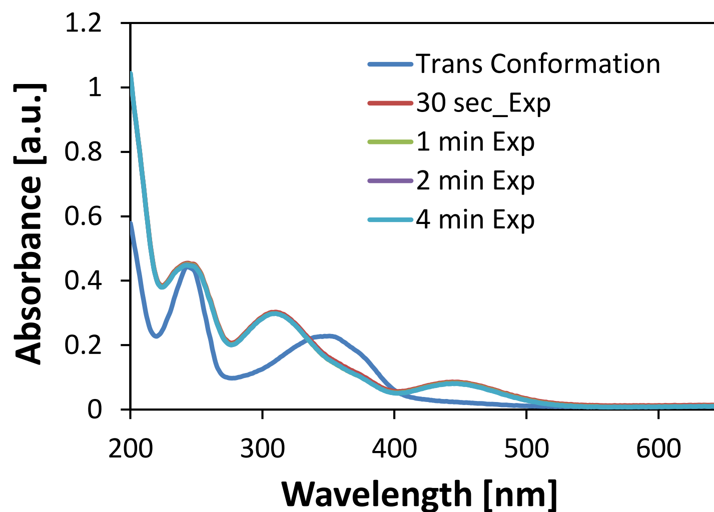

Figure F.4: UV–vis absorption spectra of the film (141 nm thick) after various exposure times with 365 nm UV light.

F4. Viscosity of P5Az6A upon UV Exposure

Polymer viscosity was characterized before and during UV irradiation under steady shear using a TA Instruments AR-2000ex rheometer and the result is shown in Figure F.5. For this experiment, a copolymer of 4-(acryloyloxyhexyloxy)-4'-pentylazobenzene and hexyl acrylate (21 mol % azobezene containing monomers, P5Az6A, in the polymer chain) with bulk T_g = -12 °C (DSC) was used in order to increase the light penetration depth and ensure full irradiation of the bulk polymer. Before UV irradiation, the polymer viscosity was constant for shear rates ranging from 0.01 to 1 s^{-1}. However, once the polymer was exposed to UV light during shear, the viscosity reduced by 52 %. This reduction in viscosity can be explained by the free volume created upon photo-isomerization of azobenzene.[16,17]

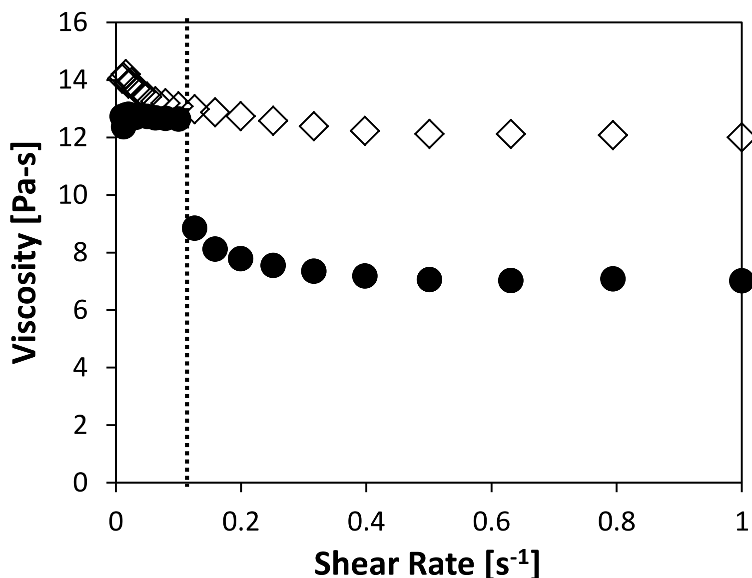

Figure F.5: Zero shear viscosity measurements before and during UV exposure. Open diamonds are measurements made in an absence of UV irradiation while the filled circles are data taken during UV irradiation. The dotted line in this figure indicates when the UV irradiation was initiated.

F5. Cis to Trans Relaxation Time

In order to estimate the characteristic relaxation time scale from *cis* to *trans*-isomers at room temperature, a series of UV-vis spectra was collected with increasing room temperature annealing time after exposure to 365 nm light (30 s) without photomasks. The characteristic absorbance for a *cis* isomer (at 444 nm) monotonically reduced in intensity with time. Based on literature,[18] this peak reduction corresponds to a decrease in concentration of the *cis*-isomer, which can be described with an exponential form of

$$\Delta A_t = \Delta A_\infty + \Delta A_0 exp(-t/\tau), \qquad (F.1)$$

where ΔA_t, ΔA_0 and ΔA_∞ correspond to the absorbance change at time t, zero and infinity, respectively, and τ is the characteristic relaxation time of the corresponding *cis* isomer. By fitting the UV-vis data with the Equation F.1, τ^{-1} was estimated to be 0.036 hr^{-1} (see Figure F.7).

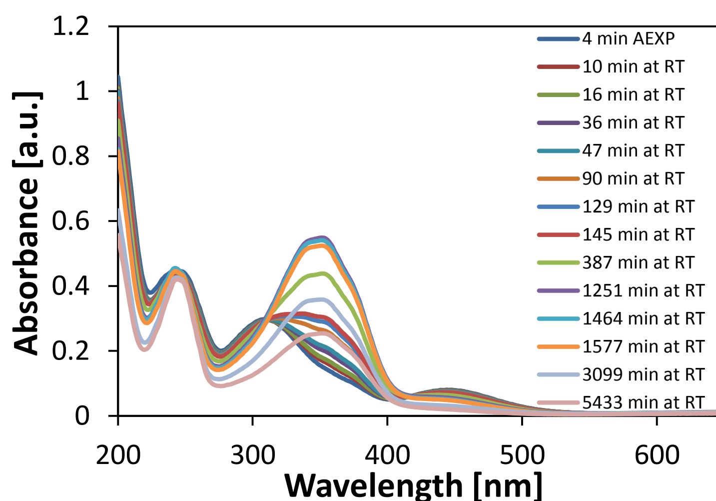

Figure F.6: UV–vis absorption spectra of the UV exposed (365 nm) film (141 nm thick) after various annealing intervals at room temperature.

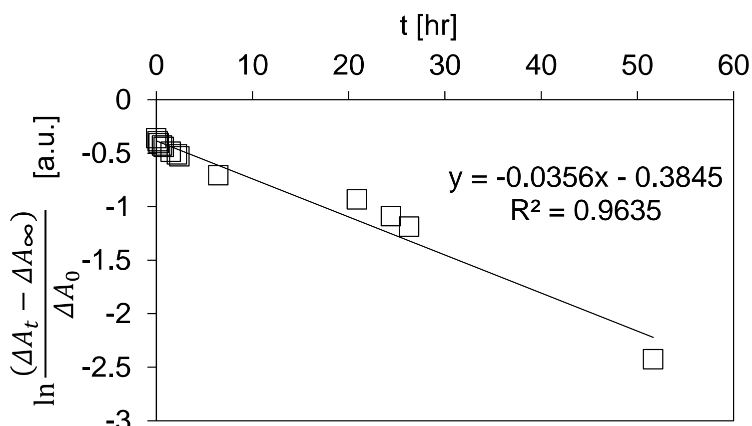

Figure F.7: Extraction of τ from the UV-vis absorption spectra shown in Figure S10. Using Equation F.1, τ can be extracted from the reduction in the characteristic absorbance peak for cis at wavelength = 444 nm over various intervals of annealing at room temperature.

REFERENCES

1. Fukuhara, K.; Nagano, S.; Hara, M.; Seki, T. *Nat. Commun.* **2014**, 5, 3320.
2. Cognard, J.; *Mol. Cryst. Liq. Cryst.* **1982**, 1, 71−77.
3. Fukuhara, K.; Fujii, Y.; Nagashima, Y.; Hara, M.; Nagano, S.; Seki, T. *Angew. Chem., Int. Ed.* **2013**, 52, 5988−5991.
4. Komura, M.; Yoshitake, A.; Komiyama, H.; Iyoda, T.; *Macromolecules* **2015**, 48, 672−678.
5. Okano, K. *Jpn. J. Appl. Phys*. **1983**, 22, L343.
6. Schmitt, F. J.; Müller, M. *Thin Solid Films* **1997**, 310, 138−147.
7. Kimura, H.; Nakano, H. *J. Phys. Soc. Jpn.* **1985**, 54, 1730−1736.
8. Tanaka, D.; Nagashima, Y.; Hara, M.; Nagano, S.; Seki, T. *Langmuir* **2015**, 31, 11379−11383
9. Yamashita, N.; Watanabe, S.; Nagai, K.; Komura, M.; Iyoda, T.; Aida, K.; Tadac, Y.; Yoshida, H. *J. Mater. Chem. C,* **2015**, 3, 2837 -2847.
10. Nakai, T.; Tanaka, D.; Hara, M.; Nagano, S.; Seki, T. *Langmuir* **2016**, *32*, 909–914.
11. Zettsu, N.; Seki, T. *Macromolecules* **2004**, 37, 8692-8698.
12. Zhang, H.; Zhang, J.; Li, H,; Liu, Z,; Li, H. *Mater Sci Eng. C* **1999**, 8–9, 179–185.
13. Nakahara, H.; Fukuda, K. *J. Colloid Interface Sci*. **1983**, 93, 530-539.
14. Lin-Vien, D.; Colthup, N. B; Fateley, W. G.; Grasselli, J. G.The Handbook of Infrared and Raman Characteristic Frequencies of Organic Molecules, Academic Press, Boston, 1991.
15. His, A.; Uvdal, K.; Liedberg, B. *Langmuir* **1993**, 9, 733-739.
16. Yager, K. G.; Tanchak, O. M.; Godbout, C.; Fritzsche, H.; Barrett, C. J. *Macromolecules* **2006**, 39, 9311-9319.

17. Tanchak, O. M.; Barrett, C. J. *Macromolecules* **2005,** 38*,* 10566-10570.
18. Garcia-Amoros, J.; Sanchez-Ferrerz, A.; Massad, W. A.; Nonell, S.; Velasco, D. *Phys. Chem. Chem. Phys.* **2010**, 12, 13238–13242.

References

1. Nie, Z.; Kumacheva, E. *Nat. Mater*. **2008**, 7, 277–290.
2. Campo A. D.; Arzt E. Generating Micro- and Nanopatterns on Polymeric Materials; Wiley-VCH: Weinheim, **2011**.
3. Thery, M. ; Racine, V.; Pepin, A.; Piel, M.; Chen, Y.; Sibarita, J. B.; Bornens, M. *Nature Cell Biol.* **2005**, 7, 947–953.
4. Thery, M.; Racine, V.; Piel, M.; Pepin, A.; Dimitrov, A.; Chen, Y.; Sibarita, J. B. *Proc. Natl Acad. Sci. USA* **2006**, 103, 19771–19776.
5. Hollister, S. J. *Nature Mater.* **2005**, 4, 518–524.
6. Efimenko, K.; Finlay, J.; Callow, M. E.; Callow, J. A.; Genzer, J. *ACS Appl. Mater. Interfaces* **2009**, 1, 1031−1040.
7. Bixler, G. D.; Bhushan B. *Adv. Funct. Mater.* **2013**, 23, 4507-4528.
8. Davis, C. S.; Martina, D.; Creton, C.; Lindner, A.; Crosby, A. J. *Langmuir*, **2012**, 28, 14899−14908.
9. Feng, L.; Li, S.; Li, Y.; Li, H.; Zhang, L.; Zhai, J.; Song, Y.; Liu, B.; Jiang, L.; Zhu, D. *Adv. Mater.* **2002**, 14, 1857−1860.
10. Schumacher, J. F.; Carman, M. L.; Estes, T. G.; Feinberg, A. W.; Wilson, L. H.; Callow, M. E.; Callow, J. A.; Finlay, J. A.; Brennan, A. B. *Biofouling* **2007**, 23, 55−62.
11. Kim, J. B.; Kim, P.; Pegard, N. C.; Oh, S. J.; Kagan, C. R.; Fleischer, J. W.; Stone, H. A.; Loo, Y.-L. *Nat. Photon*. **2012**, 6, 327-332.
12. Bay, A.; André, N.; Sarrazin, M.; Belarouci, A.; Aimez, V.; Francis, L. A.; Vigneron, J. P. *Opt. Express* **2013**, 21, A179-A189.
13. Koo, W. H.; Jeong, S. M.; Araoka, F.; Ishikawa, K.; Nishimura, S.; Toyooka, T.; Takezoe, H. *Nat. Photon.* **2010**, 4, 222-226.
14. Park, B.; Jeon, H. G. *Opt. Express* **2011**, 19, A1117-A1125.
15. Thompson, S. E.; Parthasarathy, S.; *Mater. Today* **2006**, 9, 20–25, 7747-7759.
16. Aubin, H.; Nichol, J. W.; Hutson, C. B.; Bae, H.; Sieminski, A. L.; Cropek, D. M.; Akhyari, P.; Khademhosseini, A. *Biomaterials* **2010**, 31, 6941-6951.
17. Moungthai, S.; Mahadevapuram, N.; Ruchhoeft, P.; Stein, G. E. *ACS Appl. Mater. Interfaces* **2012**, 4, 4015-4023.
18. Bruning, J. H.; *Proc. SPIE* **2007**, 6520, 652004
19. Thompson, S. E.; Parthasarathy, S. *Mater. Today* **2006**, 9, 20–25.
20. Chou, S. Y.; Krauss, P. R.; Preston, J. R. *Science* **1996**, 272,85–87.
21. Resnick, D. J. Sreenivasan, S. V.; Willson, C. G; Mater. Today 2005, 8, 34–42.
22. Herr, D. J. C. *J. Mater. Res.* **2011**, 26, 122–139.
23. Liu, C.-C.; Thode, C. J.; Delgadillo, P. A. R.; Craig, G. S. W.; Nealey, P. F.; Gronheid, R. *J. Vac. Sci. Technol. B* **2011**, 29, 06F203.
24. Stoykovich, M. P.; Kang, H.; Daoulas, K. C.; Liu, G.; Liu, C.-C.; de Pablo, J.J.; Muller, M.; Nealey, P. F. *ACS Nano* **2007**, 1,168–175.
25. Steiner, U. In Nanoscale Assembly Chemical Techniques; W. T. S. Huck, Ed.; Springer Science Business Media, Inc.: New York, **2005**, p 1–24.

26. Han, W.; Lin, Z. Q. *Angewandte Chemie-International Edition* **2012**, 51, 1534-1546.
27. Singer, J. P.; Lin, P. T.; Kooi, S. E.; Kimerling, L. C.; Michel, J.; Thomas, E. L. *Adv. Mater.* **2013**, 25, 6100-6105.
28. Chou, S. Y.; Zhuang, L. *J. Vac. Sci. Technol. B* **1999**, 17, 3197-3202.
29. Schaffer, E.; Thurn-Albrecht, T.; Russell, T. P.; Steiner, U. *Nature* **2000**, 403, 874-877.
30. Verma, R.; Sharma, A.; Kargupta, K.; Bhaumik, J. *Langmuir* **2005**, 21, 3710-3721.
31. Katzenstein, J. M.; Janes, D. W.; Cushen, J. D.; Hira, N. B.; McGuffin, D. L.; Prisco, N. A.; Ellison, C. J. *ACS Macro Lett.* **2012**, 1, 1150-1154.
32. Larson, R. G. *Angewandte Chemie International Edition* **2012**, 51, 2546-2548.
33. Scriven, L. E.; Sternling, C. V. *Nature* **1960**, 187, 186-188.
34. Thomson, J. On certain curious motions observable at the surfaces of wine and other alcoholic liquors, **1855**.
35. Marangoni, C. Sull'espansione delle gocce liquide, **1865**.
36. Bron, A. J.; Tiffany, J. M.; Gouveia, S. M.; Yokoi, N.; Voon, L. W. *Exp. Eye Res.* **2004**, 78, 347-360.
37. Cazabat, A. M.; Heslot, F.; Troian, S. M.; Carles, P. *Nature* **1990**, 346, 824-826.
38. Bush, J. W. M.; Hu, D. L. *Annu. Rev. Fluid Mech.* **2006**, 38, 339–369.
39. Haas, D. E.; Birnie, D. P., III. *J. Mater. Sci.* **2002**, 37, 2109-2116.
40. Janes, D. W.; Katzenstein, J. M.; Shanmuganathan, K.; Ellison, C. J. *J. Polym. Sci., Part B: Polym. Phys.* **2013**, 51, 535–545.
41. Millan, M. D.; Locklin, J.; Fulghum, T.; Baba, A.; Advincula, R. C. *Polymer* **2005**, 46, 5556-5568.
42. Nagai, N.; Matsunobe, T.; Imai, T. *Polym. Degrad. Stabil.* **2005**, 88, 224-233.
43. Nurmukhametov, R.; Volkova, L.; Kabanov, S. *Journal of Applied Spectroscopy* **2006**, 73, 55-60.
44. Simons, J. K.; Chen, J. M.; Taylor, J. W.; Rosenberg, R. A. *Macromolecules* **1993**, 26, 3262-3266.
45. Zhang, D.; Dougal, S. M.; Yeganeh, M. S. *Langmuir* **2000**, 16, 4528-4532.
46. Rochon, P.; Batalla, E.; Natansohn, A. *Appl. Phys. Lett.* **1995**, 66, 136.
47. Kim, D.Y.; Tripathy, S.K.; Li, L.; Kumar, J. *Appl. Phys. Lett.* **1995**, 66, 1166.
48. Park, S. M.; Stoykovich, M. P.; Ruiz, R.; Zhang, Y.; Black, C. T.; Nealey, P. E. *Adv. Mater.* **2007**, 19, 607-611.
49. Bita, I.; Yang, J. K. W.; Jung, Y. S.; Ross, C. A.; Thomas, E. L.; Berggren, K. K. *Science* **2008**, 321, 939-943.
50. Segalman, R. A.; Yokoyama, H.; Kramer, E. J. *Adv. Mater.* **2001**, 13, 1152-1155.
51. Weinkauf, D. H.; Kim, H. D.; Paul, D. R. *Macromolecules* **1992**, 25,788-796.
52. Park, J. Y.; Paul, D. R.; Haider, I.; Jaffe, M. *J. Polym. Sci., Part B: Polym. Phys.***1998**, 34,1741-1745.
53. Grell, M.; Bradley, D. D. C.; Inbasekaran, M.; Woo, E. P. *Adv Mater.* **1997**, 9, 798-802.
54. Wu, N.; Pease, L. F.; Russel, W. B. *Langmuir* **2005**, 21, 12290-12302.

55. Amarandei, G.; Beltrame, P.; Clancy, I.; O'Dwyer, C.; Arshak, A.; Steiner, U.; Corcoran, D.; Thiele, U. *Soft Matter* **2012**, 8, 6333-6349.
56. Roberts, S. A.; Kumar, S. *J. Fluid Mech.* **2009**, 631, 255-279.
57. Verma, R.; Sharma, A.; Kargupta, K.; Bhaumik, J. *Langmuir* **2005**, 21, 3710-3721.
58. Dickey, M.; Raines, A.; Collister, E.; Bonnecaze, R.; Sreenivasan, S. V.; Willson, C. G. *J. Mater. Sci.* **2008**, 43, 117-122.
59. McLeod, E.; Liu, Y.; Troian, S. M. *Phys. Rev. Lett.* **2011**, 106, 175501.
60. Pease, L. F.; Russel, I. W. B. *J. Chem. Phys.* **2006**, 125, 184716.
61. Schäffer, E.; Harkema, S.; Roerdink, M.; Blossey, R.; Steiner, U. *Macromolecules* **2003**, 36, 1645-1655.
62. Kumar, S. *Langmuir* **2003**, 19, 2473-2478.
63. Paretkar, D.; Xu, X.; Hui, C.-Y.; Jagota, A. *Soft Matter* **2014**, 10, 4084-4090.
64. Casper, M. D.; Gozen, A. O.; Dickey, M. D.; Genzer, J.; Maria, J.-P. *Soft Matter* **2013**, 9, 7797-7803.
65. Jensen, O. E.; Grotberg, J. B. *J. Fluid Mech.* **1992**, 240, 259-288.
66. Gaver, D. P.; Grotberg, J. B. *J. Fluid Mech.* **1990**, 213, 127-148.
67. Janes, D. W.; Katzenstein, J. M.; Shanmuganathan, K.; Ellison, C. J. *J. Polym. Sci., Part B: Polym. Phys.* **2013**, 51, 535-545.
68. Williams, M. L. *J. Appl. Phys.* **1958**, 29, 1395-1398.
69. Brandrup, J.; Immergut, E. H.; Grulke, E. A.; Abe, A.; Bloch, D. R., *Polymer Handbook*. 4th ed.; John Wiley & Sons: Hoboken, 2005.
70. Bicerano, J., *Prediction of Polymer Properties*. 3rd ed.; Marcel Dekker, Inc.: New York, 2002.
71. Fleischer, G. *Polym. Bull.* **1984**, 11, 75-80.
72. Urakawa, O.; Swallen, S. F.; Ediger, M. D.; von Meerwall, E. D. *Macromolecules* **2004**, 37, 1558-1564.
73. Rouse, P. E. *J. Chem. Phys.* **1953**, 21, 1272-1280.
74. Harris, D. J.; Hu, H.; Conrad, J. C.; Lewis, J. A. *Phys. Rev. Lett.* **2007**, 98.
75. Arshad, T. A.; Bonnecaze, R. T. *Nanoscale* **2013**, 5, 624-633.
76. Katzenstein, J. M.; Janes, D. W.; Hocker, H. E.; Chandler, J. K.; Ellison, C. J. *Macromolecules* **2012,** 45, 1544-1552.
77. Edelstein, A.; Amodaj, N.; Hoover, K.; Vale, R.; Stuurman, N. Computer Control of Microscopes Using μManager; John Wiley & Sons, Inc., 2001.
78. Dalnoki-Veress, K.; Forrest, J. A.; Murray, C.; Gigault, C.; Dutcher, J. R. *Phys. Rev. E* **2001,** 63, 031801.
79. Fleischer, G. *Polym. Bull.* **1984**, 11, 75-80.
80. Arshad, T.; Kim, C. B.; Prisco, N. A.; Katzenstein, J. M.; Janes, D. W.; Bonnecaze, R. T.; Ellison, C. J. *Soft Matter* **2014**, 10, 8043–8050.
81. Katzenstein, J. M.; Kim, C. B.; Prisco, N. A.; Katsumata, R.; Li, Z.; Janes, D. W.; Blachut, G.; Ellison, C. J. *Macromolecules* **2014**, 47, 6804–6812.
82. Mansky, P.; Liu, Y.; Huang, E.; Russell, T. P.; Hawker, C. *Science* **1997**, 275, 1458−1460.
83. Vitt, E.; Shull, K. R. *Macromolecules* **1995**, 28, 6349–6353.

84. Balkeneende, A. R.; van de Boogaard, H. J. A. P.; Scholten, M.; Willard, N. P. *Langmuir* **1998**, 14, 5907–5912.
85. Song, S.; Yokoyama, S.; Takahara, S.; Yamaoka, T. *Polym. Adv. Technol.* **1998,** 9, 326–333.
86. Song, S.; Takahara, S.; Yamaoka, T. *J. Photopolym. Sci. Tech.* **1998,**11, 171–172.
87. Gurkaynak, A.; Tubert, F.; Yang, J.; Matyas, J.; Spencer, J. L.; Gryte, C. C. *J. Polym. Sci. Part A: Polym. Chem.* **1996**, 34, 349–355.
88. Benzaquen, M.; Fowler, P.; Jubin, L.; Salez, T.; Dalnoki-Veress, K.; Raphaël, E. *Soft Matter* **2014**, 10, 8608–8614.
89. Benzaquen, M.; Ilton, M.; Massa, M. V.; Salez, T.; Fowler, P.; Raphaël, E.; Dalnoki-Veress, K. 2015, arXiv:1503.08728 [cond-mat.soft]. arXiv.org e-Print archive. http://arxiv.org/abs/1503.08728 (accessed May 1, 2015).
90. Namasté, Y. M. N.; Obendorf, S. K.; Anderson, C. C.; Krasicky, P. D.; Rodriguez, F.; Tiberio, R. *J. Vac. Sci. Technol. B1* **1983**, 4, 1160−1165.
91. La, Y.; Edwards, E. W.; Park, S.; Nealey, P. F. *Nano Lett.* **2005**, 5, 1379−1384.
92. Okada, K.; Tokudome, Y.; Makiura, R.; Konstas, K.; Malfatti, L.; Innocenzi, P.; Ogawa, H.; Kanaya, T.; Falcaro, P.; Takahashi, M. *Adv. Funct. Mater.* **2014**, 24, 2801–2809.
93. Ubukata, T.; Moriya, Y.; Yokoyama, Y. *Polym. J.* **2012**, 44, 966–972.
94. National Institute of Advanced Industrial Science and Technology. Spectral Database for Organic Compounds. http://sdbs.riodb.aist.go.jp/sdbs/
95. Tung, P. H.; Kuo, S. W.; Chan, S. C.; Hsu, C. H.; Wang, C. F.; Chang, F. C., *Macromol. Chem. Phys.* **2007,** *208*, 1823-1831.
96. Daugaard, A. E.; Hvilsted, S. *Macromol. Rapid Commun.* **2008,** *29*, 1119-1125.
97. Vogt, B. D.; Kang, S.; Prabhu, V. M.; Lin, E. K.; Satija, S. K.; Turnquest, K.; Wu, W. L. *Macromolecules* **2006,** *39*, 8311-8317.
98. Conlon, D. A.; Crivello, J. V.; Lee, J. L.; Obrien, M. J. *Macromolecules* **1989,** *22*, 509-516.
99. Augsburg, A.; Grundke, K.; Poschel, K.; Jacobasch, H. J.; Neumann, A. W., *Acta Polym.* **1998,** *49*, 417-426.
100. Willson, C. G.; Ito, H.; Frechet, J. M. J.; Tessier, T. G.; Houlihan, F. M. *J. Electrochem. Soc.* **1986,** *133*, 181-187.
101. Olabisi, O.; Robeson, L. M.; Shaw, M. T., *Polymer-Polymer Miscibility*. Academic Press: New York, 1979.
102. Sehgal, A.; Ferreiro, V.; Douglas, J. F.; Amis, E. J.; Karim, A. *Langmuir* **2002,** *18*, 7041-7048.
103. Zhang, Z. X.; Wang, Z.; Xing, R. B.; Han, Y. C. *Polymer* **2003,** *44*, 3737-3743.
104. Karim, A.; Slawecki, T. M.; Kumar, S. K.; Douglas, J. F.; Satija, S. K.; Han, C. C.; Russell, T. P.; Liu, Y.; Overney, R.; Sokolov, O.; Rafailovich, M. H. *Macromolecules* **1998,** *31*, 857-862.
105. Andrews, R. J.; Grulke, E. A., *Polymer Handbook*. 4th ed.; John Wiley & Sons: Hoboken, 1999; Vol. 1, p 209-213.
106. Rahman, S. S. A.; Kawaguchi, D.; Ito, D.; Takano, A.; Matsushita, Y. *J. Polym. Sci., Part B: Polym. Phys.* **2009,** *47*, 2272-2280.

107. Nakamura, K.; Hatakeyama, T.; Hatakeyama, H. *Polymer* **1981,** *22*, 473-476.
108. Koning, C.; van Duin, M.; Pagnoulle, C.; Jerome, R. *Prog. Polym. Sci.* **1998,** *23*, 707-757.
109. Hsu, C. H.; Kuo, S. W.; Chen, J. K.; Ko, F. H.; Liao, C. S.; Chang, F. C. *Langmuir* **2008,** *24*, 7727-7734.
110. Ardekani, A. M.; Sharma, V.; McKinley, G. H. *J. Fluid Mech.* **2010,** *665*, 46-56.
111. Zhang, Y. R.; Sharma, V. *Soft Matter* **2015,** *11*, 4408-4417.
112. Wu, S., *Polymer Handbook*. 4th ed.; John Wiley & Sons: Hoboken, 1999; Vol. 2, p 525.
113. Palacios, M.; Garcia, O.; Hernandez, J. R. *Langmuir*, **2013**, 29, 2756-2763.
114. Wochnowski, C.; Eldin, M. A. S.; Metev, S. *Polym. Degrad. Stab.*, **2005**, 89, 252-264.
115. Suzuki, K.; Matsui, S.; Ochiai, Y.; Eds. Sub-Half-Micron Lithography for ULSIs; Cambridge University Press: New York, 2000.
116. Bratschkov, C.; Karpuzova, P.; Mullen, K.; Klapper, M.; Schopov, I. *Polym. Bull.*, **2001**, 46, 345-349.
117. Lapouyade, R.; Desvergne, J. P; Laurent, H. B. *Bull. Soc. Chim. Fr.*, **1975**, 9-10, 2137-2142.
118. Popov, A. P.; Shelekhov, N. S.; Bandyuk, O. V.; Ratner, O. B.; Vember, T. M.; Rebezov, A. O.; Lashkov, G. I. *Teor. Eksp. Khim.*, **1986**, 22, 235-240.
119. DeRosa, M. C.; Crutchley, R. J. *Coord. Chem. Rev.*, **2002**, 233-234, 351-371.
120. Fudickar, W. Linker, T. *Chem. Eur. J.*, **2006**, 12, 9276-9283.
121. Sheats, J. R. *J. Phys. Chem.*, **1990**, 94, 7194-7200.
122. Wong, H. C.; Higgins, A. M.; Wildes, A. R.; Douglas, J. F.; Cabral, J. T. *Adv. Mater.*, **2013**, 25, 985-991.
123. Lee, J.; Maddipatla, M. V. S. N.; Joy, A.; Vogt, B. D.; *Macromolecules,* **2014**, 47, 2891–2898.
124. Balta, D. K.; Arsu, N.; Yagci, Y.; Sundaresan, A. K.; Jockusch, S.; Turro, N. J. *Macromolcules*, **2011**, 44, 2531-2535.
125. Lauer, A.; Dobryakov, A. L.; Kovalenko, S. A.; Fidder, H.; Heyne, K. *Phys. Chem. Chem. Phys*. **2011**, 13, 8723-8732.
126. Bratschkov, C. *Eur. Polym. J.,* **2001,** 37, 1145-1149.
127. Hargreaves, J. S. *J. Polym. Sci., Part A: Polym. Chem.,* **1989,** 27, 203-216.
128. Popov, A. P.; Veniaminov, A. V.; Goncharov, V. F. *SPIE*, **1994**, 2215, 113-124.
129. Cui, L.; Ranade, A. N.; Matos, M. A.; Dubois, G.; Dauskardt, R. H. *ACS Appl. Mater. Interfaces*, **2013**, 5, 8495-8504.
130. Yang, P.; Yang, W.; *ACS Appl. Mater. Interfaces*, **2014**, 6 , 3759–3770.
131. Gonzalez, E.; Hicks, R. F. *Langmuir*, **2010**, 26, 3710−3719.
132. Gonzalez, E.; Barankin, M. D.; Guschl, P. C.; Hicks, R. F. *Langmuir*, **2008**, 24, 12636−12643.
133. Doi, M.; Edwards, S. F. The Theory of Polymer Dynamics; Clarendon Press: Oxford, **1986**.

134. Carman, M. L.; Estes, T. G.; Feinberg, A. W.; Schumacher, J. F.; Wilkerson, W.; Wilson, L. H.; Callow, M. E.; Callow, J. A.; Brennan, A. B. *Biofouling* **2006,** 22, 11-21.
135. Zhao, Y.; Xie, Z.; Gu, H.; Zhu, C.; Gu, Z. *Chem. Soc. Rev.* **2012,** 41, 3297-3317.
136. Perera-Costa, D.; Bruque, J. M.; González-Martín, M. L.; Gómez-García, A. C.; Vadillo-Rodríguez, V. *Langmuir* **2014**.
137. Oster, G.; Oster, G. K.; Moroson, H. *J. Polym. Sci.* **1959,** 34, 671-684.
138. Carroll, G. T.; Sojka, M. E.; Lei, X.; Turro, N. J.; Koberstein, J. T. *Langmuir* **2006,** 22, 7748-7754.
139. Carroll, G. T.; Turro, N. J.; Koberstein, J. T. *J. Colloid Interface Sci.* **2010,** 351, 556-560.
140. Carroll, G. T.; Devon Triplett, L.; Moscatelli, A.; Koberstein, J. T.; Turro, N. J. *J. Appl. Polym. Sci.* **2011,** 122, 168-174.
141. Ubukata, T.; Yamamoto, S.; Moriya, Y.; Fujii, S.; Yokoyama, Y. *J. Photopolym. Sci. Technol.* **2012,** 25, 675-678.
142. Maher, M. J.; Bates, C. M.; Blachut, G.; Sirard, S.; Self, J. L.; Carlson, M. C.; Dean, L. M.; Cushen, J. D.; Durand, W. J.; Hayes, C. O.; Ellison, C. J.; Willson, C. G. *Chem. Mater.* **2014,** 26, 1471-1479.
143. Hall, D. B.; Underhill, P.; Torkelson, J. M. *Polym. Eng. Sci.* **1998,** 38, 2039-2045.
144. National Institute of Advanced Industrial Science and Technology. Spectral Database for Organic Compounds. http://sdbs.riodb.aist.go.jp/sdbs/
145. Carbone, N. D.; Ene, M.; Lancaster, J. R.; Koberstein, J. T. *Macromolecules* **2013**.
146. Prucker, O.; Naumann, C. A.; Rühe, J.; Knoll, W.; Frank, C. W. *J. Am. Chem. Soc.* **1999,** 121, 8766-8770.
147. Christensen, S. K.; Chiappelli, M. C.; Hayward, R. C. *Macromolecules* **2012,** 45, 5237-5246.
148. Inoue, T.; Cicerone, M. T.; Ediger, M. D. *Macromolecules* **1995,** 28, 3425-3433.
149. Cicerone, M. T.; Blackburn, F. R.; Ediger, M. D. *Macromolecules* **1995,** 28, 8224-8232.
150. Siebrand, W.; Wildman, T. A. *Acc. Chem. Res.* **1986,** 19, 238-243.
151. Albery, W. J.; Bartlett, P. N.; Wilde, C. P.; Darwent, J. R. *J. Am. Chem. Soc.* **1985,** 107, 1854-1858.
152. Levin, P. P.; Khudyakov, I. V. *J. Phys. Chem. A* **2011,** 115, 10996-11000.
153. Macosko, C. W.; Miller, D. R. *Macromolecules* **1976,** 9, 199-206.
154. Miller, D. R.; Macosko, C. W. *Macromolecules* **1976,** 9, 206-211.
155. Brown, R. G.; Porter, G. *J. Chem. Soc., Faraday Trans. 1* **1977,** 73, 1569-1573.
156. Deeg, F. W.; Pinsl, J.; Braeuchle, C. *J. Phys. Chem.* **1986,** 90, 5715-5719.
157. Millan, M. D.; Locklin, J.; Fulghum, T.; Baba, A.; Advincula, R. C. *Polymer* **2005,** 46, 5556-5568.
158. Russell, T. P.; Coulon, G.; Deline, V. R.; Miller, D. C. *Macromolecules* **1989,** 22, 4600-4606.
159. Mansky, P.; Russell, T. P.; Hawker, C. J.; Pitsikalis, M.; Mays, J. *Macromolecules* **1997,** 30, 6810-6813.

160. Peters, R. D.; Yang, X. M.; Kim, T. K.; Sohn, B. H.; Nealey, P. F. *Langmuir* **2000,** 16, 4625-4631.
161. Janes, D. W.; Thode, C. J.; Willson, C. G.; Nealey, P. F.; Ellison, C. J. *Macromolecules* **2013,** 46, 4510-4519.
162. Rochon, P.; Batalla, E.; Natansohn, A. *Appl. Phys. Lett.* **1995**, 66, 136.
163. Kim, D.Y.; Tripathy, S.K.; Li, L.; Kumar, J. *Appl. Phys. Lett.* **1995**, 66, 1166.
164. Viswanathan, N. K.; Kim, D. Y.; Bian, S.; Williams, J.; Liu, W.; Li, L.; Samuelson, L.; Kumar, J.; Tripathy, S. K. *J. Mater. Chem.* **1999**, 9, 1941–1955.
165. Fukuda, T.; Matsuda, H.; Shiraga, T.; Kimura, T.; Kato, M.; Viswanathan, N. K.; Kumar, J.; Tripathy, S. K. *Macromolecules* **2000**, 33, 4220–4225.
166. Lagugne-Labarthet, F.; Buffeteau, T.; Sourisseau, C. *Phys. Chem. Chem. Phys.* **2002**, 4, 4020–4029.
167. Aissou, K.; Shaver, J.; Fleury, G.; Pecastaings, G.; Brochon, C.; Navarro, C.; Grauby, S.; Rampnoux, J.; Dilhaire, S.; Hadziioannou, G. *Adv. Mater.* **2013**, 25, 213–217.
168. Rho, Y.; Aissou, K.; Mumtaz, M.; Kwon, W.; Pecastaings, G.; Mocuta, C.; Stanecu, S.; Cloutet, E.; Brochon, C.; Fleury, G.; Hadziioannou, G. *Small* **2015**, 11, 6377–6383.
169. Snell, K. E.; Stéphant, N.; Pansu, R. B.; Audibert, J.; Lagugné-Labarthet, F.; Ishow, E. *Langmuir* **2014**, 30, 2926–2935.
170. Lee, S.; Jeong, Y.-C.; Park, J.-K. *Opt. Express* **2007**, 15, 14550–14559.
171. Ishow, E.; Brosseau, A.; Clavier, G.; Nakatani, K.; Pansu, R. B.; Vachon, J.; Tauc, P.; Chauvat, D.; Mendonça, C. R.; Piovesan, E. *J. Am. Chem. Soc.* **2007**, 129, 8970–8971.
172. Gritsai, Y.; Goldenberg, L. M.; Kulikovska, O.; Stumpe, J. *J. Opt. A Pure Appl. Opt.* **2008**, 10, 125304.
173. Priimagi, A.; Shevchenko, A. *J. Polym. Sci., Part B: Polym. Phys.* **2014**, 52, 163–182.
174. Lee, S.; Kang, H.S.; Park, J. *Adv. Mater.* **2012**, 24, 2069–2103.
175. Yager, K.G.; Barrett, C.J. *Curr. Opin. Solid State Mater. Sci.* **2001**, 5, 487–494.
176. Yager, K.G.; Barrett, C.J. *J. Photochem. Photobiol. A* **2006**, 182, 250–261.
177. Yager, K.G.; Barrett, C.J. *Macromolecules* **2006**, 39, 9320-9326.
178. Lim, H. S.; Han, J. T.; Kwak, D.; Jin, M.; Cho, K. *J. Am. Chem. Soc.* **2006**, 128, 14458-14459.
179. Ichimura, K.; Oh, S. K.; Nakagawa, M. *Science*, **2000**, 288, 1624-1626.
180. Delorme, N.; Bardeau, J. F.; Bulou, A.; Poncin-Epaillard, F. *Langmuir* **2005,** *21,* 12278-12282.
181. Ahmad, N. M.; Lu, X.; Barrett, C. J. *J. Mater. Chem.*, **2010**, 20, 244–247.
182. Yamashita, N.; Watanabe, S.; Nagai, K.; Komura, M.; Iyoda, T.; Aida, K.; Tadac, Y.; Yoshida, H. *J. Mater. Chem. C,* **2015**, 3, 2837 -2847.
183. Nakai, T.; Tanaka, D.; Hara, M.; Nagano, S.; Seki, T. *Langmuir* **2016**, *32*, 909–914.
184. Zettsu, N.; Seki, T. *Macromolecules* **2004**, 37, 8692-8698.
185. Isayama, J.; Nagano, S.; Seki, T. *Macromolecules* **2010**, 43, 4105–4112.

186. Hayata, Y.; Nagano, S.; Takeoka, Y.; Seki, T. *ACS Macro Lett.* **2012**, *1*, 1357-1361.
187. Nakahara, H.; Fukuda, K. *J. Colloid Interface Sci*, **1983**, 93, 530-539.
188. Lin-Vien, D.; Colthup, N.B.; Fateley, W.G.; Grasselli, J.G.The Handbook of Infrared and Raman Characteristic Frequencies of Organic Molecules, Academic Press, Boston, 1991.
189. Ihs, A.; Uvdal, K.; Liedberg, B. *Langmuir* **1993**, 9, 733-739.
190. Kurita, N.; Tanaka, S.; Itoh, S. *J. Phys. Chem. A* **2000**, 104, 8114-8120.
191. Bouwstra, J. A.; Schouten, A.; Kroon, J. *Acta Crystallogr.* **1983**, C39, 1121.
192. Traetteberg, M.; Hilmo, I.; Hagen, K. *J. Mol. Struct.* **1977**, 39, 231.
193. Hurduc, N.; Donose, B. C.; Macovei, A.; Paius, C.; Ibanescu, C.; Scutaru, D.; Hamel, M.; Branza-Nichita, N.; Rocha, L. *Soft Matter*, **2014**, 10, 4640–4647.
194. Fang, G. J.; Maclennan, J. E.; Yi, Y.; Glaser, M. A.; Farrow, M.; Korblova, E.; Walba, D. M.; Furtak, T. E.; Clark, N. A. *Nat. Commun*., **2013**, 4, 1521.
195. Karageorgiev, P.; Neher, D.; Schulz, B.; Stiller, B.; Pietsch, U.; Giersig M.; Brehmer, L. *Nat. Mater.*, **2005**, 4, 699–703.
196. Yager, K. G.; Tanchak, O. M.; Godbout, C.; Fritzsche, H.; Barrett, C. J. *Macromolecules* **2006**, 39, 9311-9319.
197. Tanchak, O. M; Barrett, C. J. *Macromolecules* **2005,** 38*,* 10566-10570.
198. Sachan, P.; Kulkarni, M.; Sharma, A. *Langmuir*, **2015**, 31, 12505–12511.
199. Li, W.; Dohi, T.; Hara, M.; Nagano, S.; Haba, O.; Yonetake, K.; Seki, T. *Macromolecules* **2012**, 45, 6618−6627.
200. Zettsu, N.; Ogasawara, T.; Arakawa, R; Nagano, S.; Ubukata, T.; Seki, T. *Macromolecules* **2007**, 40, 4607−4613.
201. Benzaquen, M.; Fowler, P.; Jubin, L.; Salez, T.; Dalnoki-Veress, K.; Raphael, E. *Soft Matter*, **2014**, 10, 8608–8614.
202. Benzaquen, M.; Ilton, M.; Massa, M. V.; Salez, T.; Fowler, P.; Raphael, E.; Dalnoki-Veress, K. *Appl. Phys. Lett.* **2015**, 107, 053103.
203. Garcia-Amoros, J.; Sanchez-Ferrerz, A.; Massad, W. A.; Nonell, S.; Velasco, D. *Phys. Chem. Chem. Phys.* **2010**, 12, 13238–13242.
204. Balkeneende, A. R.; van de Boogaard, H. J. A. P.; Scholten, M.; Willard, N. P. *Langmuir* **1998**, 14, 5907-5912.
205. Fukuhara, K.; Nagano, S.; Hara, M.; Seki, T. *Nat. Commun.* **2014**, 5, 3320.
206. Cognard, J.; *Mol. Cryst. Liq. Cryst.* **1982**, 1, 71−77.
207. Fukuhara, K.; Fujii, Y.; Nagashima, Y.; Hara, M.; Nagano, S.; Seki, T. *Angew. Chem., Int. Ed.* **2013**, 52, 5988−5991.
208. Komura, M.; Yoshitake, A.; Komiyama, H.; Iyoda, T.; *Macromolecules* **2015**, 48, 672−678.
209. Okano, K. *Jpn. J. Appl. Phys*. **1983**, 22, L343.
210. Schmitt, F. J.; Müller, M. *Thin Solid Films* **1997**, 310, 138−147.
211. Kimura, H.; Nakano, H. *J. Phys. Soc. Jpn.* **1985**, 54, 1730−1736.
212. Tanaka, D.; Nagashima, Y.; Hara, M.; Nagano, S.; Seki, T. *Langmuir* **2015**, 31, 11379−11383

213. Yamashita, N.; Watanabe, S.; Nagai, K.; Komura, M.; Iyoda, T.; Aida, K.; Tadac, Y.; Yoshida, H. *J. Mater. Chem. C,* **2015**, 3, 2837 -2847.
214. Nakai, T.; Tanaka, D.; Hara, M.; Nagano, S.; Seki, T. *Langmuir* **2016**, *32*, 909–914.
215. Zettsu, N.; Seki, T. *Macromolecules* **2004**, 37, 8692-8698.
216. Zhang, H.; Zhang, J.; Li, H,; Liu, Z,; Li, H. *Mater Sci Eng. C* **1999**, 8–9, 179–185.
217. Nakahara, H.; Fukuda, K. *J. Colloid Interface Sci*. **1983**, 93, 530-539.
218. Lin-Vien, D.; Colthup, N. B; Fateley, W. G.; Grasselli, J. G.The Handbook of Infrared and Raman Characteristic Frequencies of Organic Molecules, Academic Press, Boston, 1991.
219. His, A.; Uvdal, K.; Liedberg, B. *Langmuir* **1993**, 9, 733-739.
220. Tanchak, O. M.; Barrett, C. J. *Macromolecules* **2005,** 38*,* 10566-10570.
221. Park, S. M.; Stoykovich, M. P.; Ruiz, R.; Zhang, Y.; Black, C. T.; Nealey, P. E., *Adv. Mater.* **2007,** 19, 607-611.
222. Bita, I.; Yang, J. K. W.; Jung, Y. S.; Ross, C. A.; Thomas, E. L.; Berggren, K. K., *Science* **2008,** 321, 939-943.
223. Segalman, R. A.; Yokoyama, H.; Kramer, E. J., *Adv. Mater.* **2001,** 13, 1152-1155.
224. Weinkauf, D. H.; Kim, H. D.; Paul, D. R. *Macromolecules* **1992**, 25,788-796.
225. Park, J. Y.; Paul, D. R.; Haider, I.; Jaffe, M. *J. Polym. Sci., Part B: Polym. Phys.***1998**, 34,1741-1745.
226. Grell, M.; Bradley, D. D. C.; Inbasekaran, M.; Woo, E. P. *Adv Mater.* **1997**, 9, 798-802.
227. Koren, I.; Koren, Z. *Proceedings of the IEEE* **1998,** *86*, 1819-1838.
228. Park, S. M.; Stoykovich, M. P.; Ruiz, R.; Zhang, Y.; Black, C. T.; Nealey, P. E. *Adv. Mater.* **2007**, 19, 607-611.
229. Ruiz, R.; Kang, H. M.; Detcheverry, F. A.; Dobisz, E.; Kercher, D. S.; Albrecht, T. R.; de Pablo, J. J.; Nealey, P. F. *Science* **2008**, 321, 936-939.
230. Cheng, J. Y.; Rettner, C. T.; Sanders, D. P.; Kim, H.-C.; Hinsberg, W. D. *Adv. Mater.* **2008**, 20, 3155-3158.
231. Inoue, T.; Janes, D. W.; Ren, J.; Suh, H. S.; Chen, X.; Ellsion, C. J.; Neaely, P. F. *Adv. Mater. Interfaces* **2015**, 2, 1500133.
232. Pujari, S.; Keaton, M. A.; Chaikin, P. M.; Register, R. A. *Soft Matter* **2012**, *8*, 5358-5363.
233. Gupta, V. K.; Krishnamoorti, R.; Chen, Z. R.; Kornfield, J. A.; Smith, S. D.; Satkowski, M. M.; Grothaus, J. T. *Macromolecules* **1996**, *29*, 875-884.
234. Alt. D. J.; Hudson, S. D.; Garay, R. O.; Fujishiro, K. *Macromolecules* **1995**, 28, 1575-1579.
235. Geary, J. M.; Goodby, J. W.; Kmetz, A. R.; Patel, J. S. *J. Appl. Phys.* **1987**, 62, 4100-4108.
236. Park, S.; Lee, D. H.; Xu, J.; Kim, B.; Hong, S. W.; Jeong, U.; Xu, T.; Russell, T. P. *Science* **2009,** *323*, 1030-1033.
237. Kim, B. H.; Lee, H. M.; Lee, J-H.; Son, S-W.; Jeong, S-J.; Lee, S.; Lee, D. I.; Kwak, S. U.; Jeong, H.; Shin, H.; Yoon, J-B.; Lavrentovich, O. D.; Kim, S. O. *Adv. Funct. Mater*. **2009**, 19, 2584-2591.

238. Madou, M. J. *Fundamentals of Microfabrication: The Science of Miniaturization*; Second Edition ed.; CRC Press: Boca Raton, Florida, **2002**.
239. Ma, S. J.; Mannino, S. J.; Wagner, N. J.; Kloxin, C. J. *ACS Macro Lett.* **2013**, 2, 474−477.
240. Chiche, A.; Stafford, C. M.; Cabral, J. T. *Soft Matter* **2008**, 4, 2360−2364.
241. Chung, J. Y.; Nolte, A. J.; Stafford, C. M. *Adv. Mater*. **2009**, 21, 1358−1362.
242. Chandra, D.; Crosby, A. J. *Adv. Mater*. **2011**, 23, 3441−3445.